Lehrstuhl für Steuerungs- und Regelungstechnik
Technische Universität München
Prof. Dr./Univ. Tokio habil. Martin Buss

Exploitation of physical coupling for human-robot collaborative object manipulation

Philine Meister (geb. Donner)

Vollständiger Abdruck der von der Fakultät für Elektrotechnik und Informationstechnik der Technischen Universität München zur Erlangung des akademischen Grades eines

Doktor-Ingenieurs (Dr.-Ing.)

genehmigten Dissertation.

Vorsitzender: Prof. Dr. Eckehard Steinbach

Prüfer der Dissertation:

1. Prof. Dr./Univ. Tokio habil. Martin Buss
2. Prof. Dr. Torsten Kröger

Die Dissertation wurde am 23.04.2018 bei der Technischen Universität München eingereicht und durch die Fakultät für Elektrotechnik und Informationstechnik am 07.09.2018 angenommen.

Preface

The present thesis would not have been possible without the great support from many people to whom I would like to thank in the following. First, I would like thank my doctoral advisor Prof. Martin Buss for his trust in my work and the freedom and independence I had during my 5 years at his chair not only to shape my research, but also with respect to student theses supervision and teaching. For the possibility to delve into the world of academic research by visiting top conferences all over the world, substituting for him at a conference committee meeting, attending collaboration weeks with world-renowned research groups and also for the opportunity to teach in Singapore, I am truly thankful. Lastly, I would like to express my gratefulness for his encouragement to further pursue a career in academia. Many thanks as well to Marion Leibold, Dirk Wollherr and the administration and technical staff for providing support whenever needed.

Furthermore, I would like to thank Prof. Sandra Hirche for scientific discussions, for the possibility to collaborate with visitors, PostDocs and other PhD students at her lab and for being able to use her lab space and equipment for my experiments. I would like to express my gratitude to my collaborators and co-authors, Alex, Ivana and Satoshi. Thank you, Alex, for being a mentor in the beginning of my PhD; special thanks for the great support during my first conference paper submission "all nighter". Thank you, Ivana, for interesting discussions and for your efforts in bringing together our research approaches. I am deeply grateful to Satoshi for introducing me into psychology and statistics and for his great help and efforts during many rounds of paper improvement. Special thanks also go to Denis for fun discussions and joint experiments and to Dominik for his great help with setting up two KUKA robots.

Likewise, I thank all my colleagues and especially the SHRINE team for the friendly, open and supportive atmosphere and prompt help whenever needed. Special thanks go to Markus, Stefan F. and Stefan K. for numerous scientific discussions. Sincere thanks also to my office mate Laith Alkurdi for all the discussions and fun moments we shared.

Many thanks also to my students Julian, Gabriel, Philipp W., Philipp A., Christian, Alisa, Jonas, Dimitrij, Janis, Robert, Max, Martin, Marco, Marius, Florian, Jing and Franz. Foremost, I thank you, Franz, for your commitment, enthusiasm and valuable input. You were a great collaborator and you have contributed a great deal to this thesis. Special thanks also go to Florian and Jing for adding important contributions to this thesis.

Finally, I would like to express my gratitude to my family, my friends and, most importantly, to you, Will. Thank you for your love, encouragement and understanding during this challenging period of my live.

Munich, April 2018 Philine Donner

Acknowledgment

The research leading to these results has received funding partly from the European Research Council under the European Union's Seventh Framework Programme (FP/2007-2013) / ERC Grant Agreement n. [267877] (shrine-project.eu) and the Technical University of Munich - Institute for Advanced Study (tum-ias.de), funded by the German Excellence Initiative.

Abstract

As robots leave the confines of industrial production, we envision robot assistants that physically support the elderly, help with the transport of objects and take over labor intensive rehabilitation. In order to fully exploit the benefits of physical human-robot collaboration (pHRC), robot behavior that is goal-oriented, efficient, intuitive and comfortable for a human partner is desirable.

To achieve the above desired characteristics, this thesis follows the approach to first study physical human-human collaboration (pHHC). The gained insights are then combined with system theoretic approaches to synthesize controllers for pHRC. We investigate two distinct human-robot collaborative object manipulation scenarios: collaborative object transport as an example of kinematic manipulation and collaborative energy injection into flexible objects as an example of dynamic manipulation. The forces and torques (i.e., wrench) applied by the partners during collaborative object transport generally do not fully contribute to the resultant object wrench, but partly compensate each other. Studies in controlled laboratory environments indicate that compensation wrench is a source of haptic information exchange among the agents, including disagreement and action intention. The importance of wrench-based intention communication during collaborative object transport in realistic environments has not been throughly investigated to date. One reason could be that the state of the art lacks a general physically consistent method to decompose wrench applied by multiple agents into its compensation and manipulation components. Consequently, measures needed for controller synthesis and evaluation are missing. In contrast to kinematic manipulation of rigid objects, the state of flexible objects during dynamic manipulation cannot be inferred through simple kinematic relationships, but requires consideration of the object dynamics. Force and torque measurements can then provide robust and immediate feedback about the object state. Collaborative dynamic manipulation enlarges the manipulation repertoire of human-robot teams, but has hardly been explored to date. This thesis takes a first step into this new but promising field by investigating collaborative energy injection into bulky and flexible objects.

The main contributions of this thesis with respect to the above challenges are as follows. We present a general physically consistent wrench decomposition method and extend it to the quantification of measures for pHHC and pHRC such as disagreement, and load and energy share. We then apply the derived measures to a full-scale human-human object transport study. The study investigates haptic and legible motion-based intention communication and emerging coordination patterns during human dyadic object manipulation. In order to approach the complex task of collaborative flexible object swinging, we first separately investigate rigid and pendulum-like object swinging, which represent extremes of the physical coupling strength imposed by the object. Accounting for the strong coupling imposed by rigid objects, we conduct a human-human study. The study indicates that the arm – rigid object – arm system can be approximated by an abstract simple pendulum. We tackle the other extreme, collaborative swinging of pendulum-like objects, from a system theoretic perspective. We derive the fundamental dynamics representing the desired simple pendulum-like oscillation and design leader and follower controllers that rely on wrench measurements at their individual interaction points only. Finally, we combine the insights of human-human rigid object swinging with the fundamental dynamics-based approach to achieve collaborative swinging of unknown flexible objects.

Zusammenfassung

Nun, da Roboter die Käfige industrieller Produktion verlassen, stellen wir uns Robotergehilfen vor, die ältere Menschen unterstützen, beim Transport von Objekten helfen und körperlich anstrengende Rehabilitationsaufgaben übernehmen. Um die Vorteile physikalischer Mensch-Roboter Kollaboration (pMRK) vollständig zu nutzen, sollten Roboter zielgerichtet, effizient und für Menschen intuitiv und angenehm agieren.

Zur Erreichung der oben genannten, gewünschten Charakteristiken folgt diese Arbeit dem Prinzip, zuerst physikalische Mensch-Mensch Kollaboration (pMMK) zu untersuchen. Die dabei gewonnenen Erkenntnisse werden anschließend mit systemtheoretischen Ansätzen kombiniert, um Regler für pMRK zu synthetisieren. Zwei Mensch-Roboter kollaborative Objektmanipulationsszenarien werden genauer beleuchtet: kollaborativer Objekttransport als ein Beispiel kinematischer Manipulation und kollaborative Energiezufuhr in flexible Objekte als ein Beispiel dynamischer Manipulation. Die Kräfte und Momente, die durch die Partner während kollaborativem Objekttransport aufgebracht werden, tragen im Normalfall nicht vollständig zur/zum resultierenden Kraft/Moment bei, sondern kompensieren sich teilweise gegenseitig. Studien in kontrollierbarer Laborumgebung deuten darauf hin, dass Kompensationskräfte/-momente Quelle haptischen Informationsaustausches zwischen Teilnehmern, z.B. hinsichtlich Uneinigkeit und Intention sind. Die Bedeutung der kraft-/momentenbasierten Kommunikation von Intentionen während kollaborativem Objekttransport in realistischen Umgebungen ist bis heute nicht ausreichend untersucht worden. Ein möglicher Grund dafür ist der Mangel einer generell anwendbaren, physikalisch konsistenten Zerlegung aufgewendeter Kräfte/Momente in ihre kompensierten und manipulierenden Anteile. Somit fehlt die Möglichkeit, Regler systematisch zu bewerten und zu vergleichen. Im Gegensatz zu kinematischer Manipulation von starren Objekten kann der Zustand flexibler Objekte während dynamischer Manipulation nicht rein aus kinematischen Zusammenhängen ohne Betrachtung der Objektdynamik erschlossen werden. Kraft- und Momentenmessungen können hier robust und instantan Rückmeldung über den Objektzustand geben. Kollaborative dynamische Manipulation vergrößert das Manipulationsrepertoire von Mensch-Roboter Teams, wurde jedoch bisher kaum erforscht. Durch die Untersuchung kollaborativer Energiezufuhr in unhandliche und flexible Objekte geht die vorliegende Dissertation einen ersten Schritt in dieses neue, doch vielversprechende Gebiet.

Die zentralen wissenschaftlichen Beiträge dieser Dissertation zur Bewältigung oben genannter Herausforderungen setzen sich wie folgt zusammen: Eine allgemein gültige, physikalisch konsistente Kraft-/Momentenzerlegung wird hergeleitet und auf quantitative Maße für pMMK und pMRK wie beispielsweise Uneinigkeit und Last- und Energieverteilung erweitert. Die hergeleiteten Maße werden des Weiteren genutzt, um haptische und bewegungsbasierte Intentionskommunikation und sich entwickelnde Koordinationsverhaltensmuster einer Mensch-Mensch Objekttransportstudie zu untersuchen. Durch die separate Untersuchung des Schwingens starrer und pendelartiger Objekte, die Extreme in Bezug auf die durch das Objekt eingeprägte Kopplungsstärke darstellen, wird die komplexe Aufgabe kollaborativen Schwingens angegangen. In Anbetracht der starken Kopplung durch starre Objekte wird eine Mensch-Mensch Studie durchgeführt, die darauf hindeutet, dass das Arm - starres Objekt - Arm System als ein abstraktes Einfachpendel modelliert werden kann. Das andere Extrem kollaborativen Schwingens pendelartiger Objekte wird aus systemtheoretischer Sicht betrachtet. Basierend auf der fundamentalen Dynamik, die der gewünschten Einfachpendelschwingung zu Grunde liegt, werden Führer- und Nachfolgeregler synthetisiert, die nur auf Kraft-/Momentenmessungen am eigenen Interaktionspunkt angewiesen sind. Schließlich werden die Erkenntnisse der Mensch-Mensch Interaktion beim Schwingen starrer Objekte mit dem Ansatz fundamentaler Dynamik kombiniert, um kollaboratives Schwingen unbekannter flexibler Objekte zu erreichen.

Contents

1 Introduction **1**
1.1 Example scenarios and challenges 4
1.2 Contributions and outline 6

2 Physically consistent wrench decomposition for multi-effector manipulation of rigid objects **9**
2.1 Motivation 9
2.2 Related work 10
2.3 Problem formulation 12
2.3.1 Background 12
2.3.2 SoA in wrench decomposition 13
2.3.3 Force decomposition in 1D for two effectors 14
2.3.4 Problem statement for physically consistent wrench decomposition . 16
2.4 Wrench decomposition formulated as an optimization problem 20
2.4.1 Special case: point mass 21
2.4.2 Special case: three-fingered grasping 23
2.4.3 Special case: 2D beam 24
2.4.4 General rigid objects 25
2.5 Measures for analysis 25
2.5.1 Load share 26
2.5.2 Energy share 26
2.5.3 Disagreement 27
2.6 Evaluation in simulation 27
2.6.1 Shared control of a mobility assistance robot 28
2.6.2 Collaborative object transport 30
2.7 Discussion of Limitations 34
2.7.1 Uniqueness of the wrench decomposition solution 34
2.7.2 Computational cost of the optimization problem 35
2.8 Conclusions 35

3 Intention communication and coordination patterns during human-human collaborative object transport **37**
3.1 Motivation 37
3.2 Related work 38
3.3 Problem formulation 41
3.4 Experimental setup and procedure 42
3.4.1 Setup 42
3.4.2 Design 43

3.4.3 Procedure . . . 44
3.4.4 Data processing . . . 44
3.4.5 Measures . . . 45
3.5 Qualitative results . . . 45
3.5.1 Intention communication . . . 45
3.5.2 Coordination patterns . . . 46
3.6 Quantitative results . . . 47
3.6.1 Intention communication . . . 47
3.6.2 Coordination patterns . . . 52
3.7 Discussion . . . 54
3.7.1 Intention communication . . . 54
3.7.2 Coordination patterns . . . 56
3.7.3 From pHHC to pHRC . . . 56
3.8 Conclusions . . . 58

4 Controller synthesis for human-robot collaborative swinging of rigid objects based on human-human experiments 59
4.1 Motivation . . . 59
4.2 Related work . . . 60
4.3 Problem formulation . . . 63
4.3.1 A simple pendulum model for human-human collaborative swinging of rigid objects . . . 63
4.3.2 Controller synthesis for human-robot collaborative swinging of rigid objects . . . 65
4.4 Simple pendulum preliminaries . . . 66
4.4.1 The abstract torque-pendulum . . . 66
4.4.2 Energy equivalent, natural frequency and phase angle . . . 66
4.5 Human-human rigid object swinging experiments . . . 69
4.5.1 Experimental setup and procedure . . . 70
4.5.2 Experimental results and discussion . . . 70
4.6 Controller synthesis . . . 74
4.6.1 Leader control approach for the abstract torque-pendulum . . . 75
4.6.2 Application to two-agent rigid object swinging . . . 77
4.7 Evaluation in simulation . . . 79
4.7.1 Simulation setup . . . 79
4.7.2 Simulation conditions . . . 79
4.7.3 Simulation results and discussion . . . 80
4.8 Conclusions . . . 81

5 Energy control for collaborative swinging of known complex pendulum-like objects 83
5.1 Motivation . . . 83
5.2 Related work . . . 83
5.3 Problem formulation . . . 86
5.3.1 Pendulum-like objects . . . 86

5.3.2 Problem statement 87
5.4 Energy-control for the abstract cart-pendulum 89
5.4.1 The abstract cart-pendulum 89
5.4.2 Control approach 90
5.5 Application to two-agent object manipulation 92
5.5.1 Projection onto the abstract cart-pendulum 92
5.5.2 Energy control of the desired oscillation through excitation at the natural frequency 94
5.5.3 Damping of the undesired oscillation 96
5.6 Virtual reality experiments 98
5.6.1 Experimental setup 98
5.6.2 Experimental conditions and procedure 99
5.6.3 Measures for analysis 100
5.6.4 Results and Discussion 102
5.7 Real world experiments 105
5.7.1 Experimental setup 105
5.7.2 Measures for analysis 106
5.7.3 Experimental conditions and procedure 107
5.7.4 Results and Discussion 108
5.8 Conclusions 111

6 Adaptive energy control for collaborative swinging of unknown complex pendulum-like objects 114
6.1 Motivation 114
6.2 Related work 114
6.3 Problem formulation 116
6.3.1 The t-pendulum 116
6.3.2 Problem statement 118
6.4 Fundamental dynamics of the abstract cart-pendulum 119
6.4.1 The abstract cart-pendulum 119
6.4.2 Cartesian to polar state transformation 120
6.4.3 Extraction of the fundamental dynamics 121
6.5 Fundamental dynamics-based adaptive leader/follower structures 124
6.5.1 Natural frequency estimation 124
6.5.2 Amplitude factor based leader/follower design 125
6.5.3 Analysis of leader-follower structures 127
6.6 Application to the t-pendulum 128
6.7 Evaluation in simulation 129
6.7.1 Simulation setup 129
6.7.2 Measures 129
6.7.3 Stability limits of natural frequency estimation 131
6.7.4 Reference dynamics tracking 132
6.7.5 Energy share of the follower 132
6.8 Real-world experiments 134
6.8.1 Experimental setup 134

6.8.2 Measures for analysis 134
6.8.3 Experimental conditions and procedure 135
6.8.4 Results and Discussion 136
6.9 Conclusions 140

7 Combining results from rigid and pendulum-like object manipulation for adaptive energy control of unknown flexible objects 142
7.1 Motivation 142
7.2 Related work 143
7.3 Problem formulation 146
7.3.1 The afa-system 146
7.3.2 Problem statement 147
7.4 Fundamental dynamics of the abstract torque-pendulum 148
7.4.1 Extraction of fundamental dynamics 148
7.5 Fundamental dynamics-based adaptive leader/follower structures 149
7.6 Application to the afa-system 149
7.6.1 Fundamental dynamics-based controllers 149
7.6.2 Projection and energy-based controller for the afa-system 152
7.7 Evaluation in simulation 153
7.7.1 Simulation setup 153
7.7.2 Measures 153
7.7.3 Stability limits of natural frequency estimation 153
7.7.4 Reference dynamics tracking 154
7.7.5 Follower contribution 155
7.8 Real-world experiments 155
7.8.1 Experimental setup 156
7.8.2 Measures for analysis 157
7.8.3 Experimental conditions and procedure 158
7.8.4 Results and Discussion 158
7.9 Discussion of the fundamental dynamics-based approach 161
7.9.1 Embedding of proposed controllers in a robotic architecture 161
7.9.2 Dependence of robot follower performance on the human interaction partner 162
7.9.3 Alternatives to energy-based swing-up controllers 162
7.9.4 Alternative parameter estimation approaches 162
7.9.5 Stability of human-robot object manipulation 163
7.10 Conclusions 163

8 Conclusions and future directions 165
8.1 Outlook 169

A Work vs. force constraints 173

B The 2D beam solution 175
B.1 Case 1 175

B.2 Case 2 176
B.3 Case 3 180
B.4 Case 4 180

C Comparison of SoA wrench decomposition methods based on pHHI data 184

D Detailed derivations for the analysis of the fundamental dynamics based leader-follower structure 186

Bibliography 188

Notations

Abbreviations

SoA	state of the art
HRC, HHC	human-robot/human-human collaboration
pHRI, pHHI	physical human-robot/human-human interaction
DoF	degree of freedom
1D, 2D, 3D	1/2/3 dimensional
CoM	center of mass
RMSD	root-mean-square deviation
Ai	agent number i
$\mathcal{L}$	leader agent
$\mathcal{F}$	follower agent
v-pendulum	2-agent pointmass pendulum (v-shaped)
t-pendulum	2-agent pendulum with cylindrical mass (trapezoidal shape)
ara-systm	"arm - rigid object - arm" system
afa-system	"arm - flexible object - arm" system

Conventions

Scalars, Vectors and Matrices

Scalars are denoted by upper and lower case letters in italic type. *Vectors* are denoted by bold lower case letters in italic type, as the vector $\boldsymbol{x}$ is composed of elements x_i. *Matrices* are denoted by bold upper case letters in italic type, as the matrix $\boldsymbol{M}$ is composed of elements M_{ij} (i^{th} row, j^{th} column).

x or X	scalar
$\boldsymbol{x}$	vector
$\boldsymbol{X}$	matrix
$(\cdot)^\top$	transposed
$\boldsymbol{X}^{-1}$	inverse of $\boldsymbol{X}$
$\boldsymbol{X}^{+}$	pseudoinverse of $\boldsymbol{X}$
$\Vert \cdot \Vert$	2-norm

Symbols

$\boldsymbol{g}$	gravity vector
$\boldsymbol{I}_{(i\times i)}$	unity matrix $\in \mathbb{R}^{i\times i}$
$\mathbf{0}_{(i\times i)}$	zero matrix $\in \mathbb{R}^{i\times i}$
$\{\mathrm{w}\}$	world coordinate system
$\{\mathrm{o}\}$	object coordinate system
$\boldsymbol{p}$	3D point
$\boldsymbol{f}$	force vector
$\boldsymbol{t}$	torque vector
E, $\dot{E}$	energy and energy flow
$f(\cdot)$	function of $(\cdot)$
t	time
$\boldsymbol{u}$	input
$\boldsymbol{y}_{\mathrm{m}}$	measured output
$\dot{\boldsymbol{r}}$, $\boldsymbol{\Omega}$, $\boldsymbol{\xi}$	twist with translational and rotational velocity, $\boldsymbol{\xi} = \left[\dot{\boldsymbol{r}}^\top, \quad \boldsymbol{\Omega}^\top\right]^\top$
$m, j, \boldsymbol{J}, \boldsymbol{M}$	mass, moment of inertia entry and tensor, mass matrix
l	length
C	distance

Kinematic manipulation

All vectors are given in object coordinates {o}, unless stated otherwise.

$\boldsymbol{h}_i$	wrench $\boldsymbol{h}_i = \left[\boldsymbol{f}_i^\top \; \boldsymbol{t}_i^\top\right]^\top$ with force $\boldsymbol{f}_i$ and torque $\boldsymbol{t}_i$ of effector i
$\boldsymbol{r}_i$	position of effector i
$\boldsymbol{G}$, $\boldsymbol{G}^\dagger$, $\boldsymbol{G}^+_\Delta$, $\boldsymbol{G}^+_M$	grasp matrix and its Moore-Penrose/”nonsqueezing” [175]/ parametrized [55] pseudoinverses
$\boldsymbol{t}_f$	force induced torque
f_{A}	1D axial force acting inside a body
$\boldsymbol{a}$	axis of idealized spring
J	cost function
w	weighting factor for torque against force in J
s	selection parameter to in/exclude force induced torque in J
ϕ	factor weighting effector contributions
$\boldsymbol{\lambda}$	vector of Lagrange multipliers
$\boldsymbol{\mu}$	vector of Kuhn-Tucker multipliers
α	load share
γ	energy share
F_{c}, T_{c}	translational/rotational disagreement measure
β	combined translational and rotational disagreement measure
θ	beam rotation angle

Dynamic manipulation

All vectors are given in world coordinates {w}, unless stated otherwise.

$\boldsymbol{x}$	state vector

$\boldsymbol{r}, \dot{\boldsymbol{r}}, \ddot{\boldsymbol{r}}$	position, velocity, acceleration with respect to initial position
$r, \dot{r}, \ddot{r}$	position, velocity, acceleration in x-direction
Θ, θ, ψ	general, desired and undesired oscillation DoF
ρ	arm deflection angle of the afa-system
ϑ	oscillation DoF of abstract cart- and torque-pendulums
w, h	width, height
k, d	stiffness, damping
c_j	distance of pivot point of oscillation j to center of mass
$\mathcal{O}$	periodic orbit
E_j, j_E	energy of oscillation j, amplitude of oscillation j (energy equivalent)
t	torque around z-axis
a	amplitude factor
δ	energy threshold for amplitude factor computation
K_P, T_I, T_D, N	PID controller parameters
τ	inverse time constant
ϵ	(desired) energy range
ω	natural frequency
φ	phase angle
ϑ_r	phase space radius of ϑ-oscillation
$G_k(s)$, T_k, D_k	transfer function, time constant and damping of filter k
G_lp, G_hp	low pass filter, high pass filter
B	fundamental dynamics system parameter
T	time constant, instance or period
T_s, T_c, T_ps, T_pw	settling/completion/pulse start/pulse width time
$\boldsymbol{l}$	observer gain vector
Γ	integrated energy share
η	energy efficiency
e, o	error, overshoot
V	Lyapunov function
Ξ, Υ, M, Σ	sets
k	variable summarizing several system parameters
$\mathcal{D}$	discriminant

Subscripts and Superscripts

x^d	desired value of x
$\hat{x}$	estimated value of x
x_i, x_{iz}	x of agent/effector i, z-component of x_i
x_o	x of object/resultant x at object CoM
${}^\mathrm{w}x$, ${}^\mathrm{o}x$	x in world $\{\mathrm{w}\}$/ object $\{\mathrm{o}\}$ coordinates

Kinematic manipulation

x_c	compensation x
x_m	manipulation x

x_{lin}, x_{rot}	linear/rotational x
$x_{y\parallel}$, $x_{y\perp}$	component of x parallel/perpendicular to y
$x_{\mathrm{iso,l}}$, $x_{\mathrm{iso,r}}$	x of left/right isolation of an object cut at r_{cut}
x_{obs}	x to/of obstacle
$\bar{x}$	average x

Dynamic manipulation

x_{vP}, x_{tP}	x of v-/t-pendulum
x_{araS}, x_{afaS}	x of ara-/afa-system
x_{acP}, x_{atP}	x of abstract cart-/torque-pendulum
x^*	projection of x onto xy-plane
x_{h}, x_{a}, x_{s}, x_{w}, x_{j}	x of handle/arm/shoulder/wrist/joint
x_0	small angle approximation of frequency x
x_{eq}	equivalent x
x_{dis}	discrete x
$x_{j,i}$	x of/for oscillation j and agent i
x^{ref}	reference x
x_{id}, x_{gh}	x of initial display/first goal hit of goal sphere
x_{in}, x_{m}	input/measured x
$\bar{x}$	steady state of x
x_{l}, x_{u}	lower/upper x
$\tilde{x}$	estimation error of x

1 Introduction

The robots of today are leaving industrial cages and are slowly entering human workspaces. As vacuum robots or autonomous vehicles, robots have already become part of human daily life. New research fields as social robotics [62] evolved from the desire of creating robotic partners who can seamlessly support humans in all aspects of their daily activities. Although a lot of research is devoted to non-contact situations, contact cannot be avoided as soon as human and robot workspaces overlap and can even be desirable.

By making use of physical interaction, the robots of tomorrow will be able to physically assist the elderly and impaired [92, 112]. In workshops, cooperative object transport enables purely robotic or mixed human-robot teams to move heavy and bulky objects, which would be too heavy to be carried by an individual [84]. Furthermore, robots have great potential to take over labor-intensive rehabilitation [100] and can be used to train and assist surgeons [82]. Examples for social interaction and leisure scenarios that require physical contact are handshaking [178] or dancing [99].

Collaboration versus cooperation

Interaction scenarios as the ones above can be categorized according to the nature of the *roles* the agents take on; do they cooperate, collaborate or compete [86]. The category competition distinguishes itself through conflicting goals of the agents. The difference between *cooperation* and *collaboration*, however, is less obvious and highly debated. Roschelle and Teasley [153] differentiate between cooperation and collaboration based on whether the joint task is divided into subtasks that are solved by the agents individually (cooperation) or whether the agents are mutually engaged in a coordinated effort to solve the task together (collaboration). During physical interaction, the agents are directly coupled to each other, which limits the possibilities to divide the joint task into subtasks that can be solved individually. In [86], Jarrassé et al. classify physical interaction tasks according to role symmetry. Cooperation features asymmetric roles which are prescribed before task execution and stay constant until completion of the task. For example, during rehabilitation or surgeon training, the robot acts as a teacher with the goal to reduce the human's errors while gradually reducing its own task contribution. In elderly care or when supporting an expert surgeon, the robot would take on the role of an assistant, with the goal to take over as much task effort as possible. In contrast, during collaboration the agents are equal - thus, their roles are symmetric - while working towards the same goal. A human and a robot jointly transporting a bulky object to a goal location is an example for a collaborative task. However, the definitions above are not free of ambiguities [35]. It is known that humans tend to specialize and thus divide labor among each other also during collaboration [129, 152]. Thus, to achieve seamless human-robot collaboration, robots need to be able to take on roles and to dynamically adapt these roles to the human partner and the current situation.

In this thesis, we use the term collaborative in order to express the goal of designing robots that are capable of continuously coordinating and synchronizing with their partner for shared problem solving [153]. To this end, we look into human-human interaction to understand collaborative behavior and synthesize controllers that exhibit distinct roles. The distinct behaviors can then be combined with the knowledge of human-human interaction to dynamically switch between roles to suitably assist a human partner in different situations.

From human-human collaboration to human-robot collaboration

Physical human-robot interaction (pHRI) research started with passive robots which mainly compensated for gravity during human-robot collaborative object transport. The admittance controlled robots allowed humans to pull the object and with it the robot into a desired direction [98]. Such passive robot behavior does not only require the human to apply high forces to move object and robot, but also leaves the human with the complete planning and decision making effort. As we are interested in true collaboration, the goal is to design robots to act as actively contributing partners instead of passive tools. Active contribution requires the robot to contribute with own intentions, i.e. to plan actions towards the goal. Besides being *goal-oriented*, the interaction needs to be *efficient* in the sense that the agents work towards the same goal and share the task effort. Furthermore, the robot behavior should be *intuitive* and *comfortable* for the human partner; the interaction should require only minimum mental effort on the human side, i.e. the human should not have to learn how to interact with the robot. *Safety*, above all, is a prerequisite that needs to be ensured at all times.

The desired characteristics above necessitate an understanding of physical human-human collaboration (pHHC), which literature is lacking. Only if we understand the underlying principles of human trajectory planning, effort sharing, intention communication and negotiation we can synthesize robot controllers for seamless physical human-robot collaboration [132]. On the other hand, human likeness is not necessarily optimal with respect to robotic hardware or task performance. Therefore, in this thesis we follow the approach as displayed in Fig. 1.1: We study pHHC and combine the gained insights with system theoretic approaches in order to synthesize controllers for physical human-robot collaboration (pHRC).

Haptic communication

Consideration and exploitation of the mutual influence interacting agents have on each other is of great importance when designing controllers for natural human-robot interaction [171]. Mutual influence plays an even greater role during physical human-robot interaction, where the human and the robot are in physical contact, directly or indirectly via an object. Besides verbal communication, the physical coupling between the agents represents a powerful and especially fast channel for *haptic communication* [65, 74]. In this thesis, we focus on haptic information exchange. We are interested in better understanding the haptic modality in pHHC and to fully exploit it for pHRC before integrating further modalities as speech or gestures.

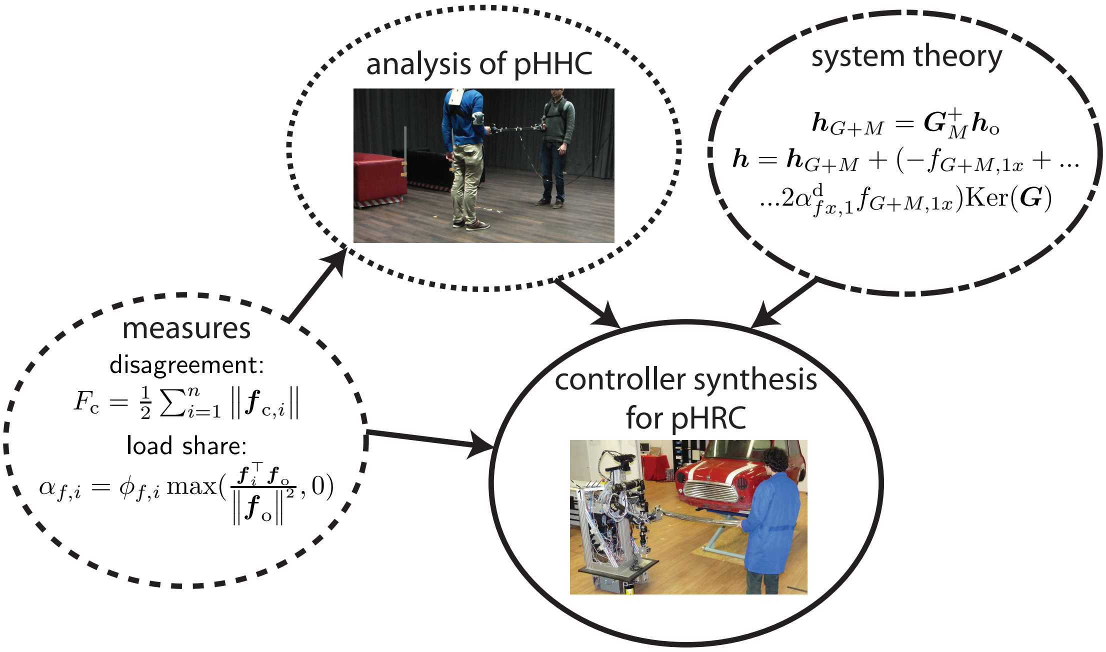

Fig. 1.1: Design methodology: Controller synthesis for physical human-robot collaboration (pHRC) [79] based on system theory [131] and insights from physical human-human collaboration (pHHC). Measures are required to analyze pHHC and to evaluate controllers for pHRC.

The forces and torques (i.e. wrench) applied during physical interaction do not fully contribute to motion but also partly compensate each other. Compensation wrench is considered as a source for haptic information exchange among the agents, including disagreement [152] and action intention [74]. However, up to now, no *physically consistent* method exists to *decompose applied wrench* into its compensation and manipulation components for multiple effectors and general objects. As a consequence, measures as *load share* and *disagreement* can only be evaluated for special cases, as, e.g., simplified 1D settings. Thus, the state of the art (SoA) lacks measures to analyze general pHHC and pHRC as needed for controller synthesis and evaluation (see Fig. 1.1).

Alongside developing physically consistent measures to analyze haptic information exchange, we are also interested in exploiting haptic signals to achieve manipulation goals. Force and torque measurements provide robust and immediate feedback about the object to be manipulated.

Kinematic versus dynamic manipulation

In this thesis, we focus on tasks where a human and a robot collaboratively manipulate an object. Thus, the human and the robot are not in direct contact, but are connected via the object they manipulate. On the one hand side, object manipulation poses interesting challenges; the object impedes direct intention estimation via transmitted forces due to grasp configuration and object dynamics. On the other hand side, the direct contact case can be regarded as a special case of object manipulation, such that our results can be directly transferred to direct contact scenarios as, e.g., during rehabilitation.

Mason and Lynch established a taxonomy of manipulation based on the considerations needed to plan, perform or analyze the manipulation operation [123]. *Kinematic manipulation* requires only kinematic considerations. Examples are pick and place operations during which the motion of the object is completely specified through the motion of the robotic end effector. The object is rigidly grasped and light enough such that forces and torques required for the manipulation do not have to be considered, and can simply be taken care of by a low level robot controller that enforces the desired end effector motion. Required considerations increase from *static manipulation* (consideration of static forces, e.g., for stable grasps) over *quasi-static manipulation* (consideration of friction forces, e.g., when pushing an object on a surface) to *dynamic manipulation*. Dynamic manipulation requires to take into account the object dynamics including the object inertia. Examples are juggling, throwing, catching ([119, 142, 157]) as well as the manipulation of underactuated mechanisms ([32]). Dynamic manipulation exploits the object dynamics instead of just tolerating it. As a consequence, objects can be manipulated faster, by simple end effectors and in an increased workspace.

Humans and animals show outstanding performance when it comes to explosive as well as cyclic motion as apparent in dynamic manipulation. Human-robot collaborative dynamic object manipulation combines the advantages of collaborative and dynamic manipulation to yield an increased manipulation repertoire; bulkier and heavier objects can be manipulated faster while explicitly considering kinematics and dynamics of the robot, the human and the object. Nevertheless, only few works exist on collaborative dynamic object manipulation; specifically only on rope turning [97, 121] and sawing and polishing [143, 144].

1.1 Example scenarios and challenges

In the present thesis, we make use of the following two human-robot collaborative object manipulation scenarios as exemplary kinematic and dynamic manipulation tasks:

Kinematic manipulation: Collaborative transport of rigid objects

A human and a robot collaboratively transport an object to a given goal location, e.g., through the door displayed in Fig. 1.2. We categorize this object transport scenario as kinematic manipulation: We assume that the agents rigidly grasp the object such that the object motion is defined by the effector motions based on kinematic considerations only. Such kinematic manipulation could theoretically be achieved through a centralized controller that operates on effector motion feedback only. However, physical interaction of two independent agents as a robot and a human, does require consideration of interaction forces and torques. The desired object trajectories of the two agents will never perfectly match, but need to be negotiated and adapted continuously. On a *low-level*, a combination of inverse dynamics and impedance controllers can yield goal-directed and at the same time compliant interaction. On a *high-level*, decisions as “who enters through the door first” have to be made. The strong coupling through the rigid object establishes a haptic communication channel that can be used to adapt to the partner on a low- and high-level:

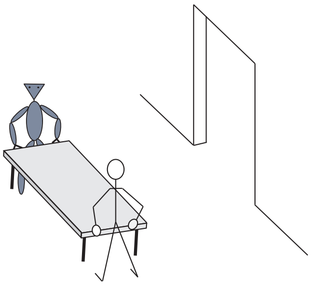

Fig. 1.2: Kinematic manipulation scenario: A human and a robot collaboratively transport a table from one room to another. Dependent on their configuration it might be unclear who enters through the door first.

For example, controller parameters can be tuned towards more passive behavior in case high resistance from the partner is felt and the intent of a desired entry order can be communicated and negotiated.

Dynamic manipulation: Collaborative energy injection into flexible objects

A human and a robot collaboratively inject energy into a flexible object during synchronized swing motion in order to place the object at an elevated location or outside their accessible workspace, e.g., placing of a sports mat onto a stack of mattresses as displayed in Fig. 1.3(b). The manipulation task is under-actuated due to the flexibility of the object. Consequently, the object dynamics needs to be taken into account. Based on this example scenario, we investigate collaborative swinging of underactuated objects as a first step towards combining the advantages of collaborative and dynamic object manipulation. The swinging motion naturally synchronizes the motion of the collaborating agents. Energy can be injected in a favorable arm configuration for a human interaction partner (stretched arm) and task effort can be shared among the agents. Furthermore, the accessible workspace of the human arm and robotic manipulator is increased by the swing motion of the object and by a possible subsequent throwing phase.

Open challenges

Along the scenarios above we address the following open challenges with respect to kinematic and dynamic collaborative object manipulation:

- **Haptic interaction measures:** Development of a physically consistent force and torque decomposition as a basis for load share and disagreement measures to analyze general human-human and human-robot kinematic object manipulation tasks. Introduction of suitable measures for the new field of dynamic manipulation and objects of varying flexibility.
- **Human modeling:** Extraction of models of pHHC with a focus on the manipulation of objects that induce a strong physical coupling between the human partners, i.e. during collaborative transport of rigid objects and collaborative energy injection into rigid objects.

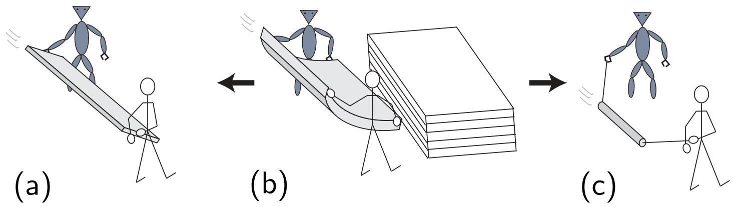

Fig. 1.3: Dynamic manipulation scenario: Collaborative energy injection into a sports mat to lift it onto a stack of mattresses (b). Interpretation of flexible object swinging (b) as a combination of rigid object swinging (a) and pendulum-like object swinging (c).

- **Exploitation of physical coupling:** Investigation of haptic intention communication strategies used by humans during collaborative object transport. Development of strategies to exploit the physical coupling during dynamic manipulation for different objects and thus different coupling strengths, i.e. in Fig. 1.3 rigid (a), flexible (b) and pendulum-like objects (c).
- **New research field "dynamic collaborative manipulation":** Investigation of collaborative energy injection into flexible objects as a first step towards the uncharted field of dynamic collaborative manipulation. Establishment of suitable leader and follower behavior.

1.2 Contributions and outline

Throughout this thesis, we address the challenges detailed in Section 1.1 along the design methodology of combining human insights with system theoretic approaches for the synthesis of robot controllers for pHRC as depicted in Fig. 1.1. The outline of the present thesis is illustrated in Fig. 1.4. Chapters 2 and 3 address open challenges particular to kinematic collaborative object transport. Chapters 4-7 investigate collaborative energy injection into flexible objects as a first step towards dynamic collaborative object manipulation. Exploitation of the physical coupling as a haptic communication channel is a common focus of all chapters. With respect to the kinematic manipulation task we investigate the importance and meaning of interaction forces and torques during human-human object transport. For the dynamic manipulation tasks we limit the robotic agents to measurements of its own applied force and torque. Thus, the robot has to use the haptic communication channel to infer both, the intention of the partner and the state of the object. Details on the contributions of the individual chapters are given in the following.

Chapter 2 presents a novel force and torque (i.e. wrench) decomposition method that allows to split applied wrench into its manipulation and compensation components. The proposed wrench decomposition method is the first to be generalizable to realistic settings such as when quantifying haptic communications in physical human-human interaction (pHHI) and pHRI tasks. We formulate wrench decomposition as a convex optimization problem which minimizes the Euclidean norms of manipulation forces and torques. By constraining the compensation and manipulation wrench by the actually applied wrench,

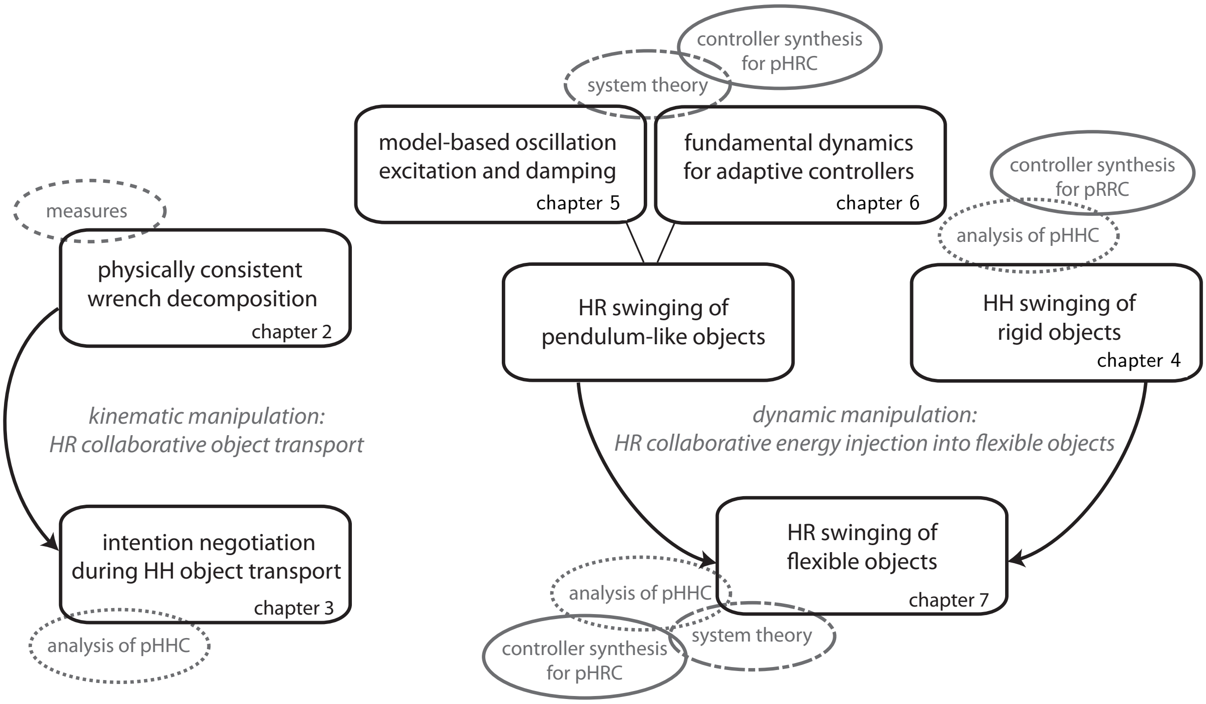

Fig. 1.4: Thesis overview: Chapters 2 and 3 address object transport as a human-robot collaborative kinematic manipulation task. Chapters 4-7 address energy injection into flexible objects as a human-robot collaborative dynamic manipulation task.

the optimization yields physically consistent solutions. We derive an analytical solution for the case that forces do not produce torque. Furthermore, we analyze specific cases of three-digit grasping and 2D beam manipulation, and show the applicability of our method to general object manipulation with multiple effectors. The wrench decomposition method is then extended to quantification of measures of interest found in pHHI and pHRI literature such as control disagreement, and load and energy share. We validate our approach via comparison to the SoA in simulated assistance and object transport scenarios. The results of this chapter were published previously in [41].

Chapter 3 studies haptic and legible motion-based intention communication and emerging coordination patterns during human dyadic object manipulation. For this purpose, we conduct a full-scale object transport study in which pairs of male participants transport a heavy object from different start configurations to a goal platform. The experimental setup requires the participants to make a decision on the entry order to the goal platform, similar to deciding on “who enters through the door first” in Fig. 1.2. We focus on decision making by means of motion and wrench adaptation at the interaction points with the object by prohibiting explicit communication via speech or gestures. Variation of the distance to the goal platform and guiding instructions allows to study the effect of environmental restrictions, task knowledge and role assignment on intention communication strategies and coordination patterns. We analyze the experimental data based on the measures derived in Chapter 2 and measures related to object pose and velocity. The results of this chapter were partly published previously in [41].

In order to approach the complex task of collaborative flexible object swinging displayed in Fig. 1.3(b), we split it up into its two extremes: swinging of pendulum-like objects, which oscillate themselves (Fig. 1.3(c)) and swinging of rigid objects, where the agents' arms together with the rigid object form an oscillating entity (Fig. 1.3(a)).

In Chapter 4, we investigate collaborative swinging of rigid objects (Fig. 1.3(a)). The strong coupling of the rigid object requires a robot partner to move human-like for comfortable pHRC. To this end, we conduct a human-human study. The results indicate that the arm – rigid object – arm system can be approximated by an abstract simple pendulum with two-sided unidirectional pulsed torque actuation. Based on these results, we synthesize robotic leader and follower controllers. Here, a leader excites the desired oscillation to a goal energy level and a follower damps undesired oscillations. The results of this chapter were published previously in [42].

In Chapter 5, we tackle the other extreme, collaborative swinging of pendulum-like objects (Fig. 1.3(c)) from a system theoretic perspective. The comparably loose coupling through the pendulum-like object prohibits direct access of the system states. By projecting the under-actuated mechanism in Fig. 1.3(c) onto an abstract cart-pendulum, we are able to separate desired and undesired oscillations. Employment of an energy-based controller allows to excite the desired oscillation up to a desired energy level, while actively damping an undesired oscillation. Leader and follower behavior is rendered based on the energetic state of the abstract cart-pendulum. We introduce energy flow imitation as a novel follower control concept for active task assistance even when the goal energy is unknown. The results of this chapter were partly published previously in [37, 38, 43].

The approach of Chapter 5 requires certain model parameters to be knwon, i.e. the length and mass of the abstract cart-pendulum approximation as well as the frequency of the undesired oscillation. In Chapter 6, we eliminate this requirement and present an adaptive swing-up controller that does not require a priori parameter knowledge. For this purpose, we derive the fundamental dynamics of the abstract cart-pendulum. Based on the fundamental dynamics, a simple adaptive mechanism identifies the natural frequency of the system. Through adaptation of an amplitude factor the robot renders leader or follower behavior. We analyze properties as stability of two proposed leader-follower structures based on the fundamental dynamics assumption. The results of this chapter were partly published previously in [39, 40, 44].

Chapter 7 combines the findings of Chapters 4-6 for human-robot collaborative energy injection into flexible objects as displayed in Fig. 1.3. We approximate the desired oscillation of the arm – flexible object – arm system by an abstract torque-pendulum. The fundamental dynamics of the abstract torque pendulum proves to essentially be the same as the one for the abstract cart-pendulum derived in Chapter 6. Thus, the same follower and leader controllers can be employed. The results of this chapter were partly published previously in [44].

The properties of the proposed controllers in Chapters 4-7 are continuously evaluated in simulation, virtual reality and real-world experiments. We extend the energy share measure of Chapter 2 and introduce energy efficiency as a novel measure to quantify effort sharing in collaborative dynamic object manipulation. In Chapter 8 we draw our conclusions and give directions for future work.

2 Physically consistent wrench decomposition for multi-effector manipulation of rigid objects

Summary. *This chapter derives a physically consistent wrench decomposition method that allows to separate wrench applied by multiple effectors to a general rigid object into its manipulation and compensation components. While the manipulation wrench accelerates the object, the part of the wrench that is compensated causes object stress and can indicate disagreement among the effectors. The chapter demonstrates*

- *formulation of wrench decomposition as a convex optimization that minimizes a manipulation wrench based cost function*
- *inequality constraints on force and torque level that ensure a physically consistent solution*
- *analysis of special cases: point mass, three fingered grasping and beam transport in 2D*
- *derivation of measures load and energy share and disagreement for the analysis of physical human-human and human-robot interaction*
- *method verification via simulated mobility assistance and 2D beam transport scenarios.*

The results of this chapter were published in [41].

2.1 Motivation

We envision future robotic helpers capable of relieving humans of physical and cognitive effort, e.g., in manufacturing, medical and home environments. Consequently, when a human moves an object together with a robot, the robot's behavior should be goal-oriented and efficient and the interaction should be intuitive, comfortable and safe for the human. Robot controllers that achieve the features above can be designed by investigating human-human collaborative object manipulation and combining the insights gained with, e.g., advanced motion planning methods.

On the one hand side, the strong coupling through a jointly grasped rigid object requires safety measures and the continuous interaction makes causality analyses challenging. On the other hand side, the object allows communication via the haptic modality: one can push the partner into the desired direction or signify disagreement by opposing the partner's applied force and torque (i.e. wrench).

When multiple human or robotic agents share the load of a rigid object, the applied wrench at the effectors will partly move the object and partly be compensated by the

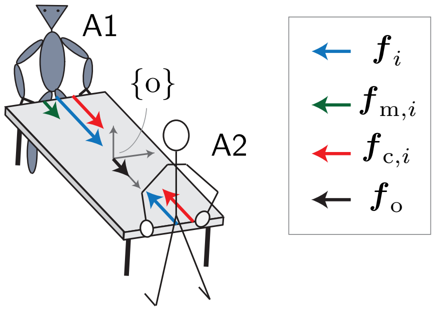

Fig. 2.1: Kinematic manipulation scenario: A robot (A1) and a human (A2) jointly transport a table. Applied forces by the effectors/hands of the two agents are combined to effective applied forces $\boldsymbol{f}_1$ and $\boldsymbol{f}_2$, respectively. The force applied by the robot $\boldsymbol{f}_1$ is partly compensated through the counteracting force applied by the human $\boldsymbol{f}_2 = \boldsymbol{f}_{\mathrm{c},2} = -\boldsymbol{f}_{\mathrm{c},1}$ and partly yields to the resultant force acting at the center of mass of the table at $\{\mathrm{o}\}$ that causes motion $\boldsymbol{f}_{\mathrm{o}} = \boldsymbol{f}_{\mathrm{m},1}$, with $\boldsymbol{f}_1 = \boldsymbol{f}_{\mathrm{m},1} + \boldsymbol{f}_{\mathrm{c},1}$. The compensation force could be interpreted as the desire of the human to slow down the motion or to even change the direction of the motion.

other agents (see Fig. 2.1). The part of the applied wrench that is compensated can serve as a source for haptic information exchange in which control disagreement [131, 141, 152] and action intention [74] need to be understood through the haptic signal. Thus, decomposition of an applied wrench into *manipulation wrench*, which potentially causes motion, and *compensation wrench*[1] is imperative to analyses of human-human and human-robot collaborative object manipulation and will be the focus of this chapter.

2.2 Related work

Wrench decomposition does also play a role in purely robotic multi-effector object manipulation and in robotic grasping. When multiple robotic effectors jointly control an object through rigid grasps, compensation wrench is often undesired as it produces stress inside the object [56, 175]. On the other hand, if objects are not grasped rigidly, as, e.g., when performing a precision grip, a certain level of compensation force is desired to generate sufficient friction to lift an object [19, 94].

Wrench decomposition based on pseudoinverse solutions

In the robotics case, the common approach is to use a pseudoinverse of the grasp matrix to compute the manipulation wrench the effectors need to apply to achieve a desired object state [13, 94, 175]. The grasp matrix relates applied wrench to the resultant wrench acting at the center of mass (CoM) of the object [156]. Compensation forces, that lie in the null-space of the grasp matrix and consequently do not influence the object acceleration [134],

---

[1] We use the term *compensation wrench* instead of the commonly used term *internal wrench* in order to avoid confusion; in mechanics, internal wrench exists inside an object and resists external wrench, e.g., [16, 147]. For objects that consist of multiple bodies, internal wrench can generate motion, e.g., [113, 114].

are added to the manipulation forces as needed by a task requirement [191, 197]. Kumar and Waldron interpret the difference of forces projected onto the connection lines of the interaction points as compensation force. They show that this compensation force is zero if the Moore-Penrose pseudoinverse is used to compute applied forces for three fingered grasping [105]. Further extensions of the pseudoinverse wrench decomposition have been successfully used for wrench synthesis, e.g., the virtual linkage model [181] for humanoid robots in complex multi-contact situations [159].

Approaches towards physically consistent wrench decomposition

However, such pseudoinverse solutions do not differentiate applied wrench in terms of how it leads to motion or object stress. Yoshikawa and Nagai [190] were among the first to recognize that the compensation force based on the pseudoinverse solutions does not show how tight an object is grasped. They instead used heuristics for a physically more consistent definition of compensation forces in a precision grasp, such that forces can only push but not pull. Groten et al. [72] build upon [190] and present force decomposition for the analysis of pHHI and pHRI tasks, though their application is limited to two effectors and one dimensional cases [131].

The lack of a generally applicable wrench decomposition method might have been the reason to refrain from compensation wrench based analysis in, e.g., [96] and analysis of resultant load share in [21]. Other works derived task specific definitions, with a focus on obtaining, e.g., disagreement measures tailored to the task of interest rather than physically consistent results. In [67], the one dimensional force decomposition solution of [72] was extended to the plane to evaluate a shared control strategy of a mobility assistance robot. Different force decompositions that allow to analyze human five fingered grasping were proposed in [66] and [162]. An alternative, but also task specific approach without physical consistency considerations was recently presented in [136], where minimum-jerk trajectories were used as a human motion model to decompose applied forces during a simple dyadic object transport task.

An important step towards physically consistent wrench decomposition was recently taken by Schmidts et al. in [158], by introducing force decomposition constraints motivated by mechanical work. The wrench decomposition solution for two effectors proposed in [127] satisfies the proposed constraints of [158] and constitutes a special case of the general wrench decomposition solution proposed by us in this chapter. Erhart and Hirche recently suggested a different decomposition approach for cooperative object manipulation that also includes the application of torque in [56] and is based on kinematic constraint violation of desired accelerations as presented in [172]. One of the main findings of their work is the existence of infinite different pseudoinverses of the grasp matrix that specify desired load shares of the effectors, although their computation of compensation wrench does not necessarily comply with the constraints of [158].

In order to overcome the case specificities and lack of physical consistency in existing approaches, this study contributes

- an extension of the force constraints proposed by [158] to the application of torque,

- a reformulation of the optimization proposed by [158] based on physical consistency considerations yielding a convex optimization problem,
- derivation of analytic solutions for special cases
- and wrench measures for analysis of pHRI and pHHI tasks.

The result is a physically consistent wrench decomposition into manipulation and compensation components for rigid object manipulation. Our wrench decomposition method extracts compensation wrench, for the first time, in a form generalizable to realistic settings such as when quantifying haptic communications in pHHI and pHRI tasks beyond simplified laboratory settings as, e.g., in [74, 151].

Chapter overview

The remainder of this chapter is organized as follows. In Section 2.3, we motivate the need for a physically consistent wrench decomposition by a comparison to the state of the art (SoA) pseudoinverse solutions and formally state our problem. In Section 2.4, we formulate physically consistent wrench decomposition as an optimization problem and discuss the solutions for several special cases. Based on the proposed wrench decomposition, we introduce measures for the analysis of pHHI and pHRI tasks in Section 2.5 and apply them to simulation examples in Section 2.6. In Section 2.7 we discuss limitations and possible extensions of our work. Section 2.8 concludes the chapter.

2.3 Problem formulation

In this chapter, we address the problem of decomposing the wrench applied by n effectors to a rigid object into its motion and internal stress-inducing components in a physically consistent manner.

2.3.1 Background

We consider a rigid object as depicted in Fig. 2.2 with its object-fixed coordinate system $\{\mathrm{o}\}$ at the CoM. All vectors throughout this chapter are given in this coordinate system, unless stated otherwise. Force $\boldsymbol{f}_i \in \mathbb{R}^3$ and torque $\boldsymbol{t}_i \in \mathbb{R}^3$ at the i-th effector position at $\boldsymbol{r}_i \in \mathbb{R}^3$ are combined to the wrench vector $\boldsymbol{h}_i = \begin{bmatrix}\boldsymbol{f}_i^\top & \boldsymbol{t}_i^\top\end{bmatrix}^\top$. The grasp matrix $\boldsymbol{G} \in \mathbb{R}^{6\times 6n}$ relates the applied wrench $\boldsymbol{h} = \begin{bmatrix}\boldsymbol{h}_1^\top \dots \boldsymbol{h}_n^\top\end{bmatrix}^\top \in \mathbb{R}^{6n}$ to the resultant object wrench $\boldsymbol{h}_\mathrm{o} = \begin{bmatrix}\boldsymbol{f}_\mathrm{o}^\top & \boldsymbol{t}_\mathrm{o}^\top\end{bmatrix}^\top \in \mathbb{R}^6$ such that

$$\boldsymbol{h}_\mathrm{o} = \boldsymbol{G}\boldsymbol{h}, \tag{2.1}$$

with

$$G = \begin{bmatrix} \boldsymbol{I}_{3\times3} & \boldsymbol{0}_{3\times3} & \dots & \boldsymbol{I}_{3\times3} & \boldsymbol{0}_{3\times3} \\ [\boldsymbol{r}_1]_\times & \boldsymbol{I}_{3\times3} & \dots & [\boldsymbol{r}_n]_\times & \boldsymbol{I}_{3\times3} \end{bmatrix}, \tag{2.2}$$

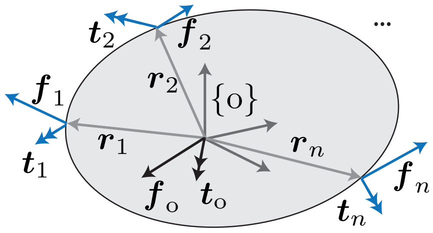

Fig. 2.2: Rigid object with kinematic quantities: The wrenches $\boldsymbol{h}_i = \left[\boldsymbol{f}_i^\top\ \boldsymbol{t}_i^\top\right]^\top$ with $i = 1, \ldots, n$ are applied at effector positions $\boldsymbol{r}_i$ in the object fixed coordinate system $\{\mathrm{o}\}$ and cause a resultant object wrench $\boldsymbol{h}_\mathrm{o} = \left[\boldsymbol{f}_\mathrm{o}^\top\ \boldsymbol{t}_\mathrm{o}^\top\right]^\top$ at the CoM of the object.

where $\boldsymbol{I}_{3\times 3}, \boldsymbol{0}_{3\times 3} \in \mathbb{R}^{3\times 3}$ are identity and zero matrices, and $[\boldsymbol{r}_i]_\times \in \mathbb{R}^{3\times 3}$ is the skew-symmetric matrix performing the cross product operation [156]. In the following, we refer to the torque induced by the applied force $\boldsymbol{f}_i$ as

$$\boldsymbol{t}_{f,i} = [\boldsymbol{r}_i]_\times \boldsymbol{f}_i \tag{2.3}$$

and to the resultant torque induced by each effector as

$$\boldsymbol{t}_{\mathrm{o},i} = \boldsymbol{t}_{f,i} + \boldsymbol{t}_i. \tag{2.4}$$

2.3.2 SoA in wrench decomposition

Wrench decomposition refers to splitting the applied wrench $\boldsymbol{h}$ into *manipulation wrench* $\boldsymbol{h}_\mathrm{m} = \left[\boldsymbol{h}_{\mathrm{m},1}^\top \ldots \boldsymbol{h}_{\mathrm{m},n}^\top\right]^\top \in \mathbb{R}^{6n}$ and *compensation wrench* $\boldsymbol{h}_\mathrm{c} = \left[\boldsymbol{h}_{\mathrm{c},1}^\top \ldots \boldsymbol{h}_{\mathrm{c},n}^\top\right]^\top \in \mathbb{R}^{6n}$

$$\boldsymbol{h} = \boldsymbol{h}_\mathrm{m} + \boldsymbol{h}_\mathrm{c}. \tag{2.5}$$

The compensation wrench lies in the null-space of the grasp matrix, and consequently it does not produce any resultant wrench $\boldsymbol{0}_{6\times 1} = \boldsymbol{G}\boldsymbol{h}_\mathrm{c}$. The manipulation wrench $\boldsymbol{h}_\mathrm{m}$ is responsible for the resultant object wrench $\boldsymbol{h}_\mathrm{o}$

$$\boldsymbol{h}_\mathrm{o} = \boldsymbol{G}\boldsymbol{h}_\mathrm{m} = \boldsymbol{G}\boldsymbol{h}. \tag{2.6}$$

The SoA in wrench decomposition is to use a pseudoinverse of the grasp matrix $\boldsymbol{G}^+$ to compute the manipulation wrench, which yields the decomposition

$$\boldsymbol{h}_{G+,\mathrm{m}} = \boldsymbol{G}^+\boldsymbol{G}\boldsymbol{h} \quad \text{and} \quad \boldsymbol{h}_{G+,\mathrm{c}} = (\boldsymbol{I}_{6n\times 6n} - \boldsymbol{G}^+\boldsymbol{G})\boldsymbol{h}. \tag{2.7}$$

The Moore-Penrose pseudoinverse $\boldsymbol{G}^+ = \boldsymbol{G}^\dagger$ yields the minimum norm solution for the manipulation wrench $\boldsymbol{h}_\mathrm{m}$, as used in [181, 191]. The Moore-Penrose pseudoinverse was put into question by a different "nonsqueezing" pseudoinverse $\boldsymbol{G}^+ = \boldsymbol{G}_\Delta^+$ by Walker et al. in [175], which computes manipulation wrenches that yield equal effector contributions to the resultant wrench $\boldsymbol{h}_\mathrm{o}$.

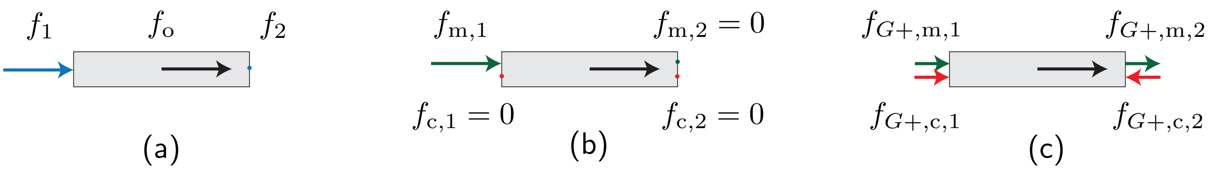

Fig. 2.3: Simple 1D example to illustrate the problem of wrench decomposition based on pseudoinverses: (a) Applied forces (blue) $f_1 = 2\,\mathrm{N}$ and $f_2 = 0$ and resultant object force (black) $f_\mathrm{o} = 2\,\mathrm{N}$, (b) proposed physically consistent wrench decomposition with manipulation forces (green) $f_{\mathrm{m},1} = f_1 = f_\mathrm{o} = 2\,\mathrm{N}$ and $f_{\mathrm{m},2} = 0$ and zero compensation forces $f_{\mathrm{c},1} = f_{\mathrm{c},2} = 0$, (c) wrench decomposition based on pseudoinverses with fixed load share yields manipulation forces $f_{\mathrm{m},1} = f_{\mathrm{m},2} = 0.5 f_\mathrm{o} = 1\,\mathrm{N}$ and compensation forces (red) $f_{\mathrm{c},i} = f_i - f_{\mathrm{m},i}$ with $i = 1, 2$.

Alternative approaches have been proposed to endow the compensation forces $\boldsymbol{f}_\mathrm{c}$ with a physical meaning. The virtual linkage model by Williams and Khatib proposes to interpret compensation forces as the forces that lock virtual prismatic actuators that connect the effectors [181]. Their extension to compensation torques that lock virtual spherical joints is a simplification and, as stated in their work, does not lead to a physically consistent decomposition. In [189], on the other hand, compensation forces are characterized as the forces that act inside a determinate truss that connects the effectors.

2.3.3 Force decomposition in 1D for two effectors

As stated in [55, 127, 158, 190], the use of pseudoinverse methods as described above does not allow for a physically consistent wrench decomposition. We illustrate the issues by a one dimensional (1D) example[2]. Consider the beam in Fig. 2.3(a) to which $f_1 = 2\,\mathrm{N}$ is applied at the left side but not at the right $f_2 = 0$. The resultant force that accelerates the object is $f_\mathrm{o} = 2\,\mathrm{N}$. No force is compensated and f_1 fully contributes to the resultant object acceleration. We thus conclude $f_{\mathrm{m},1} = 2\,\mathrm{N}$ and $f_{\mathrm{m},2} = f_{\mathrm{c},1} = f_{\mathrm{c},2} = 0$ (see Fig. 2.3(b)). The solution for the manipulation force in (2.7), however, equally distributes the resultant wrench $\boldsymbol{h}_\mathrm{o} = \boldsymbol{G}\boldsymbol{h}$ across the effector positions through multiplication with the pseudoinverse $\boldsymbol{G}^+$. For our simple example, (2.7) yields the same manipulation forces for the Moore-Penrose and the “non-squeezing” pseudoinverse where $f_{G+,\mathrm{m},1} = f_{G+,\mathrm{m},2} = 0.5 f_\mathrm{o} = 1\,\mathrm{N}$. The difference to the actually applied wrench $\boldsymbol{h}$ is interpreted as the compensation force where $f_{G+,\mathrm{c},1} = -f_{G+,\mathrm{c},2} = 1\,\mathrm{N}$ (see Fig. 2.3(c)). Thus, the decomposition is physically inconsistent; although no force is applied at r_2, this decomposition method claims that a force of $f_{G+,\mathrm{c},2} = -1\,\mathrm{N}$ at r_2 was compensated.

In order to better understand the commonly used pseudoinverse wrench decomposition, we compute the internal forces in the axial direction, f_A, that act inside the object body due to the applied external forces f_1 and f_2 [16] for the three 1D examples displayed on the left side of Fig. 2.4. In addition to the example of Fig. 2.3, where effector 1 alone produces the resultant object force f_o (Fig. 2.4(a)), we examine one example for equal

---

[2] For simplicity, we use scalars $f_i \in \mathbb{R}$ instead of vectors $\boldsymbol{f}_i \in \mathbb{R}^3$ for the one dimensional considerations in this section.

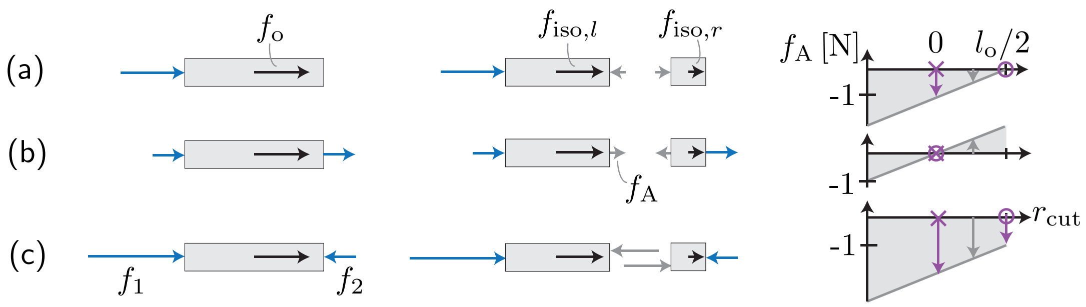

Fig. 2.4: Illustration of internal forces f_A inside an object subject to external forces f_1 and f_2: Left: 1D beam examples with applied forces f_1 and f_2 (blue) and resultant object force f_o (black) including (a) zero contribution of effector 2, (b) equal applied forces $f_1 = f_2$, (c) opposing applied force of effector 2. Center: Left and right isolations for an example cut at $r_\mathrm{cut} = \frac{l_\mathrm{o}}{4}$ and inscribed accelerating forces $f_\mathrm{iso,l}$ and $f_\mathrm{iso,r}$ (black) and internal force f_A (gray). Right: Resultant internal force diagrams for $r_\mathrm{cut} \in \left[-\frac{l_\mathrm{o}}{2}, \frac{l_\mathrm{o}}{2}\right]$ with inscribed internal force of the example cut at $r_\mathrm{cut} = \frac{l_\mathrm{o}}{4}$ in gray. The compensation forces for common pseudoinverse solutions ($\times$) and the proposed physically consistent decomposition ($\circ$) are inscribed in purple.

object force contributions with $f_1 = f_2 = 1\,\mathrm{N}$ (Fig. 2.4(b)) and one example where effector 2 applies an opposing force $f_1 = 3\,\mathrm{N}$ and $f_2 = -1\,\mathrm{N}$ (Fig. 2.4(c)). The internal force at a location r_cut acting inside the body can be obtained from the free body diagrams that result from virtually cutting the beam at r_cut, as illustrated in the center of Fig. 2.4. We assume the beam as rigid with uniform mass distribution and without loss of generality zero rotational velocity $\Omega_\mathrm{o} = 0$. For the three simple examples in Fig. 2.4(a), the resultant force and torque are $f_\mathrm{o} = 2\,\mathrm{N}$ and $t_\mathrm{o} = 0$. Thus, ${}^\mathrm{w}\dot{\Omega}_\mathrm{o} = 0$ and ${}^\mathrm{w}\ddot{r}_\mathrm{iso,l} = {}^\mathrm{w}\ddot{r}_\mathrm{iso,r} = {}^\mathrm{w}\ddot{r}_\mathrm{o} = \frac{f_\mathrm{o}}{m_\mathrm{o}}$, where ${}^\mathrm{w}\ddot{r}_\mathrm{iso,l}$ and ${}^\mathrm{w}\ddot{r}_\mathrm{iso,r}$ are the accelerations of the corresponding left and right isolations in world fixed coordinates $\{\mathrm{w}\}$. We deduce that the left isolation of mass $m_\mathrm{iso,l}$ must be accelerated by a force $f_\mathrm{iso,l} = \frac{m_\mathrm{iso,l}}{m_\mathrm{o}} f_\mathrm{o}$. The internal force present at r_cut can now be computed from the sum of forces $f_\mathrm{iso,l} = f_1 + f_\mathrm{A}$ (see center of Fig. 2.4). Variation of the cut location along the beam $r_\mathrm{cut} \in \left[-\frac{l_\mathrm{o}}{2}, \frac{l_\mathrm{o}}{2}\right]$ with beam length l_o yields the internal force diagrams[3] $f_\mathrm{A}(r_\mathrm{cut})$ shown on the right side of Fig. 2.4.

The pseudoinverse solutions ($\boldsymbol{G}^+ = \boldsymbol{G}^\dagger$ or $\boldsymbol{G}^+ = \boldsymbol{G}^+_\Delta$) are restricted to fixed load shares of the effectors $i = 1, 2$; for the beam in Fig. 2.3 and Fig. 2.4 $f_{G+,\mathrm{m},i} = 0.5 f_\mathrm{o}$. The results are physically inconsistent compensation forces whenever $f_i \neq 0.5 f_\mathrm{o}$: for (a) $f_{G+,\mathrm{c},2} = -1\,\mathrm{N}$ of applied force $f_2 = 0$ and for (c) $f_{G+,\mathrm{c},2} = -2\,\mathrm{N}$ of applied force $f_2 = -1\,\mathrm{N}$, i.e. the compensation forces exceed the applied forces. Purple crosses within the internal force diagrams on the right side of Fig. 2.4 indicate at which location r_cut the compensation force obtained by the pseudoinverse solutions $f_{G+,\mathrm{c},2} = -f_{G+,\mathrm{c},1}$ matches the internal force f_A within the beam.

Intuitively, a physically consistent wrench decomposition should yield zero compensation force for (a) and (b), as the applied forces fully contribute to the object acceleration. For (c), the force applied by effector 2 is compensated; i.e. we deduce $f_{\mathrm{c},1} = -f_{\mathrm{c},2} = 1\,\mathrm{N}$ and

---

[3] We adopt the common convention that $f_\mathrm{A} > 0$ when directed along the surface normal [16].

$f_{\mathrm{m},1} = f_\mathrm{o} = 2\,\mathrm{N}$, $f_{\mathrm{m},2} = 0$. Purple circles within the internal force diagrams on the right side of Fig. 2.4 indicate at which location r_cut the physically consistent compensation force solutions match the internal force f_A.

From the examples in Fig. 2.4 we observe:

- the beam subject to applied forces is never free of internal force $f_\mathrm{A} \neq 0$, also for equal load sharing, i.e. when the applied forces f_1 and f_2 are computed according to $\boldsymbol{h} = \boldsymbol{G}^{+}\boldsymbol{h}_\mathrm{o}$ (Fig. 2.4(b)).
- the pseudoinverse solutions yield compensation forces equal to the internal force acting at the CoM $f_{G+,\mathrm{c},2} = -f_{G+,\mathrm{c},1} = f_\mathrm{A}(r_\mathrm{cut} = 0)$.
- a physically consistent force decomposition should only yield nonzero compensation force, when forces are applied into opposing directions, e.g., $f_{\mathrm{c},2} = -f_{\mathrm{c},1} = -1\,\mathrm{N}$ (Fig. 2.4(c)). Different load shares (Fig. 2.4(a) and (b)) should not cause compensation forces, i.e. it should be possible to shift the zero crossing of $f_\mathrm{A}(r_\mathrm{cut})$ between $-\frac{l_\mathrm{o}}{2}$ and $\frac{l_\mathrm{o}}{2}$ with $f_{\mathrm{c},2} = f_{\mathrm{c},1} = 0$.

Based on the observations above, we propose analogously to [72] to compute compensation forces in 1D for effectors $i = 1, 2$ by

$$f_{\mathrm{c,i}} = \frac{1}{2}\,\mathrm{sgn}(f_i)(|f_1| + |f_2| - |f_1 + f_2|). \tag{2.8}$$

Note that for wrench synthesis, the Moore-Penrose pseudoinverse $\boldsymbol{G}^{\dagger}$ yields desired wrenches $\boldsymbol{h}^\mathrm{d} = \boldsymbol{G}^{\dagger}\boldsymbol{h}_\mathrm{o}^\mathrm{d}$ for given desired resultant wrenches $\boldsymbol{h}_\mathrm{o}^\mathrm{d}$ which result in zero compensation wrenches $\boldsymbol{h}_\mathrm{c} = 0$. The main drawback of $\boldsymbol{G}^{\dagger}$ is the fixed load shares among effectors which do not allow for a physically consistent analysis of measured wrench $\boldsymbol{h}$. As shown in [55] for a simple example, the "nonsqueezing" pseudoinverse $\boldsymbol{G}_{\Delta}^{+}$ can yield desired wrenches $\boldsymbol{h}^\mathrm{d}$ that are not free of compensation wrenches $\boldsymbol{h}_\mathrm{c} \neq 0$. Erhart and Hirche derive a parametrized pseudoinverse that represents infinite different load shares that will yield zero compensation wrench [55]. Based on the Gauss' principle, they compute applied effector wrenches given desired effector accelerations and object and effector kinematics and dynamics. Motivated by the reasoning that compensation wrench occurs whenever desired effector accelerations violate kinematic constraints, they propose to compute compensation wrench similarly to the effector wrenches in [55], but by exclusively considering the effector constraints [56]. However, the compensation wrench computation in [56] yields results that differ from our proposed physically consistent wrench decomposition[4].

2.3.4 Problem statement for physically consistent wrench decomposition

Compensation wrench is defined to lie in the null space of the grasp matrix. Thus, the virtual work by the compensation wrench $\boldsymbol{h}_\mathrm{c}$ needs to be zero for any virtual displacement

---

[4] Consider the example displayed in Fig. 2.4(a) wherein desired effector accelerations $\ddot{x}_1^\mathrm{d} = \frac{8}{3}\,\mathrm{m/s^2}$ and $\ddot{x}_2^\mathrm{d} = \frac{4}{3}\,\mathrm{m/s^2}$, effector masses $m_1 = m_2 = 1\,\mathrm{kg}$ and object mass $m_\mathrm{o} = 1\,\mathrm{kg}$ result in applied forces $f_1 = 2\,\mathrm{N}$ and $f_2 = 0$. However, compensation wrench computed according to [56] yields $f_{\mathrm{c},2} = -f_{\mathrm{c},1} = -\frac{2}{3}\,\mathrm{N}$. Thus, the compensation force $f_{\mathrm{c},2}$ exceeds the applied force f_2. See [55, 56] for details.

of the object [134] or of the effectors that satisfy the kinematic constraints [55]. We agree with the definitions above, but add further restrictions for physical consistency through the following definition of compensation wrench $\boldsymbol{h}_{\mathrm{c}}$.

Definition 1. *A* physically consistent compensation wrench $\boldsymbol{h}_{\mathrm{c}}$ *lies in the null space of the grasp matrix* $\mathbf{0}_{6\times 1} = \boldsymbol{G}\boldsymbol{h}_{\mathrm{c}}$ *and the components* $\boldsymbol{h}_{\mathrm{c},i}$ *of the effectors* $i = 1, \dots, n$ *obey the constraints*

$$\left\|\boldsymbol{f}_{\mathrm{c},i}\right\| \leq \boldsymbol{f}_i^\top \frac{\boldsymbol{f}_{\mathrm{c},i}}{\left\|\boldsymbol{f}_{\mathrm{c},i}\right\|}, \tag{2.9}$$

$$\left\|\boldsymbol{t}_{f\mathrm{c},i}\right\| \leq \boldsymbol{t}_{f,i}^\top \frac{\boldsymbol{t}_{f\mathrm{c},i}}{\left\|\boldsymbol{t}_{f\mathrm{c},i}\right\|}, \tag{2.10}$$

$$\left\|\boldsymbol{t}_{\mathrm{c},i}\right\| \leq \boldsymbol{t}_i^\top \frac{\boldsymbol{t}_{\mathrm{c},i}}{\left\|\boldsymbol{t}_{\mathrm{c},i}\right\|}, \tag{2.11}$$

where $\left\|\cdot\right\|$ *denotes the Euclidean norm.*

Fig. 2.5 illustrates the implications of the definition above in 2D for applied force $\boldsymbol{f}_i$. Let the applied force $\boldsymbol{f}_i$ in Fig. 2.5(a) be not fully contributing to the resultant object acceleration, but partly compensated by an opposing force. Here, we illustrate the opposing force by an idealized linear spring, where the spring can only generate opposing forces along its axis $\boldsymbol{a} \in \mathbb{R}^{3\times 1}$. The Euclidean norm of compensation force $\boldsymbol{f}_{\mathrm{c},i}$ is then upper bounded by the projection of the applied wrench $\boldsymbol{f}_i$ onto $\boldsymbol{a}$ in negative direction

$$\left\|\boldsymbol{f}_{\mathrm{c},i}\right\| \leq -\boldsymbol{f}_i^\top \boldsymbol{a}. \tag{2.12}$$

Variation of the direction of $\boldsymbol{a}$ changes the direction of possible compensation, as illustrated for another example in Fig. 2.5(b). All directions of $\boldsymbol{a}$ have in common that the compensation force $\boldsymbol{f}_{\mathrm{c},i}$ and the manipulation force $\boldsymbol{f}_{\mathrm{m},i}$ enclose a 90 deg angle for maximum Euclidean compensation force norm $\left\|\boldsymbol{f}_{\mathrm{c},i}\right\|$. Consequently, all physically consistent force decompositions of $\boldsymbol{f}_i$ are bounded by the dashed circle inscribed in Fig. 2.5(c). In 3D, the circular constraint extends to a sphere. As compensation can only occur in the opposite direction of $\boldsymbol{a}$, we can replace $\boldsymbol{a}$ with the negative normalized compensation force $\boldsymbol{a} = -\boldsymbol{f}_{\mathrm{c},i}\left\|\boldsymbol{f}_{\mathrm{c},i}\right\|^{-1}$ in (2.12) and obtain the constraint (2.9). The force inequality in (2.9) was first introduced by [158]. In Appendix A, we show that although the proposed circular constraint is required for a physically consistent wrench decomposition, it does not obey work constraints as stated in [158].

Fig. 2.5(d) shows a 2D example for constraint (2.10) with respect to force induced torque. Force $\boldsymbol{f}_i$ results in a torque $\boldsymbol{t}_{f,i}$ at the CoM around the negative z-axis, which again does not fully contribute to the resultant object acceleration, but is partly compensated by an opposing torque. The opposing torque is illustrated by an idealized torsional spring with axis $\boldsymbol{a}$ such that the torsional spring can only generate opposing torque around its axis $\boldsymbol{a}$. The Euclidean norm of the compensation torque $\boldsymbol{t}_{f\mathrm{c},i}$ is upper bounded by the projection of the applied force induced torque $\boldsymbol{t}_{f,i}$ onto $\boldsymbol{a}$ in negative direction

$$\left\|\boldsymbol{t}_{f\mathrm{c},i}\right\| \leq -\boldsymbol{t}_{f,i}^\top \boldsymbol{a}. \tag{2.13}$$

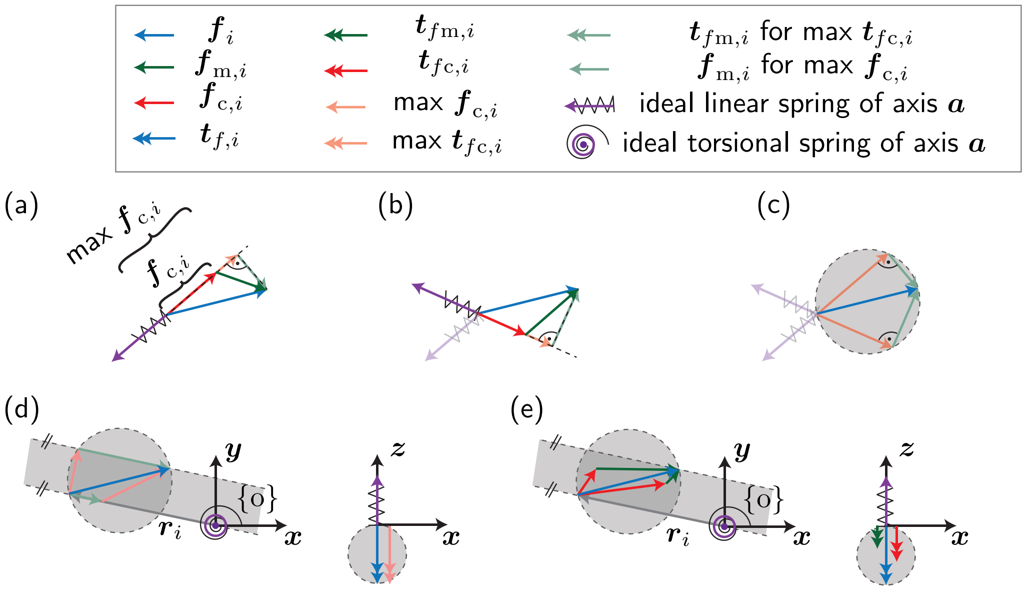

Fig. 2.5: Illustration of physically consistent compensation force in 2D: (a,b) Linear springs of axis $\boldsymbol{a}$ partly compensate applied force $\boldsymbol{f}_i$ in two different directions, (c) circular constraint for physically consistent compensation force $\boldsymbol{f}_{\mathrm{c},i}$ obtained via variation of compensation axis $\boldsymbol{a}$, (d,e) Torsional spring with axis $\boldsymbol{a}$ compensates torque $\boldsymbol{t}_{f,i}$ (right) induced by applied force $\boldsymbol{f}_i$ (left). Two different example decompositions where the torque induced by $\boldsymbol{f}_i$ is (d) completely compensated and (e) partly compensated, but to the same extent. The restriction that compensation torque cannot exceed the torque induced by $\boldsymbol{f}_i$ yields a band parallel to $\boldsymbol{r}_i$ as additional constraint in 2D force space, which is equivalent to a circular constraint in 2D torque space. 1D torque arrows along $\boldsymbol{z}$ are shown side by side for better visibility

For the 2D case in Fig. 2.5(d) this results in an additional constraint: the band delimited by the parallel dashed lines. The band constraint ensures that the compensation force $\boldsymbol{f}_{\mathrm{c},i}$ cannot represent a higher torque around the negative z-axis than the applied force $\boldsymbol{f}_i$ can induce. In 3D the constraint forms a cylinder spanned by the vector $\boldsymbol{r}_i$ and the applied force $\boldsymbol{f}_i$ in force space. In torque space, the constraint for force induced torque is a circle in 2D and a sphere in 3D. As torque compensation can only occur around the opposite direction of $\boldsymbol{a}$, we replace $\boldsymbol{a}$ with the normalized compensation torque $\boldsymbol{a} = -\boldsymbol{t}_{f\mathrm{c},i}\left\|\boldsymbol{t}_{f\mathrm{c},i}\right\|^{-1}$ in (2.13), and obtain the constraint (2.10). Analogously, constraint (2.11) for compensation torque $\boldsymbol{t}_{\mathrm{c},i}$ can be derived, which forms a circle in 2D and a sphere in 3D.

Complementary to Definition 1, we can also define physically consistent manipulation wrench.

Definition 2. *A* physically consistent manipulation wrench $\boldsymbol{h}_{\mathrm{m}}$ *achieves the object wrench* $\boldsymbol{h}_{\mathrm{o}} = \boldsymbol{G}\boldsymbol{h}_{\mathrm{m}}$ *and the components* $\boldsymbol{h}_{\mathrm{m},i}$ *of the effectors* $i = 1, \ldots, n$ *obey the constraints*

$$\left\|\boldsymbol{f}_{\mathrm{m},i}\right\| \leq \boldsymbol{f}_i^{\top} \frac{\boldsymbol{f}_{\mathrm{m},i}}{\left\|\boldsymbol{f}_{\mathrm{m},i}\right\|}, \tag{2.14}$$

$$\left\|\boldsymbol{t}_{f\mathrm{m},i}\right\| \;\leq\; \boldsymbol{t}_{f,i}^{\top}\frac{\boldsymbol{t}_{f\mathrm{m},i}}{\left\|\boldsymbol{t}_{f\mathrm{m},i}\right\|}, \tag{2.15}$$

$$\left\|\boldsymbol{t}_{\mathrm{m},i}\right\| \;\leq\; \boldsymbol{t}_{i}^{\top}\frac{\boldsymbol{t}_{\mathrm{m},i}}{\left\|\boldsymbol{t}_{\mathrm{m},i}\right\|}, \tag{2.16}$$

where $\left\|\cdot\right\|$ *denotes the Euclidean norm.*

Proposition 1. *The constraints* (2.9)-(2.11) *are equivalent to constraints* (2.14)-(2.16).

Proof. Multiplication of the inequalities (2.9)-(2.11) with the respective Euclidean norms $\left\|\boldsymbol{x}_{\mathrm{c}}\right\|$ with $\boldsymbol{x}_{\mathrm{c}} = \{\boldsymbol{f}_{\mathrm{c},i}, \boldsymbol{t}_{f\mathrm{c},i}, \boldsymbol{t}_{\mathrm{c},i}\}$ on both sides and insertion of $\left\|\boldsymbol{x}_{\mathrm{c}}\right\|^2 = \boldsymbol{x}_{\mathrm{c}}^{\top}\boldsymbol{x}_{\mathrm{c}}$ and $\boldsymbol{x}_{\mathrm{c}} = \boldsymbol{x} - \boldsymbol{x}_{\mathrm{m}}$ of (2.5) yields

$$\boldsymbol{x}_{\mathrm{m}}^{\top}\boldsymbol{x}_{\mathrm{m}} \;\leq \boldsymbol{x}^{\top}\boldsymbol{x}_{\mathrm{m}} \tag{2.17}$$

with pairs $(\boldsymbol{x}, \boldsymbol{x}_{\mathrm{m}}) = \{(\boldsymbol{f}_i, \boldsymbol{f}_{\mathrm{m},i}), (\boldsymbol{t}_{f,i}, \boldsymbol{t}_{f\mathrm{m},i}), (\boldsymbol{t}_i, \boldsymbol{t}_{\mathrm{m},i})\}$. Insertion of $\boldsymbol{x}_{\mathrm{m}}^{\top}\boldsymbol{x}_{\mathrm{m}} = \left\|\boldsymbol{x}_{\mathrm{m}}\right\|^2$ and rearrangements yield the constraints (2.14)-(2.16). □

Fig. 2.6 illustrates the implications of the manipulation based physical consistency definition in 2D for applied force $\boldsymbol{f}_i$. The decomposition example in Fig. 2.6(a) is physically inconsistent, because the Euclidean norm of the manipulation force $\boldsymbol{f}_{\mathrm{m},i}$ exceeds the projection of the applied force $\boldsymbol{f}_i$ onto the manipulation force $\boldsymbol{f}_{\mathrm{m},i}$. Thus, $\boldsymbol{f}_{\mathrm{m},i}$ violates the force constraint (2.14). In other words, the acceleration the manipulation force would cause at the CoM is not physically attainable by the applied force $\boldsymbol{f}_i$. Fig. 2.6(b) shows an example of a physically consistent force decomposition. Fig. 2.6(c) and (d) show examples for physically inconsistent and consistent force decompositions with respect to force induced torque, respectively. The manipulation force $\boldsymbol{f}_{\mathrm{m},i}$ in Fig. 2.6(c) would cause a rotational acceleration that exceeds the rotational acceleration induced by $\boldsymbol{f}_i$: $\left\|\boldsymbol{t}_{f\mathrm{m},i}\right\| > \left\|\boldsymbol{t}_{f,i}\right\|$. In contrast, the torque induced by the manipulation force example in Fig. 2.6(d) obeys constraints (2.14) and (2.15). Consequently, the manipulation force $\boldsymbol{f}_{\mathrm{m},i}$ would cause an acceleration of the object $\{\mathrm{o}\}$, which is physically attainable by the applied force $\boldsymbol{f}_i$.

Within the null space of the grasp matrix $\boldsymbol{G}$, Definition 1 and equivalently Definition 2, further restrict the compensation wrench solutions to obey $3n$ constraints for physical consistency. Still, infinite wrench decomposition solutions exist. We are interested in identifying the part of a given applied wrench $\boldsymbol{h}$ which was minimally necessary to achieve the resultant object wrench $\boldsymbol{h}_{\mathrm{o}}$: the manipulation wrench $\boldsymbol{h}_{\mathrm{m}}$. The difference of $\boldsymbol{h}_{\mathrm{m}}$ to h was then not necessary for manipulation, but was compensated: the compensation wrench $\boldsymbol{h}_{\mathrm{c}}$. Thus, we formulate our problem as follows.

Problem 1. *Decompose a given applied wrench* $\boldsymbol{h}$ *into manipulation wrench* $\boldsymbol{h}_{\mathrm{m}}$ *and compensation wrench* $\boldsymbol{h}_{\mathrm{c}}$ *for a given grasp matrix* $\boldsymbol{G}$ *with* $\boldsymbol{h} = \boldsymbol{h}_{\mathrm{m}} + \boldsymbol{h}_{\mathrm{c}}$*, such that the manipulation wrenches* $\boldsymbol{h}_{\mathrm{m},i}$ *applied by effectors* $i = 1, \ldots, n$ *represent a set of forces and torques of minimum Euclidean norm required to achieve a resultant object wrench* $\boldsymbol{h}_{\mathrm{o}} = \boldsymbol{G}\boldsymbol{h}$*, and such that the compensation wrench* $\boldsymbol{h}_{\mathrm{c}}$ *and the manipulation wrench* $\boldsymbol{h}_{\mathrm{m}}$ *are physically consistent according to Definition 1 and Definition 2, respectively.*

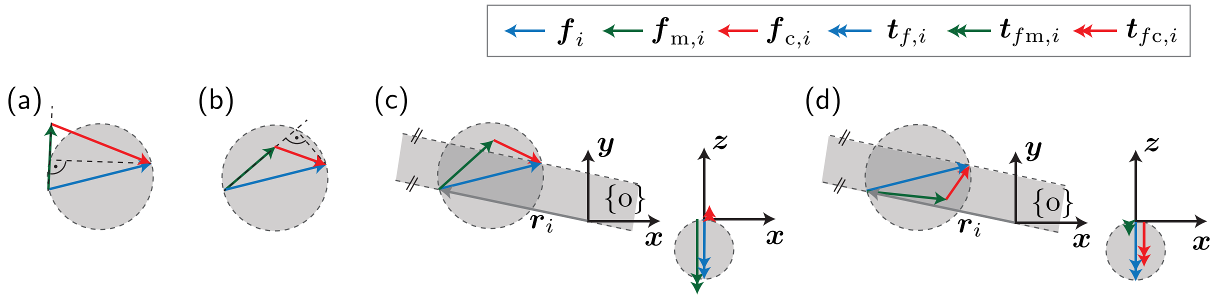

Fig. 2.6: Illustration of physically consistent manipulation force in 2D: Examples for physically inconsistent (a,c) and consistent (b,d) force decompositions. (a) The manipulation force $\boldsymbol{f}_{\mathrm{m},i}$ violates the circular force constraint, i.e. the linear acceleration produced by $\boldsymbol{f}_{\mathrm{m},i}$ is not attainable by the applied force $\boldsymbol{f}_i$; the Euclidean norm of the manipulation force $\boldsymbol{f}_{\mathrm{m},i}$ exceeds the projection of the applied force $\boldsymbol{f}_i$ onto the manipulation force $\boldsymbol{f}_{\mathrm{m},i}$. (c) The manipulation force $\boldsymbol{f}_{\mathrm{m},i}$ violates the band shaped force induced torque constraint, i.e. the rotational acceleration of the object $\{\mathrm{o}\}$ produced by manipulation force $\boldsymbol{f}_{\mathrm{m},i}$ is not attainable by the applied force $\boldsymbol{f}_i$.

2.4 Wrench decomposition formulated as an optimization problem

We propose that the solution to Problem 1 can be formulated as a convex scalarized multi-objective optimization that minimizes a manipulation wrench $\boldsymbol{h}_{\mathrm{m}}$ dependent cost function J for a given applied wrench $\boldsymbol{h}$

$$\text{minimize}$$

$$J = \sum_{i=1}^{n} (1-w)\left\|\boldsymbol{f}_{\mathrm{m},i}\right\| + sw\left\|\boldsymbol{t}_{f\mathrm{m},i}\right\| + w\left\|\boldsymbol{t}_{\mathrm{m},i}\right\| \tag{2.18}$$

$$\text{subject to}$$

$$\boldsymbol{G}\boldsymbol{h}_{\mathrm{m}} = \boldsymbol{G}\boldsymbol{h}, \tag{2.19}$$

$$\boldsymbol{f}_{\mathrm{m},i}^{\top}\boldsymbol{f}_{\mathrm{m},i} \leq \boldsymbol{f}_i^{\top}\boldsymbol{f}_{\mathrm{m},i}, \tag{2.20}$$

$$\boldsymbol{t}_{f\mathrm{m},i}^{\top}\boldsymbol{t}_{f\mathrm{m},i} \leq \boldsymbol{t}_{f,i}^{\top}\boldsymbol{t}_{f\mathrm{m},i}, \tag{2.21}$$

$$\boldsymbol{t}_{\mathrm{m},i}^{\top}\boldsymbol{t}_{\mathrm{m},i} \leq \boldsymbol{t}_i^{\top}\boldsymbol{t}_{\mathrm{m},i}, \tag{2.22}$$

$$i = 1, \ldots, n,$$

where $s = \{0, 1\}$ includes or excludes the manipulation torques induced through forces $\boldsymbol{t}_{f\mathrm{m},i}$ (2.3) in the cost J. The scalarized multi-objective cost function J yields the Pareto-optimal points associated with a weighting $w \in (0,\ 1)$ between the objectives of Euclidean norm minimization of manipulation forces and torques [14]. As forces and torques are of different units, a plausible weighting w must be selected. The choice of including ($s = 1$) or excluding ($s = 0$) the force induced torque $\boldsymbol{t}_{f\mathrm{m},i}$ in the cost function relates to this issue. We discuss the effects of weighting w and selection parameter s in the following subsections in greater detail.

The inequality constraints (2.20)-(2.22) ensure a physically consistent decomposition as stated formally in the following Theorem.

Theorem 1. *A physically consistent wrench decomposition according to Definition 1 must obey the inequality constraints* (2.20)-(2.22).

Proof. See proof of Proposition 1 with intermediate result (2.17). □

The computation of a physically consistent force decomposition has been written as an optimization problem in [158], but as a non-convex maximization of compensation force $J = \boldsymbol{f}_{\mathrm{c}}^T \boldsymbol{f}_{\mathrm{c}}$ with $\boldsymbol{f}_{\mathrm{c}} = \left[\boldsymbol{f}_{\mathrm{c},1}^\top \dots \boldsymbol{f}_{\mathrm{c},n}^\top\right]^\top$ subject to the inequality constraint (2.20). Based on Definition 1, we complete the force constraints by also considering force induced torque through inequality constraint (2.21). Inequality constraint (2.22) further extends the constraints to the application of torques. In summary, a total of $3n$ inequality constraints must be met for a physically consistent wrench decomposition according to Problem 1.

For some special cases, maximization of compensation wrench $J = \boldsymbol{h}_{\mathrm{c}}^T \boldsymbol{h}_{\mathrm{c}}$ as proposed in [158] and minimization of manipulation wrench according to (2.18), both subject to constraints (2.19)-(2.22), yield the same solution. However, as we show by our examples in the following subsections, maximization of $J = \boldsymbol{h}_{\mathrm{c}}^T \boldsymbol{h}_{\mathrm{c}}$ does not generally comply with Problem 1.

The complexity of the convex optimization problem defined in (2.18)-(2.22) rises with the number of effectors n. However, analytic solutions can be found for some special cases as presented in the following.

2.4.1 Special case: point mass

Proposition 2. *The optimization problem* (2.18)-(2.22) *has the following analytical solutions for a point mass*[5]

$$\boldsymbol{f}_{\mathrm{m},i} = \phi_{f,i} \max\left(\frac{\boldsymbol{f}_i^\top \boldsymbol{f}_{\mathrm{o}}}{\left\|\boldsymbol{f}_{\mathrm{o}}\right\|^2}, 0\right) \boldsymbol{f}_{\mathrm{o}}, \quad \boldsymbol{t}_{\mathrm{m},i} = \phi_{t,i} \max\left(\frac{\boldsymbol{t}_i^\top \boldsymbol{t}_{\mathrm{o}}}{\left\|\boldsymbol{t}_{\mathrm{o}}\right\|^2}, 0\right) \boldsymbol{t}_{\mathrm{o}}, \tag{2.23}$$

with $\phi_{f,i} \in [0,\ 1]$ *and* $\phi_{t,i} \in [0,\ 1]$ *such that* $\boldsymbol{f}_{\mathrm{o}} = \sum \boldsymbol{f}_{\mathrm{m},i}$ *and* $\boldsymbol{t}_{\mathrm{o}} = \sum \boldsymbol{t}_{\mathrm{m},i}$, *independent of* s, w *in* (2.18).

Proof. For a point mass ($\boldsymbol{t}_{f\mathrm{m},i} = \boldsymbol{0}_{3\times 1}$), the optimization problem (2.18)-(2.22) can be solved separately for forces and torques, with analogous results. The Lagrangian for the minimization of manipulation force is

$$L = \sum_{i=1}^{n} \left\|\boldsymbol{f}_{\mathrm{m},i}\right\| + \boldsymbol{\lambda}^\top (\boldsymbol{f}_{\mathrm{o}} - \sum_{i=1}^{n} \boldsymbol{f}_{\mathrm{m},i}) + \sum_{i=1}^{n} \mu_i (\boldsymbol{f}_{\mathrm{m},i}^\top \boldsymbol{f}_{\mathrm{m},i} - \boldsymbol{f}_i^\top \boldsymbol{f}_{\mathrm{m},i}), \tag{2.24}$$

with 3 Lagrange multipliers concatenated in $\boldsymbol{\lambda} \in \mathbb{R}^3$ and n Kuhn-Tucker multipliers $\boldsymbol{\mu} = [\mu_1 \dots \mu_n]^\top \in \mathbb{R}^n$. For $\mu_i = 0$

$$\nabla_{\boldsymbol{f}_{\mathrm{m},i}} L = \frac{\boldsymbol{f}_{\mathrm{m},i}}{\left\|\boldsymbol{f}_{\mathrm{m},i}\right\|} - \boldsymbol{\lambda}. \tag{2.25}$$

---

[5] With the term point mass we refer to the case $\boldsymbol{f}_i \times \boldsymbol{r}_i = \boldsymbol{0}_{3\times 1}$ and consequently $\boldsymbol{t}_{f,i} = \boldsymbol{0}_{3\times 1}$ for $i = 1, \dots, n$. The solution is independent of the actual mass and moment of inertia properties.

From (2.25) and because $\boldsymbol{f}_{\mathrm{o}} = \sum_{i=1}^{n} \boldsymbol{f}_{\mathrm{m},i}$ we see that every non-zero manipulation force has to point into the same direction as the resultant force $\boldsymbol{f}_{\mathrm{o}}$

$$\frac{\boldsymbol{f}_{\mathrm{m},i}}{\left\|\boldsymbol{f}_{\mathrm{m},i}\right\|} = \frac{\boldsymbol{f}_{o}}{\left\|\boldsymbol{f}_{o}\right\|}. \tag{2.26}$$

A unique solution exists for the special case $\boldsymbol{f}_{\mathrm{m},i}^{\top}\boldsymbol{f}_{\mathrm{m},i} = \boldsymbol{f}_{i}^{\top}\boldsymbol{f}_{\mathrm{m},i}$ for all $i = 1, ..., n$. In this case, the manipulation forces $\boldsymbol{f}_{\mathrm{m},i}$ are equal to the projections of the applied forces $\boldsymbol{f}_{i}$ onto the resultant force $\boldsymbol{f}_{\mathrm{o}}$: $\boldsymbol{f}_{\mathrm{m},i} = (\boldsymbol{f}_{i}^{\top}\boldsymbol{f}_{\mathrm{o}})\boldsymbol{f}_{\mathrm{o}}\left\|\boldsymbol{f}_{\mathrm{o}}\right\|^{-2}$.

Note that this solution only exists if all $\boldsymbol{f}_{i}$ projections onto $\boldsymbol{f}_{\mathrm{o}}$ point along $\boldsymbol{f}_{\mathrm{o}}$. From (2.26) it follows that $\boldsymbol{f}_{\mathrm{m},i} = \mathbf{0}_{3\times 1}$ if $\mathrm{sgn}(\boldsymbol{f}_{i}^{\top}\boldsymbol{f}_{\mathrm{o}}) < 0$. This is equivalent to force compensation along $\boldsymbol{f}_{\mathrm{o}}$, with the consequence that a unique solution might not exist for $n > 2$. The family of solutions with equal minimum cost J can be described via (2.23). The solutions (2.23) are the global minimum due to the convexity of the optimization problem. □

Fig. 2.7(a,b) illustrate the point mass solution for forces $\boldsymbol{f}_{i}$ applied by three effectors $i = 1, 2, 3$. The same holds for torques. The weighting factor $\phi_{f,i}$ in (2.23) determines the extent to which projected forces $\boldsymbol{f}_{f_{\mathrm{o}}\|,i}$ pointing into the same direction as the resultant force $\boldsymbol{f}_{\mathrm{o}}$ belong to manipulation force. Infinite solutions for $\phi_{f,i}$ can lead to the same cost J, e.g., the resultant force $\boldsymbol{f}_{\mathrm{o}} = \begin{bmatrix} 4 & 2 & 0 \end{bmatrix}^{\top}$ can be formed through manipulation forces $\boldsymbol{f}_{\mathrm{m},1} = \begin{bmatrix} 2 & 1 & 0 \end{bmatrix}$ and $\boldsymbol{f}_{\mathrm{m},2} = \begin{bmatrix} 2 & 1 & 0 \end{bmatrix}$ or through $\boldsymbol{f}_{\mathrm{m},1} = \begin{bmatrix} 3 & 1.5 & 0 \end{bmatrix}$ and $\boldsymbol{f}_{\mathrm{m},2} = \begin{bmatrix} 1 & 0.5 & 0 \end{bmatrix}$ (displayed in Fig. 2.7(b)). A parsimonious selection for $\phi_{f,i} = \phi(\boldsymbol{x} = \boldsymbol{f}_{f_{\mathrm{o}}\|})$ from an analysis point of view is

$$\phi(\boldsymbol{x}) = 1 - \frac{A_x - B_x}{A_x + B_x}, \quad A_x = \sum_{i=1}^{n} \left\|\boldsymbol{x}_i\right\|, \quad B_x = \left\|\textstyle\sum_{i=1}^{n} \boldsymbol{x}_i\right\| \tag{2.27}$$

which yields $\left\|\boldsymbol{f}_{\mathrm{m},i}\right\| \propto \left\|\boldsymbol{f}_{f_{\mathrm{o}}\|,i}\right\|$ for same direction of $\boldsymbol{f}_{f_{\mathrm{o}}\|,i}$ and $\boldsymbol{f}_{\mathrm{o}}$. Note that $\phi(\boldsymbol{x} = \boldsymbol{f}_{f_{\mathrm{o}}\|})$ is equal for all effectors.

Fig. 2.7(c) displays the solution for a maximization of compensation force $J = \boldsymbol{f}_{\mathrm{c}}^{\top}\boldsymbol{f}_{\mathrm{c}}$ as proposed in [158] also subject to (2.19)-(2.22). The cost function $J = \boldsymbol{f}_{\mathrm{c}}^{\top}\boldsymbol{f}_{\mathrm{c}}$ leads to solutions on the circular force constraints, with the effect that the summed Euclidean norms are not only greater for internal force $\sum_{i=1}^{3}\left\|\boldsymbol{f}_{\mathrm{c},i}\right\| = 9.69\,\mathrm{N}$, but also for manipulation force $\sum_{i=1}^{3}\left\|\boldsymbol{f}_{\mathrm{m},i}\right\| = 5.58\,\mathrm{N}$ compared to the manipulation wrench based cost (2.18), $\sum_{i=1}^{3}\left\|\boldsymbol{f}_{\mathrm{c},i}\right\| = 7.85\,\mathrm{N}$ and $\sum_{i=1}^{3}\left\|\boldsymbol{f}_{\mathrm{m},i}\right\| = 4.47\,\mathrm{N}$. Thus, the force decomposition components are of greater Euclidean norm than necessary, which conflicts with Problem 1. It also indicates that the approach proposed by Schmidts et al. did not achieve its goal of finding a decomposition free of “virtual forces” [158]. Hence, this example illustrates a rationale for minimization of the cost function based on manipulation wrench (2.18). Fig. 2.7(d) shows the pseudoinverse force decomposition results which are physically inconsistent according to Definition 1; the Euclidean norm of the compensation force $\left\|\boldsymbol{f}_{\mathrm{c},3}\right\|$ exceeds the Euclidean norm of the applied force $\left\|\boldsymbol{f}_{3}\right\|$.

The wrench decomposition of [127] is equivalent to (2.23) for $n = 2$ and if forces do not produce torque, i.e. $\boldsymbol{t}_{f,i} = 0$. In [127], the point mass decomposition is also used when force does produce torque, i.e. $\boldsymbol{t}_{f,i} \neq 0$, by inserting $\boldsymbol{t}_{\mathrm{o},i} = \boldsymbol{t}_i + \boldsymbol{t}_{f,i}$ for $\boldsymbol{t}_i$. We refer to this decomposition as “point mass approximation” in the following.

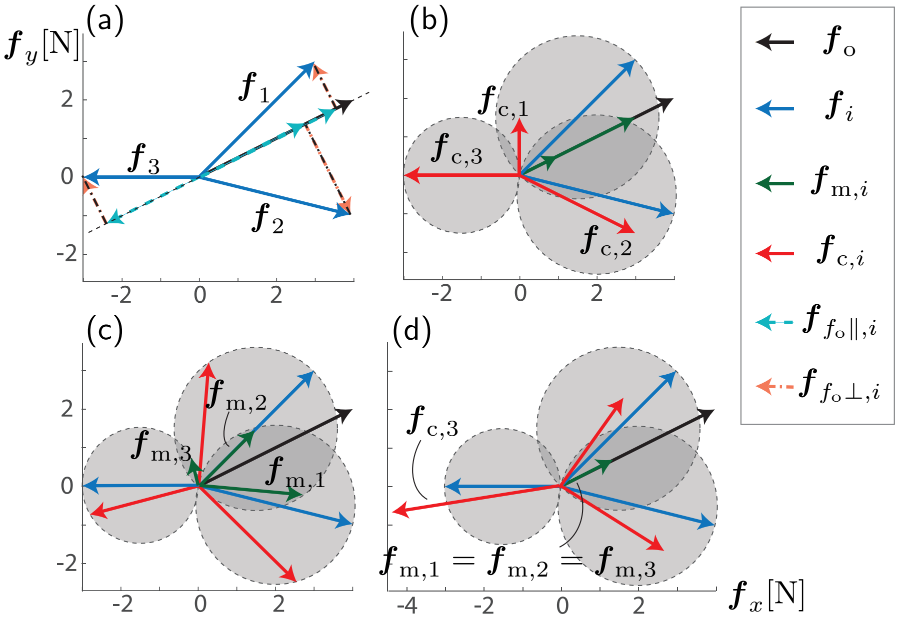

Fig. 2.7: Point mass example $n = 3$: (a,b) Minimization of manipulation wrench (2.18). Projections onto the resultant force $\boldsymbol{f}_{f_\mathrm{o}\|,i}$ represent maximum possible contributions to $\boldsymbol{f}_\mathrm{o}$ and, thus, potential manipulation force $\boldsymbol{f}_{\mathrm{m},i}$. Perpendicular components $\boldsymbol{f}_{f_\mathrm{o}\perp,i}$ belong to compensation force. Components $\boldsymbol{f}_{f_\mathrm{o}\|,i}$ that point into the opposite direction of $\boldsymbol{f}_\mathrm{o}$ belong to compensation force. Thus, $\boldsymbol{f}_{\mathrm{c},3} = \boldsymbol{f}_{f_\mathrm{o}\|,3} + \boldsymbol{f}_{f_\mathrm{o}\perp,3} = f_3$. (c) Maximization of $J = \boldsymbol{f}_\mathrm{c}^\top \boldsymbol{f}_\mathrm{c}$ leads to manipulation forces that are not parallel to the resultant force $\boldsymbol{f}_\mathrm{o}$ and consequently to manipulation forces of greater Euclidean norm than necessary. (d) Pseudoinverse based decomposition with $\boldsymbol{G}^+ = \boldsymbol{G}^\dagger = \boldsymbol{G}^+_\Delta$ for point masses result in equal manipulation forces for all effectors that violate the force constraints. Only (a,b) represents a physically onsistent wrench decomposition according to Problem 1.

2.4.2 Special case: three-fingered grasping

Fig. 2.8 displays an example presented in [190] for a three-fingered grasp. Frictional point contact was assumed, such that each finger only applies force, but no torque. Fig. 2.8(a) shows that the force decomposition based on the heuristics given in [190] violates the force constraints for force induced torque (2.21). Fig. 2.8(b) and (c) show optimization solutions according to (2.18)-(2.22). While for $s = 0$ the cost does not include torque and consequently the solution is independent of weighting w, for $s = 1$ weighting has an effect. Based on the results of Fig. 2.8(b,c), we recommend to set $s = 0$. Intuitively, it makes more sense to minimize the Euclidean norms of force that need to be applied than accepting forces of higher Euclidean norms as long as these forces have a minimum effect on torque production.

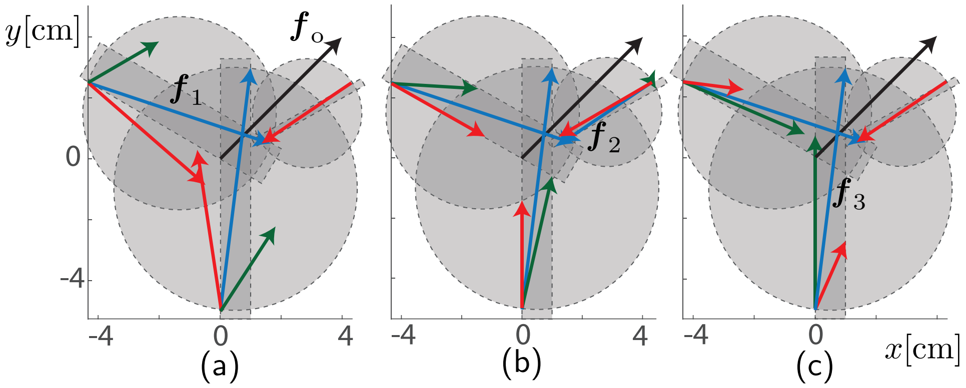

Fig. 2.8: Three fingered grasping example $n = 3$: (a) Result from [190] violates the constraints for force induced torque. Manipulation forces $f_{\mathrm{m},1}$ and $f_{\mathrm{m},2}$ induce torques of higher Euclidean norm than the applied forces f_1 and f_2. (b) Result for cost (2.18) $s = 1$, $w = 0.001$ and $s = 0$. (c) Result for cost (2.18) $s = 1$, $w = 0.5$ and $w = 0.999$. For $s = 1$, increasing weighting w shifts the results from minimization of unnecessary force to minimization of unnecessary force induced torque. Length of force arrows $1\,\mathrm{cm} \hat{=} 1\,\mathrm{N}$, $\boldsymbol{f}_{\mathrm{c},i}$ in red, $\boldsymbol{f}_{\mathrm{m},i}$ in dark green.

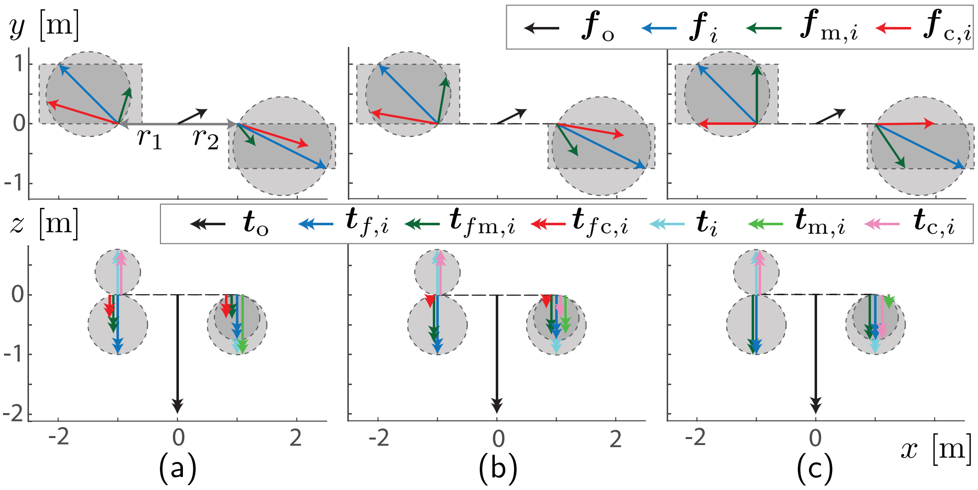

Fig. 2.9: Beam example $n = 2$ for special case with s, w dependent solution: Results for cost (2.18) with (a) $s = 0$, $w = 0.001$ and $s = 1$, (b) $s = 0$, $w = 0.5$, (c) $s = 0$, $w = 0.999$ and pTtTC. For $s = 0$, increasing w shifts the results from torque through force compensation ($t_{\mathrm{c},2} = 0$) and unnecessary force minimization to torque through torque compensation ($t_{f\mathrm{c},1} = t_{f\mathrm{c},2} = 0$) and unnecessary torque minimization. Length of force and torque arrows $1\,\mathrm{m} \hat{=} 1\,\mathrm{N}$ and $1\,\mathrm{m} \hat{=} 1\,\mathrm{Nm}$.

2.4.3 Special case: 2D beam

We consider a beam as displayed in Fig. 2.3 and Fig. 2.4 as a 2D special case for two effectors applying forces in the x/y-plane and torque around the z-axis $\boldsymbol{h}_i = \begin{bmatrix} f_{ix} & f_{iy} & \boldsymbol{0}_{1\times 3} & t_{iz} \end{bmatrix}^\top$, $i = 1, 2$. For the 2D case, analytic solutions equal for all $s \in \{0, 1\}$ and $w \in (0,\ 1)$ can be found, by dividing the problem into cases according to the signs and magnitudes of applied forces and torques, e.g., $t_{\mathrm{c},iz} = 0$ if $\mathrm{sgn}(t_{iz}) = \mathrm{sgn}(t_{f,1z}) = \mathrm{sgn}(t_{f,2z})$ for $i = 1, 2$, where $t_{f,1z}$ is the torque around the z-axis caused by applied force $\boldsymbol{f}_1$. Only one special case requires optimization

$$\{\boldsymbol{h} \in \mathbb{R}^{12} | (\mathrm{sgn}(t_{f,1z}) = \mathrm{sgn}(t_{f,2z}) = \mathrm{sgn}(t_{kz}) \neq \mathrm{sgn}(t_{jz})) \\ \wedge (|2t_{f\mathrm{c,max}z} + t_{kz}| > |t_{jz}|) \, \forall k, j \in \{1,\ 2\}, k \neq j\}, \quad (2.28)$$

where $t_{f\mathrm{c,max}z} = \min(t_{f,1z}, t_{f,2z})$. An example for this case is displayed in Fig. 2.9. The torque applied by effector 1 ($\boldsymbol{t}_1$) is fully compensated. However, the allocation of $\boldsymbol{t}_{\mathrm{c},1}$ to $\boldsymbol{t}_{\mathrm{c},2}$, $\boldsymbol{t}_{f\mathrm{c},1}$ and $\boldsymbol{t}_{f\mathrm{c},2}$ requires optimization. The results for this optimization differ based on the cost function parameters s and w. In contrast to the three fingered grasping example, $s = 1$ yields results independent of weighting w, while for $s = 0$ weighting w affects the solution (see Fig. 2.9(b,c)) The solution to the optimization problem at cost (2.18) with $s = 0$ and $w \to 1$ can be found analytically with the advantage such that the wrench decomposition does not require any optimization and it is suitable for real-time applications. We refer to this case as "prioritized torque through torque compensation" (pTtTC). See Appendix B for a detailed derivation of the analytic beam solution.

Based on our conclusions from the grasping example of the previous section and the need for a meaningful measure for analysis, we recommend to use the cost function (2.18) with $s = 0$, $w = 0.5$. However, in some tasks, the efficient pTtTC can yield results that are almost equal to the optimization with $s = 0$, $w = 0.5$.

2.4.4 General rigid objects

The optimization (2.18)-(2.22) decomposes applied wrenches of any number of effectors n located at any position $\boldsymbol{r}_i$ with $i = 1, \ldots, n$. For general rigid bodies, the solutions are weighting dependent for $s = 0$ and $s = 1$. The effect of w can be summarized as follows:

- $\sum_{i=1}^{n} \left\| \boldsymbol{f}_{\mathrm{m},i} \right\|$ increases with increasing w for $s = \{0, 1\}$
- $\sum_{i=1}^{n} \left\| \boldsymbol{t}_{\mathrm{m},i} \right\|$ decreases with increasing w for $s = \{0, 1\}$, stronger decrease for $s = 0$
- $\sum_{i=1}^{n} \left\| \boldsymbol{t}_{f\mathrm{m},i} \right\|$ decreases with increasing w for $s = 1$

Fig. 2.10 shows a 3D wrench decomposition example for 3 effectors based on cost (2.18) with $s = 0$ and $w = 0.5$.

2.5 Measures for analysis

In the following, we present applications of the wrench decomposition for analysis in pHRI and pHHI tasks based on our derivations in the previous sections.

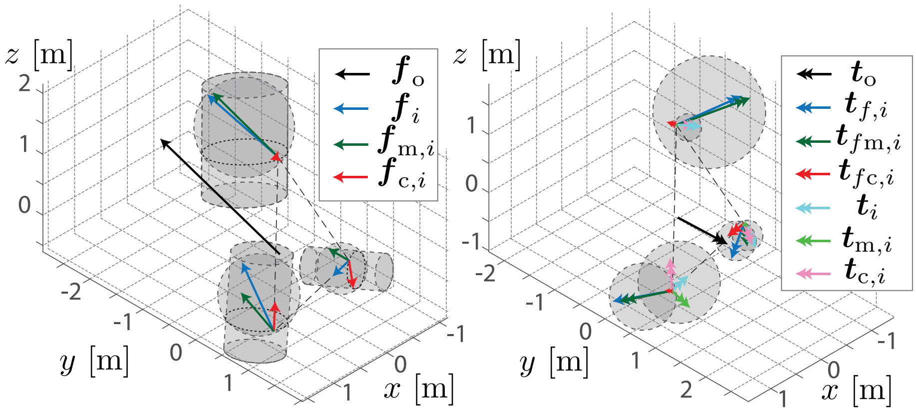

Fig. 2.10: 3D example decomposition for $n = 3$: Forces (left, $1\,\mathrm{m} \hat{=} 1\,\mathrm{N}$) and torques (right, $1\,\mathrm{m} \hat{=} 1\,\mathrm{Nm}$) with spherical force and torque constraints, (2.20) and (2.22). The force induced torque constraints (2.21) are cylinders in force space (left) and spheres in torque space (right).

2.5.1 Load share

The *load share* parameter $\alpha_{f,i}$ ($\alpha_{t,i}$) describes the fraction of force (torque) contributed by effector i to the resultant force $\boldsymbol{f}_\mathrm{o}$ (torque $\boldsymbol{t}_\mathrm{o}$) and can be computed as

$$\alpha_{f,i} = \phi_{f,i} \max\left(\frac{\boldsymbol{f}_i^\top \boldsymbol{f}_\mathrm{o}}{\left\|\boldsymbol{f}_\mathrm{o}\right\|^2}, 0\right), \quad \alpha_{t,i} = \phi_{t_\mathrm{o},i} \max\left(\frac{\boldsymbol{t}_{\mathrm{o},i}^\top \boldsymbol{t}_\mathrm{o}}{\left\|\boldsymbol{t}_\mathrm{o}\right\|^2}, 0\right), \tag{2.29}$$

where the force load share $\alpha_{f,i}$ is equivalent to the point mass solution in (2.23) with $\phi_{f,i} = \phi(\boldsymbol{x} = \boldsymbol{f}_{f_\mathrm{o}\|})$ in (2.27). The torque load share $\alpha_{t,i}$ also considers torque induced through forces with $\phi_{t_\mathrm{o},i} = \phi(\boldsymbol{x} = \boldsymbol{t}_{\mathrm{o},t_\mathrm{o}\|})$ in (2.27), where $\boldsymbol{t}_{\mathrm{o},t_\mathrm{o}\|,i}$ is the projection of $\boldsymbol{t}_{\mathrm{o},i}$ in (2.4) onto the resultant torque $\boldsymbol{t}_\mathrm{o}$. Note that $\sum_{i=1}^n \alpha_{f,i} = \sum_{i=1}^n \alpha_{t,i} = 1$.

The load shares above were introduced in [127] for $n = 2$. The force load share $\alpha_{f,i}$ is related to the weighting introduced in [184] for precise object positioning and to the assistance level in shared control for pHRI [140]. For the 1D case and two effectors, Groten et al. [72] computed the force load share as $\alpha_{f,i} = \frac{f_{\mathrm{m},i}}{f_\mathrm{o}}$. For the general 3D case, we cannot use the manipulation force $\boldsymbol{f}_{\mathrm{m},i}$ and torque $\boldsymbol{t}_{\mathrm{o,m},i}$ at the CoM to compute load share, but we need to relate applied forces to the CoM as in (2.29). This is due to the fact that manipulation wrench $\boldsymbol{h}_\mathrm{m}$ still contains parts that can cancel on force or torque level (see for example Fig. 2.8 and Fig. 2.9).

2.5.2 Energy share

In addition to the load share above, the energy transfer among the effectors and the object can be of interest (see, e.g., [61] for a 1D analysis). For a lossless system, the change in object energy is equal to the sum of the effectors' energy flows $\dot{E}_\mathrm{o} = \sum_{i=1}^n \dot{E}_i$. Effector i can cause a change in translational and rotational energy $\dot{E}_i = \dot{E}_{\mathrm{lin},i} + \dot{E}_{\mathrm{rot},i} = \boldsymbol{f}_i^\top \dot{\boldsymbol{r}}_\mathrm{o} + \boldsymbol{t}_{\mathrm{o},i}^\top \boldsymbol{\Omega}_\mathrm{o}$. The energy flow transferred between the effectors, without influencing the object energy E_o, can be calculated similarly to compensation forces in the 1D case (2.8)

$\dot{E}_\text{c} = \frac{1}{2}(\sum_{i=1}^{n} |\dot{E}_i| - |\sum_{i=1}^{n} \dot{E}_i|)$. Similar to the load share, we define the parameter *energy share* of effector i for the complete energy flow

$$\gamma_i = \phi_{\dot{E},i}\text{max}(\frac{\dot{E}_i}{\dot{E}_\text{o}}, 0), \tag{2.30}$$

and for rotational and translational energy flows

$$\gamma_{\text{lin},i} = \phi_{\dot{E}\text{lin},i}\text{max}(\frac{\dot{E}_{\text{lin},i}}{\dot{E}_\text{lin,o}}, 0), \qquad \gamma_{\text{rot},i} = \phi_{\dot{E}\text{rot},i}\text{max}(\frac{\dot{E}_{\text{rot},i}}{\dot{E}_\text{rot,o}}, 0), \tag{2.31}$$

with $\phi_{\dot{E}(\text{lin/rot}),i} = \phi(x = \dot{E}_{(\text{lin/rot})})$ in (2.27).

2.5.3 Disagreement

Compensation wrench can indicate disagreement [120, 131, 141] and allow to communicate intention through the haptic channel [74]. However, previous works were limited to 1D cases. In order to compare compensation wrench within a trial or among different trials, the sum of Euclidean norms of compensation force and torque can serve as a measure of disagreement in translational and rotational directions

$$F_\text{c} = \frac{1}{2}\sum_{i=1}^{n} \left\|\boldsymbol{f}_{\text{c},i}\right\|, \qquad T_\text{c} = \frac{1}{2}\sum_{i=1}^{n} \left\|\boldsymbol{t}_{\text{o,c},i}\right\|. \tag{2.32}$$

As a combined measure for translation and rotation, we propose the measure *relative cost* β

$$\beta = 1 - \frac{J(\boldsymbol{h}_\text{m})}{J(\boldsymbol{h})}. \tag{2.33}$$

The cost function (2.18) is evaluated twice, once at its minimum $J(\boldsymbol{h}_\text{m})$ and another at its maximum $J(\boldsymbol{h})$. The relative cost returns values $\beta \in [0,\ 1]$, where $\beta = 1$ signifies maximum disagreement, i.e. $\boldsymbol{h}_\text{o} = \boldsymbol{0}_{6x1}$ and $\boldsymbol{h} = \boldsymbol{h}_\text{c}$, and $\beta = 0$ signifies no disagreement in the sense that the complete applied wrench was needed to produce the resultant wrench $\boldsymbol{h}_\text{o}$, i.e. $\boldsymbol{h} = \boldsymbol{h}_\text{m}$. The need for an interpretable measure β strengthens our recommendation not to choose extreme values for w but rather $w = 0.5$ and $s = 0$.

2.6 Evaluation in simulation

In real pHHI and pHRI tasks, the internal state of human agents (i.e. the control disagreement) cannot be precisely and systematically controlled, and the lack of ground truth impedes an interpretation of the results. Thus, we first use simulations to evaluate the proposed method, and assess the quality of the wrench decomposition solutions. Based on the relevant use cases discussed in the introduction, we chose two different simulation scenarios: shared control of a mobility assistance robot [67] and an object transport task [127, 136]. For multi-digit grasping examples see [158][6]. In the following, we use agents to refer to effectors to highlight their autonomy in contrast to a centralized controllers in case of robotic grasping.

---

[6] Although the cost function differs and the force induced torque constraint is missing, we expect qualitatively similar results as in [158] for our proposed wrench decomposition.

We compare the proposed wrench decomposition to the following SoA approaches:

- PM: Point mass approximation [127]
- $G^{\dagger}$: Moore-Penrose pseudoinverse, e.g. [94]
- G^{+}_{Δ}: “Nonsqueezing” pseudoinverse [175]
- VL: Virtual linkage model [181]

Based on the applied wrench $\boldsymbol{h}(t)$ in simulation, we first computed the compensation wrench $\boldsymbol{h}_{\mathrm{c}}(t)$ based on the proposed and the above SoA wrench decompositions. For the particular simulation scenarios, the proposed wrench decomposition was independent of optimization parameters $s = \{0, 1\}$ and $w \in (0,\ 1)$. From $\boldsymbol{h}_{\mathrm{c}}(t)$ the proposed measures for disagreement $F_{\mathrm{c}}(t)$, T_{c} and β in (2.32) and (2.33) were obtained. We furthermore computed the load shares $\alpha_{f,1}$ and $\alpha_{t,1}$ in (2.29) and the energy shares $\gamma_{\mathrm{lin},1}$, $\gamma_{\mathrm{rot},1}$ and γ_1 in (2.30) for agent A1[7]. All computations were solely based on the observed $\boldsymbol{h}(t)$, i.e. we assumed not to have any knowledge on a desired trajectory, controllers or load sharing strategies.

2.6.1 Shared control of a mobility assistance robot

Let us consider a walker that can actively support an elderly human during walking. Inspired by [67], we examined two scenarios (see Fig. 2.11):

- the walker (agent A2) generated torque to support the human (agent A1) during turning
- the walker generated opposing forces to avoid an obstacle

Computation of applied wrench

The agents determined the necessary object wrench $\boldsymbol{h}_{\mathrm{o}}$ to track the desired trajectories through a combination of equal inverse dynamics and impedance controllers. We computed the wrench to be applied at the human interaction point based on the reduced Moore-Penrose pseudoinverse $\boldsymbol{h}_{G\dagger 1} = \boldsymbol{G}_1^{\dagger}\boldsymbol{h}_{\mathrm{o}}$, but then assigned all pure torque to the walker: $\boldsymbol{t}_2 = \boldsymbol{t}_{G\dagger 1}$, $\boldsymbol{t}_1 = 0$. For obstacle avoidance, the walker applied an additional force $\boldsymbol{f}_{\mathrm{obs},2x} = -(\frac{1}{C_{\mathrm{obs}}} - \frac{1}{C_{\mathrm{max}}})\frac{1}{C_{\mathrm{obs}}^2}\dot{\boldsymbol{r}}_{\mathrm{o}}$ when approaching obstacles ($\dot{C}_{\mathrm{obs}} < 0$). Obstacle avoidance was active when the distance to the obstacle C_{obs} (inflated by $0.5 l_{\mathrm{o}}$ of the walker length) was smaller than $C_{\mathrm{max}} = 2\,\mathrm{m}$.

Results collaborative turning

For the collaborative turning task, the agents agreed on the same trajectory p (Fig. 2.12(a)), while the human (agent A1) applied the necessary forward force f_{1x} (Fig. 2.12(b)) and the walker (agent A2) the torque t_{1z} (Fig. 2.12(c)). Fig. 2.12(d) and (e) show that only the point mass approximation and our proposed optimization yield the correct result of zero

---

[7] We set the load and energy shares to NaN where otherwise meaningless, e.g., $\alpha_{f,1} = \mathrm{NaN}$ when $f_{\mathrm{o}} \approx 0$.

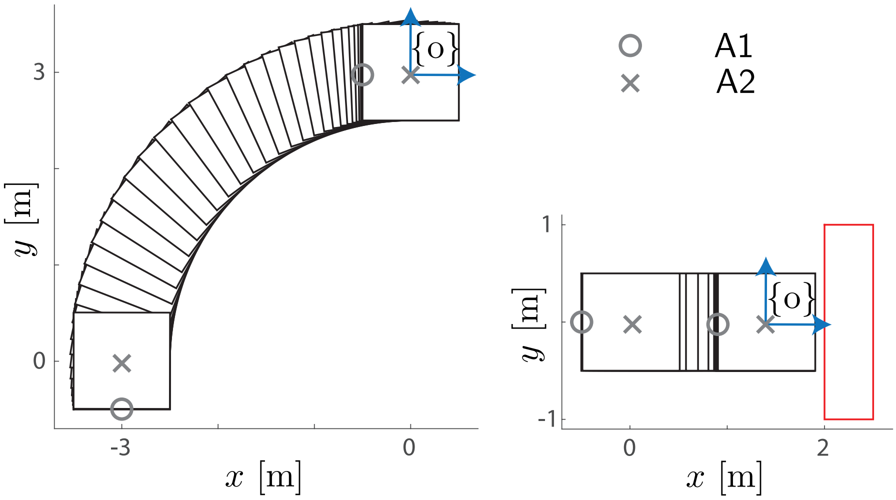

Fig. 2.11: Walker motion during mobility assistance scenarios: A quadratic nonholonomic walker of length $l_\mathrm{o} = 1\,\mathrm{m}$, mass $m_\mathrm{o} = 25\,\mathrm{kg}$, and moment of inertia $j_{\mathrm{o}z} = \frac{1}{6} m_\mathrm{o} l_\mathrm{o}^2 = 4.17\,\mathrm{kg\,m^2}$ subject to viscous friction on translation $f_{dx} = -d_\mathrm{lin}\dot{\boldsymbol{r}}_\mathrm{o}$ with $d_\mathrm{lin} = 1\,{}^\mathrm{Ns}/_\mathrm{m}$ and rotation $t_{dz} = -d_\mathrm{rot}\Omega_{\mathrm{o}z}$ with $d_\mathrm{rot} = 100\,\mathrm{Nm\,s}$. The human (agent A1) interaction with the walker aggregated in one interaction point at $\boldsymbol{r}_1 = [-0.5 l_\mathrm{o}\ 0\ 0]$ and the walker (agent A2) applying wrench directly at its CoM. (Left) Walker motion during turning, (right) walker motion during obstacle avoidance. Agent positions at their initial and final positions in gray.

disagreement: $F_\mathrm{c} = T_\mathrm{c} = 0$. The pseudo-inverse based methods assume fixed equal load shares on force and torque level. In this case, however, agent A1 took over the complete load share on force level ($\alpha_{f,1} = \gamma_{\mathrm{lin},1} = 1$) and agent A2 on torque level ($\alpha_{t,1} = \gamma_{\mathrm{rot},1} = 0$) in Fig. 2.12(f).

Results obstacle avoidance

During the obstacle avoidance scenario, the human (agent A1) intended to move from ${}^\mathrm{w}r_{\mathrm{o}x} = 0$ to ${}^\mathrm{w}r_{\mathrm{o}x} = 3\,\mathrm{m}$ along the trajectory ${}^\mathrm{w}r^d_{\mathrm{o},1x}(t)$ displayed in Fig. 2.13(a). The active obstacle avoidance through counteracting forces f_{2x} stops the walker in front of the obstacle: ${}^\mathrm{w}r_{\mathrm{o}x}(t) <^\mathrm{w} r_{\mathrm{obs}x}(t)$. Fig. 2.13(c) and (d) show the disagreement measures F_c and β. As for the turning scenario, the point mass approximation and our proposed optimization yield the same F_c. Note that the point mass approximation yields valid solutions for this setup, because the interaction point of the walker coincides with the CoM. The other decomposition methods inflate disagreement F_c due to their underlying assumptions. The peak in disagreement F_c and β and the switch from $\alpha_{f,1} = \gamma_1 = 1$ to 0 (Fig. 2.13(e)) at $t = 2.1\,\mathrm{s}$ occur when the applied forces of the agents reach equal values: for $t < 2.1\,\mathrm{s}$ agent A1 dominates accelerating the walker, for $t > 2.1\,\mathrm{s}$ agent A2 dominates decelerating the walker.

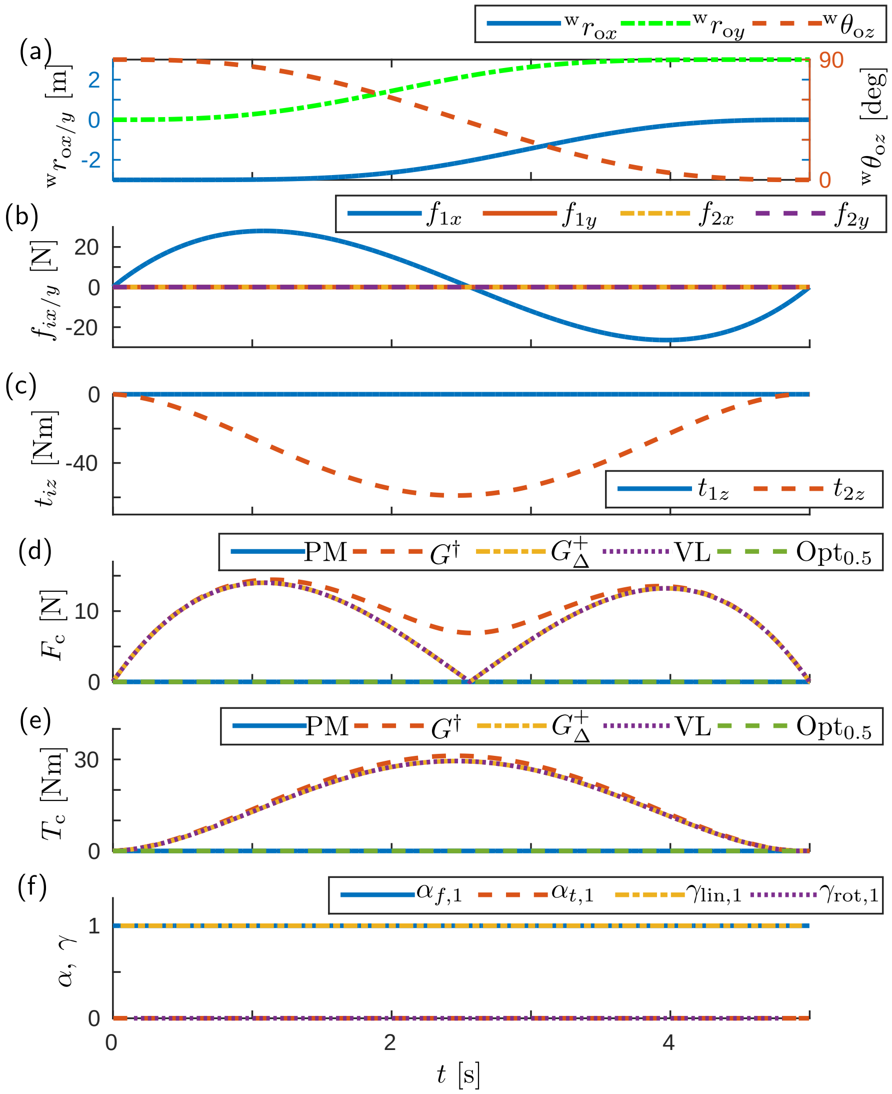

Fig. 2.12: Analysis of the simulated assisted turning task: (a) Trajectory, (b) applied forces f_{ix}, f_{iy} and (c) torques t_{iz} in the plane by agents Ai with $i = 1, 2$, (d) disagreement on force and (e) on torque level based on SoA wrench decompositions PM, $G^{\dagger}$, G_{Δ}^{+} and VL, and our proposed optimization (Opt), (f) load shares $\alpha_{f,1}$, $\alpha_{t,1}$ and energy shares $\gamma_{\mathrm{lin},1}$, $\gamma_{\mathrm{rot},1}$. Only the proposed wrench decomposition (Opt) and the point mass approximation (PM) consistently yield the correct result $F_{\mathrm{c}} = T_{\mathrm{c}} = 0$.

2.6.2 Collaborative object transport

In simulation, two agents transported a beam from a start to a goal configuration in 2D as displayed in Fig. 2.14 and Fig. 2.15(a). Thus, a phase of pure rotation was followed by a phase of combined rotation and translation, and a phase of pure translation. We furthermore varied how the agents share the load and to which extent forces or torques were applied to induce the required object torque for rotation. Throughout the simulation, the agents agreed on the same trajectory and used the same controller parameters. Thus, we expect the analysis to reveal zero disagreement $F_{\mathrm{c}} = T_{\mathrm{c}} = 0$.

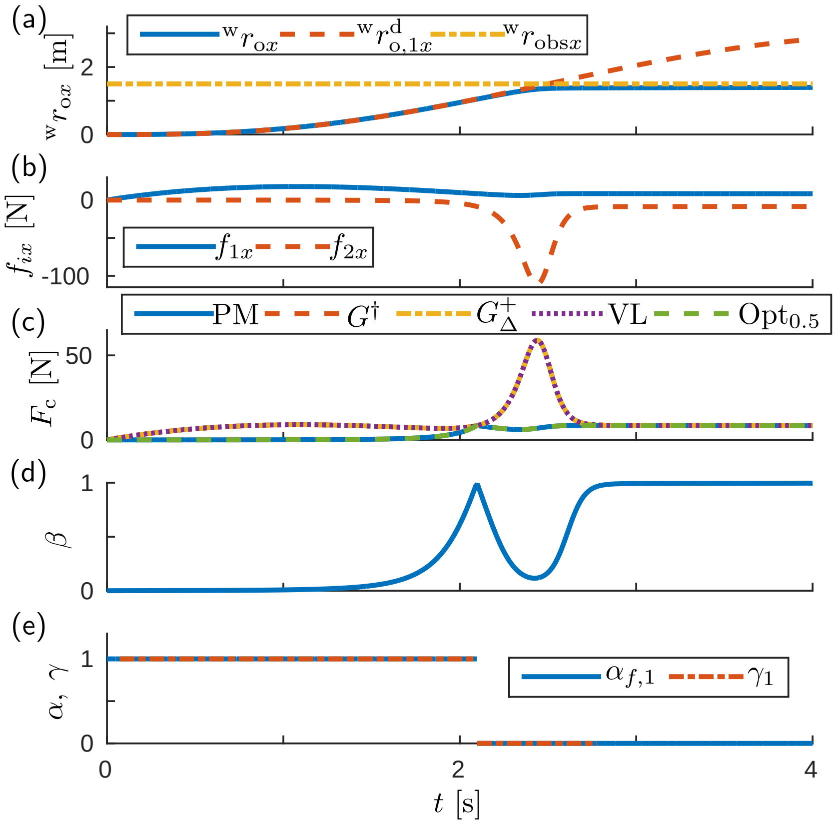

Fig. 2.13: Analysis of the simulated assisted obstacle avoidance task: (a) Actual $^{\mathrm{w}}r_{\mathrm{o}x}$ and planned $^{\mathrm{w}}r^{\mathrm{d}}_{\mathrm{o},1x}$ trajectory and inflated obstacle border $^{\mathrm{w}}r_{\mathrm{obs}x}$, (b) applied forces f_{ix} by agents Ai with $i = 1, 2$ ($f_{iy} = t_{iz} = 0$), (c) disagreement on force level based on SoA wrench decompositions PM, $G^{\dagger}$, G^{+}_{Δ} and VL, and our proposed optimization (Opt), (d) disagreement β, (e) load share $\alpha_{f,1}$ and energy share $\gamma_1 = \gamma_{\mathrm{lin},1}$. High forces required for deceleration in front of the obstacle are interpreted as internal forces by the wrench decomposition methods $G^{\dagger}$, G^{+}_{Δ} and VL.

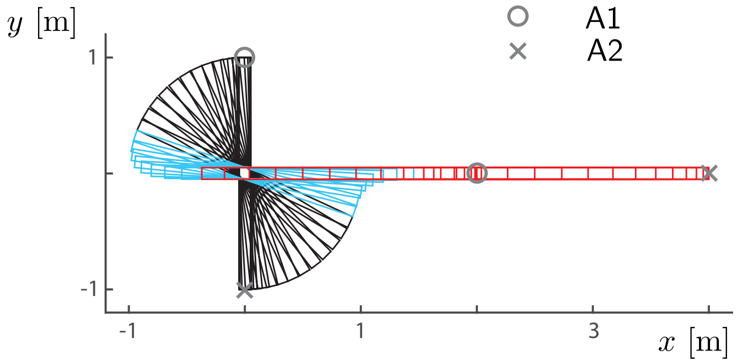

Fig. 2.14: Beam motion for the simulated 2D transport task: Phase of pure rotation (black), followed by phase of combined rotation and translation (blue), followed by phase of pure translation (red). Agent positions at their initial and final positions in gray.

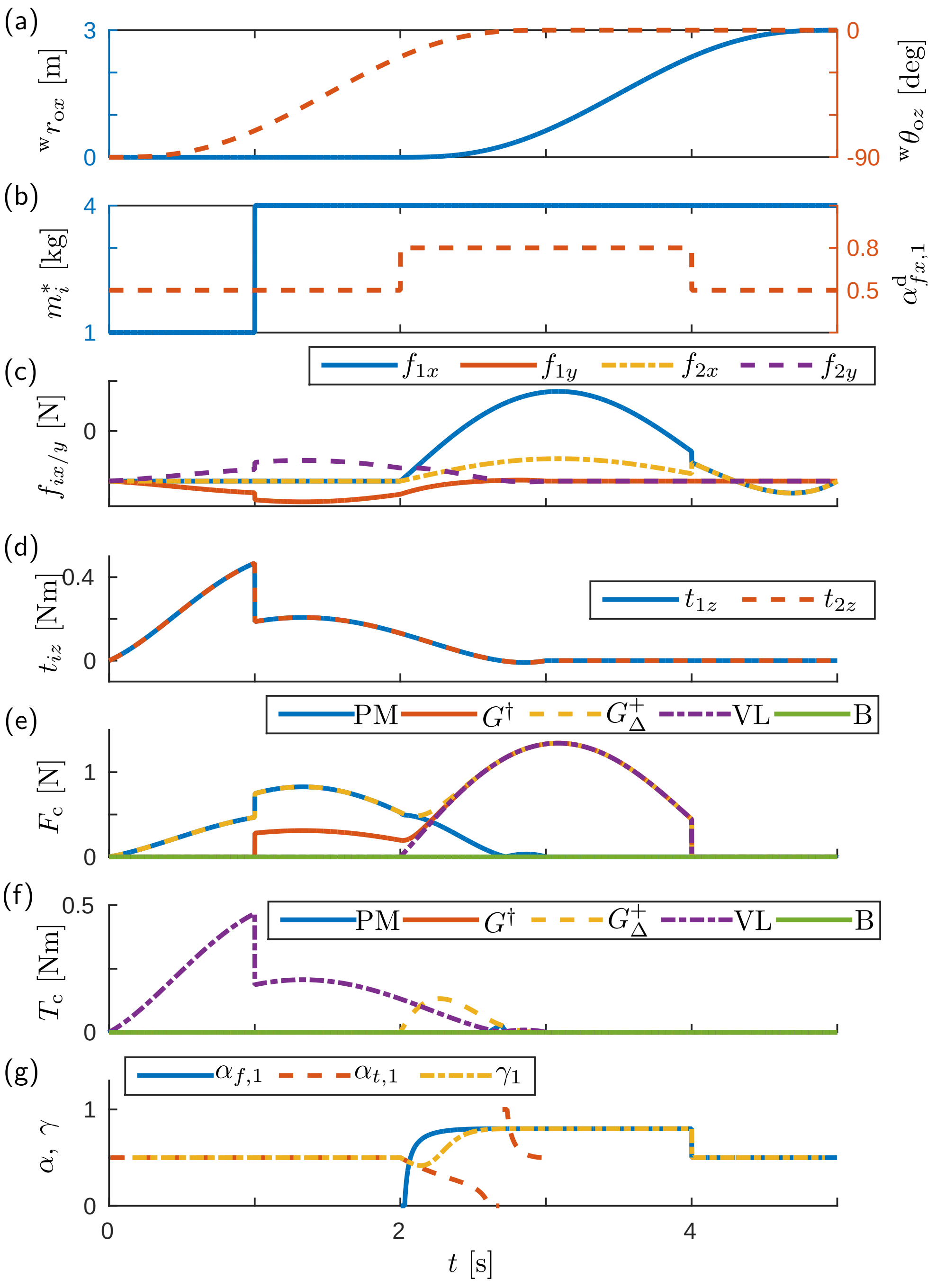

Fig. 2.15: Analysis of the simulated 2D beam transport task: (a) Trajectory with ${}^{\mathrm{w}}r_{oy} = 0$, (b) parameter m_i^* of pseudoinverse [55] and 1D load share $\alpha_{fx,1}$ [131], (c) applied forces f_{ix}, f_{iy} and (d) torques t_{iz} in the plane by agents Ai with $i = 1, 2$, (e) disagreement on force and (f) on torque level based on SoA wrench decompositions PM, $G^{\dagger}$, G^{+}_{Δ} and VL, and our proposed 2D beam wrench decomposition (B), (g) load shares $\alpha_{f,1}$ and $\alpha_{t,1}$ and energy share γ_1. Only the proposed 2D beam wrench decomposition (B) consistently yields the correct result $F_{\mathrm{c}} = T_{\mathrm{c}} = 0$.

Computation of applied wrench

The agents determined the necessary object wrench $\boldsymbol{h}_\mathrm{o}$ to track the desired trajectory through a combination of equal inverse dynamics and impedance controllers. The applied wrench was computed from the necessary object wrench $\boldsymbol{h}_\mathrm{o}$ based on the parametrized pseudoinverse of [55] for two agents

$$\boldsymbol{h}_{G+M} = \boldsymbol{G}_M^{+}\boldsymbol{h}_\mathrm{o} = \begin{bmatrix} m_1^*(m_\mathrm{o}^*)^{-1}\boldsymbol{I}_{3\times3} & m_1^*(\boldsymbol{J}_\mathrm{o}^*)^{-1}\left[\boldsymbol{r}_1\right]_\times^\top \\ \boldsymbol{0}_{3\times3} & \boldsymbol{J}_1^*(\boldsymbol{J}_\mathrm{o}^*)^{-1} \\ m_2^*(m_\mathrm{o}^*)^{-1}\boldsymbol{I}_{3\times3} & m_2^*(\boldsymbol{J}_\mathrm{o}^*)^{-1}\left[\boldsymbol{r}_2\right]_\times^\top \\ \boldsymbol{0}_{3\times3} & \boldsymbol{J}_2^*(\boldsymbol{J}_\mathrm{o}^*)^{-1} \end{bmatrix} \boldsymbol{h}_\mathrm{o}, \tag{2.34}$$

with virtual masses m_i^* and moment of inertias $\boldsymbol{J}_i^* \in \mathbb{R}^{3\times3}$ with $i = 1, 2$ as parameters, which have to obey

$$m_\mathrm{o}^* = \sum_i^{n=2} m_i^*, \tag{2.35}$$

$$\boldsymbol{J}_\mathrm{o}^* = \sum_i^{n=2} \boldsymbol{J}_i^* + \sum_i^{n=2} \left[\boldsymbol{r}_i\right]_\times m_i^* \left[\boldsymbol{r}_i\right]_\times^\top, \tag{2.36}$$

$$\sum_i^{n=2} \boldsymbol{r}_i m_i^* = \boldsymbol{0}_{3\times1}. \tag{2.37}$$

From the last equality (2.37) follows $m_1^* = m_2^*$ for a symmetric beam as in Fig. 2.3 and Fig. 2.9. We further set $\boldsymbol{J}_1^* = \boldsymbol{J}_2^* = \boldsymbol{I}_{3\times3}\mathrm{kg\,m}^2$ and vary m_i^* between 1 kg and 4 kg as displayed in Fig. 2.15(b)). Variation of the virtual masses m_i^* regulates to which extent torque $\boldsymbol{t}_{\mathrm{o},i}$ is induced by $\boldsymbol{t}_i$ or $\boldsymbol{f}_i$. For $m_i^* = 1\,\mathrm{kg}$, the parametrized pseudoinverse $\boldsymbol{G}_M^{+}$ is equal to the Moore-Penrose pseudoinverse $\boldsymbol{G}^\dagger$, which yields the minimum norm solution for $\boldsymbol{h}$. For increasing m_i^*, the required torque $\boldsymbol{t}_{\mathrm{o},i}$ is induced to a higher extent through applied force $\boldsymbol{f}_i$ than applied torque $\boldsymbol{t}_i$.

Due to the restriction on $m_1^* = m_2^*$, the parametrized pseudoinverse $\boldsymbol{G}_M^{+}$ cannot be used to design a desired load share but it yields balanced load sharing among the agents. As presented in [131], we varied the desired load share $\alpha_{fx,i}^\mathrm{d}$ along the redundant x-direction of the beam (see Fig. 2.15(b)). This was done by further modifying the x-values $f_{G+M,ix}$ of the computed wrench $\boldsymbol{h}_{G+M}$ from (2.34) in the null space of the grasp matrix $\mathrm{Ker}(\boldsymbol{G}) = \begin{bmatrix}1 & \boldsymbol{0}_{1\times5} & -1 & \boldsymbol{0}_{1\times5}\end{bmatrix}^\top$ according to

$$\boldsymbol{h} = \boldsymbol{h}_{G+M} + (-f_{G+M,1x} + 2\alpha_{fx,1}^\mathrm{d} f_{G+M,1x})\mathrm{Ker}(\boldsymbol{G}). \tag{2.38}$$

Thus, for $\alpha_{fx,1}^\mathrm{d} = 0.5$ we kept $\boldsymbol{h} = \boldsymbol{h}_{G+M}$ and consequently $f_{1x} = f_{2x}$. In contrast for, e.g., $\alpha_{fx,1}^\mathrm{d} = 1$ agent A1 would take over the complete load in x-direction.

Results object transport

In simulation, the two agents applied the wrench $h(t)$ displayed in Fig. 2.15(c) and (d) to track the desired trajectory and achieve the desired load share displayed in Fig. 2.15(a) and (b), respectively. Fig. 2.15(e) and (f) show the results for the disagreement F_c and T_c in (2.32). Our proposed wrench decomposition yields the correct result of zero disagreement between the agents[8]. The point mass approximation proposed in [127] neglects that forces also induce torque for the computation of $\boldsymbol{f}_{\mathrm{m},i}$. As a consequence, opposing forces that were applied to induce torque are interpreted as compensation force, which results in $F_\mathrm{c} \neq 0$ during rotation. Wrench decomposition according to the Moore-Penrose pseudoinverse $\boldsymbol{G}^\dagger$ only results in zero disagreement when the agents use $\boldsymbol{G}^\dagger$ to compute $\boldsymbol{h}_1$ and $\boldsymbol{h}_2$. This is the case for $m_i^* = 1\,\mathrm{kg}$ during rotation and $\alpha_{fx,i}^\mathrm{d} = 0.5$ during translation. Similar to the Moore-Penrose pseudoinverse-based wrench decomposition, the nonsqueezing pseudoinverse-based wrench decomposition of [175] only yields zero compensation force and torque, when $\boldsymbol{h} = \boldsymbol{G}_\Delta^+ \boldsymbol{h}_\mathrm{o}$ holds. For the simulation under consideration, this was only the case during the last second, i.e. pure translation and equal load sharing $\alpha_{fx,i}^\mathrm{d} = 0.5$. Wrench decomposition according to the virtual linkage model of [181] assumes that rotation around the z-axis should be caused by forces instead of torques and interprets any applied torque along z as compensation torque. Furthermore, according to the virtual linkage model, compensation force only occurs along the x-direction of the beam. Thus, $F_\mathrm{c} = 0$ during pure rotation. However, the virtual linkage model essentially computes the internal force $\boldsymbol{f}_\mathrm{A}$ in the center of the beam and assigns its absolute value to F_c (see Fig. 2.4), which results in $F_\mathrm{c} \neq 0$ for load distributions $\alpha_{fx,i}^\mathrm{d} \neq 0.5$.

Fig. 2.15(g) shows the load and energy shares of (2.29) and (2.30) for agent A1[9]. The load share $\alpha_{fx,1}^\mathrm{d}$ distributes the demanded object force along the redundant x-direction and is therefore restricted to 1D. Consequently, $\alpha_{f,1} = \alpha_{fx,1}^\mathrm{d}$ only during pure translation. The energy share γ_1 combines the force and torque load shares in one measure.

2.7 Discussion of Limitations

2.7.1 Uniqueness of the wrench decomposition solution

Wrench decomposition aims at splitting applied wrench into its motion inducing and compensated components. Without further restrictions, infinite decomposition solutions can be found. Pseudo-inverse based approaches find a unique solution by fixing the load shares among the effectors a priori. While this procedure allows for efficient wrench synthesis, it cannot be used to analyze applied wrench, e.g., with respect to load sharing. In this work, we derived physically motivated constraints and formulated wrench decomposition as a convex optimization problem. We showed that the optimization results are in line with solutions proposed in literature, which however only produce physically consistent results for special cases, e.g., [67, 72, 127, 158]. Our approach is the first to yield physically consistent results for general manipulation tasks without assumptions. Only the applied wrenches and the locations of the effector interaction points have to be known. However,

---

[8] The decompositions proposed in [72] and [55] yield zero disagreement as well, but are restricted to 1D or require knowledge of desired velocities with the associated problems outlined in the problem formulation, respectively.

[9] We set the load and energy shares to NaN where otherwise meaningless, e.g., $\alpha_{f,1} = \mathrm{NaN}$ during pure rotation.

the proposed scalarized multi-objective optimization does not yield a unique solution for general manipulation tasks, but depends on the choice of weighting and selection parameters[10]. The multitude of solutions leads us to the conclusion that it is possible to find physically consistent decompositions, but the one and only correct wrench decomposition solution does not exist.

2.7.2 Computational cost of the optimization problem

The advantage of yielding physically consistent wrench decompositions comes at the cost of having to solve an optimization problem. The optimization is convex and thus can be efficiently solved. We used the *MATLAB* software *CVX*, a package for specifying and solving convex programs [70, 71][11]. The presented analytic solutions for a point mass in Section 2.4.1 and the "prioritized torque through torque compensation" approximation for the 2 effector 2D beam in Section 2.4.3 yield solutions within less than 1 ms, and can thus be directly used for realtime haptic interaction control. For the general 3D case (see Section 2.4.4), in contrast, the computational cost increased as follows with the number of effectors: $\bar{t}(n = 2) = 0.8\,\mathrm{s}$, $\bar{t}(n = 4) = 1.1\,\mathrm{s}$, $\bar{t}(n = 10) = 2.1\,\mathrm{s}$ using CVX with MATLAB R2015a and solver *SeDuMi* v1.34 [168] on a desktop pc[12].

Note that CVX is a modeling framework that allows for convenient solving of convex optimization problems written in natural MATLAB syntax, taking over the effort, among others, of transformation into solvable form and the choice of an appropriate solver. Significant speed-up can be achieved by using more efficient commercial solvers [4, 77] and by splitting the solver up into an initialization routine that is performed once and a real-time routine that efficiently solves instances of the same problem [36]. Also, for many interaction scenarios wrench decomposition can be approximated by analytic solutions. For the mobility assistance scenario in Section 2.6.1, the point mass approximation as an analytic solution was found. In the next chapter, we will analyze the interaction of two humans during a joint object transport task, by projecting the task into the 2D plane and applying the analytic pTtTC solution.

2.8 Conclusions

The proposed wrench decomposition allows for the first time to separate applied wrench into compensation and manipulation wrench for general rigid objects manipulated by multiple effectors, while ensuring physically consistent results. We defined manipulation wrench as the wrench with minimum Euclidean norm to produce the resultant object wrench. Physical consistency was achieved by constraining the compensation and manipulation

---

[10] Note that the problem of weighting does exist for other methods as well. The Moore Penrose pseudoinverse solution ignores this problem by equally weighting the physically distinct quantities force and torque [127].

[11] For the non convex problems, e.g., Fig. 2.7(c), we used *fmincon* of the *Optimization Toolbox* by *MathWorks*

[12] Processor Intel(R) Core(TM) i5-2500K CPU @ 3.30GHz x 4, no hyper threading, 15.6 GB RAM, ubuntu 14.04 LTS

wrenches by the applied wrench. The proposed optimization is convex and has an intuitive analytic solution for a point mass. The solution for a 2D beam requires optimization only for one special case, which can be approximated through an analytic solution. The efficient 2D beam implementation can potentially be used for real-time control and analysis for various 2-agent object manipulation tasks. Applications in example measures such as load and energy share were defined based on the analytic point mass solution. The extent to which the applied wrench is not used for manipulation, but, e.g., for communication or to express disagreement, can be characterized by the wrench decomposition-based relative cost and Euclidean compensation force and torque norms. Simulations of mobility assistance scenarios and 2D beam transportation by two agents shows that our method was able to correctly evaluate the control disagreement based on the measured wrench unlike other existing methods.

Open problems

By extension, this work is targeted towards wrench decomposition for analysis of haptic communication in pHHI and pHRI tasks. In the following chapter we will use the presented wrench decomposition and measures to analyze human-human collaborative object transportation.

Although the common pseudoinverse approaches do not allow for a physically consistent wrench decomposition, they can be straightforwardly applied for wrench synthesis. Nonetheless, pseudoinverse solutions are restricted in the sense of how the load is shared among the agents. How to extend the presented wrench decomposition to wrench synthesis that realizes desired load and energy shares or compensation wrench for communication remains an open question. Such wrench synthesis applied to robot control will allow more accurate tuning of the robot to the user behavior and intention in pHRI tasks.

3 Intention communication and coordination patterns during human-human collaborative object transport

Summary. *This chapter studies intention communication strategies and coordination patterns underlying human-human collaborative object transport. The chapter demonstrates*

- *the application of the wrench-based measures introduced in Chapter 2 to physical human-human interaction,*
- *motion- and wrench- and rule-based intention communication strategies,*
- *emerging passive/dominant and specialized coordination patterns*
- *and the influence of task setup and task knowledge including role assignments onto coordination and communication strategies.*

The results of this chapter were partly published in [41]. The student works [93, 179] contributed to this chapter.

3.1 Motivation

Two people are able to transport a table from one room to another without explicitly communicating via speech or gestures. The partners naturally adapt to each other on different levels [75]. On a *high level*, they decide on a common action plan with respect to who will enter through the door first. This decision might be based on their start configuration and the environment or also on who takes the initiative. Even after a door entry order is found, the strong coupling through the table forces the two partners to continuously negotiate the trajectory of the object locally, i.e. adapt their motion on a *low level* to the one of the partner. When a robot replaces one of the humans as illustrated in Fig. 3.1, the interaction should not deteriorate with respect to goal-directedness, efficiency and intuitiveness, i.e. the robot should not be a burden to the human and the human should not have to learn how to interact with the robot. In this thesis, we work towards achieving such seamless human-robot interaction by studying the principles underlying human-human collaboration and combining the results with system theoretic approaches, as, e.g., interaction controllers and trajectory generation methods.

Robotics literature provides solutions for interaction controllers with human-like low-level adaptation to the partner [148, 185]. Furthermore, various methods have been developed to generate trajectories for collaborative object transport [21, 109, 110, 154]. Few approaches have considered high-level decision making, as on which side an obstacle will be surrounded or who will enter through a door first [126, 187]. Such semantically different

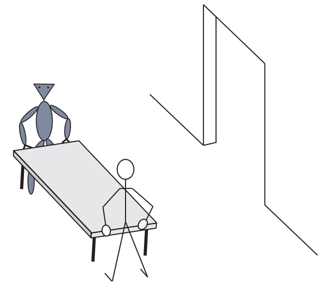

Fig. 3.1: A human and a robot collaboratively transport a table from one room to another. Dependent on their configuration it might be unclear who goes first. This chapter studies how such high-level trajectory decisions are made during human-human collaborative object transport.

trajectories that can all lead to the same final goal configuration can be interpreted as different intermediate goal configurations, i.e. position to the left or right of an obstacle and different orientations at the door. High-level decision making would then select an intermediate goal for trajectory generation based on the inferred partner's intention and own preferences. Furthermore, the partners could adapt to each other on a high level by, e.g., generating trajectories aiming at conveying their own intention. Dragan et al. studied how modification of a reaching trajectory towards increased legibility allows observers to easily disambiguate between different goals, in their case different objects to be grasped [46]. To the best of the authors knowledge, legible trajectory generation has not been investigated in the area of collaborative object transport. In contrast to observation of a reaching trajectory, partners during physical interaction are not limited to intention recognition based on visual information. The coupling through a rigid object that is rigidly grasped allows to compute the partner's motion through a simple kinematic relationship and can also serve as a haptic communication channel [74]. However, inference of the intended motion from interaction forces and torques is not trivial due to ambiguities apparent for large objects: a torque felt at the own interaction point can be the result of an intended translation to the side or rotation, or any combination of the two [187]. In this chapter, we present a physical human-human collaboration (pHRC) study designed to investigate the role of haptic communication and legible motion for high-level adaptation during collaborative object transport.

3.2 Related work

Legibility

Successful human-robot collaboration necessitates robots and humans to be able to anticipate each others' intentions such that they can implicitly coordinate their actions. Human-human studies showed that less variability results in increased predictability of the others' actions during joint action coordination [173]. Different studies investigated the underlying intent conveying features of human locomotion and their transfer to robot locomotion. Gestures as pointing, torso direction and gaze [10, 115], repetitive, stereotypical behavior

[11, 115] and human-likeness [23] were found to support intention conveyance.

The importance of straight lines as stereotypical behavior during walking found by [115] is in contrast to the theory developed by Dragan et al. for robot reaching motion. Dragan et al. differentiate between predictability and legibility [46]. According to their definitions, predictable motion matches the human observer's expectation when the goal is known to the human observer. In contrast, legible motion allows an uninformed human observer to quickly infer the goal of the reaching task. With respect to reaching, predictable trajectories can be generated by minimizing the sum of squared velocities yielding smooth motion directly towards the goal [149]. In [48], Dragan and Srinivasa generate legible reaching trajectories by altering step by step the predictable trajectory above towards a trajectory that makes the desired goal more likely and the other goals less likely given the preceding trajectory observation. The result are trajectories that purposefully deviate from stereotypical behavior as straight lines: e.g., for two objects in the scene that could possibly be the goal of the reaching motion, a trajectory that bends away from the undesired object makes an observer believe that the other object is the goal. Care has to be taken not to too extensively optimize for legibility, as the result can be unpredictable trajectories that confuse human observers [49]. Application of the approach above to a collaborative tea preparation setting where a human had to collect ingredients based on a cup picked by a robot, showed that such legible motion led to more efficient collaboration [50]. In [81], the work above was extended to legible pointing. Goal prediction from observation of reaching motions was further investigated in [195], identifying the end effector orientation during the reaching motion as another important legibility feature.

Stulp et al. tackle the need for task specific cost functions to enable legible trajectory generation based on functional gradients in [167]. They propose to achieve legibility as a side effect when penalizing indirect legibility measures as efficiency and robustness instead of trying to explicitly optimize for legibility. Using model-free reinforcement learning in direct trial and error human-robot interaction with a Baxter robot, they validated their approach with respect to goal reaching and pick and place tasks.

The SoA on legibility covers applications that do not [46] or only weakly [23, 47] couple the intent conveying and the observing agent. This is in contrast to the physical collaboration targeted in this thesis. Actions by one agent directly affect the other agent via the physical coupling through the object. Thus, not only the own motion could be used to convey intention about the entry order for our scenario in Fig. 3.1, but also applied wrench could be used to make one's own goal legible for the partner.

Non-verbal communication

While incorporation of interaction forces and torques within a low-level controller or via mechanical compliance is crucial for safe physical interaction, additional modalities can ease collaboration. The haptic modality has the advantage of immediate information exchange, whereas communication via, e.g., speech or gestures is slow and causes delays, especially when performed by a technical system as a robot. For the reasons above, haptic interaction has been mostly used for fast low-level adaptation, while speech can be used to convey information on a high-level. In [187], the problem of ambiguous force information was remedied by using voice instructions of a human leader to switch between translation and rotation. Medina et al. made use of speech input to label semantically different paths in [126]. The difference between verbal and non-verbal communication during joint object manipulation in a human-human leader-follower setting was investigated in [139], however without wrench analysis. Vision can be used to acquire additional task information about the state of the object [2] and the human partner's intention, e.g., by interpreting gaze [155] and gestures [88]. The importance of the haptic modality for dyadic interaction tasks has been shown in laboratory settings [74, 150]. Studies as [61, 73] highlight the importance of the haptic interaction for continuous negotiation during physical interaction.

In the previous chapter, we proposed a decomposition method to split applied wrench into *manipulation wrench*, which causes acceleration, and *compensation wrench*, which causes stress inside the object. Opposing forces applied along an object can indicate disagreement among the agents with respect to desired direction and speed and have been used for low-level adaptation of impedance-based controllers [131]. On the other hand, human-human experiments indicate that a certain level of compensation wrench is desirable as it allows to establish a haptic communication channel [180]. In [51], Duchaine et al. interpret sudden increase in measured interaction force along the current direction of motion as the partner's intent to accelerate the object. They extend the low-level variable damping controller proposed in [83] through a term dependent on the force derivative.

With respect to high-level decision making, [20] and [52] investigate the use of interaction force measurements on the robot side to decide when and how to switch between predefined motions and [22] when to modify the direction of simple straight line reference motions. Bussy et al. preferred to switch among motion primitives based on velocity instead of force thresholds, due to the clear relationship of velocity to their motion primitives [20] and due to dyad dependent levels of compensation force [21]. Dumora et al. found a combination of wrench and twist information more robust and capable to initiate switching in free space for an uninformed robot [53]. However, in contrast to [21] they considered a smaller workspace that allowed a human and a robot to use their arms only. Thus, their wrench and twist data did not contain disturbances caused by walking.

Most works simplify the interpretation of interaction force by considering coinciding interaction points of the two partners [51, 124, 130] or forces only along one dimension, i.e. the connection line between the partners [72, 83, 120, 131]. The work of [52] constitutes one of the few studies that also considers torque information. However, they do not analyze the effect of applied wrench with respect to whether it led to motion or was compensated.

Coordination patterns and roles

Bimanual manipulation studies showed that humans specialize: while one arm takes over the energy intensive part of the work, the other arm performs the fine tuning [76]. Also during physical interaction, specialization in form of temporarily consistent coordination patterns were observed, which can be interpreted as the human partners taking on different roles [152]. While one of the partners contributed more to acceleration, the other partner was mainly responsible for deceleration during a crank moving task. Another study used force load share to analyze dominance differences during human dyadic collaboration [72]. Effort distributions appeared to be partly person-specific and partly interaction-dependent. Based on further simplified 1D physical interaction tasks, human roles were analyzed with respect to energy exchange [61] and categorized into the roles executor, the one who contributes most of the energy, and conductor, the one responsible for the object acceleration [166]. In [150], Reed et al. design a robot controller based on the human behavior observed in [152], such that a human partner was not able to distinguish between a robot and a human. However, in contrast to the pHHC experiments, no specialization was observable during pHRC, showing the challenges in transferring human behavior to robots. In [57], Evrard and Kheddar propose a homotopy switching model to blend between follower and leader roles. Mörtl et al. found that humans prefer constant over highly dynamic load sharing strategies during collaborative transport of bulky objects. In their study, the desired robot load share along a redundant task direction is interpreted as a so called effort role. The learning based control approaches of [126] and [144] propose to start a task with a robot follower that gradually increases its task contribution during interaction. Peternel et al. further monitor human fatigue in [144] to increase the robot contribution when appropriate. Blending between leader and follower roles based on the confidence of the human intended motion prediction was proposed by [170]. Also the risk-sensitive optimal feedback controller in [125] takes into account the uncertainty of the robot prediction on the human movement intention and furthermore allows to change the robot role with respect to the extend that the robot follows its prediction or adapts to the forces applied by the human partner. See [87] for an extensive overview of roles during physical interaction.

Chapter overview

The remainder of this chapter is structured as follows. In Section 3.3, we formulate two hypotheses related to communication and coordination strategies on which we base our problem statement. Section 3.4 introduces the experimental setup and procedure. We first report on our qualitative results from questionnaire answers in Section 3.5, before presenting motion- and wrench-based quantitative results in Section 3.6. In Section 3.7, we discuss our results and in Section 3.8 we draw conclusions and identify open problems.

3.3 Problem formulation

In this thesis, we aim at investigating haptic communication in order to be able to fully exploit its potential before incorporating additional modalities. We further assume that information of the state of the rigid object is available, as it can be inferred from the robot end effector motion for rigid grasps. Given the observed importance of haptic communication during small scale physical human-human collaboration (pHHC) experiments in laboratory settings, we choose to investigate its relevance for realistic tasks by analyzing collaborative transport of an heavy object. Inspired by the SoA on intention conveying legible motion during non-physical interaction, we are interested in analyzing legibility during pHHC. We adopt the definition of Dragan et al. that legible behavior purposefully deviates from stereotypical behavior, i.e. predictable behavior, to clarify intent with respect to a desired goal. For our kinematic manipulation scenario, the goal is represented through the entry order, i.e. who enters through a door first (see Fig. 3.1). In order to

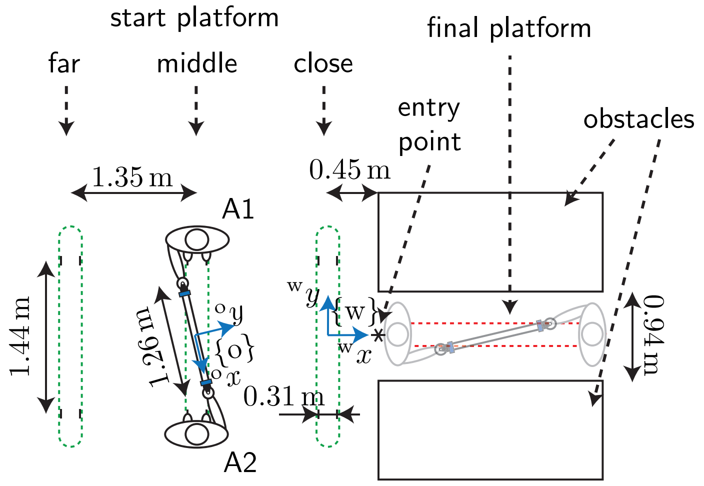

Fig. 3.2: Experimental setup from a top view: The participants held the beam on the starting platform (green) and moved to the final platform (red) between the obstacles (white boxes).

investigate the meaning of predictable and legible behavior for pHHC, we alter the guiding instruction of the entry order. Besides defined and open guiding instructions, we analyze assigned leader/follower roles. While a *leader* $\mathcal{L}$ knows the goal in terms of the desired entry order, a *follower* $\mathcal{F}$ does not and has to infer the intent of the partner during the interaction. We formulate our first hypothesis as follows.

Hypothesis 1. *Humans make use of a combination of haptic communication and legible motion depending on task setup and role assignments in order to convey intent during collaborative object transport.*

Besides legibility, we are also interested in emerging coordination patterns as dominance and specialization during realistic pHHC, which leads to our second hypothesis.

Hypothesis 2. *Humans form different coordination patterns during collaborative object transport, reflecting their task knowledge.*

From Hypotheses 1 and 2 follows the problem statement:

Problem 2. *Conduct human-human collaborative object transport experiments under different role assignments and task instructions (guiding instructions) to experimentally test Hypotheses 1 and 2.*

3.4 Experimental setup and procedure

3.4.1 Setup

Figures 3.2 and 3.3 show the experimental setup. In this study, a pair of participants carried a beam with a handle attached at each longitudinal edge. At the base of the handle connecting to the beam, a 6 DoF force/torque sensor (JR3 Inc., USA) was attached to

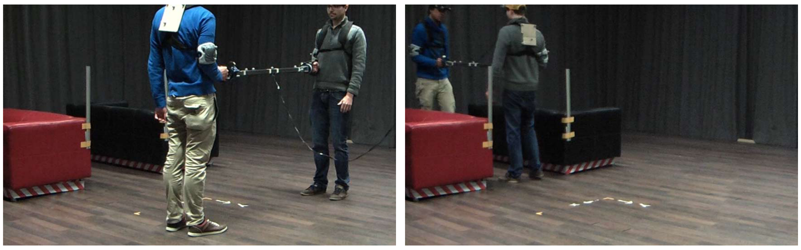

Fig. 3.3: Experimental setup: (left) The participants held the beam on the starting platform, here at middle Distance and moved to the final platform between two 3 seater couches acting as obstacles (right). Two poles were attached to the couch corners to prevent the participants from carrying the beam over the couches. The obstacles constrained the final platform in a way that caused the participants to naturally rotate the object. The participants were told to keep the beam parallel to the ground and approximately a 90 deg angle at their right elbow, while keeping their elbow close to their body. The final platform was reached once the last participant had entered the space between the couches. The cables of the force/torque sensors were hanged from the ceiling to minimize the distraction to the participants' movements.

measure the force and torque exerted by the participants. The beam weighed $m = 7.7\,\mathrm{kg}$ including handles and sensors and the mass was symmetrically distributed between the pair. The position and orientation of the beam was tracked using an *Oqus* motion capture system (Qualisys, Sweden).

The three start platforms were indicated by 4 stripes of black tape on the wooden floor. The tape stripes marked the positions the participants' feet had to be placed on initially. The final platform was orthogonally placed, and the distance from the start platform was identical between the paired participants. The couches served as obstacles and let us study how the object transport task changed from initially free space motion to motion under environmental restrictions. This manipulation results in one of the partner taking a goal position near the starting platform and the other taking the far goal position.

3.4.2 Design

The experiment was a 3 x 3 within-subject design. The first independent variable was the *Distance* to the final platform for which the start position was varied to three levels of distances. The second independent variable was the *Guiding instruction*. In the One-Guide condition, one of the two partners was assigned the leader role (A1=$\mathcal{L}$) and was always given an instruction about who had to enter the final platform first. In the Two-Guide condition, both participants were told about the orientation of the beam at the final platform. In the Free-Guide condition, no instructions were given. In the following we refer to *Entry Order* 1 when the participant who acted as a leader during One-Guide (A1=$\mathcal{L}$) entered the final platform first, and to Entry Order 2 when the follower (A2=$\mathcal{F}$) entered the final platform first. The start platform and side at which the participants stood on the start platform was counterbalanced and quasi-randomly assigned in each trial. The experimental conditions were block-randomized and the participants performed

10 trials per condition, which resulted in a total of 90 trials per pair. The participants were prohibited from making conversations or intentional communication using their body such as hand gesture.

3.4.3 Procedure

This study recruited 12 pairs of two male participants, who were right-handed and approximately matched based on their height. Prior to participating in the study, the participants received written instructions on the experiment and gave informed consent. In order to prevent any psychological biases they were not given any further information. One of the participants was randomly chosen to be the leader during One-Guide. At the beginning of each trial, the experimenter put the beam on the respective start platform and told the participants who had to stand on which side. The experimenter further gave instructions on the Entry Order based on the current Guide. After the participants had lifted the beam and were standing properly on their platform, the experimenter told the participants when to start via a countdown: 'Three, two, one, go'. Once the participants reached the final platform, the experimenter took the beam from the participants and placed it onto the start platform of the next trial.

The force/torque sensor was calibrated every ten trials, while being placed such that the weight of the beam was supported and no other mass but the handle masses acted onto the sensors. After each Guide condition block of 30 trials, the participants answered questions on

- whether they took a particular strategy for completing the task
- whether there was anything else they did to convey their intention to the partner (only during Free-Guide and for the leader during One-Guide)
- whether there was anything else that helped them to understand the intention of the partner (only during Free-Guide and for the follower during One-Guide)
- and whether and why they felt active or passive during the task.

The experiment took approximately 2-3 h per pair to complete. At the end of the experiment, the participants received 15 $^{\text{Euros}}/_{\text{h}}$ for their time.

3.4.4 Data processing

The force/torque sensor data was recorded at 1 kHz and the motion tracking data at 200 Hz by different computational units and subsequently streamed to a *MATLAB/Simulink Real-Time Target* model. Prior to the analysis, we applied second-order low-pass butterworth-filters to the position (cut-off frequency 6 Hz) and wrench data (cut-off frequency 24 Hz). This helped to avoid problems after numerical differentiation due to outliers and under-sampling with respect to the force data. We mirrored the wrench and motion data in a way that for the analysis the agents always started as displayed in Fig. 3.2.

Although we calibrated the force/torque sensors every ten trials, we observed within trial drift of the wrench measurements. We computed the offset of the wrench data by averaging the wrench recorded during the first 2 s of each trial when the partners waited for the 'go' signal from the experimenter and subtracted it from the wrench data of the respective trial.

3.4.5 Measures

Based on the position and orientation data of the beam and the wrench data, we computed measures as agent velocity, beam rotational angle and energy contribution of the participants as well as the wrench-based measures introduced in Chapter 2. The beam was kept approximately horizontally during the transportation task, allowing for a 2D treatment of the experimental data. We applied the efficient 2D beam wrench decomposition implementation introduced in Chapter 2.4.3, which yielded results close to the optimization based solution with $s = 0$ and $w = 0.5$. See Appendix C for a comparison of the physically consistent wrench decomposition method introduced in Chapter 2 to other SoA methods based on the experimental data. In summary, the simplifying assumptions of other SoA approaches led to an overestimation of disagreement/compensation with an impact on statistical analysis results of key behavioral measures for pHHC and pHRC.

3.5 Qualitative results

In this section, we analyze the open questionnaire answers with respect to our Hypotheses 1 and 2.

3.5.1 Intention communication

First, we extract questionnaire answers related to Hypothesis 1: do humans combine haptic communication and legible motion to communicate intent during collaborative object transport? And does this combination of wrench and motion adaptation change with task setup and role assignment?

With respect to *haptic communication*, two participants reported for the One-Guide and Free-Guide condition, "to push when going first" and one of them further described "to pull when going last." For the One-Guide condition, a follower reported to pay attention to whether his partner pushed or pulled. Another participant described his strategy during Free-Guide as "decide before start; in case of resistance wait a little and decide based on intuition." One participant described to "wait if first control impulse from partner, if not set direction," leaving open, whether this "control impulse" was wrench and/or motion related. One pair consistently reported on its strategy as "the stronger wins." Another participant reported after Two-Guide to have felt positive about the collaboration because "nobody pulled or pushed much."

Related to legibility via motion, three participants reported to "move towards the goal" when going first and to "*move away from the goal*," when going last. One participant described a similar strategy also for Two-guide: "Who goes last, moves backwards at first. Who goes first moves sideways, how far back depends on position," while his partner reported for the case that he had to go last to wait for his partner to move when starting at far and middle Distance, but to actively walk backwards at close Distance. According to the questionnaire answers, "the first step/move" was important to 6 participants to show and understand the intention of the leader during One-Guide and according to two participants the partner who took "the first step" decided on the Entry Order during Free-Guide.

Another motion-based legibility strategy was reported by a number of participants during Free-Guide as specifying the Entry Order via *beam rotation.* One participant reported that during One-Guide the beam translation only started after an initial clarifying beam rotation. Another participant mentioned that, also when the Entry Order was clear, the partner going last would walk backwards to speed up the rotation.

The questionnaires revealed a third approach to motion-based legibility: to adapt the translational *velocity* towards the goal based on the own Entry Order intention. The particpants reported for Free-Guide and and One-Guide to "observe the partner's walking speed." If the partner "walked fast towards the goal," he wanted to go first, if he "hesitated" during One-Guide or "walked slow," he wanted to go last.

In addition to the above motion- and wrench-related strategies, some pairs reported on *rules* they established without explicit communication during Free-Guide. The follower during One-Guide for one pair reported to always "go last" during Free-Guide, while the leader answered to "be the first to start for a clear situation." Another participant described his strategy as "the person on the left (negative y-start position) goes first, the person on the right walks backwards to speed up rotation." Finally, one participant reported to have "alternated" who goes first.

From the answers to the questionnaires we identified three main strategies for intention communication:

1. Haptic communication
2. Legible motion
    a) rotate early
    b) walk away from goal when going last
    c) walk fast towards goal when going first
3. Rule-based Entry Order

3.5.2 Coordination patterns

In this section, we report on questionnaire answers related to Hypothesis 2 of task knowledge reflecting coordination patterns. One participant described his strategy during One-Guide as "dominate to show partner who enters goal first." Another participant reported to have followed the strategy of "being dominant and lead" during Free-Guide. Most participants answered the question why they felt more active with terms like "taking the first step" or "pushing." One participant reported to "have actively waited for my partner to act."

All pairs consistently reported that during One-Guide the leaders felt more active/dominant and the followers more passive. For Two-Guide five and for Free-Guide three participants reported that "the partner who goes first is more active." One participant stated that "the person who had to go first had to wait for partner due to limited space." Another participant reported that at the close Distance start platform the "one going last is more passive." The comments "felt active, if a lot of rotation was needed to reach the goal" and "who has to go first is the more active, because he directs the rotation" relate perceived task contribution to beam rotation. One participant reported to have felt less active than his partner, as his "partner pushed more sometimes." Two other participants felt more active "because stronger" or "because he was able to pull or push the bar himself."

3.6 Quantitative results

3.6.1 Intention communication

In this section, we examine the strategies identified based on the questionnaire answers in Section 3.5.1 related to Hypothesis 1.

Haptic communication

In the following, all wrench values are given in the object frame {o} unless stated otherwise. In order to get an understanding of force and torque relations for the experimental setup, we computed the means of the absolute values given in Table 3.1. Overall, 63.89 % of the applied force was compensated. A comparison of the compensated force along the beam compared to the sum of compensation along the beam and perpendicular to it revealed that almost the complete force compensation occurred along the beam: $\overline{|f_{\mathrm{c},ix}|}/(\overline{|f_{\mathrm{c},ix}|} + \overline{|f_{\mathrm{c},iy}|}) = 98.60\,\%$. Applied torque added to the resultant torque acting at the CoM with $\overline{|t_{iz}|}/\overline{|t_{\mathrm{o},iz}|} = 31.54\,\%$. The rest of the resultant torque was produced by applied force. On average $\bar{T}_\mathrm{c}/\overline{|t_{\mathrm{o},iz}|} = 19.83\,\%$ of the resultant torque was compensated.

Tab. 3.1: Mean absolute applied and compensation wrench values

$\overline{\lvert f_{ix}\rvert}$	$\overline{\lvert f_{iy}\rvert}$	$\overline{\lvert f_{\mathrm{c},ix}\rvert}$	$\overline{\lvert f_{\mathrm{c},iy}\rvert}$	$\bar{F}_\mathrm{c}$	$\overline{\lvert t_{iz}\rvert}$	$\overline{\lvert t_{\mathrm{o},iz}\rvert}$	$\bar{T}_\mathrm{c}$
6.74 N	1.95 N	4.70 N	0.07 N	4.71 N	0.38 Nm	1.21 Nm	0.24 Nm

In order to analyze the importance of compensation wrench during the initial decision making process, we ran a 2-way Repeated-measures ANOVA (Guide vs. Distance) on disagreement measure β averaged over the time period from trial start until a beam rotation of 10 deg was reached. Figure 3.4 shows the resultant bar plots, for which β (Two-Guide) $= 0.43 \pm 0.10 < \beta$ (One-Guide) $= 0.46 \pm 0.11 < \beta$ (Free-Guide) $= 0.49 \pm 0.15$. The results show main effects for Distance $F(2, 22) = 15.98,\ p < .002$ and Guide $F(2, 22) = 3.46,\ p < .05$. No interaction effects were found.

Especially high compensation forces were recorded for the pair with the strategy "the stronger wins" during Free-Guide: $\bar{F}_\mathrm{c} = 15.86 \pm 4.29\,\mathrm{N}$ compared to a mean compensa-

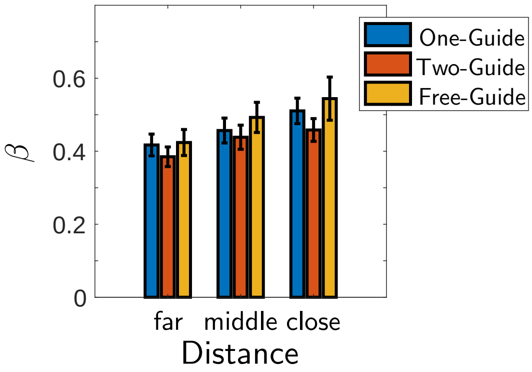

Fig. 3.4: Average disagreement measure β during the first 10 deg beam rotation of each trial. Disagreement increased from Two-Guide over One-Guide to Free-Guide and from Distance far to close. The error bar indicates one standard error.

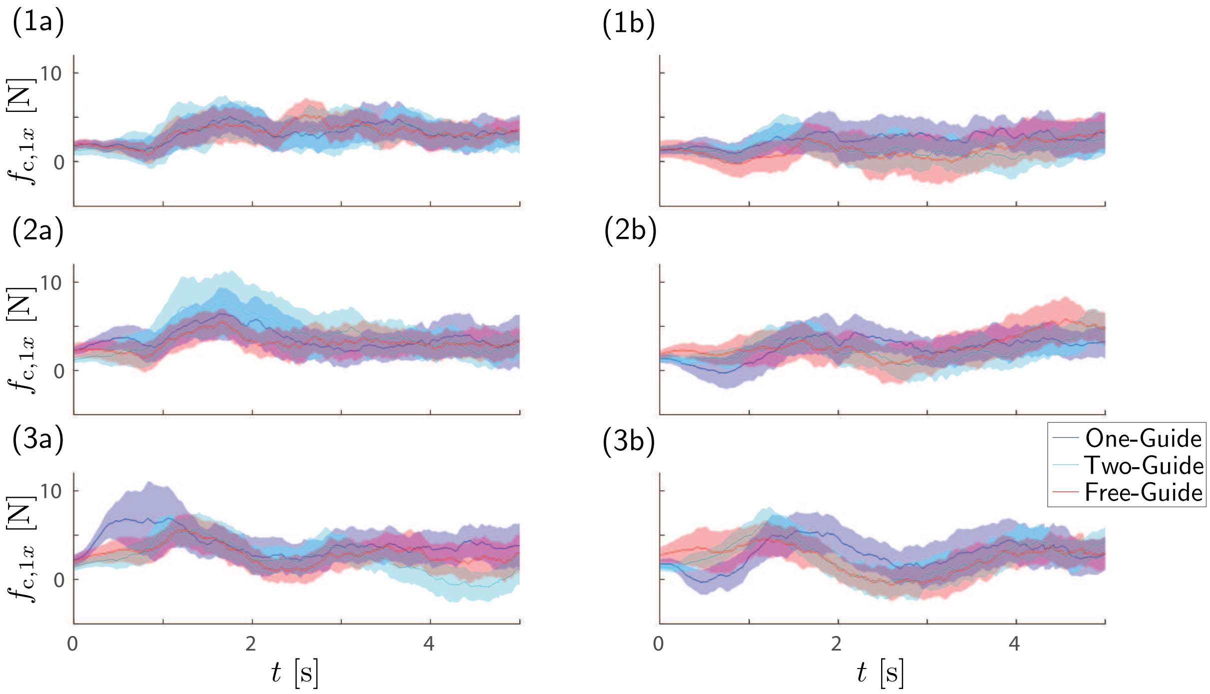

Fig. 3.5: Compensation force of agent A1 ($\mathcal{L}$ during One-Guide) during the first 5 s: (a) Entry Order 1 with A1 going first, (b) Entry Order 1 with A1 going last. Decreasing initial goal Distance from top to bottom with (1) far, (2) middle, (3) close. Compensation along the beam was not only high at the start of each trial, but also during the rest of the trial. The force profiles for One-Guide show pulling when going last ($f_{c,1x} < 0$) and pushing when going first ($f_{c,1x} > 0$). For all conditions a tendency towards pushing ($f_{c,1x} = 2.92 \pm 0.002\,\mathrm{N} > 0$) was observed.

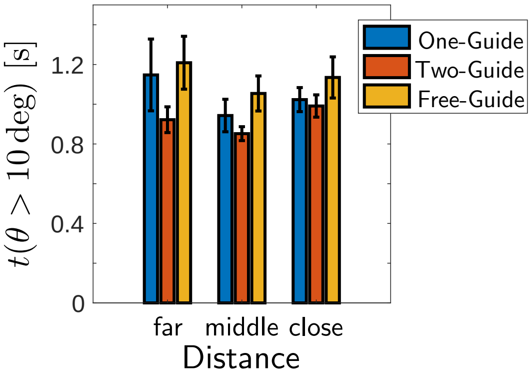

Fig. 3.6: Average time when a beam rotation of 10 deg was reached: Beam rotation time increased with level of uncertainty from Two-Guide, to One-Guide and Free-Guide. The error bar indicates one standard error.

tion force of $\bar{F}_\mathrm{c} = 4.48 \pm 2.41\,\mathrm{N}$ for all other pairs. Visual inspection of the trajectories of the respective pair further revealed especially high variability compared to the other participants. Figure 3.5 shows the mean compensation wrench of agent A1 ($\mathcal{L}$ during One-Guide) $f_{\mathrm{c},1x}$ along the beam for the first 5 s of each trial for each Guide, Distance and Entry Order combination together with the standard deviation. Here we excluded the data of the pair above with especially high compensation forces in order not to obscure visible force patterns during Free-Guide. Note that the average trial took $5.98 \pm 1.07\,\mathrm{s}$, being shorter with shorter goal Distance. We only plot the first 5 s here for better comparability between Distances and Guides. A compensation force of agent A1 $f_{\mathrm{c},1x} < 0$ signifies that the participants pulled away from each other, while $f_{\mathrm{c},1x} > 0$ signifies that the participants pushed towards each other.

Legible motion

In order to analyze the questionnaire-based strategy of *early beam rotation* for clarification of Entry Order, we ran a 2-way ANOVA on the time when a beam rotation of 10 deg was reached $t(\theta > 10\,\mathrm{deg})$ for factors Guide and Distance. The time required to achieve the first 10 deg beam rotation decreased from Free-Guide over One-Guide to Two-Guide: main effect of Guide $F(2, 22) = 4.16$, $p < .05$ with $t(\theta > 10\,\mathrm{deg}, \text{Free-Guide}) = 1.13 \pm 0.36\,\mathrm{s} > t(\theta > 10\,\mathrm{deg}, \text{One-Guide}) = 1.04 \pm 0.36\,\mathrm{s} > t(\theta > 10\,\mathrm{deg}, \text{Two-Guide}) = 0.92 \pm 0.17\,\mathrm{s}$. No effect for Distance and no interaction effect was observed.

To *move* the own beam end *away from the goal* was observed for most pairs via visual inspection, varying for Guides and Distances and among participants and pairs. Path variability was highest without instructions, i.e. during Free-Guide, and increased with goal Distance. Figure 3.7 exemplarily shows the paths for one pair grouped according to Entry Order, Guide and Distance. For the Free-Guide trials, the paths were mirrored such that the participant going last started on the bottom. For close goal Distance and Entry Order 2, the backward motion of agent A1 differs between One- and Two-Guide: During Two-Guide, agent A1 stepped into positive x- and y-direction, while during One-Guide, the leader $\mathrm{A1} = \mathcal{L}$ focused on moving straight back (into positive y-direction). This distinct

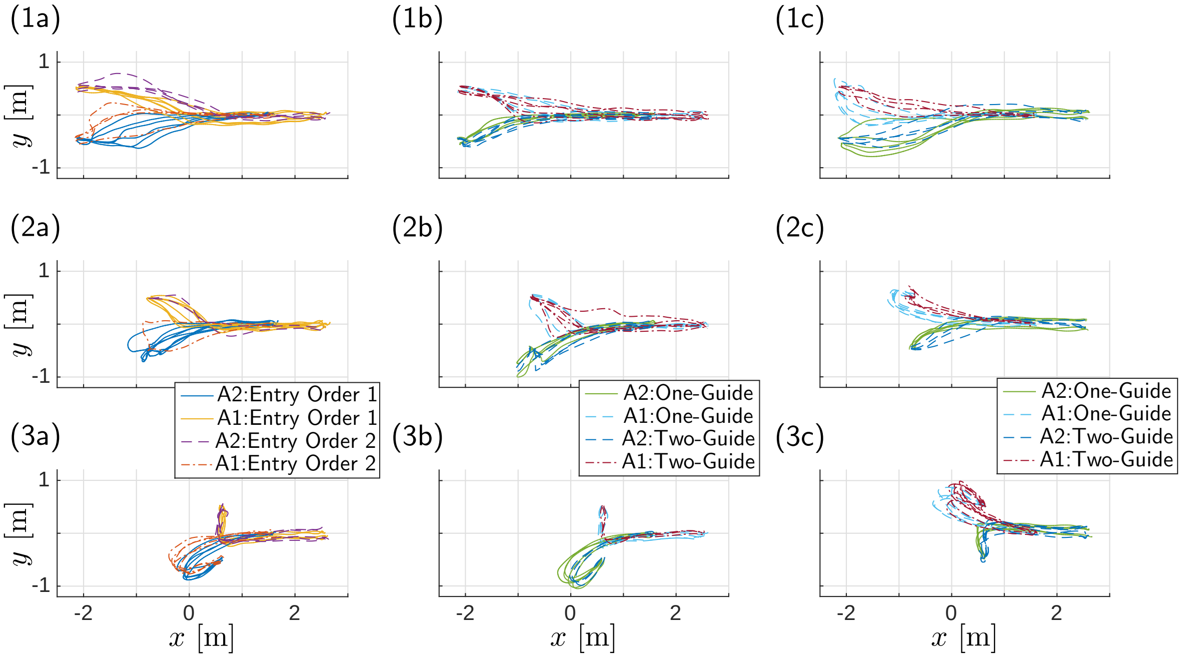

Fig. 3.7: Paths of beam interaction points of one pair: (a) Free-Guide, (b) One- and Two-Guide for Entry Order 1, (c) One- and Two-Guide for Entry Order 2. Decreasing initial goal Distance from top to bottom with (1) far, (2) middle, (3) close. Initial motion away from the goal when going last was observable for all Guides and Distances, but more dominant with decreasing goal distance and for a leader going last (One-Guide, Entry Order 2).

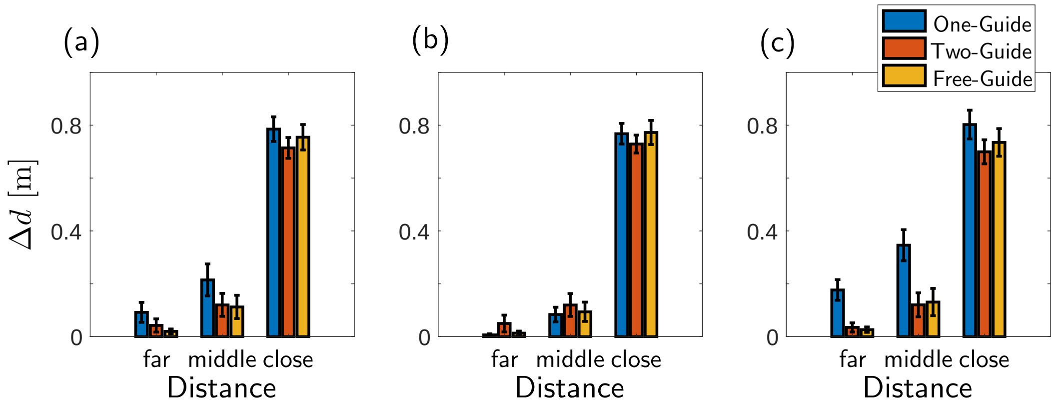

Fig. 3.8: Average distance to goal area entry point increase Δd of the beam interaction point of the participant going last: (a) Entry Order independent. (b) Entry Order 1: follower entered goal last during One-Guide. (c) Entry Order 2: leader entered goal last during One-Guide. The observed motion away from the goal is highest for a leader during One-Guide (c) and when starting closer to the final platform (close Distance). The error bar indicates one standard error.

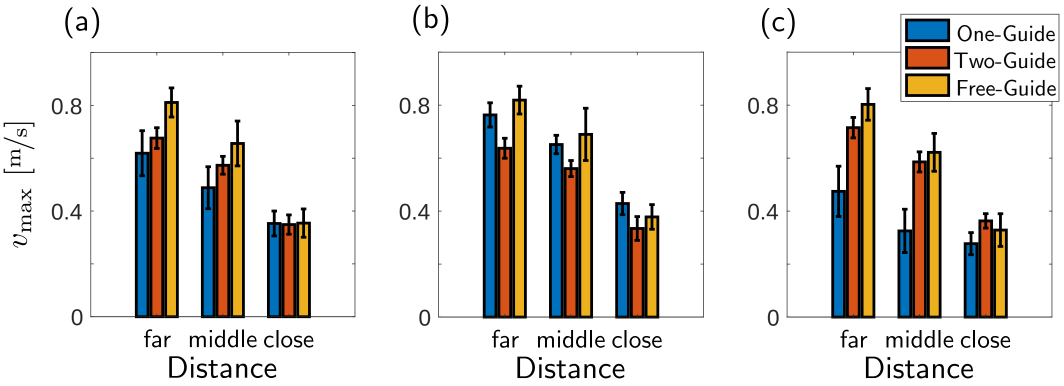

Fig. 3.9: Average peak velocity $v_{\max}$ during the first 10 deg beam rotation of each trial: (a) Entry Order independent. (b) Entry Order 1: leader entered goal first during One-Guide. (c) Entry Order 2: follower entered goal first during One-Guide. Peak velocity decreased from Distance far to close. It was highest for Free-Guide, followed by leaders during One-Guide. The error bar indicates one standard error.

motion at close Distance was observed for 6 of the 12 pairs.

We analyzed the observations above via a 2-way Repeated-measures ANOVA (Guide vs. Distance) on distance increase to entry point with respect to the start position for the participant entering the goal area last: $\Delta d = \max(\left\|{}^{\mathrm{w}}\boldsymbol{r}_i(t) -^{\mathrm{w}} \boldsymbol{r}_{\mathrm{ep}}\right\| - \left\|{}^{\mathrm{w}}\boldsymbol{r}_i(t=0) -^{\mathrm{w}} \boldsymbol{r}_{\mathrm{ep}}\right\|)$ for i being the partner going last and ${}^{\mathrm{w}}\boldsymbol{r}_{\mathrm{ep}}$ being the entry point to the final platform (see Fig. 3.2). The analysis showed main effects of Guide, $F(2,22) = 15.89$, $p < .002$, and Distance, $F(2,22) = 662.38$, $p < .002$ (see Fig. 3.8(a)). No interaction effects were observed. In order to further analyze the difference between a leader and a follower during One-Guide, we separated the results for a follower going last (Fig. 3.8(b)) and a leader going last (Fig. 3.8(c))). The results show that the observed increased movement away from the goal during One-Guide was mainly caused by the leader agent A1 $= \mathcal{L}$ (Δd (One-Guide $\mathcal{L}$) $= 0.44 \pm 0.17$ m) while for the follower and the other guides similar average values were observed (Δd (Two-Guide) $= 0.29 \pm 0.12$ m, Δd (Free-Guide) $= 0.30 \pm 0.11$ m, Δd (One-Guide $\mathcal{F}$) $= 0.29 \pm 0.78$ m).

Complementary to the above walking away from the goal when going last, the questionnaires indicated a tendency *to walk faster when going first.* We ran a 2-way Repeated-measures ANOVA (Guide vs. Distance) on peak velocity during the first 10 deg beam rotation $v_{\max} = \max \left\|{}^{\mathrm{w}}\dot{\boldsymbol{r}}_i\right\|$ and i being the partner going first. The results showed a clear effect for Distance $F(2,22) = 53.40$, $p < .002$, a smaller effect for Guide $F(2,22) = 5.03$, $p < .02$ and an interaction effect $F(4,44) = 5.70$, $p < .002$ (see Fig. 3.9(a)). While peak velocity was similarly small for all Guides when starting close to the final platform, clear Guide differences are visible at middle and far Distance: $v_{\max}$ (Free-Guide) $= 0.61 \pm 0.21$ m/s, $v_{\max}$ (Two-Guide) $= 0.53 \pm 0.12$ m/s,$v_{\max}$ (One-Guide) $= 0.49 \pm 0.23$ m/s. To examine the strategy taken by a leader during One-Guide, we separated the data for a leader going first (Fig. 3.9(b)) and a follower going first (Fig. 3.9(c)). The peak velocities were similarly high for leaders during One-Guide as for Free-Guide ($v_{\max}$ (One-Guide $\mathcal{L}$) $= 0.61 \pm 0.14$ m/s) and especially low for One-Guide followers ($v_{\max}$(One-Guide $\mathcal{F}$) $= 0.36 \pm 0.24$ m/s). Thus,

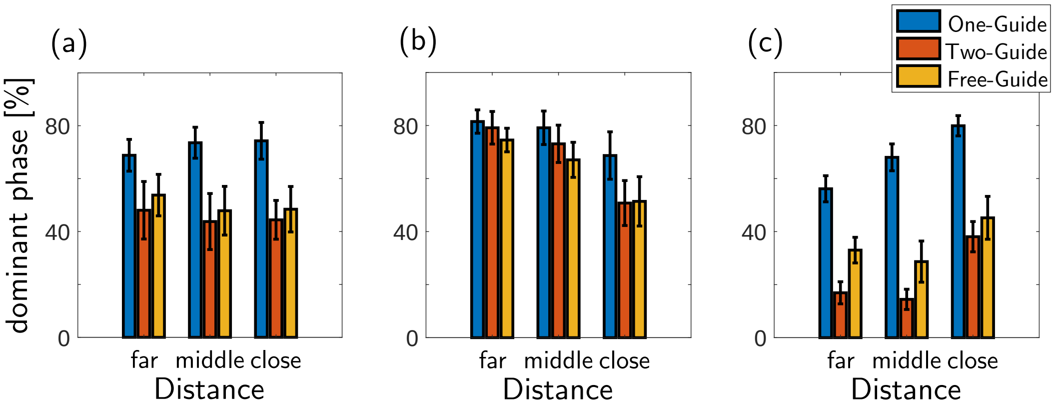

Fig. 3.10: Energy share dominance: Percentage of time during the first 10 deg beam rotation for which the energy share $\gamma_1 > 0.75$. (a) Entry Order independent. (b) Entry Order 1: leader entered goal first during One-Guide. (c) Entry Order 2: leader entered goal last during One-Guide. A1 is more dominant when taking on the leader role during One-Guide. For Two- and Free-Guide, the agent going first is more dominant. The error bar indicates one standard error.

the overall result is described via: $v_{\max}$ (One-Guide $\mathcal{L}$) $\approx v_{\max}$ (Free-Guide) $> v_{\max}$ (Two-Guide) $> v_{\max}$(One-Guide $\mathcal{F}$).

Rule-based Entry Order

The motion data showed that the strategy to always "go last" during Free-Guide, was followed by the respective pair in 26 out of the 30 Free-Guide trials. Another pair followed their rule that "the person on the left (negative x-start position) goes first" during all 30 Free-Guide trials. We observed a tendency for "the person on the right" to go first for a different pair, who did not report on this strategy: 23 out of 30 trials. The pair that reported on the strategy to "alternate" who goes first, achieved a balanced Entry Order overall. However, there were phases when during several consecutive trials the same participant entered first.

3.6.2 Coordination patterns

In this section, we examine the strategies identified based on the questionnaire answers in Section 3.5.2 related to Hypothesis 2. The load and energy measures introduced in the previous chapter (see Sec. 2.5) can be used to analyze the human-human transport task with respect to coordination patterns. The *energy share* γ_i combines translation and rotation in one measure, while further taking into account the agent's applied wrench and motion at the same time. For the following analysis, we classify participant i to be the *dominant* partner at time instance t, if $\gamma_i(t) > 0.75$. In order to analyze the dependency of Guide and Distance on energy share dominance, we ran a 2-way Repeated-measures ANOVA (Guide vs. Distance) on percentage of time for which agent A1 ($\mathcal{L}$ during One-Guide) was dominant with respect to energy share during the first 10 deg beam rotation

(Fig. 3.10(a)). The analysis revealed a main effect of Guide $F(2, 22) = 22.94, p < .002$. Leader agents $\mathcal{L}$ followed a dominant coordination strategy ($61.22 \pm 23.69\%$) during One-Guide. In contrast, during Two- and Free-Guide, A1 fell into the dominant range only for $36.33 \pm 30.41\%$ and $36.11 \pm 26.35\%$, respectively.

To analyze the coordination pattern on Entry Order related dominance suggested by the questionnaire answers, we separately display the bar plots for energy dominance of A1 entering first (Entry Order 1, Fig. 3.10(b)) and last (Entry Order 2, Fig. 3.10(c)). While a leader is slightly more dominant when going first during One-Guide than the other guides (One-Guide $76.44 \pm 21.75\%$, Two-Guide $67.67 \pm 23.95\%$, Free-Guide $64.33 \pm 22.51\%$), a clear Guide related dominance difference is present when the leader enters the goal area last (One-Guide $68.02 \pm 15.27\%$, Two-Guide $23.15 \pm 15.14\%$, Free-Guide $35.63 \pm 22.87\%$).

A 2-way Repeated-measures ANOVA (Guide vs. Distance) on energy share for a beam rotation of $70\,\text{deg} < \theta < 80\,\text{deg}$, and thus a later part of the trial showed no main or interaction effects. The percentage of time for the energy share γ_1 to fall into the dominant range was $\approx 50\,\%$ for all Guides and Distances.

Joint density estimation of force and torque *load share* separates rotation and translation and, thus, reveals the coordination strategies of the interacting pairs by large categories into quadrants (see Fig. 3.11(a,b)). For instance, a participant i with high force and torque load share at time instance t, here $\alpha_{f,i}(t) > 0.5$ and $\alpha_{t,i}(t) > 0.5$, can be classed as a *dominant* partner whereas one with low load share would be classed as a *passive* partner. In contrast, high load on one measure but low on the other indicates a *specialization*, thus each partner is largely responsible for force or torque only. Note that the joint density estimation is always diagonally symmetric between the interacting partners as their share indexes sum to 1: e.g., $\alpha_{f,1} + \alpha_{f,2} = 1$. In this way, we calculated the portion of which A1 ($\mathcal{L}$ during One-Guide) is classified into one of the quadrants.

In order to observe how the coordination patterns of the load share index is affected by our experimental manipulation, we ran a 2-way Repeated-measures ANOVA (Guide vs. Distance) on percentage of time for which the joint density of the force and torque load share fell in the dominant quadrant (Fig. 3.11(c)). Similar to the energy share results, the analysis indicates there is a main effect of Guide on the coordination, $F(2, 22) = 28.53, p < .002$. The analysis suggests that the participants formed a dominant-passive coordination strategy more often for One-Guide ($31.39 \pm 9.96\%$) than Two-Guide ($24.43 \pm 9.29\%$) or Free-Guide ($25.14 \pm 9.46\%$). In addition, a main effect of final platform Distance was found, $F(2, 22) = 7.22, p < .005$, such that the dominant-passive coordination reduced when the participants started the task close to the goal. No interaction effect was found. A separate analysis with respect to Entry Order, showed similar tendencies as for the energy share analysis: While a leader is slightly more dominant when going first during One-Guide than the other guides (One-Guide $35.44 \pm 12.83\%$, Two-Guide $32.31 \pm 11.55\%$, Free-Guide $29.65 \pm 11.29\%$), a clear Guide related dominance difference is present when the leader enters the goal area last (One-Guide $36.30 \pm 11.12\%$, Two-Guide $16.78 \pm 9.53\%$, Free-Guide $20.49 \pm 11.67\%$).

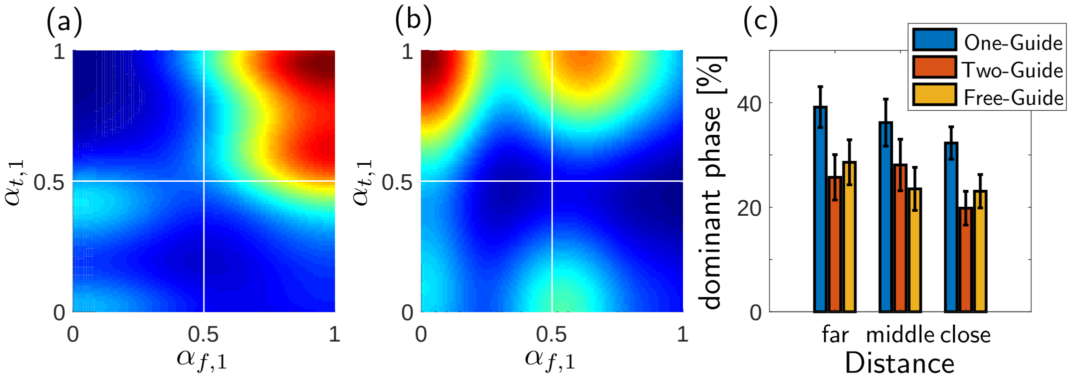

Fig. 3.11: Force and torque load share pattern based on kernel density of estimation with step size 0.01 during the first 10 deg beam rotation. (a) Dominant case: The load share is high on force and torque. (b) Specialized case: The load share is high on force or torque but low on the other. The example data from a single experimental condition ($n = 5$, (a) One-Guide and middle Distance, (b) Free-Guide and far Distance, both Entry Order 1) are used to display the results on each panel. (c) Percentage of time for which the joint density of the load share fell in the dominant quadrant. The error bar indicates one standard error.

3.7 Discussion

3.7.1 Intention communication

The human-human collaborative object transport study aimed at investigating whether humans make use of a combination of haptic communication and legible motion depending on task setup and role assignments in order to convey intent (see Hypothesis 1). The questionnaire answers provided indications that participants consciously made use of haptic communication and legible motion to understand and communicate the direction of rotation of the beam at the final platform, while more comments highlighted the importance of motion compared to wrench. Based on the questionnaire answers, we identified and investigated three aspects of legible motion: rotating the beam quickly to show the desired Entry Order, walking away from the goal to show the intent of going last and walking fast towards the goal to show the intent of going first.

Increasing uncertainty of the guiding instructions from Two-Guide over One-Guide to Free-Guide presented itself in increasing disagreement β and longer times until 10 deg beam rotation was reached. The Two-Guide condition represents the equivalent to what is reported on in the literature as stereotypical or predictable behavior [46]. Investigation of the One-Guide condition allowed to identify the underlying intention communication strategies on motion and wrench level used by assigned leaders, representing legible behavior [46]. The Free-Guide condition comprised the highest uncertainty without predefined roles. As a result, the Free-Guide condition led to the most complex decision making processes with undefined decision making times and inter-participant and inter-pair differences.

For all guides, a certain level of compensation wrench was present for the complete duration of each trial; predominantly caused by the participants pushing against each other.

Causes for a non-zero wrench compensation range from walking motion of the participants, over decision making, differing intended trajectories and the desire to "feel" the interaction partner. Questionnaire answers indicated that the participants felt positive about the collaboration if "nobody pulled or pushed much", thus relating compensation wrench to disagreement. Although compensation wrench was not only high during the initial decision making process, significant differences were observed between the different Guides and Distances at trial start: disagreement increased with uncertainty of the guiding instructions from Two-Guide over One-Guide to Free-Guide and with increasing environmental restrictions from far Distance to close Distance. Increasing environmental restrictions did also lead to more distinct force profile: e.g., when starting at close Distance, the wrench data clearly correlated with the reported leader strategy from the questionnaires to push when having to enter first and to pull when going last (see Fig. 3.5).

Increasing uncertainty of the guiding instructions presented itself not only in increasing disagreement, but also in longer times until 10 deg beam rotation was reached. Thus, the perceived importance of beam rotation to convey intention as perceived by the participants did not lead to an earlier beam rotation in situations that needed clarification. The uncertainty on the Entry Order explains the result above: while during Two-Guide both participants from the beginning on work towards a common goal, the guiding instructions One-Guide and Free-Guide require initial communication and thus hinder early collaboration. The motion data clearly supported the leader strategy to move away from the goal to convey the intention to enter the final platform last. Even during Two-Guide participants going last actively contributed to the rotation, including moving away from the goal. While environmental restrictions forced the participants to move away from the goal at the close Distance at least to a certain extent, such motion was not needed when starting further away from the goal. Thus, the participants put successful collaboration over energy sufficiency; i.e. they did not limit their own motion to the necessary minimum. During Free-Guide only for some participants clear motion away from the goal was observed, which is in line with the reported preference to be the first to enter the final platform. Complimentary to the strategy above to walk away from the goal when intending to go last, the participants increased their speed towards the goal to convey the intention of entering first. We observed highest initial peak velocities during Free-Guide, again relating to the preference of entering the final platform first.

The differences between the guides increase for legible motion from close to far Distance (see Fig. 3.8 and 3.9), but decrease for compensation wrench from close to far Distance (see Fig. 3.4). Thus, the experimental results indicate an increased usage of wrench to convey intention in confined areas, i.e. at close Distance, in contrast to the use of legible motion in free space, i.e. at far Distance. While the statistical analysis of the strategies above showed significant results over all participants, the strategy specificities differed between the pairs. Four pairs furthermore established rules during Free-Guide that defined the Entry Order without having explicitly communicated these rules beforehand. Overall, the experimental results evidenced Hypothesis 1: participants combined haptic communication and legible motion to convey intention depending on task setup and role assignments.

3.7.2 Coordination patterns

Hypothesis 2 claimed that depending on task knowledge, humans form different coordination patterns during collaborative object transport. The questionnaire answers suggested different coordination strategies depending on task knowledge related variables as Guide and role assignment for One-Guide, but also on task instruction related variable Entry Order during One- and Two-Guide, and task setup related variable Distance. Based on the energy and load share measures introduced in Chapter 2, we investigated the dominance of the partners during the initial decision making process. The quantitative results are in line with the answers to the questionnaires: under inhomogeneous task knowledge, the assigned leader was clearly more dominant than his partner. Thus, the assigned role was critical for the participants' perception on dominance. For equal task knowledge, the participant going first was more often classed as dominant, thus the Entry Order determined dominance. The clear dominance difference between the participant entering first (see Fig. 3.10(b)) and last (see Fig. 3.10(c)) during Free-Guide suggests that the initially more dominant partner entered the final platform first. We furthermore found that also the task setup had an influence on the coordination strategy: with decreasing distance to the final platform, dominance differences decreased, resulting in less distinct roles of the participants. The more confined the pair was by its surroundings, the more the manipulation task required active contribution of both participants from the beginning on, e.g., active stepping back of a follower during One-Guide to allow the leader to enter the final platform first.

Separate evaluation of linear and rotational indices allowed to identify specialization as another coordination strategy. Joint density estimation of force and torque load share showed a specialized coordination pattern for some pairs. The questionnaire answers suggest that involvement in the beam rotation is crucial for perceived task contribution. The interplay of force and torque, i.e. force can induce torque, and of linear and rotational motion, i.e. for a pure beam rotation, participants had to move linearly and rotate, impedes load share specialization.

Similar to the pair dependent strategy specificities, also the observed coordination patterns differ among pairs. These differences presented themselves on the one hand side in cooperative behavior, e.g., to always be the last to enter for clarity, and on the other hand side in competitive behavior, e.g., the stronger wins and enters the final platform first. Contrasting questionnaire answers on perceived task contribution at close Distance as "the person who had to go first had to wait for partner due to limited space" and "one going last is more passive" are in line with the observed pair-dependent coordination patterns (e.g., Fig. 3.11(a,b)).

In summary, the experimental results support Hypotheses 2: the participants formed different coordination patterns. However, not only task knowledge, but also the task setup, i.e. environmental restrictions, influenced the emerging coordination strategies.

3.7.3 From pHHC to pHRC

Our aim of pHHC analysis is to identify underlying concepts that can be incorporated into robot controllers in a next step to enable successful pHRC. From the present study we deduce that a certain level of compensation wrench is normal, where the actual level is pair dependent as also observed by [21]. While some compensation wrench also stems from walking motion, the observation of higher compensation/disagreement during guiding instructions that necessitate clarification of entry order, supports the conclusions of [180] and [74] of a haptic communication channel. Thus, although too high disagreement is undesired and a sign for competition instead of collaboration, robot controllers for pHRC should not aim for zero disagreement, as done by most SoA control approaches, e.g., [85, 125, 131].

The results of our study further revealed that besides applied wrench, participants altered and observed the motion of their own and the partner's interaction points to show and understand intent. Applied wrench and resultant motion are tightly coupled. Still, the questionnaire answers placed more emphasis on legibility through motion than applied wrench. With the partners starting at equal distance from the final platform, applied wrench along the beam at the initial configuration did not represent an unambiguous haptic signal, as it can represent desired motion to the side and/or rotation. The one-handed interaction with the beam impeded the application of torque, which would have represented an unambiguous haptic signal. Thus, further studies with different setups, e.g., two-handed manipulation, are of interest to further analyze the importance of haptic communication in realistic physical interaction.

We found evidence that humans alter predictable behavior (Two-Guide) towards legible behavior (One- and Free-Guide) in order to disambiguate between possible goals, i.e. here Entry Order 1 and 2. In [48], Dragan et al. generate legible reaching trajectories by iteratively modifying predictable trajectories. Predictable trajectories are the result of a minimization of summed squared velocities. Modification towards legible trajectories requires repeated optimization based on the same velocity dependent cost function, which can be done efficiently, e.g., using CHOMP [149]. However, the underlying cost function describing predictable object transport trajectories is unknown. In [110], the integral over squared velocity and squared applied force is used to generate trajectories for a point mass moved by a human and a virtual robot in a complex maze environment. However, the weights specifying the relation of velocity to force cost are chosen heuristically. The computational tractability analysis of Lawitzky et al. further shows that even for the simpler point mass case with reduced states (no rotational velocity and no applied torque), the optimization requires too much time for real time planning. Our observation that during Two-Guide also the partner going last moves away from the goal to actively contribute to the rotation suggests that the underlying cost function is more complex. In conclusion, the approach of repeated optimization proposed in [48] will likely not be tractable for online legible motion generation during physical interaction. The approach of Stulp et al. in [167] based on model-free reinforcement learning might offer a feasible approach, but requires learning from interaction.

Our study revealed simple strategies based on wrench and motion: push and walk fast towards goal to enter first, pull and walk away from goal to enter last. Given a predictable trajectory generator, e.g., learned in interaction, adaptation of the output trajectories according to the rules above might lead to legible interaction. Similarly, observation of the partner's action might allow for intention understanding and goal adaptation, accordingly.

3.8 Conclusions

This chapter presented a human-human study designed to examine the importance of legible motion and haptic communication for intention conveyance during collaborative object transport. In this study, two participants transported a steel beam from defined start platforms to a final platform between obstacles. The study was designed to examine how humans reach to consensus on the order when entering the final platform. We varied the task knowledge from no instructions over assigned leader/follower roles with only the leader having instructions to a predefined entry order. Furthermore, the environmental restrictions varied based on the distance of the start platform to the obstacles defining the final platform. We analyzed the physical interaction task based on open questions on strategies and perceived task contribution and based on recorded object motion and applied wrench. The study supports our hypothesis that humans make use of a combination of haptic communication and legible motion depending on task setup and role assignments in order to convey intent during collaborative object transport. We observed two legible motion strategies: moving fast towards the goal when intending to enter first and moving away from the goal when going last. The wrench based disagreement measure increased with uncertainty about the entry order during the initial decision phase, but continued to be non-zero also during the rest of the transport motion. Overall, we found that in free space legible motion is used for intention conveyance while with increased environmental restrictions haptic communication gains importance. We furthermore examined emerging coordination patterns based on load and energy measures. Equal task knowledge resulted in a dominance shift towards the participant who entered the final platform first, while during uneven task knowledge the assigned leader was more dominant. We furthermore found that not only the task knowledge but also the task setup, here environmental restrictions, led to different coordination strategies.

Open problems

With this study, we took a first step towards understanding how humans make use of legible motion and wrench to convey their intent during collaborative object transport. We focused on analyzing the interaction wrench and object motion only, although some questionnaire answers also highlighted the importance of observing the partner's motion to deduce further information. Besides aspects as body and head orientation, also more explicit communication via gestures, mimicry and speech is likely used by humans for clarification during collaborative object transport. Nevertheless, our results indicate that observation of the object motion and the interaction wrench is sufficient to understand the intent of a human partner. Verification of the result above in human-robot interaction as well as whether the human partner can also understand the robot's intent from beam motion and applied wrench, remains future work.

The task setup hindered the use of applied wrench for intention communication. Investigation of different collaborative object manipulation tasks are of interest to further investigate the importance of haptic communication.

4 Controller synthesis for human-robot collaborative swinging of rigid objects based on human-human experiments

Summary. *This chapter examines human-human rigid object swinging in order to synthesize controllers for human-robot collaborative swinging of rigid objects. The chapter demonstrates*

- *identification of a simple model for human-human rigid object swinging*
- *leader and follower controller synthesis*
- *controller verification in simulation*

The results of this chapter were published in [42]. The student work [182] contributed to this chapter.

4.1 Motivation

In factories robots assemble printed circuit boards and weld car bodies at high speeds. However, these seemingly dynamic motions are achieved through over-dimensioned motors, such that the object dynamics is negligible. Videos showing the newest achievements in, e.g., humanoid robotics or object manipulation, are mostly played at multiples of their original speed, because today's robots are actually rather slow. A reason for the slow motions is that the dynamics of the robots and the manipulated objects is often not considered. In contrast, humans and animals are capable of exploiting dynamics in order to increase performance while decreasing energy usage, e.g., during running or when throwing objects. Examples where humans inject energy using swing motion are the olympic discipline of hammer throw or children pumping a swing [146]. In [15], the formulation of a ball throwing task in terms of optimal control using a variable stiffness actuator leads to the strategy of continuous energy injection into a swinging motion to achieve high ball release velocities and consequently far throws.

Chapters 2 and 3 have addressed open topics in kinematic collaborative object manipulation, i.e. the object motion is given by the effector motions through a simple kinematic relationship. In the following chapters, we take a first step towards *dynamic manipulation* in human-robot collaborative settings by looking into joint energy injection into flexible objects via swing motion. As a motivational example for collaborative human-robot object swinging, we consider the joint manipulation of a sports mat as illustrated in Fig. 4.1(b). Through joint, continuous energy injection, the bulky flexible sports mat is brought to a higher elevation at which it can be released to be placed onto a stack of mattresses. By exploiting the task dynamics, energy can be injected in a favorable arm position for the

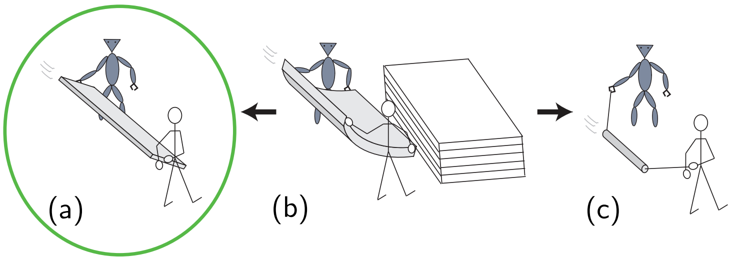

Fig. 4.1: Dynamic manipulation scenario: Collaborative energy injection into a sports mat to lift it onto a stack of mattresses (b). Interpretation of flexible object swinging (b) as a combination of rigid object swinging (a) and pendulum-like object swinging (c). This chapter presents controller synthesis for swinging of rigid objects (a) based on analysis of human-human rigid object swinging.

human (stretched arm) and the accessible work space of the agents increases. We interpret the task of collaborative flexible object swinging (b) as a combination of the extremes pendulum-like object swinging (c) and rigid object swinging (a). In this chapter, we focus on swinging of rigid objects.

Rigid object swinging can be seen as an intermediate step from kinematic to dynamic manipulation. As the agents rigidly grasp a rigid object, the motion of the object is defined by the motion of the agents' shoulders and wrists through simple kinematic relationships. However, the task belongs to the class of dynamic manipulation, as we assume that the arm configuration is not directly controlled, but indirectly through torque applied at the shoulders. This introduces underactuation in the agents' wrists. Furthermore, the goal is to control the "arm - rigid object - arm" system to reach a desired energy level represented by a desired swinging amplitude. Achievement of this goal requires to take the object dynamics into account during controller design.

4.2 Related work

Only little work exists on collaborative dynamic object manipulation in general, and in the context of human-robot interaction in particular. In [121] and [97], a human and a robot perform rope turning. For both cases, a stable rope turning motion had to be established by the human before the robot was able to contribute to sustaining it. In [143], a robot is taught to saw wood with a human partner using a two-person cross-cut saw. The sawing task requires adaptation on motion as well as on stiffness level in order to cope with the challenging saw-environment interaction dynamics. Recently, Peternel et al. extended their approach to online adapt to the human partner's fatigue and applied it to a polishing task [144].

Simple pendulum models

During rigid object manipulation, the rigid object tightly couples the robot and the human motion. Thus, human-robot collaborative swinging of rigid objects as illustrated in Fig. 4.1(a) requires the robot to move "human-like" to allow for comfort on the human

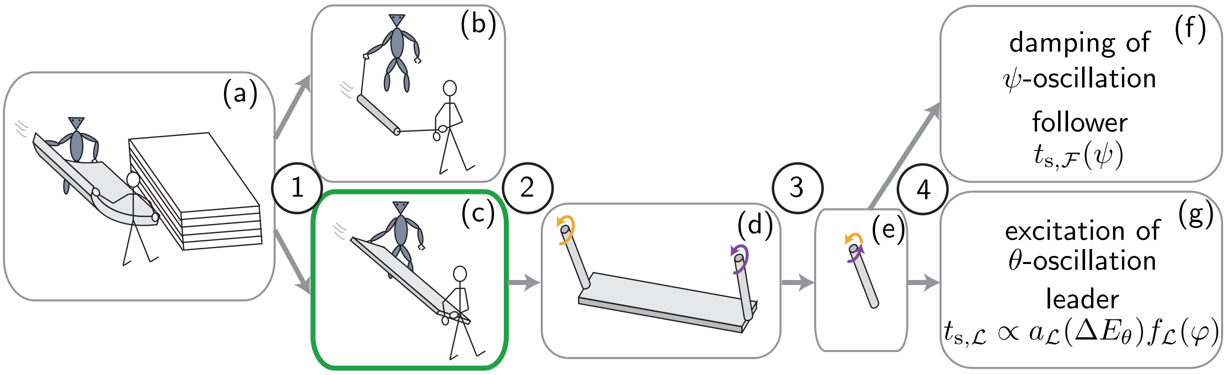

Fig. 4.2: Approach overview: (1) Interpretation of flexible object swinging as a combination of pendulum swinging and rigid object swinging. (2) Approximation of rigid object swinging by the ara-system with 1D torque inputs. (3) Projection of the ara-system onto the abstract torque-pendulum. (4) Energy-based control of the abstract torque-pendulum.

side. Lakatos *et al.* derive a human-inspired multistep bang-bang controller that can induce cyclic movements in variable impedance controlled robotic arms and simulated human arms in [107]. In [78], swinging of the lower human arm is investigated. Interestingly, the preferred frequency of swing is shown to be dictated by the physical properties of the limb rather than the central nervous system. This finding suggests that also the "arm – rigid object – arm" system during swing motion might exhibit simple pendulum-like behavior. Simple pendulums are successfully used to model and control complex mechanisms, ranging from fluid in containers [186] to biped walking [89]. Single limbs of animals are modeled as spring-driven simple pendulums in [103]. In [64], Full and Koditschek review how (spring-loaded) simple pendulums can serve as templates that are able to not only capture the essentials of locomotion of various animals, but can also be used to derive controllers for artificial locomotion. Wang and Kosuge investigate dancing as another scenario in the field of physical human-robot interaction [176]. Appropriate low-level interaction is achieved by controlling the female robotic dance partner to behave like an inverted pendulum during its single support phase. Further, in [177] the interaction between the human and the robotic dance partner is modeled as two inverted pendulums coupled by a spring and is used to investigate stability with respect to synchronization errors. Nakanishi et al. achieve successful ape-like brachiation in [135], by controlling a two link robot to behave as a simple pendulum with desired target dynamics.

In this chapter, we present human-human rigid object swing-up experiments. Our results suggest that the human arms behave as simple pendulums with torque actuation at a pivot point located in front of the agents' shoulders. This finding motivates us to model the "arm – rigid object – arm" system in Fig. 4.2(c) as two cylinders representing the agents' arms connected to the rigid object through spherical joints at the agents' wrists. In the following, we refer to this approximation of the "arm – rigid object – arm" system displayed in Fig. 4.2(d) as *ara-system*.

Energy control for simple pendulums

For a perfectly synchronized swing-up the ara-system further reduces to a single link pendulum with two-sided torque actuation in Fig. 4.2(e), which we refer to as the *abstract torque-pendulum* in the following. The *swing-up* of pendulums and their subsequent stabilization in the unstable equilibrium is a common application to test linear and nonlinear control concepts, e.g., [6, 164]. In [104] and [135], the swing-up is achieved by imposing pendulum dynamics with negative damping. Lyapunov function-based controller design is used by Lozano et al. to find a controller that brings a simple pendulum with horizontal force input to the periodic orbit equal to the energy content of an inverted pendulum [117]. We build our swing-up control for this and the following chapters on the *energy-based controller* by Yoshida [188], with the difference that we are not interested in a full swing-up but a maximum pendulum deflection below 90 deg. Here, a phase dependent torque actuation excites the ara-system at the natural frequency of the desired oscillation.

In contrast to a simple pendulum, the ara-system in Fig. 4.2(d) exhibits more than one oscillation DoF. Oscillations of the object around the vertical axis represent undesired asynchrony between the agents.

Roles

Similar to the kinematic manipulation task addressed in Chapters 2 and 3, *leader* and *follower roles* can be defined and task effort can be shared among the agents to accomplish the dynamic manipulation task under investigation in this and the following chapters. For many kinematic manipulation tasks, the leader's intention is reflected in a planned trajectory. In contrast, for the swinging task, the leader's intention is reflected in a desired object energy that is a stable periodic orbit. Consequently, the mapping of measured interaction force to leader intention as identified as possible human intention conveyance and interpretation strategy in Chapter 3 and used in kinematic manipulation tasks addressed in, e.g., [60] and [131], cannot be directly applied. In this chapter, we take a first step towards defining roles for two-agent dynamic object manipulation. The leader and the follower agent cooperate by splitting the task into two sub tasks: The leader controls the desired oscillation to reach the desired energy level (Fig. 4.2(g)), while the follower focuses on damping an undesired oscillation (Fig. 4.2(f)).

Chapter overview

The remainder of this chapter is structured along Fig. 4.2. Section 4.3 contains the problem statement, which is two-fold. On the one hand side, we want to investigate whether human-human rigid object swinging can be modeled via the ara-system in Fig. 4.2(d). On the other hand side, leader and follower controllers are to be designed based on the findings of the human-human study. In Section 4.4, we introduce the abstract torque-pendulum as a representative of the desired simple pendulum-like oscillation and recapitulate important simple pendulum fundamentals (Fig. 4.2(e)). Section 4.5 presents the human-human experiments and analyzes their results. Based on the findings of Section 4.5, a leader (Fig. 4.2(g)) and a follower (Fig. 4.2(f)) controller are designed in Section 4.6. The controllers are tested in simulation and compared to the results of the human-human experiments in Section 4.7. Finally, we draw our conclusions and discuss open problems in Section 4.8.

4.3 Problem formulation

This chapter aims at the synthesis of robot controllers for human-robot collaborative swinging of rigid objects.

4.3.1 A simple pendulum model for human-human collaborative swinging of rigid objects

In a first step, human-human experiments are conducted with the purpose of finding a desirably simple model that can capture the essentials of human-human collaborative swinging of rigid objects. Research on motor behavior suggests that the swinging of single human limbs is dictated by their pendulum-like physical properties [78]. According to a limb model proposed by [103], the small angle approximation of the frequency of swing is

$$\omega_0 = \sqrt{\frac{m_\vartheta g c_\vartheta + k_\vartheta}{j_\vartheta}} = \sqrt{\frac{g}{l_{\text{eq}}} + \frac{k_\vartheta}{j_\vartheta}}, \tag{4.1}$$

with limb mass m_ϑ, distance of pivot to center of gravity of the limb c_ϑ, internal joint stiffness k_ϑ, limb moment of inertia j_ϑ, gravity g and equivalent length l_{eq}. The index ϑ stands for the deflection angle as the single oscillation degree of freedom of the limb and will later be used as the deflection angle of the abstract torque-pendulum in Fig. 4.2(e). The finding above about human limbs raises the question, whether the combined "arm - rigid object - arm" system as displayed in Fig. 4.2(a) exhibits simple pendulum-like behavior as well.

Figure 4.3 shows the proposed simplified "arm - rigid object - arm" system, abbreviated as the ara-system. The ara-system is composed of three rigid bodies connected by spherical joints. The desired oscillation DoF θ describes oscillations of the object around the z-axis. The disturbance oscillation DoF ψ describes oscillations of the object around the y-axis. The two agents actuate the system through torque inputs $t_{\text{s},i}$ with $i = 1, 2$ applied at their shoulders around the z-axis. The state of the ara-system is fully defined by the angles θ, ψ and angular velocities $\dot{\theta}, \dot{\psi}$: $\boldsymbol{x}_{\text{araS}} = \begin{bmatrix}\theta & \psi & \dot{\theta} & \dot{\psi}\end{bmatrix}^\top$.

The objective is to control the ara-system to reach the desired periodic orbit

$$\mathcal{O}(\boldsymbol{x}_{\text{araS}}) : \begin{cases} E_\theta = E_\theta^{\text{d}} = 2 m_\vartheta g c_\vartheta (1 - \cos(\theta_E^{\text{d}})), \\ E_\psi = E_\psi^{\text{d}} = 0. \end{cases} \tag{4.2}$$

where E_θ and E_ψ are the energies contained in the ara-system due to the θ- and ψ-oscillations and the superscript d signifies their desired values. The mass m_ϑ combines the arm masses and the object mass, such that $2m_\vartheta = m_{\text{a},1} + m_{\text{a},2} + m_{\text{o}}$.

Thus, the desired oscillation DoF θ is to be excited such that the oscillation reaches the energy E_θ^{d}, which is equivalent to a maximum deflection angle θ_E^{d} or desired object

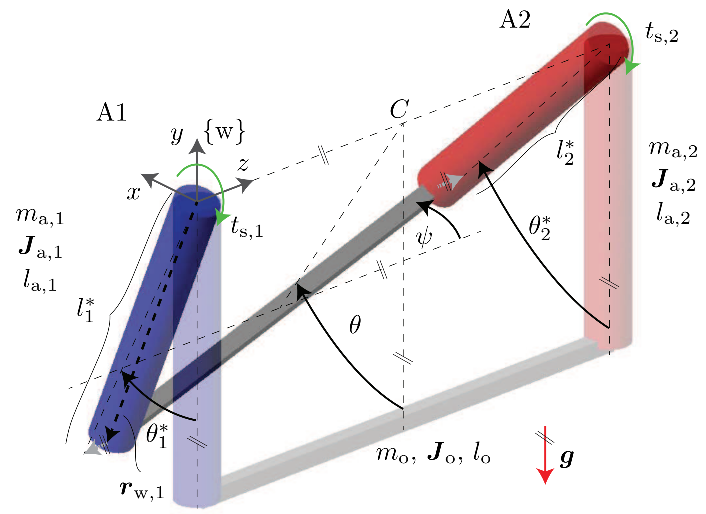

Fig. 4.3: The ara-system: Two cylindrical arms connected at their spherical wrist joints through a rigid object of mass m_{o}, length l_{o} and moment of inertia $\boldsymbol{J}_{\mathrm{o}}$ under the influence of gravity $\boldsymbol{g} = [0 \quad -g \quad 0]^\top$. The two cylindrical arms are of mass $m_{\mathrm{a},i}$, moment of inertia $\boldsymbol{J}_{\mathrm{a},i}$ and length $l_{\mathrm{a},i} = l^*$ with $i = 1, 2$ and have their pivot point at the origin of the world fixed coordinate system $\{\mathrm{w}\}$ and at $\boldsymbol{p} = [0 \quad 0 \quad C]^\top$ in $\{\mathrm{w}\}$, respectively. The projections of the cylindrical arms onto the xy-plane are of length l_i^* with $i = 1, 2$. Pairs of parallel lines at the same angle indicate parallelity.

height $y_{\mathrm{o},E}^{\mathrm{d}}$, at which the object could potentially be released. Energy E_ψ contained in the ψ-oscillation is regarded as the result of asynchrony between the partners, and is to be damped. As a consequence, during a perfectly synchronized swing-up the ara-system behaves as a simple pendulum with torque actuation.

The maximum deflection angles θ_E and ψ_E are the amplitudes of the θ- and ψ-oscillation and represent energy equivalents. We define the energy equivalent Θ_E for a general oscillation Θ as follows:

Definition 3. *The* energy equivalent $\Theta_E \in [0 \quad \pi]$ *is a continuous quantity which is equal to the maximum deflection angle the* Θ*-oscillation would reach at its turning points* ($\dot{\Theta} = 0$) *in case* $E_\Theta = const.$.

In this and the following chapters, we use θ_E, ψ_E according to Definition 3 with $\Theta = \theta, \psi$ and E_θ, E_ψ interchangeably to refer to the energies contained in the θ- and ψ-oscillations, respectively.

We formulate our hypothesis as follows:

Hypothesis 3. *The human arms during human-human collaborative swinging of rigid objects behave as simple pendulums.*

In addition to finding a simple model, we are interested in reasoning about recurring forcing patterns under different conditions, i.e. leader/follower combinations. Similar to Chapter 3, we differentiate between leader and follower agents based on the agents' knowledge about the task goal. Here the task goal is the desired energy level E_θ^{d}, which is only known to a leader. In contrast, a follower does not know the desired energy level E_θ^{d} and has to choose appropriate control actions based on the information gained from the interaction with the object.

From Hypothesis 3 and our leader/follower role definitions follows the problem statement of the first part of this chapter:

Problem 3. *Conduct human-human rigid object swinging experiments under different leader/follower role assignments to experimentally test Hypothesis 3 and to find recurring forcing patterns.*

4.3.2 Controller synthesis for human-robot collaborative swinging of rigid objects

In a second step, the results of the human-human experiments are used to design robot controllers. Without loss of generality we assume agent A1 in Fig. 4.3 to be the robot controlled through proper choice of input $u_1 = t_{\mathrm{s},1}$. Although we assume collaborative behavior, agent A1 cannot directly influence the partners applied torque, which is therefore classified as disturbance $z_2 = t_{\mathrm{s},2}$. The robot arm is part of the pendulum-like system and we assume a rigid grasp of the object. Thus, we interpret the joint between the cylindrical arms and the rigid object as the robot's wrist joint. Consequently, the robot has access to $\boldsymbol{y}_{\mathrm{m},1} = \begin{bmatrix} \boldsymbol{r}_{\mathrm{w},1}^\top & \psi \end{bmatrix}^\top$, where $\boldsymbol{r}_{\mathrm{w},1}$ is the position of its wrist/end effector in world coordinates $\{\mathrm{w}\}$ and ψ represents the rotation of the object and thus the wrist around the y-axis (see Fig. 4.3).

A *leader* $\mathcal{L}$ knows the desired periodic orbit $\mathcal{O}(\boldsymbol{x}_{\mathrm{araS}})$ including the desired energy levels E_θ^{d} and E_ψ^{d}.

Problem 4 (Leader $\mathcal{L}$)**.** *Find a control law $u_{\mathcal{L}}$ as a function of measurable output and the desired object energies*

$$u_{\mathcal{L}} = \ddot{r}_{\mathcal{L}} = f(\boldsymbol{y}_{\mathrm{m},\mathcal{L}}, E_\theta^{\mathrm{d}}, E_\psi^{\mathrm{d}} = 0)$$

such that

$$\left| E_j^{\mathrm{d}} - E_j(t > T_{\mathrm{s}}) \right| \leq \epsilon_j \textit{ with } j = \theta, \psi \quad \text{for} \quad 0 < T_{\mathrm{s}} < \infty.$$

Hence, we require the energy errors to stay within the ranges ϵ_θ and ϵ_ψ the latest after the system settling time $t = T_{\mathrm{s}}$. Instead of focusing on small ranges ϵ_θ, ϵ_ψ and short settling time T_{s}, our goal is to replicate the observed human-human swing-up behavior.

Whereas a robot leader knows the desired energy E_θ^{d}, a robot follower does not. Consequently, a follower has to infer the partner's intention from the system state in order to collaboratively contribute to the task goal.

Problem 5 (Follower $\mathcal{F}$)**.** *Find a control law $u_{\mathcal{F}}$ as a function of measurable output and zero energy contained in the undesired oscillation*

$$u_{\mathcal{F}} = \ddot{r}_{\mathcal{F}} = f(\boldsymbol{y}_{\mathrm{m},\mathcal{F}}, E_\psi^{\mathrm{d}} = 0)$$

such that

$$\left| E_j^{\mathrm{d}} - E_j(t > T_{\mathrm{s}}) \right| \leq \epsilon_j \textit{ with } j = \theta, \psi \quad \text{for} \quad 0 < T_{\mathrm{s}} < \infty.$$

All vectors throughout this and the following chapters on dynamic manipulation are given in world coordinates $\{\mathrm{w}\}$, unless stated otherwise.

4.4 Simple pendulum preliminaries

As stated in Problem 3, we want to investigate whether swinging human arms coupled via a heavy rigid object show simple pendulum behavior. In this Section, we first introduce the abstract torque-pendulum as a simple pendulum approximation of the ara-system. Subsequently, we recapitulate relevant basics of simple pendulums.

4.4.1 The abstract torque-pendulum

In case of a perfectly synchronized swing-up, the undesired deflection angle ψ of the ara-system in Fig. 4.3 equals zero. Consequently, the angle θ is equal to its projections into the agents' xy-planes $\theta = \theta_1^* = \theta_2^*$ (see gray arrows in Fig. 4.3) and the system dynamics can be rewritten in terms of the reduced state vector $\boldsymbol{x}_{\mathrm{atP}} = \left[\vartheta,\ \dot{\vartheta}\right]^\top$

$$\dot{\boldsymbol{x}}_{\mathrm{atP}} = \begin{bmatrix} \dot{\vartheta} \\ -\omega_0^2 \sin\vartheta \end{bmatrix} + \begin{bmatrix} 0 \\ \frac{1}{j_\vartheta} \end{bmatrix} \frac{t_{\mathrm{s},1} + t_{\mathrm{s},2}}{2}. \tag{4.3}$$

We call this pendulum *abstract torque-pendulum*, where *torque-pendulum* stands for a simple pendulum with torque actuation and *abstract* signifies equal influence by two agents. We use the variables ϑ for the deflection angle of the abstract torque-pendulum in contrast to the actual deflection angle θ of the ara-system. On the desired periodic orbit we have $\theta = \theta^* = \vartheta$. The small angle approximation of the natural frequency $\omega_0 = \frac{m_\vartheta c_\vartheta g}{j_\vartheta}$ depends on gravity g, object mass m_ϑ, distance between pivot point and the center of mass c_ϑ and the resultant moment of inertia around the pendulum pivot point j_ϑ. The equivalent length of the natural frequency representation of limbs in (4.1) results in $l_{\mathrm{eq}} = \frac{j_\vartheta}{m_\vartheta c_\vartheta}$ under the simplifying assumption of zero internal shoulder stiffness $k_\vartheta = 0$. The subscript ϑ stands for parameters of the abstract torque-pendulum. The parameters m_ϑ, c_ϑ and j_ϑ represent one side of the ara-system, i.e. half of the mass and moment of inertia of the rigid object and the two cylindrical arms. By dividing the input torques by 2 in (4.3), we consider the complete mass and moment of inertia of the ara-system.

Note that the abstract torque-pendulum is not meant to capture the complete system dynamics of the ara-system, which would also include joint stiffnesses and damping, but models the desired oscillation as simple pendulum-like. In the following, we investigate if human-human swinging exhibits such simple pendulum-like characteristics.

4.4.2 Energy equivalent, natural frequency and phase angle

Here, we recapitulate important simple pendulum fundamentals. The energy contained in the abstract torque-pendulum is

$$E_\vartheta = j_\vartheta \dot{\vartheta}^2 + 2 m_\vartheta g c_\vartheta \left(1 - \cos\vartheta\right). \tag{4.4}$$

Note that the overall moment of inertia and mass are $2j_\vartheta$ and $2m_\vartheta$. Thus, j_ϑ and m_ϑ represent the mass and moment of inertia to be handled by each agent under the assumption of equal effort sharing. As introduced in Section 4.3, we use the oscillation amplitude ϑ_E

as an energy equivalent. According to Definition 3, the energy ϑ_E is equal to the maximum deflection angle ϑ reached at the turning points for angular velocity $\dot{\vartheta} = 0$

$$E_\vartheta = 2m_\vartheta g c_\vartheta \left(1 - \cos\vartheta_E\right). \tag{4.5}$$

Setting (4.4) equal to (4.5), we can express ϑ_E in terms of the abstract torque-pendulum state $\boldsymbol{x}_{\mathrm{atP}}$

$$\vartheta_E = \arccos\left(\cos\vartheta - \frac{1}{2\omega_0^2}\dot{\vartheta}^2\right), \tag{4.6}$$

with $\vartheta_E \in [0 \quad \pi]$.

Simple pendulums as the abstract torque-pendulum constitute nonlinear systems with an energy dependent natural frequency $\omega(\vartheta_E)$. The small angle approximation of the natural frequency ω_0 only holds for small maximum deflection angles $\theta_E < 13\,\mathrm{deg}$. With higher energy content, the natural frequency ω decreases. This is an important fact, because we are interested in reaching maximum deflection angles up to $\theta_E = \frac{\pi}{2}$. The exact solution for ω is [9]

$$\omega = \omega_0 \frac{\pi}{2}\left[\int_0^{\frac{\pi}{2}} \frac{\mathrm{d}\phi}{\sqrt{1 - \sin^2\left(\frac{\vartheta_E}{2}\right)\sin^2(\phi)}}\right]^{-1}, \tag{4.7}$$

which cannot be solved analytically, but requires numerical approximation of the complete elliptic integral of the first kind. A numeric solution can be obtained by the arithmetic-geometric mean $M\left\{1, \cos\frac{\vartheta_E}{2}\right\}$ [24] as

$$\omega \;=\; \omega_0 M\left\{1, \cos\frac{\vartheta_E}{2}\right\}. \tag{4.8}$$

The arithmetic and the geometric mean of $\left\{1, \cos\frac{\vartheta_E}{2}\right\}$ result from the first iteration of the arithmetic-geometric mean $M\left\{1, \cos\frac{\vartheta_E}{2}\right\}$. Multiplication of the arithmetic and the geometric mean with the small angle approximation of the natural frequency ω_0 constitute good estimates for the natural frequency ω

$$\omega \approx \begin{cases} \omega_{\mathrm{a}} = \omega_0 \frac{1+\cos\frac{\vartheta_E}{2}}{2} \\ \omega_{\mathrm{g}} = \omega_0 \sqrt{\cos\frac{\vartheta_E}{2}} \end{cases}, \tag{4.9}$$

with relative error 0.748 % for the arithmetic mean approximation ω_{a} and 0.746 % for the geometric mean approximation ω_{g} at $\vartheta_E = \frac{\pi}{2}$ with respect to the sixth iteration of the arithmetic-geometric mean approximation $M\left\{1, \cos\frac{\vartheta_E}{2}\right\}$.

The pendulum nonlinearities are visualized in phase portraits on the left side of Fig. 4.4 for two constant energy levels $\vartheta_E = 0.5\pi$ and $\vartheta_E = 0.9\pi$. The inscribed phase angle φ is

$$\varphi = \operatorname{atan2}\left(-\frac{\dot{\vartheta}}{\Omega}, \vartheta\right), \tag{4.10}$$

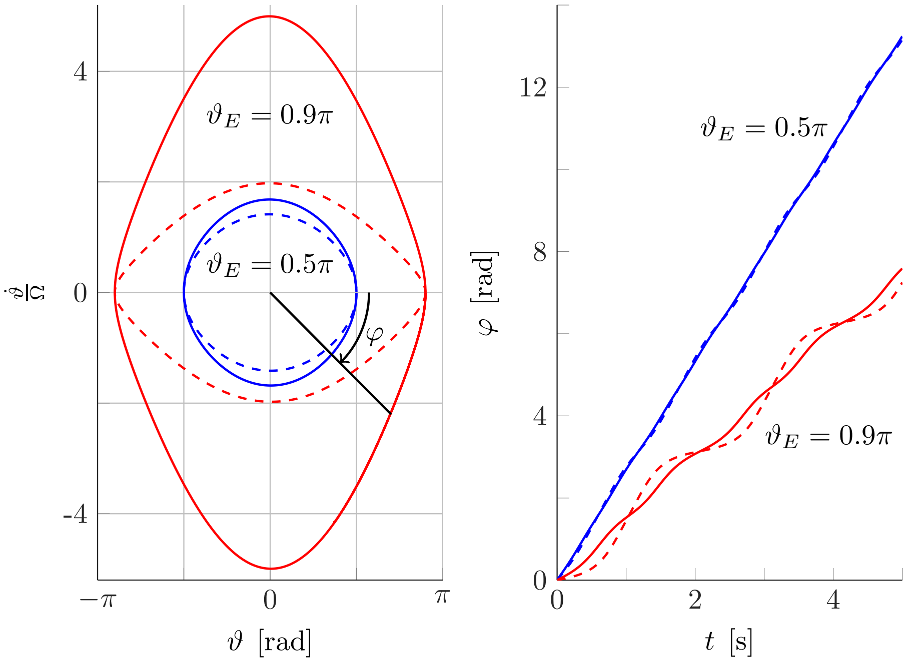

Fig. 4.4: Phase portrait (left) and phase angle φ over time (right) at constant energy levels $\vartheta_E = 0.5\pi$ (blue) and $\vartheta_E = 0.9\pi$ (red) of a lossless simple pendulum. Normalization with $\Omega = \omega_\mathrm{g}$ marked via solid lines and $\Omega = \omega_0$ via dashed lines. For energies up to $\vartheta_E = 0.5\pi$ and a normalization with $\Omega = \omega_\mathrm{g}$, the phase space is approximately a circle and the phase angle φ rises approximately linearly with time.

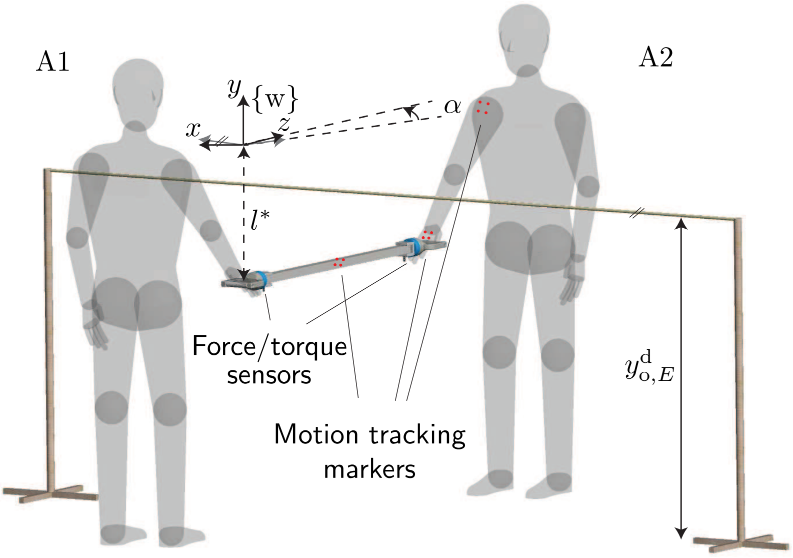

Fig. 4.5: Experimental setup.

with normalization factor Ω. The right side of Fig. 4.4 displays the phase angle φ over time. The normalization factor Ω is used to partly compensate for the pendulum nonlinearities, with the result of an almost circular phase portrait and an approximately linearly rising phase angle

$$\varphi(t) \approx \omega t + \varphi(t = 0). \tag{4.11}$$

Consequently, we can achieve a controlled swing-up of the abstract torque-pendulum to angles outside the region of the small angle approximation by applying input torques that are a function of the phase angle $t_{s,i} = f(\varphi)$ with $i = 1, 2$ in (4.3). Fig. 4.4 shows that normalization with the more accurate geometric mean approximation of the natural frequency $\Omega = \omega_{\mathrm{g}}$ allows for a better compensation of the pendulum nonlinearities than a normalization with the small angle approximation $\Omega = \omega_0$, i.e. the phase angle rises more linearly over time. For energy levels $\vartheta_E > 0.5\pi$, the geometric mean approximation less accurately approximates the actual natural frequency. Also the simple pendulum nonlinearities become more dominant and can be less well compensated via normalization with Ω. As our region of interest is limited to $\vartheta_E < 0.5\pi$, the geometric mean serves as a good natural frequency estimate and normalization factor. Therefore, we make use of the geometric mean approximation ω_{g} within derivations and as ground truth in simulations and experiments in this and the following chapters.

4.5 Human-human rigid object swinging experiments

This section describes the conducted human-human swing-up experiments and discusses their results.

4.5.1 Experimental setup and procedure

The experimental setup is displayed in Fig. 4.5. We used the same beam object with 6 DoF force/torque sensors (JR3, Inc., USA) between handles and beam as for the collaborative object transport experiments presented in Chapter 3. Here, we focus on the experimental setup related differences. See Chapter 3.4 for more details. The mass of the steel beam of 7.7 kg was increased in half the trials through attachment of an additional mass of 2.5 kg. Thus we had $m_\mathrm{o} = \{7.7\,\mathrm{kg}, 10.2\,\mathrm{kg}\}$. We tracked the position of the rigid object as well as of the wrist and the shoulder of our participants using an *Oqus* motion capture system (Qualisys, Sweden). The goal energy was displayed in form of a desired height, which was varied between $y^\mathrm{d}_{\mathrm{o},E} = \{1\,\mathrm{m}, 1.2\,\mathrm{m}\}$. Prior to the analysis, we used smoothing filters on the 200 Hz position data, to avoid problems after numerical differentiation due to outliers and undersampling with respect to the 1 kHz force data. Small time shifts between force and position data in the range of milliseconds showed to have significant impact on the energy calculations and were identified individually for each trial.

Four participants formed two couples (age of 20-24 and 54, one female and three male, all right-handed) to participate in our small pilot study. We recorded a total of 16 trials per couple composed of the two different masses and heights as well as under the following conditions:

- Both leaders A1=A2=$\mathcal{L}$ (HL-HL)
- Leader A1=$\mathcal{L}$ and follower A2=$\mathcal{F}$ (HL-HF)
- Follower A1=$\mathcal{F}$ and leader A2=$\mathcal{L}$ (HF-HL)
- No specified roles

The participants with follower roles were blindfolded, such that they could not see the desired height $y^\mathrm{d}_{\mathrm{o},E}$ and thus did not know the goal energy E^d_θ. The abbreviations HL and HF stand for human leader and human follower, respectively, and will be used to differentiate between robots and humans and leader and follower roles in the following chapters.

We asked one participant of each couple to stand at a defined location (A1) such that his body was approximately oriented as displayed in Fig. 4.5. The other participant (A2) oriented himself in a comfortable position. The participants were asked to collaboratively swing up the rigid object to the displayed height using their right hands and to keep the desired energy level for several oscillations before releasing the energy. No more instructions were given to the participants.

4.5.2 Experimental results and discussion

Approximation as abstract torque-pendulum

First, we investigate how close the *movement path* of the individual agents is to the one of the abstract torque-pendulum. As the world coordinate system {w} is defined by the swinging plane (xy-plane) and the location of the pivot point of the cylindrical arm of agent A1 (see Fig. 4.3), its exact location and orientation were unknown prior to the analysis of

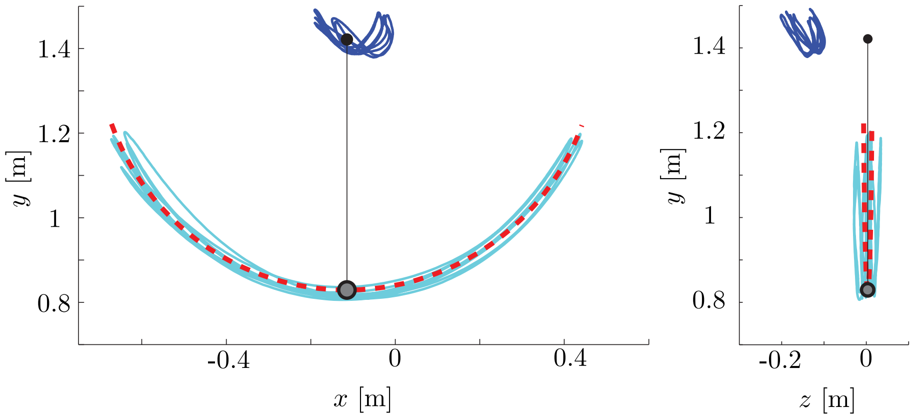

Fig. 4.6: Circle fit for movement path of agent A1 for an example trial: Shoulder (solid dark blue line), wrist (solid light blue line) and fit (dashed red line) with $l_1^* = 0.61\,\mathrm{m}$, $\alpha_1 = 0.8\,\mathrm{deg}$, $\mathrm{RMSD} = 0.014\,\mathrm{m}$. The participant's wrist motion closely matched the movement path of the abstract torque-pendulum of length l_1^* with pivot point in front of the participant's shoulder.

the data. The y-axis of $\{\mathrm{w}\}$ is defined by gravity vector $\boldsymbol{g}$. We initially aligned the world coordinate system $\{\mathrm{w}\}$ with the rope displaying the desired height. The exact orientation of the swinging plane was identified by fitting a plane along the y-axis to the wrist data of each agent and for each trial. The initial world coordinate system was then rotated around its y-axis by the identified angle α (see Fig. 4.5). In a next step, a circle lying within the identified swinging plane, now new xz-plane, was fit to the wrist data. The resultant circle radius is equal to the averaged projected pendulum length l^*.

Figure 4.6 shows the resulting fit for an example trial. For each fit we calculated the RMSD from the closest distance of each wrist data point to the circle fit. The identified projected lengths l^* varied between $l^*_{\mathrm{min}} = 0.48\,\mathrm{m}$ and $l^*_{\mathrm{max}} = 0.62\,\mathrm{m}$ with a mean value $\bar{l}^* = 0.56\,\mathrm{m}$. Low errors $\mathrm{RMSD}_{\mathrm{min}} = 0.007\,\mathrm{m}$ and $\mathrm{RMSD}_{\mathrm{max}} = 0.038\,\mathrm{m}$ indicate similarity of the human arm motion during swing up to a simple pendulum oscillation. The heavy object caused the participants to make use of their arm kinematics by keeping their arms stretched and rotating their arms mainly around the shoulders.

An additional small user study was performed to investigate the *frequency characteristics* of the participants' ara-system. Two right-handed, male participants in the age of 23-24 were asked to swing the 7.7 kg object at three different constant maximum deflection angles $\theta_E = \{0.5\,\mathrm{rad}, 1.0\,\mathrm{rad}, 1.2\,\mathrm{rad}\}$. For each deflection angle 8 trials were recorded.

Figure 4.7 displays the average frequencies ω_k over maximum deflection angle $\theta_{E,k}$ obtained from a Fourier analysis of the recorded data at each of the three desired energy levels $k = \{1, 2, 3\}$. By minimization of the distance of the data points $(\theta_{E,k}, \omega_k)$ to the geometric mean approximation of the natural frequency $\omega_{\mathrm{g}}(\theta_E)$ in (4.9), we obtain an estimate for the unknown small angle approximation of the natural frequency $\omega_0 = 3.75\,\mathrm{rad/s}$. The good fit of our experimentally obtained data to the energy dependent decrease of a simple pendulum as shown in Fig. 4.7 affirms Hypothesis 3 that the human arms behave simple pendulum-like during rigid object swinging. Our observations further suggest that our ara-system approximation and for synchronized swing-up the abstract torque-pendulum

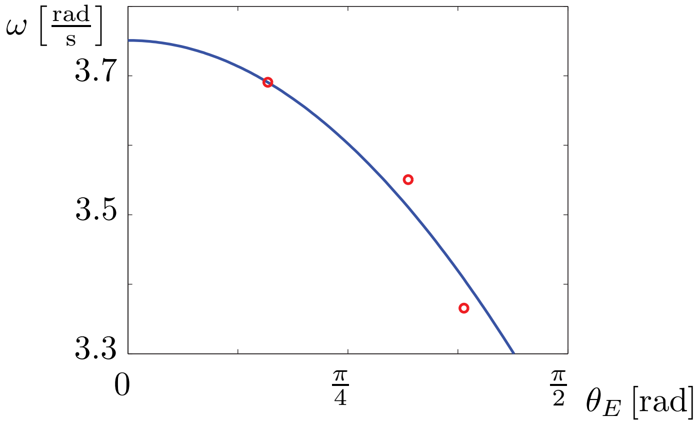

Fig. 4.7: Results of frequency analysis: Fitted curve $\omega(\theta_E)$ (blue solid line) to measured data points $(\theta_{E,k}, \omega_k)$ (red circles). The close fit supports the abstract torque-pendulum approximation.

approximation are applicable.

Recurring forcing patterns

In a next step, we investigate the energy E_i and energy flow $\dot{E}_i$ contributed by the two agents $i = 1, 2$ for recurring forcing patterns.

Neglecting air drag, the total change in object energy is calculated as the energy contributed by the two agents

$$\dot{E}_\text{o} = \dot{E}_{\text{o},1} + \dot{E}_{\text{o},2} = \dot{\boldsymbol{r}}_1^\top \boldsymbol{f}_1 + \dot{\boldsymbol{r}}_2^\top \boldsymbol{f}_2, \tag{4.12}$$

with $\boldsymbol{f}_i$ being the forces applied at the participants' interaction points and $\dot{\boldsymbol{r}}_i$ being the velocities of the participants' interaction points. The total system energy is obtained through integration of (4.12)

$$E_\text{o}(t) = E_{\text{o},1}(t) + E_{\text{o},2}(t) + E_\text{o}(t=0) = \int_0^t \dot{E}_\text{o}(\tau)\text{d}\tau + E_\text{o}(t=0). \tag{4.13}$$

Note that E_ϑ as defined in (4.4) considers the energy contained in the object and the agents' arms. In contrast, E_o does only consider the object energy, but is not restricted to the energy contained in a specific oscillation. Thus, the object energy can partly consist of energy contained in the ψ-oscillation, indicating asynchrony between the partners.

Experimental results from the leader/leader condition and the free condition did show approximately equal energy contributions of the partners. Differences between the agents can result from factors such as different levels of motivation or strength. For the rest of this analysis we focus on the leader/follower combinations.

Figure 4.8 shows an example trial for a leader and a follower swinging up the rigid object. Against our expectations, the steady state phase, during which we asked the participants to keep the desired energy level, showed significant positive and negative peaks in energy flows $\dot{E}_{\text{o},\mathcal{L}}$ and $\dot{E}_{\text{o},\mathcal{F}}$. Throughout all trials the leaders tended to contribute with more

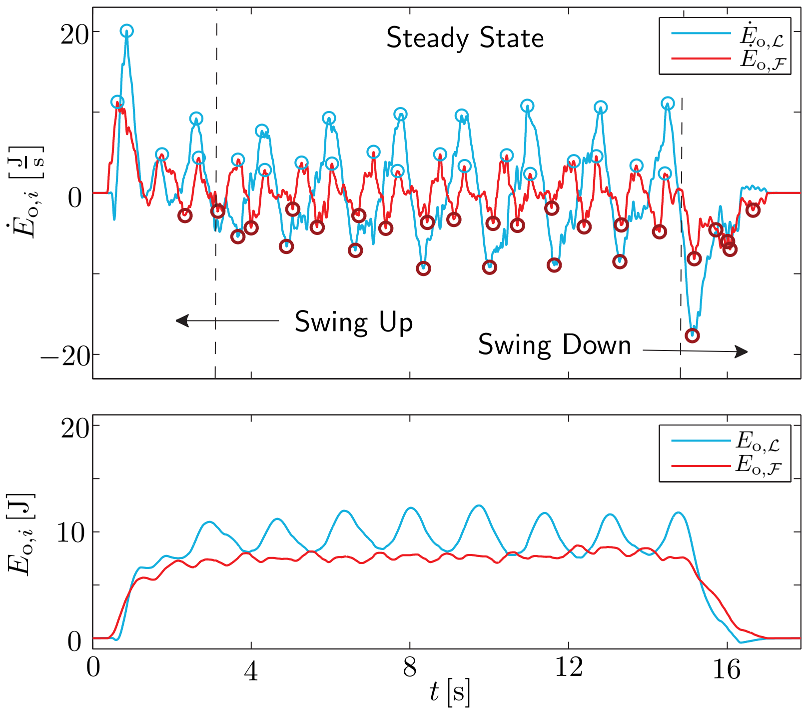

Fig. 4.8: Energy flow and contribution of an exemplary leader/follower trial: Energy flows $\dot{E}_{o,i}$ in red and resulting energy contributions $E_{o,i}$ with $i = \mathcal{L}, \mathcal{F}$. Light blue (dark red) circles mark the detected maximum (minimum) peaks of $\dot{E}_{o,i}$. Energy flows have clear peaks also during steady state, but show high variability among participants and trials.

energy $E_{o,\mathcal{L}}$ to the swing-up, also visible as higher peaks in energy flow $\dot{E}_{o,\mathcal{L}}$. However, the energy curves differ from trial to trial. An individual interpretation of the follower and leader behavior is difficult, as it emerges from the interaction due to the strong coupling to the partner.

In order to investigate for recurring forcing patterns, we plot the absolute values of the energy flow peaks $\left|\dot{E}_{o,\mathcal{L}}\right|$ and $\left|\dot{E}_{o,\mathcal{F}}\right|$ over the phase angle φ individually for leaders and followers in Fig. 4.9. The peaks were obtained using the peak-detection algorithm in *MATLAB*, with the restriction that peaks had to be above 25% of the maximum measured energy flow for the current agent and trial (see circles in Fig. 4.8). As described in Section 4.4, the phase angle φ reflects the momentary state within the swing. The phase angle φ was computed according to (4.10) with projected deflection angle θ_i^* and its numerical time derivative $\dot{\theta}_i^*$ obtained from wrist and shoulder data and $\Omega = \omega_g$. Interestingly, the leader as well as the follower tended towards injecting energy at $\varphi = \frac{\pi}{2}$ and releasing energy at $\varphi = -\frac{\pi}{2}$ from the system. In other words, the participants focused on reaching the desired energy level into one direction, here into negative x-direction. Note that the body kinematics are not the reason for this observation, as both agents used their right arm. The negative peaks in $\dot{E}_{o,\mathcal{L}}$ and $\dot{E}_{o,\mathcal{F}}$ can be interpreted as phases of relaxation. Because the shoulder damping is approximately proportional to the angular velocity $\dot{\theta}$, the energy flow caused by the damping is a function of $\dot{\theta}^2$ (4.12), which in turn is highest at $\pm\frac{\pi}{2}$.

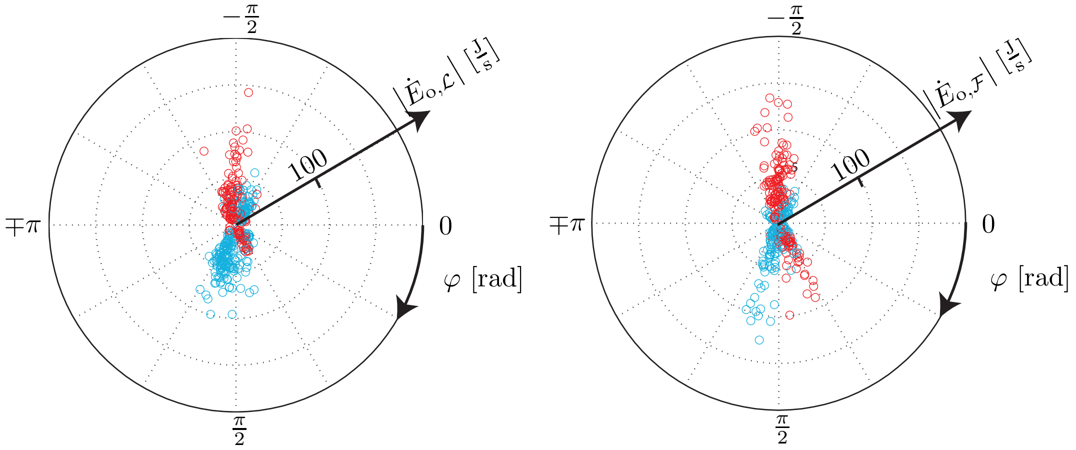

Fig. 4.9: Results forcing patterns of leader/follower combinations: Absolute values of peak energy flow for the leader $|\dot{E}_{\mathrm{o},\mathcal{L}}|$ (left) and the follower $|\dot{E}_{\mathrm{o},\mathcal{F}}|$ (right) over phase φ. Light blue (dark red) circles indicate $\dot{E}_{\mathrm{o},i} > 0$ ($\dot{E}_{\mathrm{o},i} < 0$). Leader and followers applied unidirectional forcing right after $\varphi = \frac{\pi}{2}$.

The reason for unidirectional forcing dominantly at $\frac{\pi}{2}$ and not at $-\frac{\pi}{2}$ remains as an open question, which could be investigated in an extended human-human study.

In general, higher and predominantly positive energy flow was observable for leader agents. The follower agents tended to more passive behavior, which directly resulted in less positive, in some cases even negative energy flow. Some outliers of high absolute value of $\dot{E}_{\mathrm{o},\mathcal{F}}$ can be seen in Fig. 4.9 for followers. Note however, the majority of energy flow peaks was found closer to the origin for followers compared to the leaders.

The presented energy analysis indicates that humans used unidirectional pulsed forcing to excite the pendulum-like ara-system up to the desired energy level E_θ^{d}. Human followers showed to be able to synchronize to their partners although being blindfolded and, thus, were able to contribute to a successful collaborative swing-up.

4.6 Controller synthesis

Based on the results of the human-human study, we design a leader and a follower controller in this section. The main ideas of the leader control approach presented are

i1) to project the ara-system onto the abstract torque-pendulum in (4.3) (step 3 in Fig. 4.2)

i2) to apply an energy-based controller with human-like forcing term to the abstract torque-pendulum to reach the desired periodic orbit $\mathcal{O}(\boldsymbol{x}_{\mathrm{araS}})$ (step 4 in Fig. 4.2)

In the following, we first present the leader which controls the abstract torque-pendulum to the desired periodic orbit of energy level $\vartheta_E = \theta_E^{\mathrm{d}}$ (i2). This leader controller is then extended to the ara-system (i1) and a follower controller is designed that damps undesired ψ-oscillations.

4.6.1 Leader control approach for the abstract torque-pendulum

We use an energy-based control law of the form

$$t_{\mathrm{s},\mathcal{L}} = -a_{\mathcal{L}} f_{\mathcal{L}}(\varphi), \tag{4.14}$$

were the amplitude factor $a_{\mathcal{L}}$ specifies direction and amount of energy flow induced by agent A1 $= \mathcal{L}$. The forcing function $f_{\mathcal{L}}$ times the energy injection based on the current phase of the oscillation φ. The energy-based controller above is inspired by [188] and will be used with some modifications in Chapters 5-7 as well. In the following, we present details of our choice of amplitude factor $a_{\mathcal{L}}$ and forcing function $f_{\mathcal{L}}(\varphi)$.

Energy flow timing

As discussed in Section 4.4.2, by designing the input torque $t_{s,\mathcal{L}}$ to be a function of the phase angle φ, the pendulum-like system can be excited at its natural frequency up to desired energy levels outside the region of the small angle approximation. The human-human experiments in Section 4.5 indicate unidirectional phase-triggered pulsed forcing at a phase angle $\varphi = \frac{\pi}{2}$. Thus, we design a forcing function that triggers a torque pulse of width T_{pw} and sinusoidal shape, each time $T_{\mathrm{ps}} = t(\varphi = \frac{\pi}{2})$ when the phase angle equals $\frac{\pi}{2}$

$$f_{\mathcal{L}}(\varphi, t) = \begin{cases} \sin\left(\frac{\pi}{T_{\mathrm{pw}}}(t - T_{\mathrm{ps}})\right) & \text{if } T_{\mathrm{ps}}(\varphi) < t < T_{\mathrm{ps}}(\varphi) + T_{\mathrm{pw}}, \\ 0 & \text{else.} \end{cases} \tag{4.15}$$

The pulse width is chosen to last less than a quarter of the swinging period $T_{\mathrm{pw}} < \frac{1}{4}\frac{2\pi}{\omega}$. Note that although the forcing function $f_{\mathcal{L}}$ is also a function of time, the importance is its phase angle dependency and we refer to it in the following as $f_{\mathcal{L}}(\varphi)$.

Energy flow specification

As defined in Problem 4, the goal is to reach the desired periodic orbit $\mathcal{O}(\boldsymbol{x}_{\mathrm{araS}})$ in (4.2). For the abstract torque-pendulum $\psi = 0$, $\vartheta = \theta^* = \theta$ and the desired periodic orbit reduces to $\mathcal{O}(\boldsymbol{x}_{\mathrm{atP}}) : E_\vartheta = E_\theta^{\mathrm{d}} = 2m_\vartheta g c_\vartheta(1 - \cos(\theta_E^{\mathrm{d}}))$. We use the ara-system oscillation θ for E_θ^{d} and θ_E^{d} to signify that the abstract torque-pendulum represents the desired, synchronized oscillation of the ara-system.

Theorem 2. *The energy contained in the abstract torque-pendulum converges to the desired periodic orbit* $\mathcal{O}(\boldsymbol{x}_{\mathrm{atP}}) :\ E_\theta^{\mathrm{d}} = 2m_\vartheta g c_\vartheta\left(1 - \cos(\theta_E^{\mathrm{d}})\right)$ *for a leader agent* A1 $= \mathcal{L}$ *in interaction with a passive agent* A2 ($t_{\mathrm{s},2} = 0$) *if the leader agent applies torque according to* (4.14) *with*

- *forcing function* $f_{\mathcal{L}}(\varphi)$ *in* (4.15) *with pulse width* $T_{\mathrm{pw}} < \frac{1}{4}\frac{2\pi}{\omega}$,
- *an amplitude factor* $a_{\mathcal{L}}$ *for which holds* $\mathrm{sgn}(a_{\mathcal{L}}) = \mathrm{sgn}(E_\theta^{\mathrm{d}} - E_\vartheta)$,
- $\vartheta_E < \frac{\pi}{2}$
- *and initial state* $\boldsymbol{x}_{\mathrm{atP}}(t = 0) \neq [0 \quad 0]^\top$.

Proof. The following candidate Lyapunov function

$$V = \frac{1}{2}(\Delta E_\vartheta)^2 = \frac{1}{2}\left[-j_\vartheta\dot{\vartheta}^2 + 2m_\vartheta g c_\vartheta\left(\cos(\vartheta) - \cos(\theta_E^{\mathrm{d}})\right)\right]^2 \tag{4.16}$$

is based on the energy difference $\Delta E_\vartheta = E_\theta^{\mathrm{d}} - E_\vartheta$ with E_ϑ from (4.4), such that $\Delta E_\vartheta = 0$ at the desired energy level $E_\vartheta = E_\theta^{\mathrm{d}}$. This results in $V > 0$ everywhere, except on the desired periodic orbit $\mathcal{O}(\boldsymbol{x}_{\mathrm{atP}})$ defined through $\Delta E_\vartheta^{\mathrm{d}} = 0 = -j_\vartheta\dot{\vartheta}^2 + 2m_\vartheta g c_\vartheta(\cos(\vartheta) - \cos(\theta_E^{\mathrm{d}}))$ and consequently $V = 0$.

The first time-derivative of the candidate Lyapunov function V is

$$\dot{V} = -\Delta E_\vartheta \dot{E}_\vartheta = -\Delta E_\vartheta(\dot{E}_{\vartheta,1} + \dot{E}_{\vartheta,2}). \tag{4.17}$$

The energy flows of the agents are $\dot{E}_{\vartheta,i} = t_{\mathrm{s},i}\dot{\vartheta}$ with $i = 1, 2$. Thus, we have $\dot{E}_{\vartheta,2} = 0$ due to $t_{\mathrm{s},2} = 0$ for the passive agent A2 and $\dot{E}_{\vartheta,1} = \dot{E}_{\vartheta,\mathcal{L}} = -a_{\mathcal{L}} f_{\mathcal{L}}(\varphi)\dot{\vartheta}$ for the leader agent A2 $= \boldsymbol{\mathcal{L}}$. The first time-derivative of the Lyapunov function in (4.17) results in

$$\dot{V} = \Delta E_\vartheta a_{\mathcal{L}} f_{\mathcal{L}}(\varphi)\dot{\vartheta}. \tag{4.18}$$

For $T_{\mathrm{pw}} < \frac{1}{4}\frac{2\pi}{\omega}$, the forcing function is $f_{\mathcal{L}}(\varphi) > 0$ only when $\dot{\vartheta} < 0$ and zero otherwise. Since further $\mathrm{sgn}(a_{\mathcal{L}}) = \mathrm{sgn}(\Delta E_\vartheta)$, we have $\dot{V} \leq 0$ in (4.18).

We show asymptotic stability based on LaSalle's Invariance Principle [163]. Consider the set $\Xi = \{\boldsymbol{x}_{\mathrm{atP}} \in \Sigma | V(\boldsymbol{x}_{\mathrm{atP}}) \leq V(\boldsymbol{x}_{\mathrm{atP}}(t = 0))\}$, which is compact (closed and bounded) for $E_\vartheta(\boldsymbol{x}_{\mathrm{atP}}(t = 0)) < 4m_\vartheta g c_\vartheta$, $E_\theta^{\mathrm{d}} < 4m_\vartheta g c_\vartheta$ and $\Sigma = \{\boldsymbol{x}_{\mathrm{atP}} \in \mathbb{R}^2 | -\pi < \vartheta \leq \pi\}$[1]. The set Ξ is further positively invariant because of $\dot{V}(\boldsymbol{x}_{\mathrm{atP}}) \leq 0$ for all $\boldsymbol{x}_{\mathrm{atP}} \in \Xi$. Let $\Upsilon = \{\boldsymbol{x}_{\mathrm{atP}} \in \Xi | \dot{V} = 0\}$ with M being the largest invariant set in Υ. Starting in Ξ, $\boldsymbol{x}_{\mathrm{atP}}$ will approach M for $t \to \infty$.

From (4.18) we extract the cases for which $\dot{V} = 0$:

1. $\dot{\vartheta} = 0$: $\overset{\text{Fig.4.4}}{\Rightarrow} \varphi_\vartheta = 0, \pi \overset{(4.15)}{\Rightarrow} f_{\mathcal{L}}(\varphi) = 0 \overset{(4.14)}{\Rightarrow} t_{s,1} = 0$
   $\overset{(4.3)}{\Rightarrow} \ddot{\vartheta}(\dot{\vartheta} = 0) = -\omega_{0,\vartheta}^2 \sin(\vartheta) \overset{!}{=} 0 \Rightarrow \vartheta = 0$
   $\Rightarrow$ not invariant for $\boldsymbol{x}_{\mathrm{atP}}(t = 0) \neq [0 \quad 0]^\top$

2. $f_{\mathcal{L}}(\varphi) = 0$: $\Rightarrow \dot{\vartheta} = 0$

3. $a_{\mathcal{L}} = 0 \Rightarrow \Delta E_\vartheta = 0$

4. $\Delta E_\vartheta = 0$: only invariant set M for $\boldsymbol{x}_{\mathrm{atP}}(t = 0) \neq [0 \quad 0]^\top$

Consequently, starting at $\boldsymbol{x}_{\mathrm{atP}}(t = 0) \neq [0 \quad 0]^\top$ ($E_\vartheta(t = 0) \neq 0$), $\boldsymbol{x}_{\mathrm{atP}}$ will approach the desired periodic orbit $\mathcal{O}(\boldsymbol{x}_{\mathrm{atP}})$ given through $\Delta E_\vartheta = 0$. □

Note that the desired periodic orbit is also stable for two leaders A1=A2=$\boldsymbol{\mathcal{L}}$ controlling the abstract torque-pendulum according to (4.14) if $\mathrm{sgn}(a_1 + a_2) = \mathrm{sgn}(E_\theta^{\mathrm{d}} - E_\vartheta)$.

---

[1] The limits on E_ϑ and Σ are not restrictive with respect to our control goal. Global stability can be shown using a state transformation as in [117].

4.6.2 Application to two-agent rigid object swinging

The block diagram in Fig. 4.10 shows the implementation of the leader and follower controllers. Here, we first extend the abstract torque-pendulum leader controller of the previous section to the ara-system. Subsequently, we present the *extended leader* controller which considers the undesired ψ-oscillation as well. Finally, we introduce a follower controller dedicated to damping of the undesired ψ-oscillation.

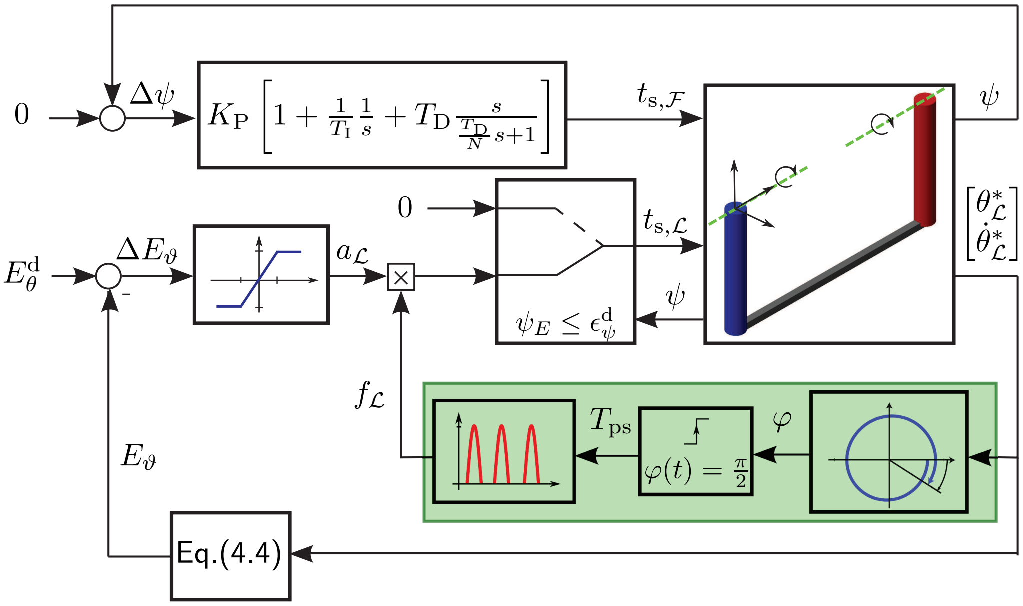

Fig. 4.10: Block diagram of extended leader $\mathrm{A1} = \mathcal{L}$ (blue cylindrical arm) and follower $\mathrm{A2} = \mathcal{F}$ (red cylindrical arm) control structures: The extended leader excites the desired θ-oscillation to the desired energy level E^d_θ through pulsed unidirectional torque inputs $t_{\mathrm{s},\mathcal{L}}$ as long as the energy contained in the undesired oscillation does not exceed $\psi_E < \epsilon^\mathrm{d}_\psi$. The follower damps the undesired ψ-oscillation through torque $t_{\mathrm{s},\mathcal{F}}$ computed by a PID controller.

Projection onto the abstract torque-pendulum

The leader controller projects the ara-system onto the abstract torque-pendulum through interpretation of the projected deflection angle $\theta^*_\mathcal{L}$ as the deflection angle of the abstract cart-pendulum ϑ. The projected deflection angle $\theta^*_\mathcal{L}$ is computed according to

$$\theta^*_\mathcal{L} = \arctan\left(\frac{r_{\mathrm{w},\mathcal{L}x}}{r_{\mathrm{w},\mathcal{L}y}}\right), \tag{4.19}$$

with wrist joint location $\boldsymbol{r}_{\mathrm{w},\mathcal{L}} = \begin{bmatrix} r_{\mathrm{w},\mathcal{L}x} & r_{\mathrm{w},\mathcal{L}y} & r_{\mathrm{w},\mathcal{L}z}\end{bmatrix}^\top$ as part of the measurement vector $\boldsymbol{y}_{\mathrm{m},\mathcal{L}}$. We compute the time derivative of $\dot{\theta}^*_\mathcal{L}$ through numerical differentiation, which leaves us with an estimate of the abstract torque-pendulum state $\hat{\boldsymbol{x}}_\mathrm{atP} = \begin{bmatrix}\theta^* & \dot{\theta}^*\end{bmatrix}^\top$.

Energy flow timing

The forcing function $f_{\mathcal{L}}(\varphi)$ in (4.15) achieves human-like energy flow timing. The phase angle φ of the ara-system is computed according to (4.10) and based on the estimated abstract torque-pendulum states $\hat{\boldsymbol{x}}_{\mathrm{atP}}$ and the geometric mean approximation $\Omega = \omega_{\mathrm{g}}$ in (4.9) for normalization. The geometric mean approximation requires an estimate of the current energy contained in the oscillation ϑ_E, which we compute according to (4.6), again based on $\hat{\boldsymbol{x}}_{\mathrm{atP}}$. The small angle approximation ω_0 is obtained based on known parameters of the abstract torque-pendulum (see Section 4.4.1).

Energy flow specification

The amplitude factor $a_{\mathcal{L}}$ in (4.14) results from a saturated linear mapping from energy error $\Delta\hat{E}_{\vartheta} = E_{\theta}^{\mathrm{d}} - \hat{E}_{\vartheta}$ to amplitude factor $a_{\mathcal{L}}$

$$a_{\mathcal{L}} = \begin{cases} a_{\max,\mathcal{L}}\ \mathrm{sgn}(\Delta\hat{E}_{\vartheta}) & \text{if} \quad |\Delta\hat{E}_{\vartheta}| \geq \delta_{\mathcal{L}}, \\ \frac{a_{\max,\mathcal{L}}}{\delta_{\mathcal{L}}}\Delta\hat{E}_{\vartheta} & \text{else,} \end{cases} \tag{4.20}$$

with $\frac{a_{\max,\mathcal{L}}}{\delta_{\mathcal{L}}}$ being the slope of the linear mapping with maximum amplitude factors $\pm a_{\max,\mathcal{L}}$. The estimate for the energy contained in the θ-oscillation $\hat{E}_{\theta}$ is calculated based on the estimated abstract torque-pendulum states $\hat{\boldsymbol{x}}_{\mathrm{atP}}$ in (4.4). The mapping above satisfies the required relationship $\mathrm{sgn}(a_{\mathcal{L}}) = \mathrm{sgn}(E_{\theta}^{\mathrm{d}} - E_{\vartheta})$ of Theorem 2.

The extended leader

The presented basic control concept results in a leader that does not react to the rigid object or its partner. The basic leader applies directed torque pulses solely based on the distance to the goal energy E_{θ}^{d} as given as our first control goal in Problem 4. The second control goal in Problem 4 of limiting energy contained in the ψ-oscillation is not being explicitly respected. Significant undesired deflection angles ψ indicating asynchrony between the partners can be the result.

We solve this issue by a simple extension, which switches the forcing off, whenever the undesired deflection angle exceeds a threshold $\psi_E > \epsilon_{\psi}^{\mathrm{d}}$. The lower control loop in Fig. 4.10 resembles the *extended leader* controlling the torque of agent A1 $= \mathcal{L}$.

Damping of the undesired oscillation through the follower

In contrast to the leader, the *follower* does not know the desired energy level E_{θ}^{d}, but to damp the undesired oscillation $E_{\psi}^{\mathrm{d}} = 0$. As discussed for the leader, angle $\psi = 0$ leads to a perfectly synchronized swing-up. Therefore, we design a simple follower controller which controls the error $\Delta\psi = 0 - \psi$ to zero through proper choice of input $t_{\mathrm{s},\mathcal{F}}$. To this end, we numerically linearize the ara-system using *MATLAB/Simulink* and subsequently remove uncontrollable/unobservable states. Based on the resulting minimal state space representation, a PID controller is designed using the *MATLAB ControlSystemToolbox*, such that a desirable phase margin of 60 deg is obtained. The upper control loop in Fig. 4.10 resembles the follower controlling the torque of agent A2 $= \mathcal{F}$.

4.7 Evaluation in simulation

This section presents an analysis of the presented control approaches of Section 4.6 in simulation.

4.7.1 Simulation setup

A multi-body simulation of the ara-system as displayed in Fig. 4.3 was setup using *SimMechanics 2nd Generation*. The human arms were modeled as cylinders with uniform mass distribution and length $l^* = 0.56\,\mathrm{m}$, representing the mean length $\bar{l}^*$ obtained from fitting the experimental data to circles in Section 4.5. The cylinders were given a mass $m_\mathrm{a} = 3.35\,\mathrm{kg}$ [25] and density $1100\,{}^{\mathrm{kg}}/_{\mathrm{m}^3}$ [34] comparable to that of an average human arm. The rigid object was designed to match the heavier $m_\mathrm{o} = 10.2\,\mathrm{kg}$ object used for our human-human experiments in Section 4.5.

We modeled the shoulders as spherical joints with damping $d_\mathrm{s} = 0.4\,{}^{\mathrm{Nms}}/_{\mathrm{rad}}$ [54] actuated through torque $t_{\mathrm{s},i}$ with $i = 1, 2$ around the world z-axis. A spring-stiffness of $k_\mathrm{w} = 0.1\,{}^{\mathrm{Nm}}/_{\mathrm{deg}}$ was applied to the spherical joints resembling the wrists. The value of the stiffness was obtained by matching the rotation of the human wrist caused by the object mass during the human-human experiments, i.e. the difference between object rotation and arm deflection.

The leader's forcing amplitude in (4.20) was obtained as $\bar{a}_\mathcal{L} = 14.9\,\mathrm{Nm}$, which was equivalent to 70% of the average maximum forces applied during the human-human experiments. The threshold in (4.20) was set to $\delta_\mathcal{L} = 2.7\,\mathrm{J}$ and the pulse width in (4.15) to $T_\mathrm{pw} = 0.4\,\mathrm{s}$, which leads to a similar swing-up time as observed in the human-human experiments. The bound on the ψ-oscillation was set to $\epsilon_\psi^\mathrm{d} = 1\,\mathrm{deg}$ for the extended leader controller. The linearization procedure described in Section 4.6.2 resulted for the given system parameters in PID gains $K_\mathrm{P} = 42.5$, $T_\mathrm{I} = 0.212$, $T_\mathrm{D} = 0.0491$ and $N = 8.85$.

4.7.2 Simulation conditions

We present simulations for the following conditions in detail:

Leader and agent with fixed actuation

First, we evaluate the basic and the extended leader controllers $\mathrm{A1} = \mathcal{L}$. In order to simulate different forcing behaviors, the forcing amplitude of agent A2 was set to a fixed value of $a_2 = 0.6\bar{a}_\mathcal{L}$. Note that according to our leader definition agent A2 was not a real leader, because knowledge of the error to the desired energy ΔE_ϑ was not incorporated. The desired energy E_θ^d was defined by a desired maximum deflection angle $\theta_E^\mathrm{d} = 60\,\mathrm{deg}$.

Leader and follower

The follower $\mathrm{A2} = \mathcal{F}$ is evaluated in interaction with the basic and the extended leader controllers $\mathrm{A1} = \mathcal{L}$. Again we set the desired energy level to $\theta_E^\mathrm{d} = 60\,\mathrm{deg}$.

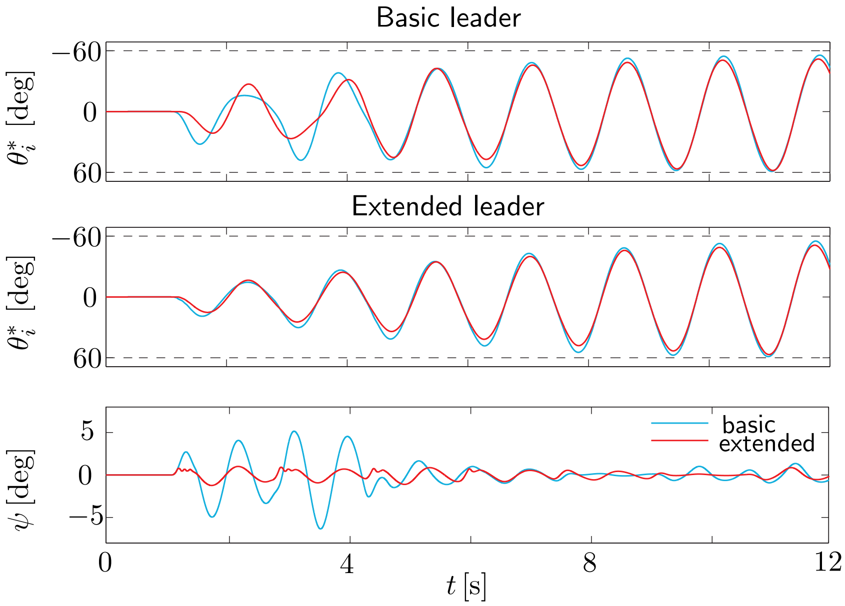

Fig. 4.11: Experimental results for a leader with forcing amplitude $a_1 = a_{\mathcal{L}} = f(\Delta E_\theta)$ interacting with an agent with fixed $a_2 = 0.6\bar{a}_{\mathrm{L}}$ for the basic and extended leader controllers: Projected deflection angles θ_1^* (solid light blue line) and θ_2^* (solid dark red line) over time, with dashed black line indicating the task goal θ_E^{d} and undesired deflection angle ψ. The extended leader successfully keeps the undesired oscillation in bounds $\psi_E \leq 1\,\mathrm{deg} = \epsilon_\psi^{\mathrm{d}}$ which yields improved synchronization during swing-up.

4.7.3 Simulation results and discussion

Evaluation of the leader

Figure 4.11 shows the simulation results for the basic and the extended leader controllers. As expected, the different forcing amplitudes resulted in an asymmetric swing-up visible in different projected deflection angles $\theta_1^* \neq \theta_2^*$ and undesired oscillation $\psi_E \neq 0$. The extended leader successfully kept the undesired deflection angle $\psi_E \leq 1\,\mathrm{deg} = \epsilon_\psi^{\mathrm{d}}$ by switching off the actuation once ψ_E exceeded these limits. The result is a clear improvement regarding the symmetry of the swing-up. As a consequence of the unidirectional forcing and the shoulder damping the desired amplitude was only reached for negative deflection angles θ, which complies with the observations from the human-human experiments.

Evaluation of the follower

The simulation results of a leader and a follower swinging up the ara-system to the desired deflection angle $\theta_E^{\mathrm{d}} = 60\,\mathrm{deg}$ are shown in Fig. 4.12. No noticeable difference in projected deflection angles $\theta_{\mathcal{L}}^*$ and $\theta_{\mathcal{F}}^*$ is visible. Thus, in simulation the simple follower controller was able to almost perfectly synchronize to its partner. Note that the same control performance was achieved with the basic as well as with the extended leader controller, as $\psi \approx 0$.

Figure 4.12 shows that the unidirectional forcing caused a steep increase in object energy after $\varphi = \frac{\pi}{2}$ ($\dot{E}_{\mathrm{o}} > 0$). The resultant local energy maximum was followed by a local

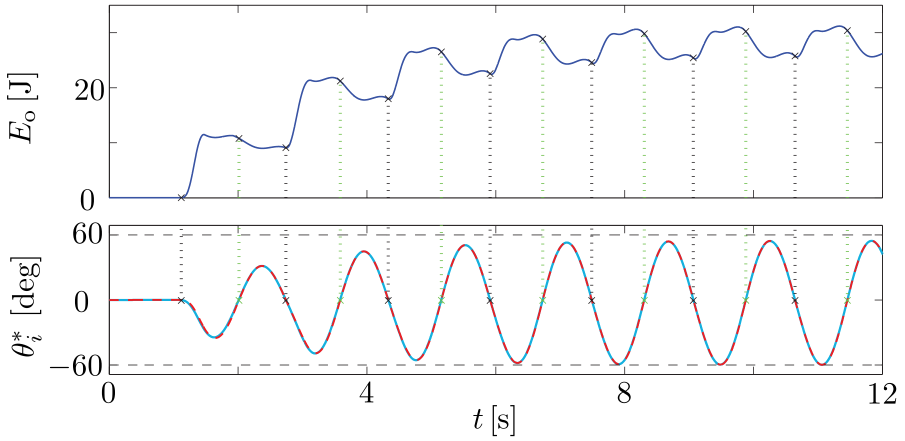

Fig. 4.12: Experimental results of the leader/follower combination: Object energy E_o and projected deflection angles $\theta_{\mathcal{L}}^*$ (solid light blue line) and $\theta_{\mathcal{F}}^*$ (dashed dark red line) over time, with dashed black line indicating the task goal $\theta_E^d = 60\,\mathrm{deg}$ and dotted lines indicating $\varphi = \pm\frac{\pi}{2}$. In simulation the follower controller achieves almost perfect synchronization. Consequently, not difference is observable between the basic and the extended leader controllers.

minimum caused by the shoulder damping, which caused a maximum energy decrease at $\varphi = -\frac{\pi}{2}$. Thus, the evolution of object energy E_o over time complied with the results from the human-human experiments.

We waive computation of settling time T_s or ranges $\epsilon_{\theta/\psi}$ of Problems 4 and 5, as our focus is not on excellent control performance but on a first controller design towards replicating human-human swing-up characteristics. The ideal simulation environment allowed for perfect PID gain tuning as well as instant reaction of the simulated robots.

4.8 Conclusions

This chapter presented first steps towards human-robot collaborative swinging of rigid objects. Movement path and frequency characteristics of human-human swing-up experiments support our hypothesis that the human arms during rigid object swinging behave simple pendulum-like. We observed unidirectional pulsed forcing, indicating that the humans predominantly focused on one direction when swinging up the object. Based on the the experimental findings, we modeled the "arm – rigid object – arm" system during synchronized swing-up as a shoulder torque driven simple pendulum and synthesized leader and follower controllers. Our simulation results replicate the experimental findings.

Open problems

Despite the outstanding control performance of the leader/follower controller combination in simulation, the applicability of the presented controllers in a real world setup remains an open question. Furthermore, our final goal is swinging of flexible objects. Flexible objects are underactuated and thus estimation of the object state cannot be performed by simple kinematic considerations as possible for the rigid object. Incomplete state feedback might further impede performance of the presented leader and follower approaches, which addressed subtasks as excitation of the desired oscillation and damping of the undesired oscillation separately. We address the challenges above by investigating swinging of pendulum-like objects as the other extreme end of flexible object swinging in the following chapter.

5 Energy control for collaborative swinging of known complex pendulum-like objects

Summary. *This chapter synthesizes controllers for collaborative swing-energy control of complex pendulum-like objects, where complex signifies that the pendulum-like object possesses not only the desired but also undesired oscillation degrees of freedom. The chapter demonstrates*

- *separation between desired and undesired oscillation through projection onto an abstract cart-pendulum*
- *simultaneous excitation of desired and damping of undesired oscillations*
- *active follower contribution through energy flow monitoring*
- *controller verification in virtual reality and real world experiments*

The results of this chapter were partly published in [37, 38, 43]. The student works [26, 68, 90, 91, 118, 183] contributed to this chapter.

5.1 Motivation

In order to approach the complex task of collaborative energy injection into flexible objects as displayed in Fig. 5.1(b), we investigated the extreme of rigid object swinging (Fig. 5.1(a)) in Chapter 4. In this chapter, we tackle the other extreme of collaborative swinging of pendulum-like objects (Fig. 5.1(c)) from a system theoretic perspective. In contrast to rigid objects, pendulum-like objects only loosely couple the interacting agents. This allows for more freedom on the choice of robot motion, but also comes with additional challenges. During rigid object swinging, the agents' arms are part of the oscillating entity and the current state of the object is known from the own arm configuration. For the pendulum-like objects, we limit the robotic agents to force measurements at the own interaction points. Thus, the state of the underactuated object as well as the intention of the partner has to be inferred from force signals only.

5.2 Related work

In the following we discuss related work relevant to the manipulation of pendulum-like objects as the one in Fig. 5.1(c). Pendulum-like objects are also referred to as slung loads or suspended loads in literature.

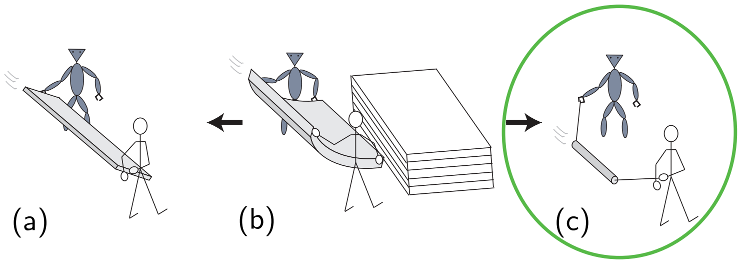

Fig. 5.1: Dynamic manipulation scenario: Collaborative energy injection into a sports mat to lift it onto a stack of mattresses (b). Interpretation of flexible object swinging (b) as a combination of rigid object swinging (a) and pendulum-like object swinging (c). This chapter presents controller synthesis for swinging of complex pendulum-like objects (c) based on known parameters of desired and undesired oscillations.

Manipulation of suspended loads

Applications for the manipulation of suspended loads are found in aerial vehicles or crane systems (see [1] for an overview). The control of aerial vehicles like helicopters or quadrocopters is a challenge in itself, due to their highly nonlinear dynamics. Therefore and for reasons of safety, the focus has been on *damping of undesired oscillations*. Most approaches look into suspended object manipulation through one agent. Two or more small helicopters jointly carrying a suspended load can be handled with the cascaded control approach of Bernhard and Kondak [12]. Their control approach is experimentally verified using three small size helicopters. Zemrovski et al. use dynamic programming to perform especially fast swing-free transport of loads using two independent robotic manipulators [193].

In contrast to the aforementionend works, we aim at *making use of oscillations* instead of only damping them. As a consequence, the manipulation repertoire is increased, energy can be injected swing by swing and the manipulator workspace can be extended, e.g., a load transported by a quadrotor could reach below overhangs. Despite these advantages, only a few works exist that exceed the control benchmark problem of simple pendulum swing-up. Recently, de Crousdaz et al. showed how controlled energy injection into a slung load transported by a quadrotor allows the system to fly through a window which is too small to be passed with the load hanging down [31]. Parametric excitation is used to control single-cable-suspended mechanisms in [32, 111, 194] and double-cable-suspended mechanisms in [69, 196]. While the suspended-objects in [193, 196] are similar to the object under consideration in this chapter (Fig. 5.1(c)), the approaches in literature either only damp oscillations [193] or use one centralized controller for both control inputs [196].

Energy control based on simple pendulum approximations

The weak coupling through the pendulum-like object allows for a robot controller design that is relatively independent of the desired human motion. Thus, we do not study human-human swinging as in Chapter 4, but take a system theoretic approach. We isolate the object from the agents' effectors and represent the agents' influence by acceleration inputs (see Fig. 5.2(d)). In the following, we refer to the isolated pendulum-like object in Fig. 5.2(d) as *t-pendulum* due to its trapezoidal shape.

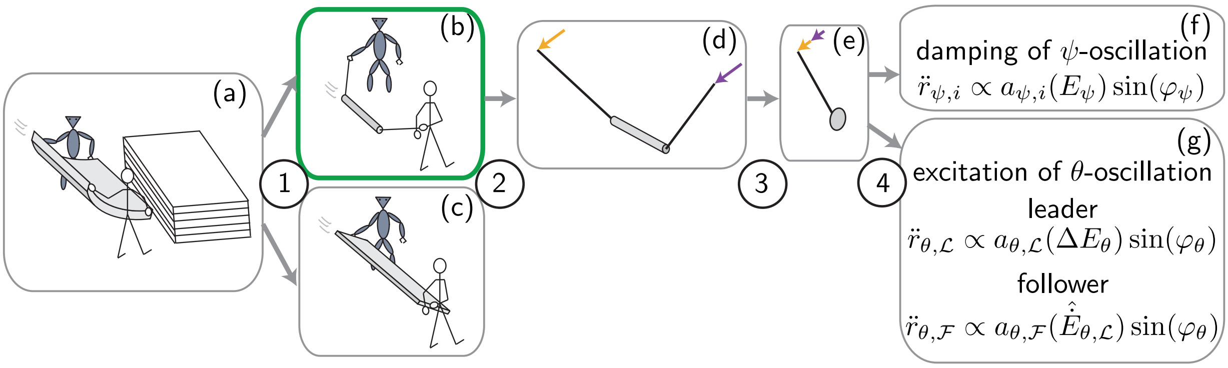

Fig. 5.2: Approach overview: (1) Interpretation of flexible object swinging as a combination of pendulum swinging and rigid object swinging. (2) Approximation of pendulum swinging by the t-pendulum with 1D acceleration inputs. (3) Projection of the t-pendulum onto the abstract cart-pendulum to separate desired θ-oscillation from undesired ψ-oscillation. (4) Energy-based control to excite the θ-oscillation as a leader or follower and to damp the ψ-oscillation.

The control goal of the collaborative swinging task discussed in this chapter is to achieve a simple pendulum-like oscillation of the complex under-actuated mechanism. Along the abstract torque-pendulum approximation of synchronized rigid object swinging in Chapter 4, we model the desired oscillation of the t-pendulum through an *abstract cart-pendulum* (see Fig. 5.2(e)). An observer with simple pendulum dynamics extracts the desired oscillation. What remains is the task to control the energy content of the desired oscillation to the desired periodic orbit. We employ the energy-based cart-pendulum swing-up controller of [188], which excites the desired oscillation of the t-pendulum at its natural frequency via phase dependent acceleration actuation.

The complexity of pendulum-like objects comes with several oscillation DoFs. In this chapter we show that in principle the same controller can be applied to damp *undesired oscillations* around the vertical axis of the pendulum-like object in Fig. 5.2(b).

Roles

As in Chapter 4, we design leader and follower controllers. Here, both the leader and the follower can actively damp undesired oscillations. Furthermore, the follower compensates for a lack of knowledge regarding the goal energy level of the desired oscillation by monitoring and imitating the energy flow produced by the leader. Strictly speaking, the task separation of the leader and follower controllers for rigid object swinging in Chapter 4 resembles cooperation rather than collaboration. In this chapter, we move to true collaboration, where leader and follower agents actively work towards the same goal.

Chapter overview

Figure 5.2 shows an overview of the control approach, along which we structure the remainder of this chapter. We approximate the agents' inputs to the complex pendulum-like object by horizontal one-dimensional accelerations, which yields the t-pendulum in

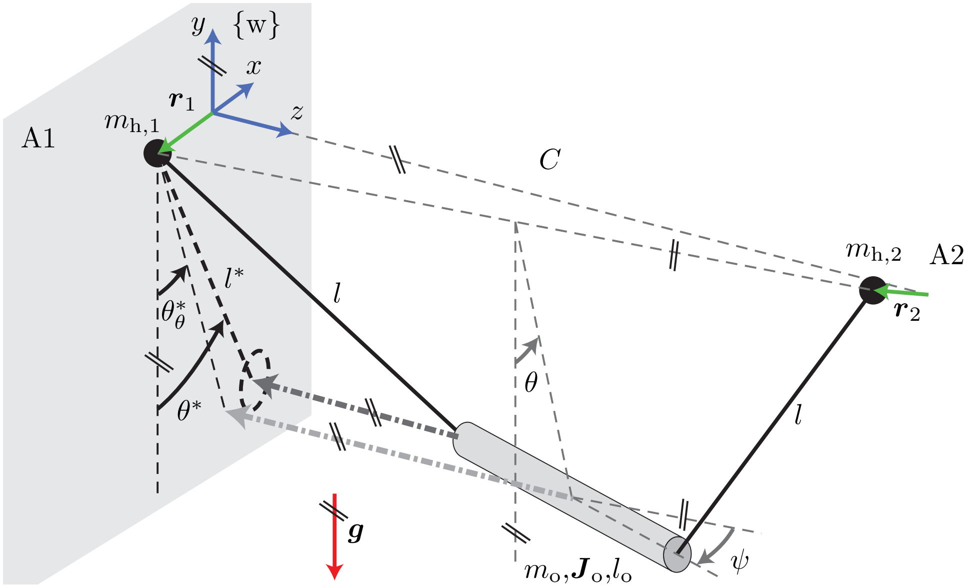

Fig. 5.3: The t-pendulum: Cylindrical pendulum object of mass m_{o}, length l_{o} and moment of inertia $\boldsymbol{J}_{\mathrm{o}}$ suspended from two handles of mass $m_{\mathrm{h},i}$ located at $\boldsymbol{r}_i$ with $i = 1, 2$ through massless ropes of length l. The pendulum is under the influence of gravity $\boldsymbol{g} = \begin{bmatrix} 0 & -g & 0 \end{bmatrix}^\top$. The initial distance between the two agents is C. The location $\boldsymbol{r}_1$ is defined with respect to the world fixed coordinate system $\{\mathrm{w}\}$. The location $\boldsymbol{r}_2$ is defined with respect to the fixed point $\boldsymbol{p} = \begin{bmatrix} 0 & 0 & C \end{bmatrix}^\top$ in $\{\mathrm{w}\}$. Pairs of parallel lines at the same angle indicate parallelity.

Fig. 5.2(d). In Section 5.3, we introduce the t-pendulum with its parameters and formally state our problem. The desired oscillation is captured by the abstract cart-pendulum in Fig. 5.2(e). In Section 5.4, we design energy-based leader and follower controllers that drive the abstract cart-pendulum to the desired periodic orbit. In Section 5.5, the abstract cart-pendulum controllers are applied to two-agent swinging of complex pendulum-like objects. By projecting the complex pendulum-like object onto the abstract cart-pendulum (step 3 in Fig. 5.2), desired and undesired oscillations are separated and can be excited or damped (see Fig. 5.2(f) and (g)). Section 5.6 presents results of a virtual reality user study and Section 5.7 evaluates the presented controllers in real world with a human interaction partner. We draw our conclusions and discuss open problems in Section 5.8.

5.3 Problem formulation

5.3.1 Pendulum-like objects

The t-pendulum

We use a dual-lift system with a cylindrical object as an example for a complex pendulum-like object (see Fig. 5.3 with details in the caption). We refer to it as the t-pendulum due to its trapezoidal shape. Under the assumption of point-mass handles, the t-pendulum has 10 DoFs. We further neglect rotations of the cylindrical object around its center line and oscillations in the t-pendulum plane[1]. This leaves us with 8 generalized coordinates that fully describe the configuration of the t-pendulum: the 3D positions of the two handles $\boldsymbol{r}_i$ and the two angles θ and ψ, which we refer to as oscillation DoFs. The desired oscillation DoF θ describes oscillations of the object around the connection line between the interaction partners. The disturbance oscillation DoF ψ describes oscillations of the object around the y-axis. The state vector results in $\boldsymbol{x}_{\mathrm{tP}} = \begin{bmatrix}\theta & \psi & \dot{\theta} & \dot{\psi} & \boldsymbol{r}_1 & \dot{\boldsymbol{r}}_1 & \boldsymbol{r}_2 & \dot{\boldsymbol{r}}_2\end{bmatrix}^\top$.

The control approach is based on a projection of the complex t-pendulum onto a cart-pendulum of length l^* and deflection angle θ^*. The projection is carried out along the z-axis as illustrated by the dark gray dash-dotted arrow in Fig 5.3. The projected deflection angle θ^* in the xy-plane is caused by a superposition of the θ-oscillation and the ψ-oscillation

$$\theta^* = \theta^*_\theta + \theta^*_\psi, \tag{5.1}$$

where θ^*_θ is the angle that results from a projection of the center of mass (CoM) of the t-pendulum onto the xy-plane (light gray dash-dotted arrow in Fig 5.3). We use the variable θ^*_ψ for the difference $\theta^* - \theta^*_\theta$, as its main origin are ψ-oscillations. For a synchronous motion of the agents, zero disturbance oscillation $\psi \approx 0$ is to be expected, leading to $\theta = \theta^* = \theta^*_\theta$. Independent motion of the agents, however, causes the initial distance C between the agents to alter and the projected length l^* to change. The presented control approach requires knowledge of l^*. We use $l^*(\boldsymbol{x}_{\mathrm{tP}} = \boldsymbol{0})$ for our controllers, which leaves us with a relatively small mistake as $C \gg \lVert \boldsymbol{r}_i \rVert$ in our setup.

The v-pendulum

For cylinder length $l_{\mathrm{o}} \to 0$, the t-pendulum simplifies to a v-shaped point mass pendulum without disturbance oscillation ψ, which we refer to as v-pendulum. For the v-pendulum, the state vector simplifies to $\boldsymbol{x}_{\mathrm{vP}} = \begin{bmatrix}\theta & \dot{\theta} & \boldsymbol{r}_1 & \dot{\boldsymbol{r}}_1 & \boldsymbol{r}_2 & \dot{\boldsymbol{r}}_2\end{bmatrix}^\top$. Since control of the t-pendulum is more challenging, we focus on the details of its control in the following, unless stated otherwise.

5.3.2 Problem statement

The objective is to control the complex pendulum-like object to reach the desired periodic orbit

$$\mathcal{O}(\boldsymbol{x}_{\mathrm{tP}}) : \begin{cases} E_\theta = E^{\mathrm{d}}_\theta = 2m_\vartheta g c_\vartheta (1 - \cos(\theta^{\mathrm{d}}_E)), \\ E_\psi = E^{\mathrm{d}}_\psi = 0, \\ \boldsymbol{r}_i = \dot{\boldsymbol{r}}_i = \boldsymbol{0} \text{ with } i = 1, 2, \end{cases} \tag{5.2}$$

where E_θ and E_ψ are the energies contained in the θ- and ψ-oscillations and the superscript d signifies their desired values. We assume massless ropes and the t-pendulum mass $m_{\mathrm{o}} = 2m_\vartheta$ to be concentrated along the centerline of the object cylinder with a resultant distance between θ-oscillation pivot point to the CoM of $c_\vartheta = l^*$. According to (5.2), the desired oscillation DoF θ is to be excited such that the oscillation reaches the energy E^{d}_θ, which

---

[1] The in plane oscillation showed to play a minor role for robot motion along the x-axis and natural human motion. Therefore, we neglect this oscillation in the following. However, essentially the same controller can be applied along the z-direction to damp these disturbance oscillations.

is equivalent to a maximum deflection angle θ_E^d or desired object height $y_{\mathrm{o},E}^\mathrm{d}$, at which the object could potentially be released. The undesired oscillation DoF ψ should be damped. The maximum deflection angles θ_E and ψ_E are the amplitudes of the θ- and ψ-oscillation and represent energy equivalents (see Definition 3).

The object state $\boldsymbol{x}_\mathrm{tP}$ can be influenced through acceleration of the agents' interaction points $\boldsymbol{u}_1 = \ddot{\boldsymbol{r}}_1$ and $\boldsymbol{z}_2 = \ddot{\boldsymbol{r}}_2$. Although we assume collaborative interaction, only the behavior of agent A1 can be directly controlled. Consequently, the input of agent A2 is defined as disturbance $\boldsymbol{z}_2$. We assume that the sensor feedback of agent A1 is limited to the forces applied at its own end effector $\boldsymbol{y}_{\mathrm{m},1} = \boldsymbol{f}_1$. While A2 might move in 3D, we limit the motion of agent A1 to the x-direction for simplicity[2], i.e. $\boldsymbol{u}_1 = \begin{bmatrix} u_1 & 0 & 0 \end{bmatrix}^\top = \begin{bmatrix} \ddot{r}_1 & 0 & 0 \end{bmatrix}^\top$.

We distinguish between a leader A1 $= \mathcal{L}$ and a follower agent A1 $= \mathcal{F}$. A *leader* $\mathcal{L}$ knows the desired periodic orbit $\mathcal{O}(\boldsymbol{x}_\mathrm{tP})$ including the desired energy levels E_θ^d and E_ψ^d.

Problem 6 (Leader $\mathcal{L}$)**.** *Find a control law $u_\mathcal{L}$ as a function of the measurable output and the desired object energies*

$$u_\mathcal{L} = \ddot{r}_\mathcal{L} = f(\boldsymbol{y}_{\mathrm{m},\mathcal{L}} = \boldsymbol{f}_\mathcal{L}, E_\theta^\mathrm{d}, E_\psi^\mathrm{d} = 0)$$

such that

$$\left| E_j^\mathrm{d} - E_j(t > T_\mathrm{s}) \right| \leq \epsilon_j \textit{ with } j = \theta, \psi \quad \text{for} \quad 0 < T_\mathrm{s} < \infty.$$

Consequently, we require the energy errors $\Delta E_j = E_j^\mathrm{d} - E_j$ to stay within the ranges ϵ_j the latest after the system settling time $t = T_\mathrm{s}$.

A *follower* $\mathcal{F}$ has partial knowledge about the desired periodic orbit $\mathcal{O}(\boldsymbol{x}_\mathrm{tP})$, i.e. the follower knows which oscillation DoFs to excite and which ones to damp, but not the value of E_θ^d. Thus, a follower needs to infer the partner's intention - increase, hold, decrease the current system energy E_θ - to actively contribute to the task goal. The follower can achieve this by monitoring and imitating the leader's energy flow $\dot{E}_{\theta,\mathcal{L}}$. We define desired follower behavior as

Problem 7 (Follower $\mathcal{F}$)**.** *Find a control law $u_\mathcal{F}$ as a function of the measurable output and zero energy contained in the undesired oscillation*

$$u_\mathcal{F} = \ddot{r}_\mathcal{F} = f(\boldsymbol{y}_{\mathrm{m},\mathcal{F}} = \boldsymbol{f}_\mathcal{F}, E_\psi^\mathrm{d} = 0)$$

such that

$$\begin{cases} \dot{E}_{\theta,\mathcal{F}} > 0 & \text{if} \quad \dot{E}_{\theta,\mathcal{L}} > \delta_{\theta,\mathcal{F}}, \\ \dot{E}_{\theta,\mathcal{F}} = 0 & \text{if} \quad -\delta_{\theta,\mathcal{F}} \leq \dot{E}_{\theta,\mathcal{L}} \leq \delta_{\theta,\mathcal{F}}, \\ \dot{E}_{\theta,\mathcal{F}} < 0 & \text{if} \quad \dot{E}_{\theta,\mathcal{L}} < -\delta_{\theta,\mathcal{F}}, \end{cases}$$

and

$$\left| E_\psi^\mathrm{d} - E_\psi(t > T_\mathrm{s}) \right| \leq \epsilon_\psi \quad \textit{for} \quad 0 < T_\mathrm{s} < \infty.$$

The threshold $\delta_{\theta,\mathcal{F}}$ can be adjusted such that the follower does not react to minor energy flow, e.g., caused by friction. The ψ-oscillation is known to the follower as being undesired. Thus, the follower behaves as a leader with respect to the ψ-oscillation ($E_\psi^\mathrm{d} = 0$).

---

[2] 1D motion is sufficient and does not restrict a human partner in his 3D motion due to the loose coupling of the agents through the pendulum-like object.

5.4 Energy-control for the abstract cart-pendulum

Along the methodology presented in Chapter 4, the main ideas of the control approach for the t-pendulum are

i1) to extract the desired and the undesired oscillation DoF by projecting the complex pendulum-like object onto the abstract cart-pendulum (step 3 in Fig. 5.2)

i2) to apply an energy-based controller to the abstract cart-pendulum to reach the desired periodic orbit $\mathcal{O}(\boldsymbol{x}_{\mathrm{tP}})$ (step 4 in Fig. 5.2)

In this section we present the energy-based controller for the abstract cart-pendulum (i2) and analyze its stability. In Section 5.5, the control approach is extended to work for realistic mechanisms as the v- and t-pendulum (i1).

5.4.1 The abstract cart-pendulum

For synchronous motion of the agents along the x-axis $\ddot{r}_i$ the disturbance angle is zero $\psi = 0$ for the t-pendulum and the t- and v-pendulum approximately behave as cart-pendulums with two-sided actuation and deflection angle $\vartheta = \theta^* = \theta$

$$\dot{\boldsymbol{x}}_{\mathrm{acP}} = \begin{bmatrix} \dot{\vartheta} \\ -\omega_{0,\vartheta}^2 \sin\vartheta \end{bmatrix} + \begin{bmatrix} 0 \\ -\frac{1}{g}\omega_{0,\vartheta}^2 \cos\vartheta \end{bmatrix} \frac{\ddot{r}_1 + \ddot{r}_2}{2}, \tag{5.3}$$

with reduced state $\boldsymbol{x}_{\mathrm{acP}} = [\vartheta \quad \dot{\vartheta}]^\top$ consisting of deflection angle ϑ and angular velocity $\dot{\vartheta}$ and the small angle approximation of the natural frequency $\omega_{0,\vartheta}$. We use the variables ϑ for the deflection angle of the abstract cart-pendulum in contrast to the actual deflection angle θ of the complex objects. The small angle approximation of the natural frequency $\omega_{0,\vartheta} = \frac{m_\vartheta c_\vartheta g}{j_\vartheta}$ depends on gravity g, object mass m_ϑ, distance between pivot point and the CoM c_ϑ and the resultant moment of inertia around the pendulum pivot point j_ϑ. Note that as for the abstract torque pendulum in Chapter 4.4.1, the parameters m_ϑ and j_ϑ represent one side of the t-pendulum, i.e. half the mass and moment of inertia of the complete pendulum-like object. We call this pendulum *abstract cart-pendulum*, where *cart* refers to the actuation through horizontal acceleration. The term *abstract* emphasizes the simplification we make by approximating the agents' influences as summed accelerations along the x-axis and neglecting $\psi \neq 0$ in case of the t-pendulum.

Equivalently to the abstract torque-pendulum in (4.4), the energy contained in the abstract cart-pendulum for zero handle velocities $\dot{r}_1 = \dot{r}_2 = 0$ is

$$E_\vartheta = j_\vartheta \dot{\vartheta}^2 + 2 m_\vartheta g c_\vartheta \left(1 - \cos\vartheta\right). \tag{5.4}$$

The time derivative of (5.4) with (5.3) results in the energy flow induced by the agents

$$\dot{E}_\vartheta = \dot{E}_{\vartheta,1} + \dot{E}_{\vartheta,2} = -2 m_\vartheta c_\vartheta \dot{\vartheta} \cos(\vartheta) \frac{\ddot{r}_1 + \ddot{r}_2}{2}. \tag{5.5}$$

5.4.2 Control approach

The idea of the swing-up controller proposed by Yoshida [188] is captured in the following control law

$$\ddot{r}_1 = a_1\omega_\vartheta^2 \sin(\varphi_\vartheta). \tag{5.6}$$

As in Chapter 4, the amplitude factor a_1 specifies direction and amount of energy flow induced by agent A1 and the phase angle φ_ϑ times the energy injection. In the following, we discuss our choice of the amplitude factor a_1 and the phase angle φ_ϑ.

Energy flow timing

As detailed in Chapter 4.4.2, simple pendulums as the abstract cart-pendulum constitute nonlinear systems with energy dependent frequency $\omega_\vartheta(E_\vartheta)$. The phase angle φ_ϑ relates to the state of the swing, e.g. $\varphi_\vartheta = \pm\pi$ for zero deflection angle ϑ and maximum angular velocity $\dot{\vartheta}$ (see Fig. 4.4). Computation of φ_ϑ according to (4.10) with normalization $\Omega \approx \omega_\vartheta$ yields an approximately linearly rising phase angle $\varphi_\vartheta(t) \approx \omega_\vartheta t + \varphi_\vartheta(t=0)$. Consequently, the term $\sin(\varphi_\vartheta)$ in (5.6) excites the pendulum at its natural frequency and allows a controlled swing-up of the pendulum outside the region of the small angle approximation. Use of the small angle approximation for normalization $\Omega = \omega_{0,\vartheta}$ leads to oscillations of higher magnitude in $\varphi_\theta(t)$, especially for high energy contents ϑ_E. However, normalization with the small angle approximation suffices for a swing-up into the inverted pendulum position [188] and with ease for our region of interest[3]: maximum deflection angles $\vartheta_E < \frac{\pi}{2}$. In contrast to the unidirectional pulsed shoulder torque in (4.14) for rigid object swinging, $\sin(\varphi_\vartheta)$ results in continuous actuation. Note that in this chapter, we add a subscript to natural frequencies and phase angles in order to differentiate between the different oscillations: e.g., $\omega_{0,\vartheta}$, ω_ψ and φ_θ.

Energy flow specification

According to Problem 6, the goal is to reach the desired periodic orbit $\mathcal{O}(\boldsymbol{x}_{\mathrm{tP}})$ in (5.2). For the abstract cart-pendulum $\psi = 0$, $\vartheta = \theta^* = \theta$ and the desired periodic orbit reduces to $\mathcal{O}(\boldsymbol{x}_{\mathrm{acP}}) : E_\vartheta = E_\theta^{\mathrm{d}} = 2m_\vartheta g c_\vartheta(1-\cos(\theta_E^{\mathrm{d}}))$. Again, we use E_θ^{d} and θ_E^{d} to emphasize that the abstract cart-pendulum represents the desired oscillation of the t-pendulum.

Theorem 3. *The energy contained in the abstract cart-pendulum converges to the desired periodic orbit* $\mathcal{O}(\boldsymbol{x}_{\mathrm{acP}}) : E_\vartheta^{\mathrm{d}} = 2m_\vartheta g c_\vartheta(1-\cos(\theta_E^{\mathrm{d}}))$ *for a leader A1=* $\mathcal{L}$ *and a follower A2=* $\mathcal{F}$ *applying accelerations according to* (5.6) *with*

- $\mathrm{sgn}(a_{\mathcal{L}}) = \mathrm{sgn}(E_\vartheta^{\mathrm{d}} - E_\vartheta)$,
- $\mathrm{sgn}(a_{\mathcal{F}}) = \mathrm{sgn}(\dot{E}_{\vartheta,\mathcal{L}})$,
- $\vartheta_E < \frac{\pi}{2}$
- *and initial state* $\boldsymbol{x}_{\mathrm{acP}}(t=0) \neq [0 \quad 0]^\top$.

---

[3] In order to be able to approximate the massless suspension ropes as rigid, we do not consider higher maximum deflection angles than $\vartheta_E = \frac{\pi}{2}$.

Proof. We use the same candidate Lyapunov function as in Chapter 4.6

$$V = \frac{1}{2}(\Delta E_\vartheta)^2 = \frac{1}{2}\left[-j_\vartheta\dot{\vartheta}^2 + 2m_\vartheta g c_\vartheta(\cos(\vartheta) - \cos(\theta_E^{\mathrm{d}}))\right]^2, \tag{5.7}$$

which is based on the energy difference $\Delta E_\vartheta = E_\theta^{\mathrm{d}} - E_\vartheta$ contained in the ϑ-oscillation, such that $\Delta E_\vartheta = 0$ at the desired energy level $E_\vartheta = E_\theta^{\mathrm{d}}$. This results in $V > 0$ everywhere, except on the desired periodic orbit $\mathcal{O}(\boldsymbol{x}_{\mathrm{acP}})$ defined through $\Delta E_\vartheta^{\mathrm{d}} = 0 = -j_\vartheta\dot{\vartheta}^2 + 2m_\vartheta g c_\vartheta(\cos(\vartheta) - \cos(\theta_E^{\mathrm{d}}))$ and consequently $V = 0$.

The first time-derivative of the candidate Lyapunov function V is

$$\dot{V} = -\Delta E_\vartheta \dot{E}_\vartheta = -\Delta E_\vartheta(\dot{E}_{\vartheta,\mathcal{L}} + \dot{E}_{\vartheta,\mathcal{F}}). \tag{5.8}$$

For both agents controlling the abstract cart-pendulum according to (5.6), the energy flow induced by the agents in (5.5) becomes

$$\dot{E}_\vartheta = \dot{E}_{\vartheta,\mathcal{L}} + \dot{E}_{\vartheta,\mathcal{F}} = -2m_\vartheta c_\vartheta \omega_\vartheta^2 \cos(\vartheta)\dot{\vartheta}\sin(\varphi_\vartheta)\frac{a_\mathcal{L} + a_\mathcal{F}}{2}. \tag{5.9}$$

For $\vartheta_E < \frac{\pi}{2}$ the first terms are zero or positive, such that $-2m_\vartheta c_\vartheta \omega_\vartheta^2 \cos(\vartheta) \leq 0$. Further, the phase portrait of Fig. 4.4 shows that $\operatorname{sgn}(\sin(\varphi_\vartheta)) = -\operatorname{sgn}(\dot{\vartheta})$ holds. Consequently, since $\operatorname{sgn}(a_\mathcal{L}) = \operatorname{sgn}(\Delta E_\vartheta)$ we have $\operatorname{sgn}(\dot{E}_{\vartheta,\mathcal{L}}) = \operatorname{sgn}(\Delta E_\vartheta)$. Since furthermore $\operatorname{sgn}(a_\mathcal{F}) = \operatorname{sgn}(\dot{E}_{\vartheta,\mathcal{L}})$ we have $\operatorname{sgn}(\Delta E_\vartheta) = \operatorname{sgn}(\dot{E}_{\vartheta,\mathcal{L}} + \dot{E}_{\vartheta,\mathcal{F}})$ and $\dot{V} \leq 0$ in (5.8).

We show asymptotic stability based on LaSalle's Invariance Principle [163]. Consider the set $\Xi = \{\boldsymbol{x}_{\mathrm{acP}} \in \Sigma | V(\boldsymbol{x}_{\mathrm{acP}}) \leq V(\boldsymbol{x}_{\mathrm{acP}}(t = 0))\}$, which is compact (closed and bounded) for $E_\vartheta(\boldsymbol{x}_{\mathrm{acP}}(t = 0)) < 4m_\vartheta g c_\vartheta$, $E_\vartheta^{\mathrm{d}} < 4m_\vartheta g c_\vartheta$ and $\Sigma = \{\boldsymbol{x}_{\mathrm{acP}} \in \mathbb{R}^2 | -\pi < \vartheta \leq \pi\}$. The set Ξ is further positively invariant because of $\dot{V}(\boldsymbol{x}_{\mathrm{acP}}) \leq 0$ for all $\boldsymbol{x}_{\mathrm{acP}} \in \Xi$. Let $\Upsilon = \{\boldsymbol{x}_{\mathrm{acP}} \in \Xi | \dot{V} = 0\}$ with M being the largest invariant set in Υ. Starting in Ξ, $\boldsymbol{x}_{\mathrm{acP}}$ will approach M for $t \to \infty$.

From (5.8) and (5.9) we extract the cases for which $\dot{V} = 0$:

1. $\cos(\vartheta) = 0$: $\Rightarrow \vartheta = \pm\frac{\pi}{2} = \text{const.}$,
   but $\ddot{\vartheta}(\vartheta = \pm\frac{\pi}{2}) \overset{(5.3)}{=} \mp\omega_{0,\vartheta}^2 \neq 0 \Rightarrow$ not invariant
2. $\dot{\vartheta} = 0$: $\overset{\text{Fig.4.4}}{\Rightarrow} \sin\varphi_\vartheta = 0 \overset{(5.6)}{\Rightarrow} \ddot{r}_\mathcal{L} = \ddot{r}_\mathcal{F} = 0$
   $\overset{(5.3)}{\Rightarrow} \ddot{\vartheta}(\dot{\vartheta} = 0) = -\omega_{0,\vartheta}^2 \sin(\vartheta) \overset{!}{=} 0 \Rightarrow \vartheta = 0$
   $\Rightarrow$ not invariant for $\boldsymbol{x}_{\mathrm{acP}}(t = 0) \neq [0 \quad 0]^\top$
3. $\sin(\varphi) = 0$: $\Rightarrow \dot{\vartheta} = 0$
4. $a_\mathcal{L} + a_\mathcal{F} = 0$: The follower imitates the leader $\Rightarrow a_\mathcal{L} = 0 \Rightarrow \Delta E_\vartheta = 0$
5. $\Delta E_\vartheta = 0$: only invariant set M for $\boldsymbol{x}_{\mathrm{acP}}(t = 0) \neq [0 \quad 0]^\top$

Consequently, starting at $\boldsymbol{x}_{\mathrm{acP}}(t = 0) \neq [0 \quad 0]^\top$ ($E_\vartheta(t = 0) \neq 0$), $\boldsymbol{x}_{\mathrm{acP}}$ will approach the desired periodic orbit $\mathcal{O}(\boldsymbol{x}_{\mathrm{acP}})$ given through $\Delta E_\vartheta = 0$. □

Note that the desired periodic orbit is also stable for two leaders A1=A2=$\boldsymbol{\mathcal{L}}$ controlling the abstract cart-pendulum according to (5.6) if $\operatorname{sgn}(a_1 + a_2) = \operatorname{sgn}(E_\theta^{\mathrm{d}} - E_\vartheta)$.

5.5 Application to two-agent object manipulation

In this section, we apply the abstract cart-pendulum controller of the previous section to the control of realistic pendulum-like objects as the v- and the t-pendulum. Through projection of the complex t-pendulum onto the abstract cart-pendulum, the controller distinguishes between desired θ- and undesired ψ-oscillation. The energies of the individual oscillations are controlled through excitation at their respective natural frequencies by applying the controller presented in Section 5.4.2. The block diagram of the complete system is given in Fig. 5.4. The underlying principles of the blocks for the *energy flow specification* and the *energy flow timing* were explained in Section 5.4.2. In the following, the *projection onto the abstract cart-pendulum* as well as extensions of the energy-based controller of the abstract cart-pendulum to the more complex t-pendulum are described.

5.5.1 Projection onto the abstract cart-pendulum

We extract estimates of the desired θ-oscillation in two steps. In a first step, we map the measured forces $\boldsymbol{f}_1$ to the projected deflection angle θ^* (Fig. 5.3)

$$\theta^* = \arctan\left(\frac{-f_{\mathrm{o},1x}}{f_{\mathrm{o},1y}}\right). \tag{5.10}$$

The force $\boldsymbol{f}_{\mathrm{o},1} = \begin{bmatrix} f_{\mathrm{o},1x} & f_{\mathrm{o},1y} & f_{\mathrm{o},1z} \end{bmatrix}^\top$ is the force exerted on the pendulum-like object through agent A1 and is obtained from the measurable applied end effector force $\boldsymbol{f}_1$ by dynamically compensating for the force caused by the handle mass $m_{\mathrm{h},1}$: $\boldsymbol{f}_{\mathrm{o},1} = \boldsymbol{f}_1 - m_{\mathrm{h},1}\begin{bmatrix}\ddot{r}_1 & -g & 0\end{bmatrix}^\top$.

In a second step, a nonlinear observer extracts estimates of the abstract cart-pendulum states $\vartheta \approx \theta^*_\theta$ and $\dot{\vartheta} \approx \dot{\theta}^*_\theta$, thus, the part of the projected deflection angle θ^* belonging to the θ-oscillation in (5.1)

$$\dot{\boldsymbol{x}}_{\mathrm{acP}} = \begin{bmatrix} \dot{\vartheta} \\ -\omega_{0,\vartheta}\sin(\vartheta) \end{bmatrix} + \boldsymbol{l}_\theta(\theta^* - y), \quad y = \begin{bmatrix} 1 & 0 \end{bmatrix} \boldsymbol{x}_{\mathrm{acP}} \tag{5.11}$$

The observer has abstract cart-pendulum dynamics (5.3) with natural frequency ω_ϑ, but without inputs. The term $\boldsymbol{l}_\theta(\theta^* - y)$ couples the observer to the t-pendulum. We summarize these two steps as *projection onto the abstract cart-pendulum* (see yellow background in Fig. 5.4).

In contrast to observers in the literature [174], this observer is not designed to capture the complete complex t-pendulum dynamics, but is meant to extract the oscillation DoF related to θ. The input to the observer is the projected deflection angle θ^* as given in (5.1), which consists of the projection of the oscillation of interest θ^*_θ, overlaid by the disturbance ψ-oscillation θ^*_ψ. The observer is designed to filter out the disturbance source ψ of natural frequency ω_ψ and consequently extract the oscillation related to the θ-oscillation of natural frequency $\omega_\theta = \omega_\vartheta$.

We linearize the observer (5.11) in order to investigate whether and for which observer gain vector $\boldsymbol{l}_\theta = \begin{bmatrix} l_{\theta,1} & l_{\theta,2} \end{bmatrix}^\top$ the oscillation related to θ can be extracted. The transfer function from observer input θ^* to observer output $y = \vartheta$ that results from a linearization around the stable equilibrium point $\boldsymbol{x}_{\mathrm{acP}} = \boldsymbol{0}_{2\times 1}$ for an unactuated simple pendulum is

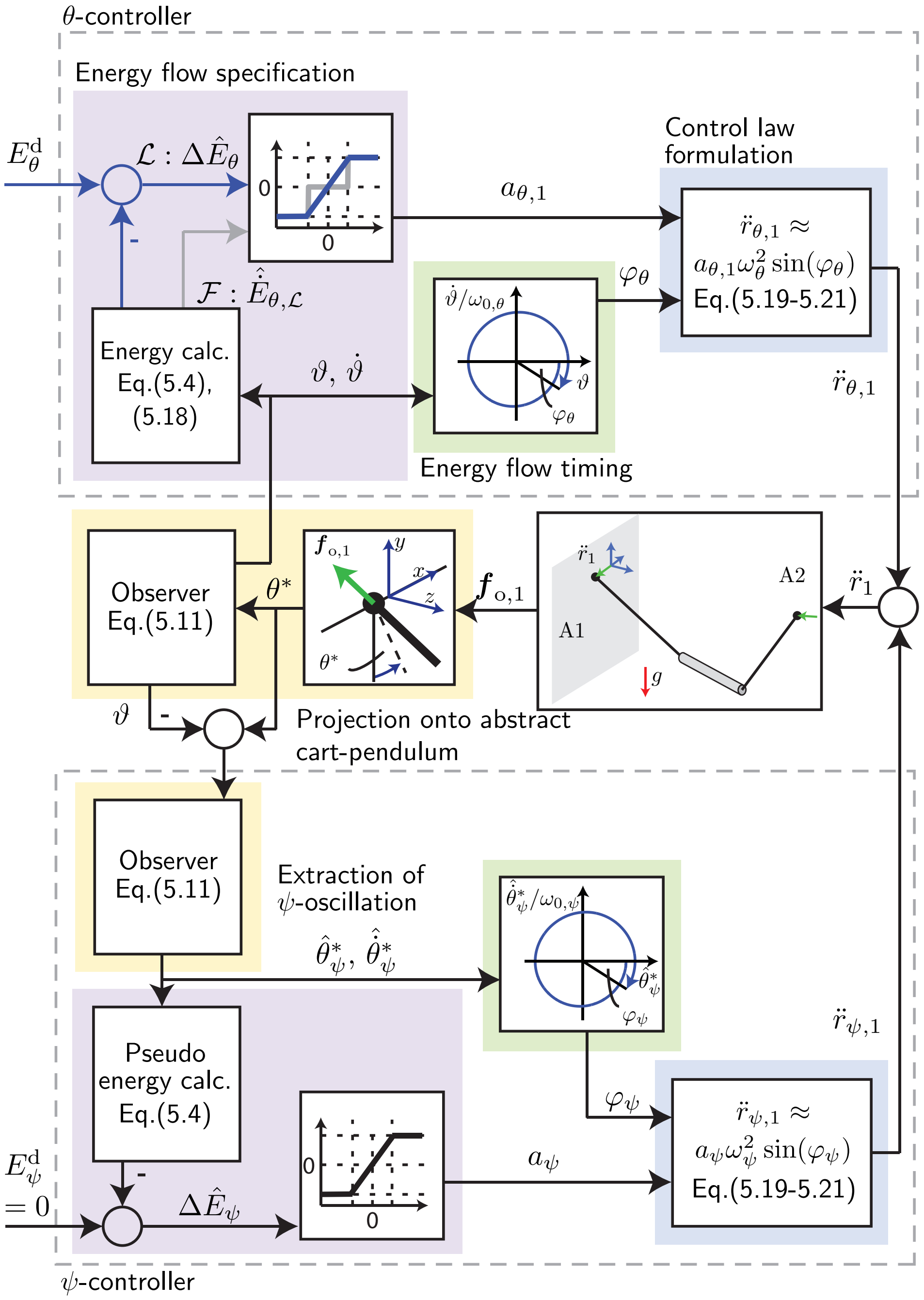

Fig. 5.4: Block diagram of the energy-based swing-up controller for the t-pendulum: The observers separate desired θ-oscillation from undesired ψ-oscillation based on knowledge of the respective natural frequencies.

$$G(s) = \frac{\vartheta(s)}{\theta^*(s)} = \frac{l_{\theta,1}s + l_{\theta,2}}{s^2 + l_{\theta,1}s + \omega_{0,\vartheta} + l_{\theta,2}}. \tag{5.12}$$

For observer gains $l_{\theta,1} = k\ \omega_{0,\vartheta}$ with $k > 0$ and $l_{\theta,2} = 0$, the observer is stable and the amplitude $|G(j\omega)|$ is equal to one for sinusoidal input signals θ^* of frequency $\omega_{0,\vartheta} = \omega_{0,\theta}$. Fig. 5.5 shows the bode diagram for different k. We can see that all frequency components

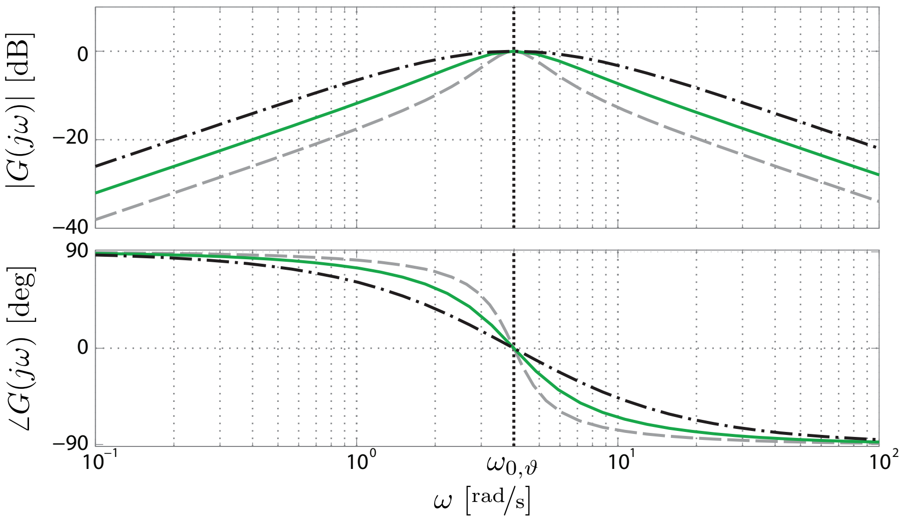

Fig. 5.5: Bode diagram of linearized observer with observer gains $l_{\theta,1} = k\ \omega_{0,\vartheta}$ and $l_{\theta,2} = 0$ for $\omega_{0,\vartheta}$ =4 rad/s: Grey dashed line $k = 0.5$, green solid line $k = 1$ and black dash-dotted line $k = 2$. Simulations of a t-pendulum with similar parameters as the one used in the experiments showed a good compromise between a sufficiently fast system response and damping of unwanted frequencies $\omega \neq \omega_{\vartheta}$ for an observer gain of $l_{\theta,1} = \omega_{0,\vartheta}$.

of the observer input θ^* are damped, except the ones close to the natural frequency $\omega_{0,\vartheta} = \omega_{0,\theta}$ of the linearized pendulum. Higher k-values result in a lower damping but in a faster observer response. Note that the observer filter performance increases with an increased difference between the natural frequencies of the θ- and the ψ-oscillations.

We are aware that the dynamics of the v-pendulum (Fig. 5.3 with a point mass $l_o \to 0$) and two agents that both only move in x-direction is already a lot more complex than the abstract cart-pendulum in (5.3), as it also depends on the agents' relative position $r_1 - r_2$ and velocity $\dot{r}_1 - \dot{r}_2$. In this thesis, we refrain from deriving the lengthy differential equations of the v- and t-pendulum[4]. Instead, we show that through the projection of the complex pendulums onto the abstract cart-pendulum, we are able to separate the oscillation DoFs such that we can control the oscillation DoFs in a desired manner and design an actively contributing follower. Consequently, we do not try to capture the complex system dynamics with (5.3), but we extract the desired oscillation by making use of the fact that the desired oscillation behaves as (5.3).

5.5.2 Energy control of the desired oscillation through excitation at the natural frequency

In order to differentiate between θ-excitation and ψ-damping, we rewrite the general idea of the control law (5.6) directed towards the θ-oscillation as

$$\ddot{r}_{\theta,1} \approx a_{\theta,1}\ \omega_{\theta}^2 \sin(\varphi_{\theta}) \tag{5.13}$$

---

[4] See, e.g., [30] for slung-load systems.

with amplitude factor $a_{\theta,1}$ specifying direction and amount of energy flow to the θ-oscillation and phase angle of the θ-oscillation φ_θ ensuring a well-timed energy injection. Implementation details on *energy flow timing*, *energy flow specification* and the *control law formulation* are given in the following.

Energy flow timing

We calculate the phase angle φ_θ by using the abstract cart-pendulum states $\boldsymbol{x}_{\mathrm{acP}}$ of the nonlinear observer[5] (5.11) and the small angle approximation for normalization $\Omega = \omega_{0,\theta}$ in (4.10).

Energy flow specification

For the *leader* $\mathcal{L}$ we apply a saturated linear mapping from energy error $\Delta\hat{E}_\theta = E_\theta^{\mathrm{d}} - \hat{E}_\theta$ to amplitude factor $a_{\theta,\mathcal{L}}$

$$a_{\theta,\mathcal{L}} = \begin{cases} a_{\max,\theta,\mathcal{L}}\ \operatorname{sgn}(\Delta\hat{E}_\theta) & \text{if} \quad |\Delta\hat{E}_\theta| \geq \delta_{\theta,\mathcal{L}}, \\ \frac{a_{\max,\theta,\mathcal{L}}}{\delta_{\theta,\mathcal{L}}}\Delta\hat{E}_\theta & \text{else}, \end{cases} \tag{5.14}$$

with $\frac{a_{\max,\theta,\mathcal{L}}}{\delta_{\theta,\mathcal{L}}}$ being the slope of the linear mapping with maximum amplitude factors $\pm a_{\max,\theta,\mathcal{L}}$, which are approximately equal to the maximum amplitude of the resultant robot motion $r_{\theta,\mathcal{L}}$. The estimate of the energy contained in the θ-oscillation $\hat{E}_\theta$ is calculated based on the observer states $\boldsymbol{x}_{\mathrm{acP}}$ in (5.4).

For the *follower* $\mathcal{F}$ a mapping from estimated leader energy flow $\dot{\hat{E}}_{\theta,\mathcal{L}}$ to three discrete amplitude factors is applied

$$a_{\mathrm{dis}} = \begin{cases} a_{\max,\theta,\mathcal{F}} & \text{if} \quad \dot{\hat{E}}_{\theta,\mathcal{L}} \geq \delta_{\mathrm{u},\theta,\mathcal{F}}, \\ 0 & \text{if} \quad \delta_{\mathrm{u},\theta,\mathcal{F}} > \dot{\hat{E}}_{\theta,\mathcal{L}} > \delta_{\mathrm{l},\theta,\mathcal{F}}, \\ -a_{\max,\theta,\mathcal{F}} & \text{else}. \end{cases} \tag{5.15}$$

Instead of the linear connection between the two maximum values $\pm a_{\max,\theta,\mathcal{L}}$ in case of the leader (5.14), we define a neutral zone for the follower for estimated energy flows within the limits[6] $]\delta_{\mathrm{l},\theta,\mathcal{F}}, \delta_{\mathrm{u},\theta,\mathcal{F}}[$. Ramps

$$\dot{a}_{\theta,\mathcal{F}} = \tau_{\mathcal{F}}\ \operatorname{sgn}(a_{\mathrm{dis}} - a_{\theta,\mathcal{F}}) \tag{5.16}$$

with inverse blending time constant $\tau_{\mathcal{F}}$ [131] prevent discontinuities in the end effector acceleration $\ddot{r}_{\theta,\mathcal{F}}$.

Computation of the leader induced energy flow estimate $\dot{\hat{E}}_{\theta,\mathcal{L}}$ requires filtering. In the following we use a second-order low-pass filter

$$G_{\mathrm{lp}}(s, D_{\mathrm{lp}}, T_{\mathrm{lp}}) = \frac{1}{T_{\mathrm{lp}}^2 s^2 + 2D_{\mathrm{lp}}T_{\mathrm{lp}}s + 1}, \tag{5.17}$$

---

[5] In [38], a Kuramoto oscillator instead of the observer was used to extract the θ-related phase angle φ_θ. Simulations and experiments show similar results for both approaches.

[6] Separate lower $\delta_{\mathrm{l},\theta,\mathcal{F}}$ and upper $\delta_{\mathrm{u},\theta,\mathcal{F}}$ limits allow to take into account that friction shifts the leader energy flow estimates towards negative values.

with damping D_{lp} and time constant T_{lp}. Under the assumption of a lossless t-pendulum, the energy flow balance results in the estimate of the leader energy flow

$$\hat{\dot{E}}_{\theta,\mathcal{L}} = \hat{\dot{E}}_{\theta} - \hat{\dot{E}}_{\theta,\mathcal{F}} = sG_{\mathcal{F}}(s)\hat{E}_{\theta}(s) - G_{\mathcal{F}}(s)\dot{E}_{\theta,\mathcal{F}}(s), \tag{5.18}$$

with $G_{\mathcal{F}}(s) = G_{\mathrm{lp}}(s, D_{\mathrm{lp}} = 1, T_{\mathrm{lp}} = T_{\mathcal{F}})$ of (5.17) and $\hat{E}_{\theta}$ and $\dot{E}_{\theta,\mathcal{F}}$ according to (5.4) and (5.5) based on the observer states $\boldsymbol{x}_{\mathrm{acP}}$, respectively.

Control law formulation

Imperfect energy estimates as well as remaining ψ-oscillation on the observer states lead to an acceleration $\ddot{r}_{\theta,1}$ with higher frequency components than the natural frequency of the desired θ-oscillation when computed according to (5.13). Higher harmonics on the phase angle φ_{θ} further disturb the sign condition which allows controlled energy injection to the pendulum (see Section 5.4.2). As suggested by Yoshida [188], we compute a reference trajectory

$$r_{\theta,1}^{\mathrm{ref}} = a_{\theta,1}\frac{1}{|G_{\theta}(j\omega_{0,\theta})|}\sin(\varphi_{\theta} - \pi - \angle G_{\theta}(j\omega_{0,\theta})), \tag{5.19}$$

which we differentiate twice and filter using the second-order low-pass filter $G_{\theta}(s) = G_{\mathrm{lp}}(s, D_{\mathrm{lp}} = 1.2, T_{\mathrm{lp}} = \frac{0.9}{\omega_{0,\theta}})$ of (5.17)

$$\ddot{r}_{\theta,1}(s) = s^2 G_{\theta}(s) r_{\theta,1}^{\mathrm{ref}}(s). \tag{5.20}$$

The resultant acceleration is dominated by the frequency of the θ-oscillation and consequently approximately equal to

$$\ddot{r}_{\theta,1} \simeq a_{\theta,1}\ {\omega_{\theta}}^2 \frac{|G_{\theta}(j\omega_{\theta})|}{|G_{\theta}(j\omega_{0,\theta})|}\sin(\varphi_{\theta} - \angle G_{\theta}(j\omega_{0,\theta}) + \angle G_{\theta}(j\omega_{\theta})) \approx a_{\theta,1}\ {\omega_{\theta}}^2 \sin(\varphi_{\theta}). \tag{5.21}$$

The sinusoidal shape of the commanded robot acceleration allows us to compensate for the amplitude and phase shift $|G_{\theta}(j\omega_{\theta})|$ and $\angle G_{\theta}(j\omega_{\theta})$ caused by the filter G_{θ} at the natural frequency ω_{θ}, by using the approximated amplitude and phase shift $|G_{\theta}(j\omega_{0,\theta})|$ and $\angle G_{\theta}(j\omega_{0,\theta})$ within the reference trajectory (5.19).

5.5.3 Damping of the undesired oscillation

This section explains how to actively damp the undesired ψ-oscillation of a t-pendulum with an approach similar to the control of the θ-oscillation. Again, we choose the following approximate control

$$\ddot{r}_{\psi,1} \approx a_{\psi}\ \omega_{\psi}^2 \sin(\varphi_{\psi}). \tag{5.22}$$

Extraction of undesired oscillation

According to (5.1) and with $\vartheta \approx \theta_{\theta}^{*}$, we can retrieve the ψ-oscillation by the simple subtractions $\theta_{\psi}^{*} = \theta^{*} - \vartheta$ and $\dot{\theta}_{\psi}^{*} = \dot{\theta}^{*} - \dot{\vartheta}$. However, noise in the force measurements leads to a highly distorted angular velocity $\dot{\theta}^{*}$ when being calculated by first-order numerical differentiation from θ^*. In order to extract smooth states $\hat{\boldsymbol{\theta}}^*_\psi = \begin{bmatrix}\hat{\theta}^*_\psi & \dot{\hat{\theta}}^*_\psi\end{bmatrix}^\top$ a second nonlinear observer of the same form as (5.11) is used with coupling term $\boldsymbol{l}_\psi((\theta^* - \vartheta) - \hat{\theta}^*_\psi)$. The projection of the ψ-oscillation cannot be easily related to a simple pendulum oscillation. However, simulations showed a better approximation of the ψ-oscillation using the nonlinear observer model than an harmonic oscillator as a filter. The small angle approximation of the natural frequency $\hat{\omega}_{0,\psi}$ as needed within the observer model was found experimentally.

Energy flow timing

The experimentally obtained approximation of the natural frequency $\hat{\omega}_{0,\psi}$ is used together with the estimated state $\hat{\boldsymbol{\theta}}^*_\psi$ to compute the phase angle φ_ψ related to the ψ-oscillation according to (4.10).

Energy flow specification

For the follower and for the leader the objective is to control the energy contained in the ψ-oscillation to zero $E^{\mathrm{d}}_\psi = 0$ (see Problems 6 and 7). The leader mapping of the θ-oscillation control (5.14) is reused to compute an amplitude factor a_ψ with parameters δ_ψ, $a_{\max,\psi}$ and based on the pseudo energy $\hat{E}_\psi$ according to (5.4) and observer state $\hat{\boldsymbol{\theta}}^*_\psi$. The pseudo energy $\hat{E}_\psi$ is not a real energy, but allows to quantify the disturbance oscillation. One drawback of its computation according to (5.4) is that $\hat{E}_\psi$ is not constant for a pure ψ-oscillation, but oscillates. We reduce these oscillations by applying the filter $G_{E,\psi}(s) = G_{\mathrm{lp}}(s, D_{\mathrm{lp}} = 1, T_{\mathrm{lp}} = T_\psi)$ of (5.17) to the pseudo energy $\hat{E}_\psi$.

Control law formulation

In contrast to the θ-controller, the extracted ψ-oscillation does not only contain higher but also lower frequency components than ω_ψ originating from the θ-oscillation. In order to damp all frequencies other than the one of interest ω_ψ, we apply a band pass filter $G_\psi(s) = s^2(\frac{0.9}{\hat{\omega}_{0,\psi}})^2 G^2_{\mathrm{lp}}(s, D_{\mathrm{lp}} = 1.2, T_{\mathrm{lp}} = \frac{0.9}{\hat{\omega}_{0,\psi}})$ based on the low-pass filter of (5.17). The filter G_ψ is applied to a reference trajectory $r^{\mathrm{ref}}_{\psi,1}$ as given for the θ-controller in (5.20). Similar to (5.19), we compute the reference trajectory $r^{\mathrm{ref}}_{\psi,1}$ based on the approximated natural frequency $\hat{\omega}_{0,\psi}$ to compensate for the amplitude and phase shift $|G_\psi(j\omega_\psi)|$ and $\angle G_\psi(j\omega_\psi)$ caused by the band pass filter G_ψ at the frequency of interest ω_ψ. The resultant acceleration $\ddot{r}_{\psi,1}$ is approximately equal to (5.22).

We add $\ddot{r}_{\psi,1}$ to the acceleration computed to control the θ-oscillation to form the final control input

$$\ddot{r}_1 = \ddot{r}_{\theta,1} + \ddot{r}_{\psi,1}. \tag{5.23}$$

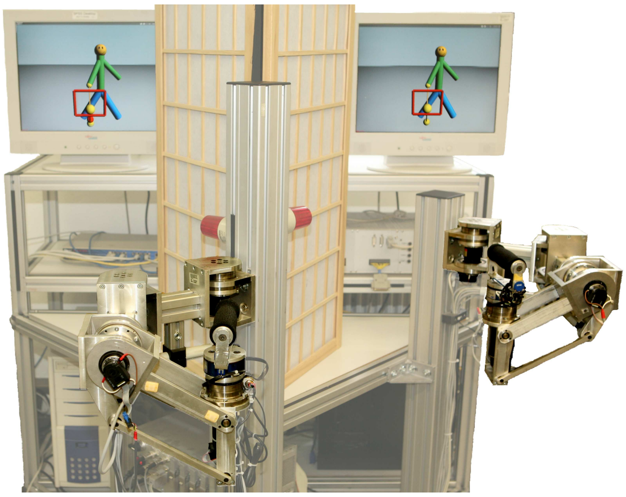

Fig. 5.6: Experimental setup: Two 4 DoF haptic interfaces with handles and two screens rendered the virtual scene; one pair for each human partner. The participants conducted the collaborative task while standing in front of the devices.

5.6 Virtual reality experiments

In order to get a first idea on the applicability of the proposed leader and follower control concept to human interaction partners, we conducted a virtual reality pilot study[7]. Four right-handed participants (1 female, 3 male, age 26-30) were told to swing up a v-pendulum in a virtual reality scene together with a human partner, with a virtual avatar and alone with one fixed end.

5.6.1 Experimental setup

Both visual and haptic feedback was provided to the participants. The details on the rendering system are given in the following.

Hardware setup

Two four DoF manipulators provided high-fidelity haptic rendering to the human participants, see Fig. 5.6 for the experimental setup. The manipulators were computed-torque position controlled and had *JR3* force/torque-sensors (JR3, Inc., USA) attached to the handles. Two screens visualized the virtual reality scene for the participants. A partition between the screens prohibited the human participants to see the other person's screen.

Software implementation

Both, the simulation of the pendulum model and the control scheme of the haptic interfaces were implemented using *MATLAB/Simulink Real-Time Workshop* and executed at

---

[7] Minor differences exist between the follower implementation introduced in Section 5.5 and the follower implementation for the virtual reality experiments. See [43] for details.

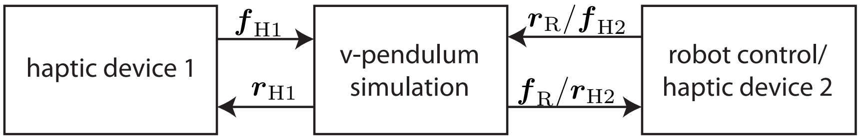

Fig. 5.7: Overall control structure for human-robot/human-human collaborative swing-up: The human side(s) of the v-pendulum was (were) actuated through the force(s) $\boldsymbol{f}_{\mathrm{H1(/H2)}}$, exerted during interaction with the haptic device. The robot control computed an actuation trajectory $\boldsymbol{r}_{\mathrm{R}}$, based on the measured force $\boldsymbol{f}_{\mathrm{R}}$.

a sampling frequency of 1 kHz on two personal computers running Linux real-time kernels. The control architecture for haptic rendering is shown in Fig. 5.7. The physical model of the pendulum was realized within the *SimMechanics First generation* toolbox of *MATLAB/Simulink* through rigid bodies linked via unconstrained spherical joints damped by d_{j}. The rigid body assumption was valid, as the rope connecting both actuation bodies m_{h} and the pendulum mass m_{p} could be considered to be fully stretched during the complete swing-up task. Whereas the robot only moved along the x-axis, we allowed the human's effector to move within the xy-plane in a rectangular area of 0.24 m × 0.18 m constrained by virtual walls (Fig. 5.8). The z-axis was controlled to a constant position. This way the human felt the forces exerted by the pendulum in x- and y-direction, which were found to be important for a realistic haptic perception of the pendulum state. The interaction of the human through the haptic interface with the virtual environment was realized by the cartesian admittance control law along directions $k = x, y$

$$f_{\mathrm{H}k} = m_{\mathrm{h,H}}\ddot{r}_{\mathrm{H}k} + d_{\mathrm{h}}\dot{r}_{\mathrm{H}k} + f_{\mathrm{o,H}k} \tag{5.24}$$

rendering a point-mass $m_{\mathrm{h,H}}$ with viscous damping d_{h} at the handle. For stability reasons a minimum damping d_{h} and a minimum mass $m_{\mathrm{h,H}}$ have to be assigned. This, in return, necessitates a relatively high pendulum mass for a sufficiently high ratio $\frac{m_{\mathrm{o}}}{m_{\mathrm{h,H}}}$. In order to decrease the gravitational load the human is exposed to, the handle mass $m_{\mathrm{h,H}}$ was gravity compensated. The parameters of the simulated v-pendulum are listed in Table 5.1. A small, negligible moment of inertia $\boldsymbol{J}_{\mathrm{o}}$ was assigned to the pendulum mass due to singularity issues within the SimMechanics model.

Tab. 5.1: Parameters of the pendulum simulation

$m_{\mathrm{h},i}$[kg]	m_{o}[kg]	$\boldsymbol{J}_{\mathrm{o}}$[kg/m²]	C[m]	l[m]	d_{j}[Nms/deg]	d_{h}[Ns/m]
4	5	$0.0005\boldsymbol{I}_{3\times3}$	1.32	0.9	0.0005	6

The v-pendulum as well as the virtual robot or human partner were visualized through an OpenGL-based implementation using the *Visualization ToolKit*. Figure 5.8 shows the displayed scene for human-human interaction. Table 5.2 lists the control parameters of the robot leader and the robot follower.

5.6.2 Experimental conditions and procedure

Each participant conducted three trials under the following experimental conditions:

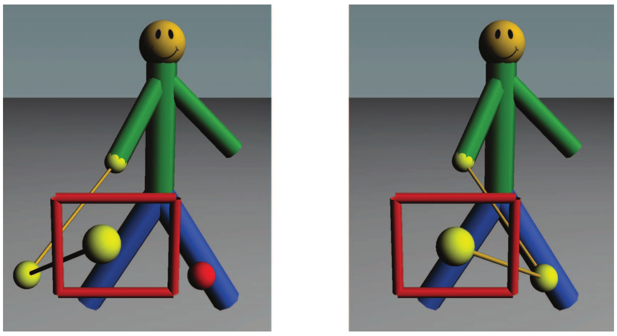

Fig. 5.8: Visualized scene for human-human collaborative swing-up: The red bounding boxes visualized the human workspace limits. The red sphere represents the goal position for the pendulum mass and was only displayed on the leader's screen.

Tab. 5.2: Control parameters

$\bar{a}_{\theta,\mathcal{L}}$[m]	$\delta_{\theta,\mathcal{L}}$[J]	$\bar{a}_{\theta,\mathcal{F}}$[m]	$\delta_{\theta,\mathcal{F}}$[W]	$\tau_{\mathcal{F}}$[1/s]
0.04	2.93	0.036	0.58	10

- alone: HL-0,
- with a human interaction partner: HL-HL, HL-HF, HF-HL,
- with a robot interaction partner: HL-RL, HL-RF, HF-RL,

where the left side refers to A1 and the right side to A2. Thus, HF-RL denotes a human follower A1=H=$\mathcal{F}$ interacting with a robot leader A2=R=$\mathcal{L}$. Condition HL-0 required the human A1=H=$\mathcal{L}$ to swing up the pendulum alone while the other end of the pendulum was fixed. An extra trial in HL-0 was conducted before the actual experiment to allow the participants to get familiar with the task. The participants where informed about their roles $\mathcal{L}$ or $\mathcal{F}$ beforehand and asked to collaborate in order to achieve the joint goal: swing-up to the energy level displayed by the goal sphere to the leader only.

The procedure was as follows: the human participants had to lift up the pendulum to the middle of the workspace. In case of an RL condition, the robot started with a small point-to-point movement to introduce slight swinging and, thus, a properly rotating phase angle φ as needed for the robot control. Then the first goal sphere at $\boldsymbol{r}^{\mathrm{d}}_{\mathrm{o},E}$ corresponding to a desired angle $\theta^{\mathrm{d}}_{E} = 30\,\mathrm{deg}$ was displayed. After reaching the goal sphere once, the goal sphere stayed for another five pendulum periods. Then a new goal sphere at $\theta^{\mathrm{d}}_{E} = 45\,\mathrm{deg}$ was displayed. After reaching that goal sphere and another five pendulum periods, the goal sphere was shifted back to angle zero. Thus, the participants were asked to completely release the pendulum energy.

5.6.3 Measures for analysis

We introduce the following measures to evaluate the conditions above.

Analysis of task performance

The *completion time* T_c was defined as the time span

$$T_\mathrm{c} = t_\mathrm{gh} - t_\mathrm{id} \tag{5.25}$$

between the time of the first goal sphere hit t_gh ($\left\|\boldsymbol{r}^\mathrm{d}_{\mathrm{o},E} - \boldsymbol{r}_\mathrm{o}\right\| < 0.04\,\mathrm{m}$) and the time of the initial display of the goal sphere t_id, where $\left\|x\right\|$ denotes the Euclidean norm.

The *goal hitting error* e_gh was computed as the root-mean-square of the six dead points of the pendulum mass $\boldsymbol{r}_{\mathrm{o},E,k}$ with $k = 1, \ldots, 6$, i.e. the points of pure potential energy, on the side of the goal sphere occurring after t_gh

$$e_\mathrm{gh} = \sqrt{\frac{1}{6}\sum_{k=1}^{6} \left\|\boldsymbol{r}_{\mathrm{o},E,k} - \boldsymbol{r}^\mathrm{d}_{\mathrm{o},E}\right\|}. \tag{5.26}$$

Analysis of effort sharing

In order to analyze how much energy each agent contributed, we calculated the energy flows of the agents to the v-pendulum based on applied force and handle velocities

$$\dot{E}_i = \boldsymbol{f}_i^\top \dot{\boldsymbol{r}}_i \quad \text{with} \quad i = 1, 2. \tag{5.27}$$

The energy contained in the v-pendulum was obtained from

$$E = m_\mathrm{o} g y_\mathrm{o} + \frac{1}{2}\dot{\boldsymbol{\xi}}_\mathrm{o}^\top \boldsymbol{M}_\mathrm{o} \dot{\boldsymbol{\xi}}_\mathrm{o}, \tag{5.28}$$

with pendulum mass height y_o, pendulum mass velocity $\dot{\boldsymbol{\xi}}_\mathrm{o} = \begin{bmatrix}\dot{\boldsymbol{r}}_\mathrm{o} & \dot{\boldsymbol{\Omega}}_\mathrm{o}\end{bmatrix}$ including translational and rotational velocities, respectively. The 6×6 mass matrix $\boldsymbol{M}_\mathrm{o}$ consists of the 3×3 diagonal matrix with the pendulum mass m_o as diagonal entries and the 3×3 moment of inertia tensor $\boldsymbol{J}_\mathrm{o}$ (see Table 5.1). All variables are expressed relative to a fixed point in the world coordinate system $\{\mathrm{w}\}$ located such that $y_\mathrm{o} = 0\,\mathrm{m}$ for $\theta = 0\,\mathrm{deg}$ and zero agent handle positions $\boldsymbol{r}_1 = \boldsymbol{0}_{3\times3}$ and $\boldsymbol{r}_2 = \boldsymbol{0}_{3\times3}$ (in the middle of the workspaces in Fig. 5.8).

Note that damping of the pendulum-like objects is not negligible in contrast to the rigid object in the previous chapter. Thus, $E(t) \neq E_1(t) + E_2(t) + E(t = 0)$ as in (4.13). Also in contrast to the ara-system, the arms of the agents are not part of the v- or t-pendulum. Thus, we have $E_\mathrm{o} = E$ in the sense that the complete system energy E is equal to the energy contained in the object of the v- or t-pendulum and an energy flow $\dot{E}_i$ computed according to 5.27 represents the complete energy flow contributed by agent Ai. Therefore, we drop the index o in the following for the v- and t-pendulum.

In Chapter 2, we defined the energy share γ_1 in (2.30) based on the relation of the energy flow caused by A1 to the sum of the energy flow contributions of all agents. In order to gain a measure that describes the energy share of a complete object swing-up task, we integrate the agents' energy flows over a certain time period. For the virtual reality task, we use the time period $[t_\mathrm{id} \quad t_\mathrm{gh}]$ and define the integrated *energy share* Γ_1 for agent A1 as

$$\Gamma_1 = \frac{\int_{t_\mathrm{id}}^{t_\mathrm{gh}} \dot{E}_1 \mathrm{d}\tau}{\int_{t_\mathrm{id}}^{t_\mathrm{gh}} (\dot{E}_1 + \dot{E}_2) \mathrm{d}\tau}. \tag{5.29}$$

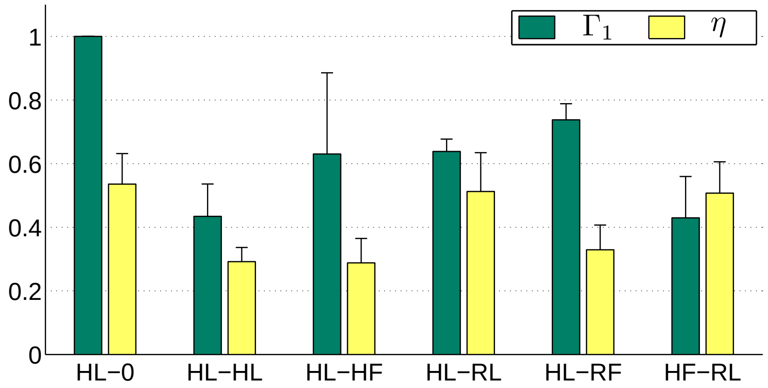

Fig. 5.9: Results energy effort: Means and standard deviations of energy share Γ_1 and energy efficiency η for the first phase with $\theta_E^{\mathrm{d}} = 30\,\mathrm{deg}$. Robotic leaders exhibited the highest energy efficiency η. In interaction with human leaders, robotic followers achieved similar energy efficiency and energy share measures compared to human followers.

The *energy efficiency* η penalizes energy flow waisted by the agents, i.e. any energy flow not directed towards the desired energy level E_θ^{d}. We define

$$\eta = \frac{|E_\theta^{\mathrm{d}} - E_\theta(t_{\mathrm{id}})|}{\int_{t_{\mathrm{id}}}^{t_{\mathrm{id}*}} (|\dot{E}_1| + |\dot{E}_2|)\mathrm{d}\tau} \tag{5.30}$$

where $t_{\mathrm{id}*}$ denotes the time when the next goal sphere is displayed. Note that all energy computations in (5.30) have to be performed with respect to the same system borders. For the ara-system of the previous chapter, we have $E_{\mathrm{o},\theta} \neq E_\theta$, as E_θ also includes the energy contained in the swinging arms. Thus, we would have to either use only object related energies $E_{\mathrm{o},\theta}$, $\dot{E}_{\mathrm{o},i}$ or energies related to the complete system E_θ, $\dot{E}_i$ including the agents' arms. The energy efficiency η takes on values between 0 and 1. Since the pendulum is slightly damped by a small d_{j}, $\eta = 1$ is never reached. As we aim to penalize time periods in which an energy flow $\mathrm{sgn}(\dot{E}_1) \neq \mathrm{sgn}(\dot{E}_2)$ is voluntarily applied by the partners, we filter the energy flows with a third-order low-pass butterworth-filter with a cut-off frequency at 1 Hz.

5.6.4 Results and Discussion

For comparison between our six different conditions, we calculated the four measures above over all trials and for each condition and goal angle separately. For the sake of brevity, we focus on the results for the desired angle $\theta_E^{\mathrm{d}} = 30\,\mathrm{deg}$ in detail.

Effort sharing

First, we analyze the energy flows into the system, and thus, the effort taken by the partners. Figure 5.9 shows the resulting energy efficiency η and the energy share of agent A1 Γ_1. The highest efficiency values were achieved for the conditions with a robotic leader. This is due to the perfectly monotonic energy flow produced by the leader controller. The

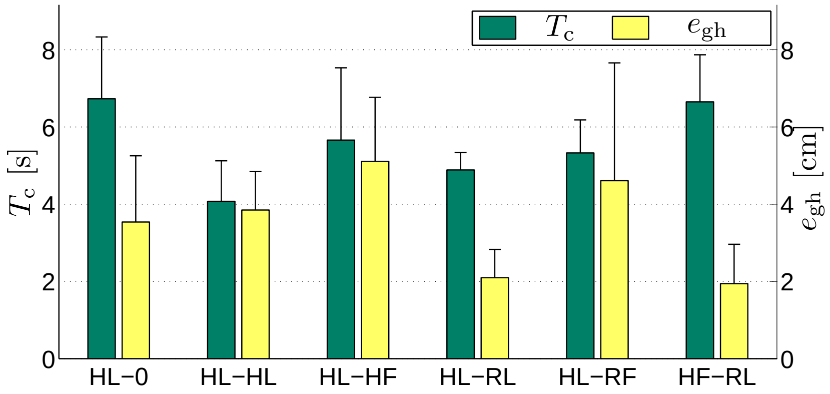

Fig. 5.10: Results task performance: Means and standard deviations of completion time T_c and goal hitting error e_{gh} for the first phase with $\theta_E^d = 30\,\text{deg}$. Continuous energy monitoring by robotic leaders led to especially small goal hitting errors e_{gh}. Similar to human followers, robot followers decreased the completion time T_c of human-leaders compared to 0-HL.

energy efficiency for a robotic follower was in the same range as for the human-human combinations. Note that a high efficiency value for the HL-0 condition was obtained, since there was no partner interaction causing efficiency losses.

The energy share of agent A1 Γ_1 evaluates the goal-directed energy input into the pendulum. Figure 5.9 suggests that for the conditions with a distinct human leader, i.e. HL-HF and HL-RF, the leader contributed more than half of the total energy needed to reach the goal. The relatively low contribution of the robotic agents was due to the rather conservative parameterization of the robot controllers (see Table 5.2) with low resultant amplitude factors $a_{\theta,\mathcal{L}}$ and $a_{\theta,\mathcal{F}}$. For the reported parameterization, the contribution of a robotic follower was comparable to the contribution of a human follower, both collaborating with a human leader. The standard deviation for the HL-HF condition was notably larger, due to the individual behavior of the participants, compared to the constant behavior of the robot follower.

Task performance

Given the task of swinging up the pendulum to coincide with a displayed goal sphere, the completion time T_c and goal hitting error e_{gh} shown in Fig. 5.10 evaluate the task performance. As expected, T_c is the smallest if both collaborating agents lead and, thus, know the desired angle. A robot follower as well as a human follower tend to decrease the completion time, compared to the human single performance. The relatively high completion time for the condition RL-HF is again a result of the conservative control parameterization.

The conditions involving a robot leader cause the lowest goal hitting error e_{gh}. The good precision originates in the robot control, which continuously tracks the pendulum energy. In contrast, humans are expected to rely to a high extend on their visual feedback. The precision similarly decreases for a human leader collaborating with a robot or a human follower. However, the high standard deviation for the HL-RF condition stands out and is

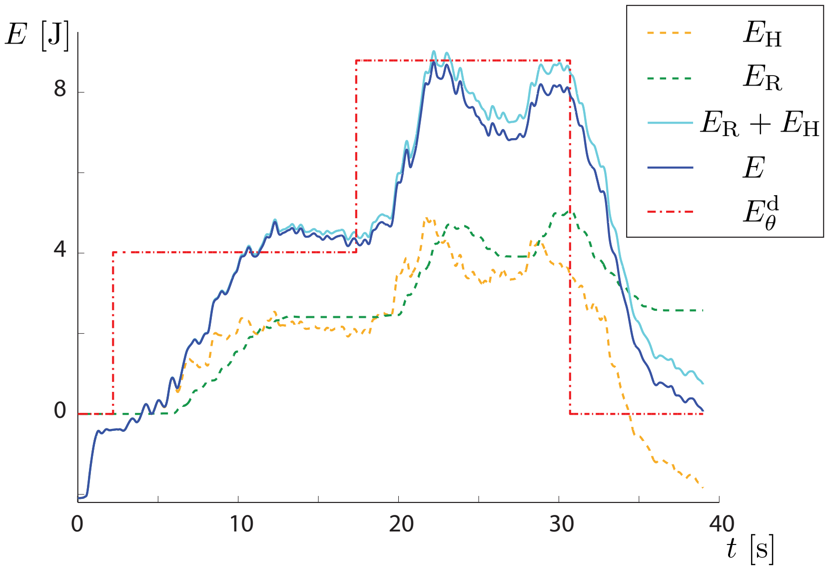

Fig. 5.11: Sample trial HL-RF condition: Energy over time for the first phase with $\theta_E^{\mathrm{d}} = 30\,\mathrm{deg}$ and second phase with $\theta_E^{\mathrm{d}} = 45\,\mathrm{deg}$. Effort sharing between the robot and the human was balanced during the first phase. Difficulties of the human leader in tracking the higher goal energy during the second phase were amplified by the robot follower.

analyzed in the following by means of an example trial.

The robot follower

A complete example trial for the HL-RF condition is given in Fig. 5.11. It shows the energy contribution of the human leader E_{H} and the robot follower E_{R}. The total energy contained in the system is given by E, which is slightly lower than $E_{\mathrm{H}} + E_{\mathrm{R}}$ due to the damping d_{j} in the pendulum joints. The desired energy E_{θ}^{d} is computed from the sequence of desired maximum deflection angles θ_E^{d}.

The trial started as the human leader lifted the handle to the workspace middle, followed by the display of the first goal sphere at $\theta_E^{\mathrm{d}} = 30\,\mathrm{deg}$. The robot was controlled to monotonically raise the energy level according to the human input with a short time delay. Once the goal angle was reached, the human stopped injecting more energy into the system, which caused the robot controller to enter the neutral zone, controlling its amplitude to zero according to (5.15). The measures goal hitting error $e_{\mathrm{gh}} = 0.023\,\mathrm{m}$ and energy efficiency $\eta = 0.43$ for the first energy level in this trial were especially good compared to the means over all trials (see Fig. 5.9 and Fig. 5.10). The reason for the worse performance during other trials can be found when observing the next phase defined by the goal maximum deflection angle $\theta_E^{\mathrm{d}} = 45\,\mathrm{deg}$. The higher energy level was harder to be tracked by the human. As a result, the robot controller did not stay in its neutral zone, which in return made it more difficult for the human to track the goal energy level. As a consequence, the measures for the second phase degraded to $e_{\mathrm{gh}} = 0.036\,\mathrm{m}$ and $\eta = 0.31$. Other participants tended to highly oscillate also around the lower energy level, which explains the high standard deviation of e_{gh} in Fig. 5.10 for the HL-RF conditions. This issue suggests that a robot follower taking into account the magnitude of the human energy flow is expected to be more beneficial. We will introduce a follower that imitates the energy flow of the pendulum-like object according to a desired energy share $\Gamma^{\mathrm{d}}_{\mathcal{F}}$ and without a neutral zone in Chapter 6.

5.7 Real world experiments

The previous section showed convincing performance of the proposed controller in virtual reality for the v-pendulum. However, in virtual reality, the robot and the object are simulated, and thus show ideal behavior. Furthermore, the v-pendulum is simpler to control as it does not posses disturbance oscillations as the t-pendulum. In this section, we evaluate the control approach for the complex t-pendulum presented in Section 5.5 in real world experiments with and without a human interaction partner. Consequently, the controller is tested under the influence of noise and non-ideal object and robot behavior.

5.7.1 Experimental setup

Hardware setup

Figure 5.12 shows the experimental setup. A *KUKA LWR 4+* under impedance control on joint level (joint stiffness $1500\,{}^{\mathrm{Nm}}/_{\mathrm{rad}}$ and damping $0.7\,{}^{\mathrm{Nm\,s}}/_{\mathrm{rad}}$) served as robotic manipulator. The one end of the pendulum-like object was attached to the robot end effector. The other end was either fixed to the environment or attached to the handle of the human interaction partner dependent on the experimental condition. We recorded the interaction forces using *JR3* 6 DoF force/torque sensors (JR3 Inc., USA). For analysis only, an *Oqus* motion capture system (Qualisys, Sweden) recorded position and orientation of the manipulated objects and of the human handle. Table 5.3 lists the pendulum parameters. Due to the small load capacity of the robotic manipulator, we used an object of relatively small mass $m_{\mathrm{o}} = 1.25\,\mathrm{kg}$ for the t-pendulum. The KUKA LWR 4+ can handle higher loads, if operated close to its singularities. However, joint velocity limits restrict the maximum end effector velocity. As we are interested in a proof of concept of the proposed approach independent of the robotic platform used, we refrained from optimizing the mounting of the robot or even the robot itself for higher loads and velocities.

Tab. 5.3: Pendulum and controller parameters

m_{o}	l_{o}	d_{o}	l	C	$\omega_{0,\theta}$	m_{h}	$\tau_{\mathcal{F}}$	$T_{\mathcal{F}}$	T_{ψ}
$1.25\,\mathrm{kg}$	$0.85\,\mathrm{m}$	$0.05\,\mathrm{m}$	$0.96\,\mathrm{m}$	$2\,\mathrm{m}$	$3.57\,{}^{\mathrm{rad}}/_{\mathrm{s}}$	$0.255\,\mathrm{kg}$	$10\,{}^{1}/_{\mathrm{s}}$	$\frac{4.5}{\omega_{0,\theta}}$	$\frac{1.5}{\omega_{0,\theta}}$
$\boldsymbol{l}_{\theta}, \boldsymbol{l}_{\psi}$	$\hat{\omega}_{0,\psi}$	$\delta_{\theta,\mathcal{L}}$	$a_{\max,\theta,\mathcal{L}}$	$a_{\max,\theta,\mathcal{F}}$	$\delta_{\mathrm{u},\theta,\mathcal{F}}$	$\delta_{\mathrm{l},\theta,\mathcal{F}}$	δ_{ψ}	$a_{\max,\psi}$	
$[\omega_{0,\theta} \quad 0]^{\top}$	$2\omega_{0,\theta}$	$0.5\,\mathrm{J}$	$0.04\,\mathrm{m}$	$0.04\,\mathrm{m}$	$0.12\,\mathrm{W}$	$0.18\,\mathrm{W}$	$0.2\,\mathrm{J}$	$0.03\,\mathrm{m}$	

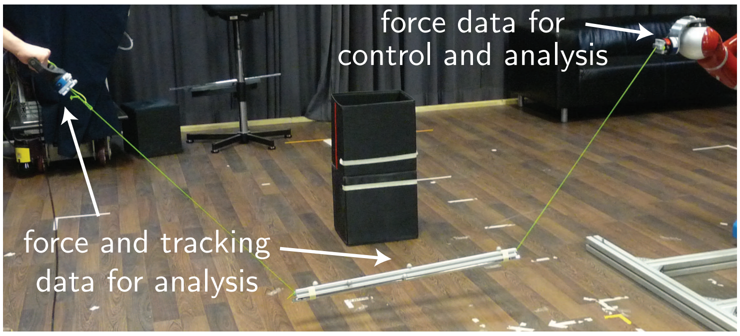

Fig. 5.12: Experimental setup.

Software implementation

The motion capture data was recorded at 200 Hz and the force/torque data at 1 kHz by individual computational units and streamed to a *MATLAB/Simulink Real-Time Target* model, which was run at 1 kHz. The same *MATLAB/Simulink Real-Time Target* model contained the presented energy-based controller as well as the low-level velocity controller of the robotic manipulator. The force/torque data[8] at the robot's interaction point was the only input to the energy-based controller. For the analysis, we applied a third-order butterworth low-pass filter with cutoff frequency 4 Hz to the motion capture data as well as the force/torque data. The filtering allowed to circumvent problems arising from numerical differentiation due to outliers or the undersampling of the motion data with respect to the force/torque data.

Controller parametrization

The controller parameters were tuned in simulation and based on initial experiments (see Table 5.3).

5.7.2 Measures for analysis

Analysis of the projection onto the abstract cart-pendulum

The projection of the complex pendulum onto the abstract cart-pendulum allows extraction of the dominant oscillation DoFs θ_θ^* and θ_ψ^* and their respective energy levels $\hat{E}_\theta$ and $\hat{E}_\psi$. We compared the approximations against the actual motion of the pendulum mass m_o obtained from the motion capture data, as the actual deflection angles θ and ψ. Based on the actual deflection angle θ, the energy contained in the θ-oscillation E_θ was calculated according to (5.4). The complete pendulum energy was obtained from (5.28), where we approximated the pendulum moment of inertia $\boldsymbol{J}_\mathrm{o}$ by a cylinder of length l_o, diameter d_o and evenly distributed mass m_o. All variables are expressed relative to a fixed point in the world coordinate system $\{\mathrm{w}\}$ located such that $y_\mathrm{o} = 0\,\mathrm{m}$ for $\theta = \psi = 0\,\mathrm{deg}$. Under

---

[8] The 8 kHz force/torque data was filtered by a first-order low-pass filter with cutoff frequency 500 Hz provided by JR3 before being sampled at 1 kHz.

the assumption of two dominant oscillation DoFs and negligible handle velocity, the actual energy contained in the ψ-oscillation is $E_\psi = E - E_\theta$.

Analysis of controller performance

To analyze the controller performance, we calculated the settling time T_s and the steady state error e. The settling time T_s is the time after which the energy E_θ stays within bounds $\pm\epsilon_\theta$ around the energetic steady state value $\bar{E}_\theta$. We chose the bounds $\epsilon_{\theta,\mathrm{RL-0}} = 16\%$ and $\epsilon_{\theta,\mathrm{RF-HL}} = 25\%$. The steady state error is defined as $e = E_\theta^\mathrm{d} - \bar{E}_\theta$.

Analysis of effort sharing

The energy flows of the human $\dot{E}_\mathrm{H}$ and the robot $\dot{E}_\mathrm{R}$ were calculated according to (5.27) based on the interaction point velocities and the measured applied forces. We analyzed the effort sharing between the robot and the human under condition RF-HL based on the energy share of the robot Γ_R

$$\Gamma_\mathrm{R} = \frac{\int_0^T \dot{E}_\mathrm{R} \mathrm{d}\tau}{\int_0^T \dot{E}_\mathrm{R} + \dot{E}_\mathrm{H} \mathrm{d}\tau}. \tag{5.31}$$

The effort share above is similar to the effort share defined for the virtual reality task in (5.29). However, we fixed the time at which the effort share is evaluated to $T = 17\,\mathrm{s}$ for comparability (vertical dash-dotted lines in Fig. 5.14).

Similarly, we adapted the energy efficiency measure of the virtual reality task in (5.30) to

$$\eta = \frac{|E_\theta^\mathrm{d} - E_\theta(t=0)|}{\int_0^T |\dot{E}_\mathrm{R}| + |\dot{E}_\mathrm{H}| \mathrm{d}\tau}, \tag{5.32}$$

where T was fixed within each experimental condition for comparability: $T_\mathrm{RL-0} = 25\,\mathrm{s}$ and $T_\mathrm{RF-HL} = 17\,\mathrm{s}$.

5.7.3 Experimental conditions and procedure

Experiments under multiple conditions were performed: v- or t-pendulum, with or without ψ-damping in case of the t-pendulum, interaction with a human or with one side of the object being fixed to the environment and different leader/follower role assignments. The following two pairs of t-pendulum experiments are presented in detail:

Robot leader and fixed end (RL-0)

The handle of agent A2 = 0 was fixed at distance C with respect to the robot A1 = R = $\mathcal{L}$. At the start of each trial, the cylindrical pendulum mass was released at a pose with significant disturbance oscillation $\psi(t=0) > 35\,\mathrm{deg}$, while the desired oscillation contained almost no energy $\theta(t=0) \approx 0\,\mathrm{deg}$. The desired energy level was set to $\theta_E^\mathrm{d} = 40\,\mathrm{deg}$.

Robot follower and human leader (RF-HL)

The trials started from rest $\theta(t=0) = \psi(t=0) \approx 0\,\mathrm{deg}$. The human interaction partner (agent $\mathrm{A2} = \mathrm{H} = \mathcal{L}$) was asked to inject energy into the pendulum such that a desired energy level of $\theta_E^{\mathrm{d}} = 40\,\mathrm{deg}$ was reached, to track the desired constant energy level and to release the t-pendulum energy again. The desired energy level was displayed to the human in form of horizontal lines to which the t-pendulum had to be aligned to at its turning points (Fig. 5.12). The robot supported the human leader as a follower $\mathrm{A1} = \mathrm{R} = \mathcal{F}$.

5.7.4 Results and Discussion

Robot leader and fixed end (RL-0)

The results of the RL-0 experiment are displayed in Fig. 5.13 with ψ-damping (1a-c) and without ψ-damping (2a-c).

Projection onto the abstract cart-pendulum: The experimental trials started with significant initial deflection of the disturbance oscillation $\psi(t=0)_{\psi\mathrm{on}} = 35.9\,\mathrm{deg}$ and $\psi(t=0)_{\psi\mathrm{off}} = 38.9\,\mathrm{deg}$, but close to zero θ-oscillation. This is in accordance with the complete system energy E and the energy contained in the θ-oscillation E_θ, with the difference being the energy contained in the ψ-oscillation. Due to initialization of the observer with the ψ-dominated initial force measurement, the estimates $\hat{\theta}_\theta^* \approx \theta_\theta^*$ and $\hat{E}_\theta$ were initially off. The estimate $\hat{E}_\theta$ approached the actual energy contained in the θ-oscillation E_θ at around 1 s. The estimated deflection angle $\hat{\theta}_\theta^* \approx \theta_\theta^*$ closely followed the actual deflection angle θ. The results show the practicability of the abstract cart-pendulum projection. The observers separate the nonlinearly coupled oscillation DoFs θ and ψ, and the abstract cart-pendulum based energies reflect the system energy.

Performance: The desired energy level E_θ^{d} was reached after settling times $T_{\mathrm{s},\psi\mathrm{on}} = 23.9\,\mathrm{s}$ and $T_{\mathrm{s},\psi\mathrm{off}} = 23.6\,\mathrm{s}$ (vertical dashed lines in Fig. 5.13) and tracked with steady state errors $e_{\psi\mathrm{on}} = -0.41\,\mathrm{mJ}$ and $e_{\psi\mathrm{off}} = -5.98\,\mathrm{mJ}$. With active ψ-damping, the disturbance angle reduced to $|\psi|_{\mathrm{max},\psi\mathrm{on}} = 7.2\,\mathrm{deg}$ within the first 7 s in contrast to $|\psi|_{\mathrm{max},\psi\mathrm{off}} = 16\,\mathrm{deg}$ without active ψ-damping. Close to the energetic steady state, the disturbance oscillation was kept within $|\psi|_{\mathrm{max},\psi\mathrm{on}} = 3.2\,\mathrm{deg}$ and $|\psi|_{\mathrm{max},\psi\mathrm{off}} = 7.2\,\mathrm{deg}$, respectively. The difference between active and inactive ψ-damping is visible in the energy contribution by the robot E_{R}. While the robot hardly influenced the system energy E during the first 6 s without active ψ-damping $E_{\mathrm{R},\psi\mathrm{off}} \approx 0\,\mathrm{J}$, the robot released energy from the ψ-oscillation with active ψ-damping $E_{\mathrm{R},\psi\mathrm{on,min}} = -0.586\,\mathrm{J}$. The controllers with and without ψ-damping achieved energy efficiency values of $\eta_{\psi\mathrm{on}} = 0.532$ and $\eta_{\psi\mathrm{off}} = 0.558$, respectively. The active ψ-damping led to a faster decrease of the disturbance oscillation and a smaller remaining disturbance oscillation. This observation confirms the practicability of the approximations made to allow the application of the cart-pendulum swing-up controller to other oscillation DoFs. With respect to controller performance as captured in settling time T_{s} and steady state error e, no significant difference was observable between the controllers with and without active ψ-damping[9]. Natural damping showed to be sufficient to keep the

---

[9] Note that the initial conditions varied slightly from experimental trial to trial, as the object was hold in the initial configuration by hand. Multiple trials yielded similar results.

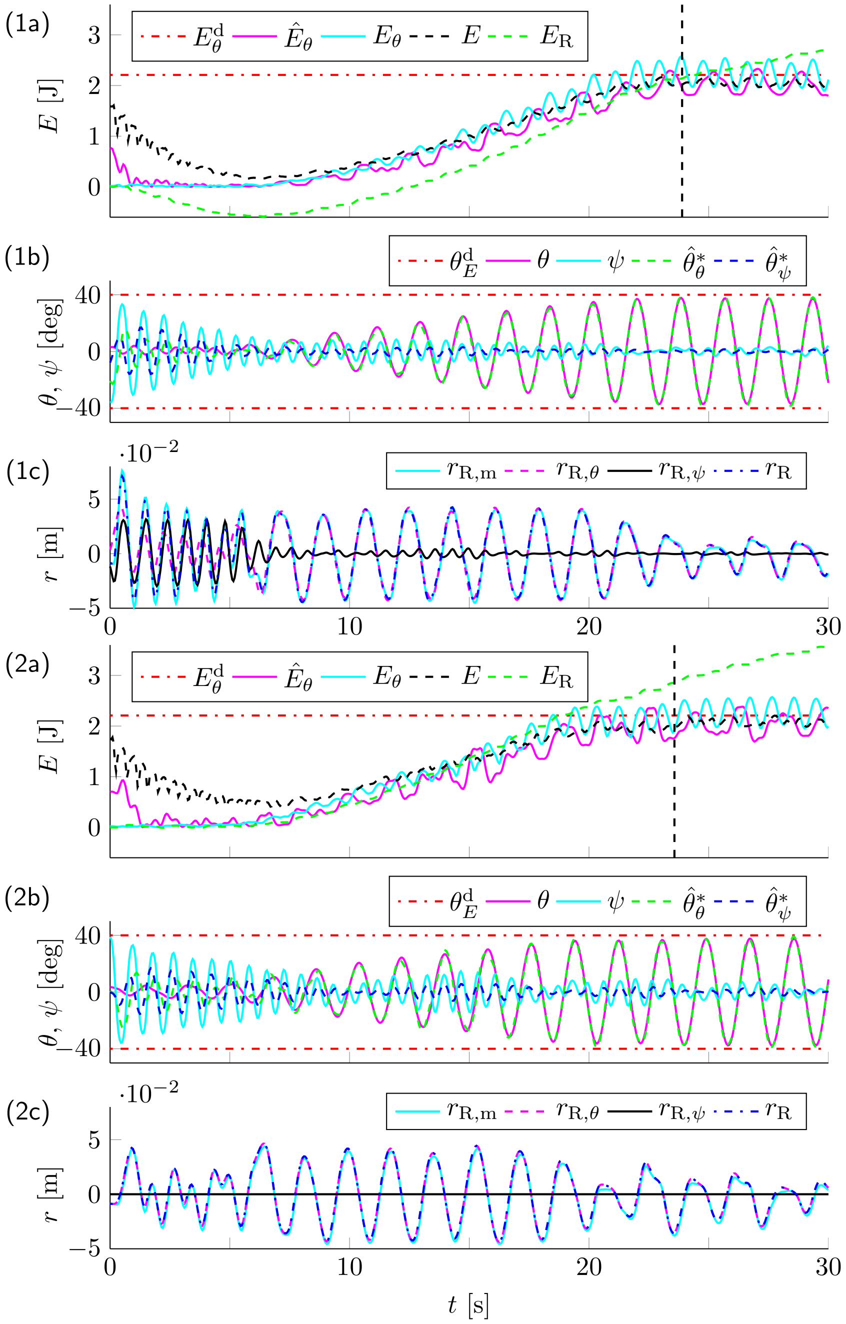

Fig. 5.13: Experimental results for RL-0 (1a-c) with ψ-damping and (2a-c) without ψ-damping: (a) desired E_θ^{d}, estimated $\hat{E}_\theta$ and actual E_θ energy contained in θ-oscillation, complete pendulum energy E, robot E_{R} energy input, (b) desired maximum θ_E^{d} deflection angle, extracted projected deflection angles θ_θ^* and θ_ψ^*, actual deflection angles θ and ψ, (c) actual robot trajectory $r_{\mathrm{R,m}}$ and commanded robot trajectory $r_{\mathrm{R}} = r_{\mathrm{R},\theta} + r_{\mathrm{R},\psi}$.

disturbance oscillation in relatively small bounds. This result is further supported by the observation that more energy E_{d} dissipated without ψ-damping: $E_{\mathrm{d},\psi\mathrm{off}} > E_{\mathrm{d},\psi\mathrm{on}}$ under conservation of energy $E = E_{\mathrm{R}} - E_{\mathrm{d}} + E(t=0)$, but with a lower ϵ_ψ for active ψ-damping.

Combination of θ-excitation and ψ-damping: A simple summation combines θ-excitation and ψ-damping to one control input. The actual robot trajectory $r_{\mathrm{R,m}}$ is a combination of θ-excitation at frequency ω_θ, ψ-damping at frequency ω_ψ (if active) and the influence of the joint impedance control of the robot. Even though the oscillation DoFs θ and ψ are nonlinearily coupled, simulations and experiments show that a separate control of the two oscillation DoFs is possible through simple addition. However, the effectiveness of our control approach depends on how similar the individual oscillations are to a simple pendulum oscillation. We conducted additional experiments to examine the limits of our controller with respect to θ_E^{d}. For high energies contained in the θ-oscillation $\theta_E > 60\,\mathrm{deg}$, the ψ-oscillation is less simple pendulum-like, the effectiveness of our active ψ-damping diminishes and active ψ-damping can even have a negative effect on the ψ-oscillation.

Robot follower and human leader (RF-HL)

Figure 5.14 displays results under experimental condition RF-HL with ψ-damping (1a-d) and without ψ-damping (2a-d).

Human interaction partner: The human partner started to inject energy into the t-pendulum at $t = 0\,\mathrm{s}$, which was initially at rest. At $t_{\psi\mathrm{on}} = 2.9\,\mathrm{s}$ and at $t_{\psi\mathrm{off}} = 2.1\,\mathrm{s}$, the estimated energy flow of the human exceeded the threshold $\hat{\dot{E}}_{\mathrm{H},\theta} > \delta_{\mathrm{u},\theta,\mathcal{F}}$ and the robot started to inject energy as well. The energetic steady state was reached after settling times $T_{\mathrm{s},\psi\mathrm{on}} = 11.6\,\mathrm{s}$ and $T_{\mathrm{s},\psi\mathrm{off}} = 4.4\,\mathrm{s}$ with steady state errors $e_{\psi\mathrm{on}} = 664\,\mathrm{mJ}$ and $e_{\psi\mathrm{off}} = -319\,\mathrm{mJ}$. The disturbance oscillation stayed within bounds of $|\psi|_{\mathrm{max},\psi\mathrm{on}} = 9\,\mathrm{deg}$ and $|\psi|_{\mathrm{max},\psi\mathrm{off}} = 7\,\mathrm{deg}$. The performance of the robot follower highly depends on the performance of the human leader. The human's precision was significantly lower compared to the one of the robot, also because the human could only estimate the pendulum energy at the turning points of the pendulum. This explains the higher steady state errors compared to the RL-0 experiments. Furthermore, the experimental results of different trials with a human interaction partner can differ significantly, as, e.g., reflected in the different steady state errors for the two trials presented. However, throughout all trials the performance values without active ψ-damping clearly outperformed the performance values with active ψ-damping in contrast to the RL-0 experiments. The feedback of the human interaction partner as well as the recorded data indicate that the active ψ-damping irritates the human interaction partner and, thus, impairs the human's performance. Without active ψ-damping the robot end effector only slightly oscillated due to the impedance control during the energetic steady state, whereas the robot constantly moved with active ψ-damping. The irritating effect of active ψ-damping is also reflected in a lower energy efficiency value of $\eta_{\psi\mathrm{on}} = 0.096$ compared to $\eta_{\psi\mathrm{off}} = 0.238$.

Effort sharing: The relative contribution of the robot with respect to the swing-up was $\gamma_{R,\psi\mathrm{on}} = 0.323$ and $\gamma_{R,\psi\mathrm{off}} = 0.295$. For both controllers, peaks were visible in the actual human energy flow $\dot{E}_{\mathrm{H}}$, which is in accordance with the observations made during human-human rigid object swinging [42]. The projection onto the abstract cart-pendulum as well as the filtering led to a delayed but smooth human energy flow estimate $\hat{\dot{E}}_{\mathrm{H},\theta}$. This estimate stayed within the follower thresholds during the energetic steady state. The energy release of the human was detected by the robot at $t_{\psi\mathrm{on}} = 27.3\,\mathrm{s}$ and $t_{\psi\mathrm{off}} = 21.0\,\mathrm{s}$

and the robot started to move to release energy from the system as well. However, the energy released by the robot was negligible compared to the energy released by the human. The correct detection of the human intention, i.e. goal directed energy injection and release, further supports the practicability of the abstract cart-pendulum projection. With and without active ψ-damping, the robot took over a significant share of the swing-up task effort. The low effort share of the robot during swing-down was due to natural damping which helped the human interaction partner to achieve especially fast energy release. Note that we adjusted the lower follower threshold $\delta_{\mathrm{l},\theta,\mathcal{F}}$ such that natural damping is not interpreted as energy release initiated by the human partner. In summary, we were able to achieve the control goal for the follower of identifying and imitating the energy flow of the leader as formulated in Problems 6 and 7.

Maximum energy content θ_E^{d}

We limited the desired energies to $\theta_E^{\mathrm{d}} = 40\,\mathrm{deg}$ for the RL-0 condition, because the fixed end caused increased ψ-oscillations for high θ_E[10], and for the RF-HL condition, in order to enable the human leader to sustain a steady state oscillation for comparability, which gets more difficult with higher θ_E. In order to find the limits of our controller, we performed additional experiments with a robot leader and a passive human, i.e. the human partner allowed his hand to passively move with the swinging pendulum. Our results show that the controller can reach $\theta_E^{\mathrm{d}} = 70\,\mathrm{deg}$. However, we had to restrict the amplitude factor to $\bar{a} = 0.12\,\mathrm{m}$ due to joint velocity limitations. As a consequence the controller saturated and was not able to reach the desired energy levels $\theta_E^{\mathrm{d}} = 80$ and $90\,\mathrm{deg}$. An energy content of $\theta_E^{\mathrm{d}} = 70\,\mathrm{deg}$ for our pendulum of $l^* = 0.77\,\mathrm{m}$ would, e.g., allow the object to reach a height $y_{\mathrm{o},E} = 0.47\,\mathrm{m}$ at a distance $x = 0.77\,\mathrm{m}$ from the pivot point after being released at $\theta = 60\,\mathrm{deg}$.

5.8 Conclusions

This chapter presented a control approach for two-agent collaborative swinging of complex pendulum-like objects. We realized robotic follower behavior through monitoring of the energy flow produced by the leading partner. This energy flow is solely estimated from the measured applied force. Experiments with a complex pendulum-like object showed that the robotic follower can take over a substantial share of the swing-up effort to a desired energy level, which is only known to the leading human partner. We compared the swing-up performance and effort sharing characteristics of mixed human and robot teams by means of a virtual reality study with a v-shaped pendulum. The results revealed that the robot leader as well as the robot follower show comparable performance to a human leader and a human follower.

By projecting the complex pendulum-like object onto an abstract cart-pendulum, desired and undesired oscillation DoFs can be separated. The energies of the individual oscillation DoFs were regulated through application of a cart-pendulum swing-up controller. Therefore, the effectiveness of the presented control approach depends on how

---

[10] This was also the case for HL-0.

simple pendulum-like the individual oscillations are. The simple pendulum-like desired oscillation DoF of the complex pendulum was excited such that a desired energy level is reached. The less simple pendulum-like undesired oscillation can be simultaneously damped for moderate energy levels of the desired oscillation through summation of two control inputs. The experiments did not reveal clear benefit of active disturbance damping, but natural damping seemed to be sufficient. Experiments with a human interaction partner indicated further that active disturbance damping irritates the human partner.

Open problems

The control approach presented in this chapter is based on known object parameters: excitation of the desired oscillation requires estimates of the projected length and object mass and active damping of the undesired oscillation requires an estimate of its natural frequency. Another shortcoming of the presented approach lies in the follower implementation based on three discrete energy flow levels, i.e. a neutral zone, negative energy flow and positive energy flow. The result is a number of tuning parameters, but still unflexible follower behavior. For instance, the conservative follower parametrization during the virtual reality experiments let to relatively low energy shares, while at the same time amplifying unsteady human leader energy flows and thus impeding tracking of higher energy levels. In the following chapter, we alleviate the assumption of known object parameters and present an adaptive approach for swinging of unknown complex pendulum-like objects. We furthermore refine the follower behavior to continuously contribute to the current energy flow by a desired energy share.

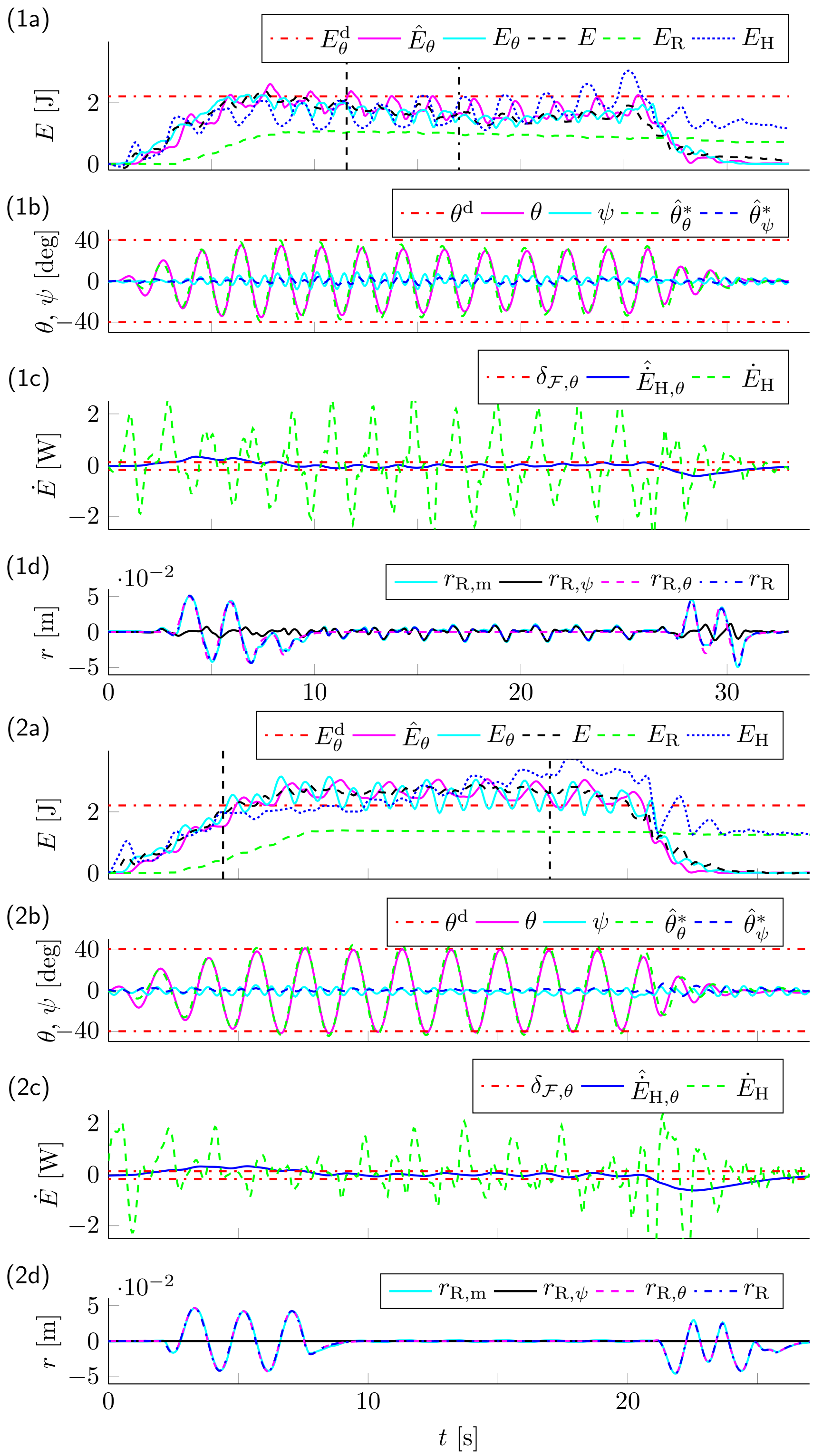

Fig. 5.14: Experimental results for RF-HL (1a-d) with ψ-damping and (2a-d) without ψ-damping: (a) Desired E_θ^{d}, estimated $\hat{E}_\theta$ and actual E_θ energy contained in θ-oscillation, complete pendulum energy E, robot E_{R} and human E_{H} energy input, (b) Desired maximum θ_E^{d} deflection angle, extracted projected deflection angles θ_θ^* and θ_ψ^*, actual deflection angles θ and ψ, (c) follower thresholds $\delta_{\mathrm{u/l},\theta,\mathcal{F}}$, estimated $\hat{\dot{E}}_{\mathrm{H},\theta}$ and actual $\dot{E}_{\mathrm{H}}$ human energy flow, (d) actual robot trajectory $r_{\mathrm{R,m}}$ and commanded robot trajectory $r_{\mathrm{R}} = r_{\mathrm{R},\theta} + r_{\mathrm{R},\psi}$.

6 Adaptive energy control for collaborative swinging of unknown complex pendulum-like objects

Summary. *This chapter extends the collaborative swing-energy control of Chapter 5 which required known object parameters to the control of unknown complex pendulum-like objects. The chapter demonstrates*

- *identification of the underlying fundamental dynamics of the desired simple pendulum-like oscillation*
- *fundamental dynamics-based*
    - *natural frequency estimation*
    - *reference dynamics tracking by a leader controller*
    - *continuous energy flow imitation of a follower controller*
- *controller verification in simulation and real world experiments*

The results of this chapter were partly published in [39, 40, 44]. The student works [27, 118] contributed to this chapter.

6.1 Motivation

In this thesis, we investigate joint energy injection into flexible objects (see Fig. 6.1(b)) as a first step towards collaborative dynamic object manipulation. We approached the task of flexible object swinging by first investigating its extreme ends: swinging of rigid objects in Chapter 4 (see Fig. 6.1(a)) and swinging of pendulum-like objects in Chapter 5 (see Fig. 6.1(c)). In both previous chapters, the energy contained in the objects was explicitly evaluated. Thus, the control approaches were based on the assumption of known object parameters, e.g., object mass and projected length. As the final goal is collaborative energy injection into unknown flexible objects which are difficult to model, we need adaptive approaches which ideally do not require any prior knowledge on object parameters. In this chapter, we take a step back and alleviate the assumption of known object parameters for pendulum-like objects by an adaptive approach.

6.2 Related work

Chapters 4 and 5 presented related work with respect to human motion modeling, role allocation, simple pendulum approximations and their control. In the following, we discuss related work in the context of adaptive control for periodic motion.

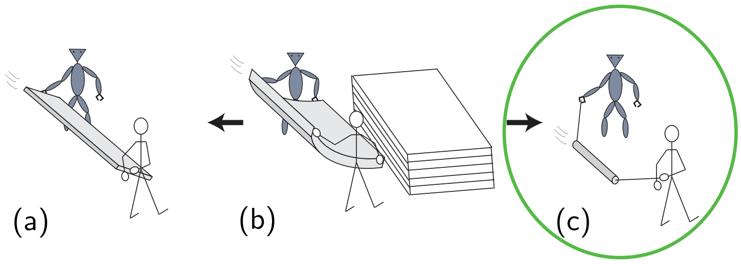

Fig. 6.1: Dynamic manipulation scenario: Collaborative energy injection into a sports mat to lift it onto a stack of mattresses (b). Interpretation of flexible object swinging (b) as a combination of rigid object swinging (a) and pendulum-like object swinging (c). This chapter presents controller synthesis for swinging of unknown complex pendulum-like objects (c).

Adaptive control for periodic motions

Wood sawing with a two-person cross-cut saw is investigated as a challenging physical human-robot collaboration task in [143]. The collaborative sawing task in [143] is achieved via learning of individual dynamic movement primitives for motion and stiffness control with a human tutor in the loop. Frequency and phase are extracted online by adaptive frequency oscillators [145].

The applicability of learning methods as learning from demonstration [8] or reinforcement learning [45] to nonlinear dynamics is frequently evaluated based on inverted pendulum tasks. In [138], we applied least square policy iteration (LSPI), a type of reinforcement learning algorithm, to the pendulum swing-up task. The temporal difference algorithm (TD-algorithm) was developed by [169]. Policy iteration iteratively evaluates and improves control policies. Least square policy iteration has been successfully implemented to balance an inverted pendulum and riding a bicycle [18], [106]. In [137], least square policy iteration was used for suspended load trajectory tracking and in [59] value iteration was applied to load swing damping in suspended load transport using a small quadrotor. The main short comings of the proposed reinforcement learning-based controller in [138] are its limitation to leader behavior only and the high number of tuning parameters. Besides a high number of tuning parameters, reinforcement learning also often suffers from the need of long interactions with the real system or at least with a sufficiently well modeled system in simulation [133]. Only recently, Deisenroth *et al.* showed how Gaussian processes allow for faster autonomous reinforcement learning with few parameters in [33].

In this work, we apply model knowledge of the swinging task to design adaptive controllers with few tuning parameters for swinging of unknown complex pendulum-like objects, without the need of a learning phase. As in Chapter 5, we make use of the t-pendulum abstraction with one-dimensional acceleration inputs to approximate two-agent swinging of complex pendulum-like objects (see Fig. 6.2(d)). Furthermore, we approximate the desired oscillation by a simple pendulum with acceleration actuation, which we refer to as the abstract cart-pendulum (see Fig. 6.2(e)). In contrast to Chapter 5, we do not apply a swing-up controller based on explicit energy evaluations, but we identify the underlying fundamental dynamics of the desired simple pendulum-like oscillation. The extracted *fun-*

damental dynamics is linear and describes the phase and energy dynamics of the abstract cart-pendulum (see Fig. 6.2(f)). This additional approximation step allows for online frequency estimation (see Fig. 6.2(g)), controlled energy injection and effort sharing among the agents (see Fig. 6.2(h)). We present leader and follower controllers which only require few parameters of distinct physical meaning.

Chapter overview

We structure the remainder of this chapter along Fig. 6.2 and Fig. 6.3. Individual variables will be introduced in subsequent sections.

Figure 6.2 illustrates the approximation steps taken that lead from the extreme of human-robot pendulum-like object swinging (Fig. 6.2(b)) to the fundamental dynamics-based controllers (Fig. 6.2(h)). The implementation with input and output variables is visualized by the block diagram in Fig. 6.3. The main assumption is a simple pendulum-like desired oscillation. As in Chapter 5, we extract the desired oscillation and control its energy content by projecting the complex t-pendulum onto the abstract cart-pendulum (step 3 in Fig. 6.2). The *projection and energy-based controller* block in Fig. 6.3 implements step 3 in Fig. 6.2. The extracted fundamental dynamics states are then fed to the *fundamental dynamics-based controller* block, which estimates the natural frequency (Fig. 6.2(g)) and realizes leader or follower behavior (Fig. 6.2(h)). The resultant control inputs are converted to end effector motion within the *projection and energy-based controller* block. The blocks will be detailed in the respective sections as indicated in Fig. 6.3. Again, the only sensor measurements the proposed robot controllers receive are the forces applied at the robot interaction point.

In Section 6.3, we give the problem formulation. This is followed by the fundamental dynamics derivations of the abstract cart-pendulum in Section 6.4. The adaptive leader and follower controllers are introduced and analyzed with respect to the fundamental dynamics in Section 6.5. In Section 6.6, we apply the fundamental dynamics-based controllers to the control of the two-agent t-pendulum. We evaluate our controllers in simulation and experiments with a human interaction partner in Section 6.7 and Section 6.8, respectively. Section 6.9 concludes the chapter and discusses open problems.

6.3 Problem formulation

In this section, we recapitulate relevant variables and parameters of the t-pendulum, which was first introduced in Chapter 5. Thereafter, we formally state our problem.

6.3.1 The t-pendulum

Figure 6.4 shows the t-pendulum of state $\boldsymbol{x}_{\mathrm{tP}} = \begin{bmatrix}\theta & \psi & \dot{\theta} & \dot{\psi} & \boldsymbol{r}_1 & \dot{\boldsymbol{r}}_1 & \boldsymbol{r}_2 & \dot{\boldsymbol{r}}_2\end{bmatrix}^\top$ with desired oscillation DoF θ and major undesired oscillation DoF ψ. The controllable input is the handle acceleration of the robot A1=R along the x-axis $u_1 = \ddot{r}_1$. The forces applied at the own handle are the only measurable quantity of agent A1, i.e. measurable output $\boldsymbol{y}_{\mathrm{m},1} = \boldsymbol{f}_1$.

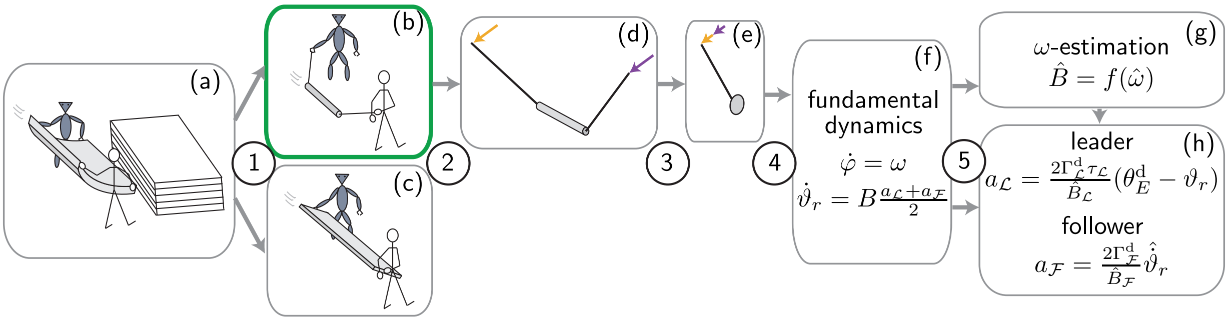

Fig. 6.2: Approach overview: (1) Interpretation of flexible object swinging as a combination of pendulum swinging and rigid object swinging. (2) Approximation of pendulum swinging by the t-pendulum with 1D acceleration inputs. (3) Projection of the t-pendulum onto the abstract cart-pendulum. (4) Extraction of the closed-loop fundamental dynamics. (5) Fundamental dynamics-based natural frequency estimation and leader and follower controller design.

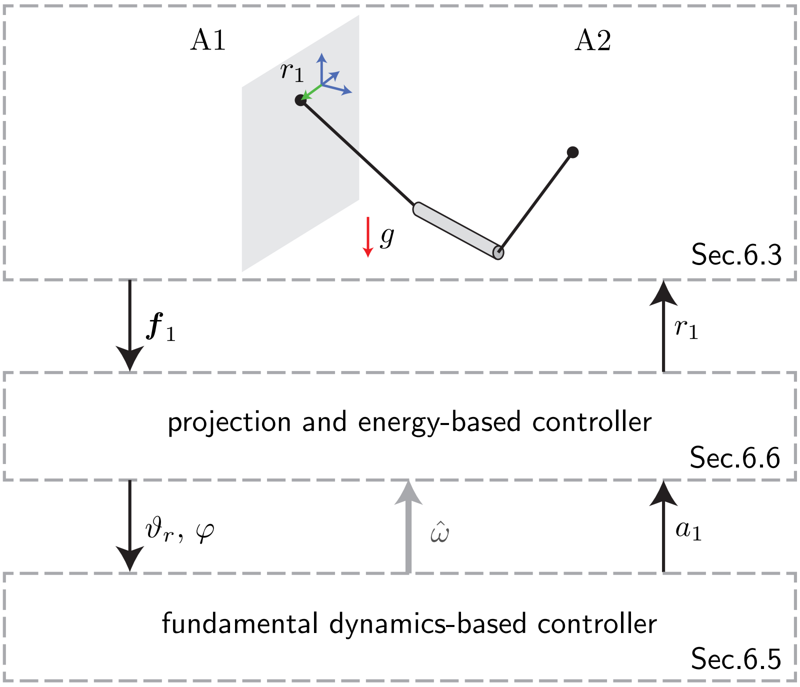

Fig. 6.3: Implementation overview block diagram.

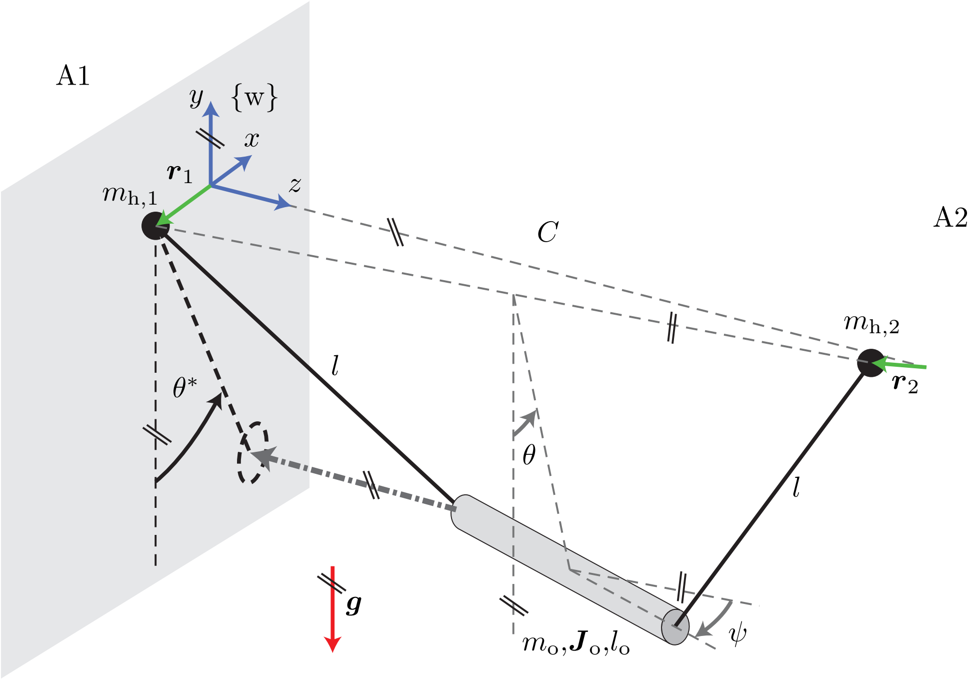

Fig. 6.4: The t-pendulum: Cylindrical object of mass m_{o}, length l_{o} and moment of inertia $\boldsymbol{J}_{\mathrm{o}}$ under the influence of gravity $\boldsymbol{g} = [0 \quad -g \quad 0]^{\top}$ attached via massless ropes of length l to two handles of mass $m_{\mathrm{h},i}$ located at $\boldsymbol{r}_i$ with $i = 1, 2$. The location $\boldsymbol{r}_1$ is defined with respect to the world fixed coordinate system $\{\mathrm{w}\}$. The location $\boldsymbol{r}_2$ is defined with respect to the fixed point $\boldsymbol{p} = [0,\ 0,\ C]^{\top}$ in $\{\mathrm{w}\}$, where C is the initial distance between the two agents. Pairs of parallel lines at the same angle indicate parallelity

.

6.3.2 Problem statement

As in Chapter 5, the objective is to reach the desired periodic orbit $\mathcal{O}(\boldsymbol{x}_{\mathrm{tP}})$ in (5.2), which is represented by a desired energy level of the θ-oscillation $E_\theta = E_\theta^{\mathrm{d}}$ and zero energy contained in the undesired oscillation $E_\psi = E_\psi^{\mathrm{d}} = 0$. Energies E_θ, E_ψ can be equivalently expressed by maximum deflection angles θ_E, ψ_E (see Definition 3). In contrast to the energy E_θ, which also depends on mass and inertia of the object, the amplitude θ_E only depends on the small angle approximation of the natural frequency $\omega_{0,\theta}$. Therefore, we rewrite the periodic orbit of Chapter 5 as

$$\mathcal{O}(\boldsymbol{x}_{\mathrm{tP}}) : \begin{cases} \theta_E = \theta_E^{\mathrm{d}}, \\ \psi_E = \psi_E^{\mathrm{d}} = 0, \\ \boldsymbol{r}_i = \dot{\boldsymbol{r}}_i = \boldsymbol{0} \text{ with } i = 1, 2. \end{cases} \tag{6.1}$$

Again, we differentiate between leader and follower agents. For a *leader* A1 $= \mathcal{L}$ the control law $u_{\mathcal{L}}$ is a function of the measurable output $\boldsymbol{y}_{\mathrm{m},\mathcal{L}}$ and the desired energies $\theta_E^{\mathrm{d}}, \psi_E^{\mathrm{d}}$.

Problem 8 (Leader $\mathcal{L}$)**.** *Find a control law $u_{\mathcal{L}}$ as a function of the measurable output and the desired object energies*

$$u_{\mathcal{L}} = t_{\mathrm{s},\mathcal{L}} = f(\boldsymbol{y}_{\mathrm{m},\mathcal{L}}, \theta_E^{\mathrm{d}}, \psi_E^{\mathrm{d}} = 0)$$

such that

$$\left|\theta_E^{\text{ref}} - \theta_E\right| \le \epsilon_\theta \textit{ with } \dot{\theta}_E^{\text{ref}} = \tau_{\mathcal{L}}(\theta_E^{\text{d}} - \theta_E^{\text{ref}}),$$

and

$$\left|\psi_E(t > T_{\text{s}})\right| \le \epsilon_\psi, \text{ for } 0 < T_{\text{s}} < \infty.$$

Hence, the energy of the θ-oscillation should follow first-order reference dynamics θ_E^{ref} within bounds ϵ_θ. The reference dynamics is of inverse time constant $\tau_{\mathcal{L}}$ and converges to the desired energy θ_E^{d}. Furthermore, the energy contained in the ψ-oscillation should stay within $\pm\epsilon_\psi$ after the settling time T_{s}.

A *follower* A1 $= \mathcal{F}$ does not know the desired energy level θ_E^{d}. We define a desired energy share for the follower $\Gamma_{\mathcal{F}}^{\text{d}} \in [0,\ 1)$ similar to the energy share measure (5.31), but in terms of the energy flow equivalents of the leader $\dot{\theta}_{E,\mathcal{L}}$ and the follower $\dot{\theta}_{E,\mathcal{F}}$

$$\Gamma_{\mathcal{F}} = \frac{\int_0^{T_{\text{s}}} \dot{\theta}_{E,\mathcal{F}} \mathrm{d}\tau}{\int_0^{T_{\text{s}}} (\dot{\theta}_{E,\mathcal{F}} + \dot{\theta}_{E,\mathcal{L}}) \mathrm{d}\tau}. \tag{6.2}$$

Our goal is to split the energy effort among the leader and the follower such that the follower has contributed the fraction $\Gamma_{\mathcal{F}}^{\text{d}}$ within bounds $\epsilon_{\mathcal{F}}$ at the settling time T_{s}. The energy of the undesired oscillation ψ_E should be kept within $\pm\epsilon_\psi$.

Problem 9 (Follower $\mathcal{F}$)**.** *Find a control law $u_{\mathcal{F}}$ as a function of the measurable output and zero energy contained in the undesired oscillation*

$$u_{\mathcal{F}} = f(\boldsymbol{y}_{\text{m},\mathcal{F}}, \psi_E^{\text{d}} = 0)$$

such that

$$\left|\Gamma_{\mathcal{F}}^{\text{d}} - \Gamma_{\mathcal{F}}\right| \le \epsilon_{\mathcal{F}}$$

and

$$\left|\psi_E(t > T_{\text{s}})\right| \le \epsilon_\psi, \text{ for } 0 < T_{\text{s}} < \infty.$$

6.4 Fundamental dynamics of the abstract cart-pendulum

In this section, we derive the fundamental dynamics of the abstract cart-pendulum, which represents the desired system dynamics of the t-pendulum (see Fig. 6.2(d)-(e)). We first recapitulate the state space description of the abstract cart-pendulum, which was first introduced in Chapter 5. The fundamental dynamics then results from a state transformation, insertion of the energy-based controller and approximations.

6.4.1 The abstract cart-pendulum

For the ideal case of $\psi_E = 0$ and agents that move along the x-direction in synchrony $r_1 = r_2$, the desired deflection angle θ is equal to the projected deflection angle θ^* (projection indicated by the dashed arrow in Fig. 6.4) and the t-pendulum behaves as a cart-pendulum with two-sided actuation (see Fig. 6.2(e))

$$\dot{\boldsymbol{x}}_{\text{c}} = \begin{bmatrix} \dot{\vartheta} \\ -\omega_0^2 \sin\vartheta \end{bmatrix} + \begin{bmatrix} 0 \\ -\frac{1}{g}\omega_0^2 \cos\vartheta \end{bmatrix} \frac{\ddot{r}_1 + \ddot{r}_2}{2}, \tag{6.3}$$

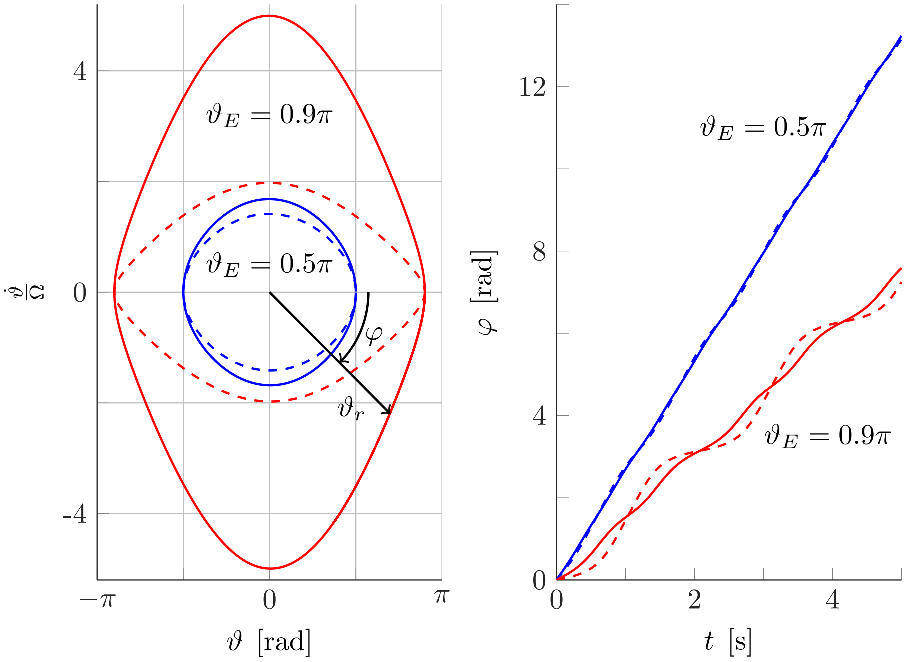

Fig. 6.5: Phase portrait (left) and phase angle φ over time (right) at constant energy levels $\vartheta_E = 0.5\pi$ (blue) and $\vartheta_E = 0.9\pi$ (red) of a lossless simple pendulum: Normalization with $\Omega = \omega_{\mathrm{g}}$ marked via solid lines and $\Omega = \omega_0$ via dashed lines. For energies up to $\vartheta_E = 0.5\pi$ and a normalization with $\Omega = \omega_{\mathrm{g}}$, the phase space is approximately a circle with radius $\vartheta_r \approx \vartheta_E$ and the phase angle φ rises approximately linear over time. The simple pendulum state can be equivalently expressed in cartesian states $\boldsymbol{x}_{\mathrm{c}} = [\vartheta,\ \dot{\vartheta}]^\top$ or polar states $\boldsymbol{x}_{\mathrm{p}} = [\varphi,\ \vartheta_r]^\top$.

with reduced state $\boldsymbol{x}_{\mathrm{c}} = [\vartheta,\ \dot{\vartheta}]^\top$ consisting of deflection angle ϑ and angular velocity $\dot{\vartheta}$ and the small angle approximation of the natural frequency $\omega_0 = \frac{m_\vartheta c_\vartheta g}{j_\vartheta}$. Here, we drop the subscript of the abstract cart-pendulum state $\dot{\boldsymbol{x}}_{\mathrm{acP}}$ for simplicity and replace it by the subscript c for cartesian states in contrast to p for polar states, which will be introduced in Section 6.4.2. In the following the natural frequency ω, its approximations and the phase angle φ relate to the desired oscillation ϑ/θ and we drop oscillation subscripts for simplicity.

6.4.2 Cartesian to polar state transformation

As discussed in the previous chapters, the abstract cart-pendulum dynamics in (6.3) is nonlinear with respect to the states $\boldsymbol{x}_{\mathrm{c}} = [\vartheta,\ \dot{\vartheta}]^\top$. Figure 6.5 shows a visualization of the nonlinearities in form of a phase portrait (left) and the phase angle φ over time t on the right. As in the previous chapters, the phase angle is computed according to

$$\varphi = \operatorname{atan2}\left(-\frac{\dot{\vartheta}}{\Omega}, \vartheta\right), \tag{6.4}$$

with normalization factor Ω. The angle ϑ and angular velocity $\dot{\vartheta}$ represent the cartesian coordinates in the phase space (see left side of Fig. 6.5). We expect the system energy ϑ_E

to ideally be independent of the phase angle φ, which motivates a state transformation to φ and ϑ_E for simple adaptive control design. Solving (6.4) for $\dot{\vartheta}$ and insertion into the relationship $\vartheta_E(\vartheta, \dot{\vartheta})$ in (4.6) yields

$$\cos\vartheta_E = \cos\vartheta - \frac{\Omega^2}{2\omega_0^2}\tan^2(\varphi)\,\vartheta^2. \tag{6.5}$$

However, there is no analytic solution for $\vartheta(\vartheta_E, \varphi)$ from (6.5). Therefore, we approximate the system energy ϑ_E through the phase space radius ϑ_r

$$\vartheta_r := \sqrt{\vartheta^2 + \left(\frac{\dot{\vartheta}}{\Omega}\right)^2}. \tag{6.6}$$

From Fig. 6.5 we see that the phase space radius is equal to the energy $\vartheta_r = \vartheta_E$ at the turning points ($\dot{\vartheta} = 0$). For our region of interest $\vartheta_E \leq \frac{\pi}{2}$ and a normalization with $\Omega = \omega_\mathrm{g}$, the phase space is almost circular and thus $\vartheta_r \approx \vartheta_E$ also for $\dot{\vartheta} \neq 0$. Furthermore, the phase angle rises approximately linearly

$$\varphi(t) \approx \omega t + \varphi(t = 0). \tag{6.7}$$

The difference between ϑ_r and ϑ_E leads to higher order oscillations in ϑ_r for constant energy levels $\vartheta_E = \text{const.}$ with increasing amplitude for increasing system energy ϑ_E.

The phase angle φ and the phase space radius ϑ_r span the polar state space $\boldsymbol{x}_\mathrm{p} = [\varphi,\ \vartheta_r]^\top$, which we mark with the subscript p. The cartesian states $\boldsymbol{x}_\mathrm{c}$ written as a function of the polar states $\boldsymbol{x}_\mathrm{p}$ are

$$\begin{aligned} \vartheta &= \vartheta_r \cos\varphi \\ \dot{\vartheta} &= -\vartheta_r \Omega \sin\varphi. \end{aligned} \tag{6.8}$$

6.4.3 Extraction of the fundamental dynamics

We actuate the abstract cart-pendulum via the same energy-based control law by [188] as in Chapter 5

$$\ddot{r}_i = a_i\,\omega^2 \sin\varphi, \tag{6.9}$$

where the amplitude factor a_i regulates the sign and amount of energy flow contributed by agent Ai to the abstract cart-pendulum, with $i = 1, 2$. A well-timed energy injection is achieved through multiplication with $\sin\varphi$, which according to (6.7) excites the pendulum at its natural frequency (see right side of Fig. 6.5).

Theorem 4. *The* fundamental dynamics *of the abstract cart-pendulum in* (6.3) *under application of the control law* (6.9) *can be written in terms of the polar states* $\boldsymbol{x}_\mathrm{p} = [\varphi,\ \vartheta_r]^\top$ *as*

$$\dot{\boldsymbol{x}}_\mathrm{p} = \begin{bmatrix} \dot{\varphi} \\ \dot{\vartheta}_r \end{bmatrix} = \begin{bmatrix} \omega \\ 0 \end{bmatrix} + \begin{bmatrix} 0 \\ B \end{bmatrix} \frac{a_1 + a_2}{2}, \tag{6.10}$$

with system parameter

$$B = \frac{1}{2g}\omega^3 \tag{6.11}$$

when neglecting higher harmonics, applying 3rd order Taylor approximations and making use of the geometric mean approximation of the natural frequency ω_g *in* (4.9)*.*

Proof. Application of the following three steps yields the dynamics of the abstract cart-pendulum (6.3) in terms of the polar states $\boldsymbol{x}_\mathrm{p}$:

S1 Differentiation of (6.4) and (6.6) with respect to time

S2 Insertion of the cartesian state dynamics (6.3)

S3 Substitution of remaining cartesian states through polar states (6.8)

$$\begin{aligned}
\dot{\varphi} &\overset{\text{S1}}{=} \frac{\Omega\dot{\vartheta}^2 - \Omega\vartheta\ddot{\vartheta}}{\Omega^2\vartheta^2 + \dot{\vartheta}^2} \\
&\overset{\text{S2}}{=} \frac{\Omega\dot{\vartheta}^2 + \Omega\omega_0^2\vartheta\sin\vartheta - \Omega\vartheta A}{\Omega^2\vartheta^2 + \dot{\vartheta}^2} \\
&\overset{\text{S3}}{=} \Omega\sin^2\varphi + \frac{\omega_0^2}{\Omega\vartheta_r}\cos\varphi\sin(\vartheta_r\cos\varphi) - \frac{1}{\Omega\vartheta_r}\cos\varphi A,
\end{aligned} \tag{6.12}$$

$$\begin{aligned}
\dot{\vartheta}_r &\overset{\text{S1}}{=} \frac{\Omega^2\vartheta\dot{\vartheta} + \dot{\vartheta}\ddot{\vartheta}}{\Omega\sqrt{\Omega^2\vartheta^2 + \dot{\vartheta}^2}} \\
&\overset{\text{S2}}{=} \frac{\Omega^2\vartheta\dot{\vartheta} - \omega_0^2\dot{\vartheta}\sin\vartheta + \dot{\vartheta}A}{\Omega\sqrt{\Omega^2\vartheta^2 + \dot{\vartheta}^2}} \\
&\overset{\text{S3}}{=} -\Omega\vartheta_r\sin\varphi\cos\varphi + \frac{\omega_0^2}{\Omega}\sin\varphi\sin(\vartheta_r\cos\varphi) \\
&\quad -\frac{1}{\Omega}\sin\varphi A,
\end{aligned} \tag{6.13}$$

with actuation term

$$A \overset{\text{S3}}{=} -\frac{\omega_0^2}{g}\cos(\vartheta_r\cos\varphi)\frac{\ddot{r}_1 + \ddot{r}_2}{2}. \tag{6.14}$$

The resultant state space representations are control affine and coupled

$$\dot{\boldsymbol{x}}_\mathrm{p} = \boldsymbol{f}_\mathrm{p}(\boldsymbol{x}_\mathrm{p}) + \boldsymbol{g}_\mathrm{p}(\boldsymbol{x}_\mathrm{p})u, \tag{6.15}$$

with control input $u := A$.

Insertion of the control law (6.9) into A in (6.15) yields the state space representation with new inputs a_1 and a_2 of the form

$$\dot{\boldsymbol{x}}_\mathrm{p} = \boldsymbol{f}_\mathrm{p}(\boldsymbol{x}_\mathrm{p}) + {}^{a}\boldsymbol{g}_\mathrm{p}(\boldsymbol{x}_\mathrm{p})\frac{a_1 + a_2}{2}. \tag{6.16}$$

Application of the following two consecutive steps to the state space representation (6.16) yields the fundamental dynamics (6.10):

- S4 Approximations through 3rd order Taylor polynomials, e.g. $\sin(\vartheta_r \cos\varphi) \approx \vartheta_r \cos\varphi - \frac{\vartheta_r^3 \cos^3\varphi}{6}$
- S5 Neglect of higher harmonics, e.g. $\cos^4\varphi = \frac{3}{8} + \frac{\cos 2\varphi}{2} + \frac{\cos 4\varphi}{8} \approx \frac{3}{8}$

Use of the actual natural frequency for normalization of the phase space $\Omega = \omega$ reduces the error caused by the approximations $\vartheta_E \approx \vartheta_r$.

Phase dynamics

$$\begin{aligned}
f_{\mathrm{p},1} &\overset{\Omega=\omega}{=} \omega \sin^2\varphi + \frac{\omega_0^2}{\omega\vartheta_r}\cos\varphi \sin(\vartheta_r\cos\varphi) \\
&\overset{\text{S4,S5}}{\approx} \frac{1}{2}\omega + \frac{1}{2}\frac{\omega_0^2}{\omega}\left(1 - \frac{1}{2}\left(\frac{\vartheta_r}{2}\right)^2\right) \\
&\overset{\text{S4}^{-1}}{\approx} \frac{1}{2}\omega + \frac{1}{2}\frac{\omega_0^2}{\omega}\left(\cos\left(\frac{\vartheta_r}{2}\right)\right) \\
&\overset{\omega_g(4.9)}{\approx} \omega, \qquad (6.17)
\end{aligned}$$

with “S4^{-1}” indicating application of the 3rd order Taylor approximation in reverse direction and insertion of the geometric mean approximation (4.9) with $\vartheta_E \approx \vartheta_r$ in the last step. For ${}^a g_{\mathrm{p},1}$, the approximation steps S4 and S5 yield ${}^a g_{\mathrm{p},1} \approx 0$. Consequently, the phase dynamics for the abstract cart-pendulum results in $\dot\varphi \approx \omega$, as expected.

Energy dynamics

Similar to ${}^a g_{\mathrm{p},1}$, the approximation steps S4 and S5 result in $f_{\mathrm{p},2} \approx 0$. The remaining term ${}^a g_{\mathrm{p},2}$ simplifies for the abstract cart-pendulum to

$$\begin{aligned}
{}^a g_{\mathrm{p},2} &\overset{\Omega=\omega}{=} \frac{\omega_0^2}{g\omega}\sin^2\varphi \cos(\vartheta_r\cos\varphi) \\
&\overset{\text{S4,S5}}{\approx} \frac{1}{2g}\omega\omega_0^2\left(1 - \frac{1}{2}\left(\frac{\vartheta_r}{2}\right)^2\right) \\
&\overset{\text{S4}^{-1}}{\approx} \frac{1}{2g}\omega\omega_0^2\left(\cos\left(\frac{\vartheta_r}{2}\right)\right) \\
&\overset{\omega_g(4.9)}{\approx} \frac{1}{2g}\omega^3 =: B. \qquad (6.18)
\end{aligned}$$

As for (6.17), we applied a reverse 3rd order Taylor approximation (S4^{-1}) and inserted the geometric mean approximation of the natural frequency ω in (4.9).

Thus, the fundamental energy dynamics linearly depends on the amplitude factors $\dot\vartheta_r \approx B\frac{a_1+a_2}{2}$. The result are the fundamental dynamics in (6.10). □

According to the fundamental dynamics, the phase φ is approximately time-linear $\dot\varphi \approx \omega$ and the influence of the actuation a_1 and a_2 on the phase is small. The energy flow $\dot\vartheta_E \approx \dot\vartheta_r$ is approximately equal to the mean of the amplitude factors a_1 and a_2 times a system dependent factor B, and thus zero for no actuation $a_1 = a_2 = 0$.

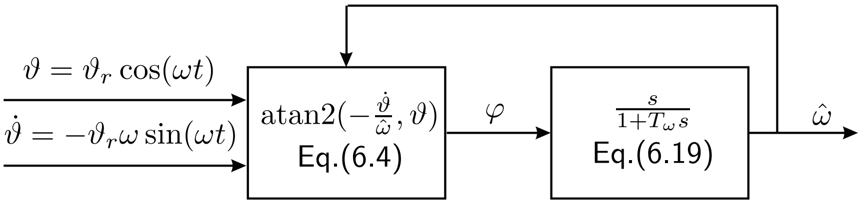

Fig. 6.6: Block diagram of the ω-estimation with normalization factor $\Omega = \hat{\omega}$ used for the computation of phase angle φ.

6.5 Fundamental dynamics-based adaptive leader/follower structures

In this section, we use the fundamental dynamics to design adaptive controllers that render leader and follower behavior according to Problems 8 and 9. For the abstract cart-pendulum fundamental dynamics, the natural frequency ω is the only unknown system parameter. An ω-estimate is not only needed for the computation of the system parameter B, but also for the computation of the phase angle φ, required for the control law (6.9). Here, we first present the natural frequency estimation. In a second step, we design the amplitude factor a_1 to render either leader or follower behavior.

6.5.1 Natural frequency estimation

Based on the fundamental phase dynamics $\dot{\varphi} = \omega$, we design simple estimation dynamics for the natural frequency estimate $\hat{\omega}$

$$\hat{\omega} = \frac{s}{1 + T_\omega s}\varphi, \tag{6.19}$$

which differentiates φ, while also applying a first-order low-pass filter with cut-off frequency $\frac{1}{T_\omega}$. Figure 6.6 shows how the ω-estimation is embedded into the energy-based controller. The feedback of the estimate $\hat{\omega}$ for the computation of the phase angle φ requires a stability analysis.

Proposition 3. *The natural frequency estimate $\hat{\omega}$ converges to the true natural frequency ω when estimated according to Fig. 6.6, the system behaves according to the fundamental dynamics* (6.10)*, the natural frequency ω is constant (changes only slowly w.r.t. the $\hat{\omega}$-dynamics in* (6.19)*) and if*

$$T_\omega > \frac{1}{2\hat{\omega}}. \tag{6.20}$$

Proof. Setting $\varphi(t = 0) = 0$ in (6.7) without loss of generality, we have $\varphi(t) = \omega t$ for an approximately constant natural frequency ω. This yields the modified state transformations $\vartheta = \vartheta_r \cos(\omega t)$ and $\dot{\vartheta} = -\vartheta_r \omega \sin(\omega t)$ compared to (6.8), and the phase computation results in

$$\varphi = \mathrm{atan2}\left(-\frac{\dot{\vartheta}}{\hat{\omega}}, \vartheta\right) = \mathrm{atan2}\left(-\frac{\omega}{\hat{\omega}}\sin(\omega t), \cos(\omega t)\right), \tag{6.21}$$

which is independent of ϑ_r. Consequently, the natural frequency estimation in Fig. 6.6 has one input, the natural frequency ω, and one output, the estimate $\hat{\omega}$. Note that we assume ω to be known only for the stability analysis, but not for the implementation displayed in Fig. 6.6.

In a next step, we derive the estimation dynamics in terms of its input ω and output $\hat{\omega}$. Differentiation of (6.21) with respect to time yields

$$\dot{\varphi} \quad = \quad \frac{\omega \left(\tan(\omega t) \left(-\frac{1}{\hat{\omega}^2} \right) \dot{\hat{\omega}} + \frac{1+\tan^2(\omega t)}{\hat{\omega}} \omega \right)}{1 + \left(\frac{\omega}{\hat{\omega}} \tan(\omega t) \right)^2}. \tag{6.22}$$

Transformation of (6.19) into time domain results in

$$\dot{\hat{\omega}} = -\frac{1}{T_\omega} (\hat{\omega} - \dot{\varphi}). \tag{6.23}$$

Insertion of (6.23) into the time derivative of the phase angle φ in (6.22), followed by some rearrangements yields the ω-estimation dynamics

$$\dot{\hat{\omega}} \quad = \quad \frac{\hat{\omega}\omega^2 - \hat{\omega}^3}{T_\omega \hat{\omega}^2 + T_\omega \omega^2 \tan^2(\omega t) - \omega \tan(\omega t)}. \tag{6.24}$$

Because ω is bounded and constant, it suffices to show stability of the estimation error dynamics $\dot{\tilde{\omega}} = \dot{\hat{\omega}} - \dot{\omega} = \dot{\hat{\omega}}$. As Lyapunov function we choose

$$V = \frac{1}{2} \left(\hat{\omega} - \omega \right)^2 \tag{6.25}$$

with time derivative

$$\dot{V} \quad = \quad \frac{-\hat{\omega}(\hat{\omega} - \omega)^2 (\hat{\omega} + \omega)}{T_\omega \omega^2 \tan^2(\omega t) - \omega \tan(\omega t) + T_\omega \hat{\omega}^2}. \tag{6.26}$$

For the numerator of (6.26) holds that $-\hat{\omega}(\hat{\omega} - \omega)^2 (\hat{\omega} + \omega) \leq 0$. The denominator is a quadratic function of $\tan(\omega t)$, with $-\infty < \tan(\omega t) < \infty$. From $T_\omega \omega^2 > 0$ we deduce that the denominator with $\tan(\omega t) = x$ is a convex parabola. Therefore, we have a positive denominator, if the discriminant $\mathcal{D}$ is negative, i.e.

$$\mathcal{D} = \omega^2 - 4 T_\omega \omega^2 T_\omega \hat{\omega}^2 < 0 \quad \Rightarrow \quad T_\omega > \frac{1}{2\hat{\omega}}. \tag{6.27}$$

Thus, for $\omega \neq \hat{\omega}$ and $T_\omega > \frac{1}{2\hat{\omega}}$, the time derivative of the Lyapunov function (6.25) is strictly negative $\dot{V} < 0$ and the ω-estimation is asymptotically stable under the fundamental dynamics assumption. This proves convergence of the estimate $\hat{\omega}$ to the true value ω for a linearly oscillating pendulum. □

The condition $T_\omega > \frac{1}{2\hat{\omega}}$ indicates that the adaption of $\hat{\omega}$ cannot be performed arbitrarily fast.

6.5.2 Amplitude factor based leader/follower design

In the following, we design the amplitude factors for leader agents $a_{\mathcal{L}}$ and follower agents $a_{\mathcal{F}}$.

Leader

Proposition 4. *For two* leader *agents* A1 = A2 = $\mathcal{L}$ *applying amplitude factors*

$$a_i = k_i(\theta_E^{\mathrm{d}} - \vartheta_r) \text{ with } k_i = \frac{2\Gamma_i^{\mathrm{d}}\tau_{\mathcal{L}}}{B}, \tag{6.28}$$

where $i = 1, 2$ *and* $\Gamma_1^{\mathrm{d}} + \Gamma_2^{\mathrm{d}} = 1$*, the energy* θ_r *of the fundamental dynamics in* (6.10) *converges to the desired energy* θ_E^{d} *and tracks the desired reference dynamics as formulated in Problem 8*

$$\dot{\theta}_E^{\mathrm{ref}} = \tau_{\mathcal{L}}\left(\theta_E^{\mathrm{d}} - \theta_E^{\mathrm{ref}}\right). \tag{6.29}$$

Furthermore, each leader agent contributes with the desired energy share $\Gamma_i = \Gamma_i^{\mathrm{d}}$ *defined in* (6.2)*.*

Proof. Differentiation with respect to time of the Lyapunov function

$$V = \frac{1}{2}\left(\vartheta_r - \theta_E^{\mathrm{d}}\right)^2 \tag{6.30}$$

and insertion of the fundamental dynamics (6.10) with (6.28) yields

$$\dot{V} = -\frac{B}{2}(k_1 + k_2)(\theta_E^{\mathrm{d}} - \vartheta_r)^2. \tag{6.31}$$

Thus, as long as $\vartheta_r \neq \theta_E^{\mathrm{d}}$ and for $k_1 + k_2, B > 0$ the Lyapunov function has a strictly negative time derivative $\dot{V} < 0$ and, thus, the desired energy level $\vartheta_r = \theta_E^{\mathrm{d}}$ is an asymptotically stable fixpoint.

Insertion of (6.28) into the fundamental dynamics in (6.10) yields

$$\dot{\vartheta}_r = \tau_{\mathcal{L}}\left(\theta_E^{\mathrm{d}} - \vartheta_r\right). \tag{6.32}$$

Comparison of (6.32) and (6.29) shows that the reference dynamics are tracked $\vartheta_r(t) = \theta_E^{\mathrm{ref}}(t)$ for equal initial values $\vartheta_r(t=0) = \theta_E^{\mathrm{ref}}(t=0)$. The energy contributed by one agent Ai according to the fundamental dynamics in (6.10) is $\dot{\vartheta}_{r,i} = \frac{B}{2}a_i$. Insertion of (6.28) yields $\dot{\vartheta}_{r,i} = \Gamma_i^{\mathrm{d}}\tau_{\mathcal{L}}\left(\theta_E^{\mathrm{d}} - \vartheta_r\right)$. With (6.32), the energy share of agent Ai according to (6.2) results in $\Gamma_i = \frac{\int_0^{T_\mathrm{s}} \dot{\vartheta}_{r,i}\mathrm{d}\tau}{\int_0^{T_\mathrm{s}} \dot{\vartheta}_r\mathrm{d}\tau} = \Gamma_i^{\mathrm{d}}$. □

Follower

Proposition 5. *A* follower *agent* A1 = $\mathcal{F}$ *applying an amplitude factor*

$$a_{\mathcal{F}} = k_{\mathcal{F}}\hat{\dot{\vartheta}}_r \text{ with } k_{\mathcal{F}} = \frac{2}{B}\Gamma_{\mathcal{F}}^{\mathrm{d}}, \tag{6.33}$$

with $\Gamma_{\mathcal{F}}^{\mathrm{d}} \in [0, 1)$ *and a correct estimate of the total energy flow* $\hat{\dot{\vartheta}}_r = \dot{\vartheta}_r$*, contributes the desired fraction* $\Gamma_{\mathcal{F}}^{\mathrm{d}} = \Gamma_{\mathcal{F}}$ *to the overall task effort.*

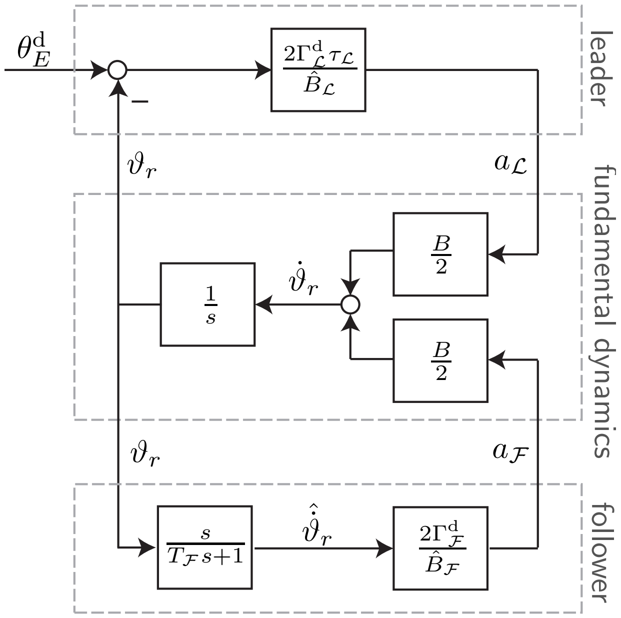

Fig. 6.7: Block diagram showing the leader and the follower controller interacting with the linear fundamental energy dynamics: The leader tracks first-order reference dynamics with inverse time-constant $\tau_{\mathcal{L}}$ to control the energy ϑ_r to θ_E^{d} with a desired energy share $\Gamma_{\mathcal{L}}^{\mathrm{d}}$. The follower achieves a desired energy share $\Gamma_{\mathcal{F}}^{\mathrm{d}}$ by imitating an estimate of the system energy flow $\hat{\dot{\vartheta}}_r$.

Proof. Insertion of (6.33) into the energy flow of the follower $\dot{\vartheta}_{r,\mathcal{F}} = \frac{B}{2}a_{\mathcal{F}}$ according to the fundamental dynamics in (6.10) yields $\dot{\vartheta}_{r,\mathcal{F}} = \Gamma_{\mathcal{F}}^{\mathrm{d}}\hat{\dot{\vartheta}}_r$ and $\Gamma_{\mathcal{F}}^{\mathrm{d}} = \Gamma_{\mathcal{F}}$ (see proof or Proposition 4). □

We obtain the total energy flow estimate through filtered differentiation $\hat{\dot{\vartheta}}_r = G_{\mathrm{hp}}\vartheta_r$, where $G_{\mathrm{hp}}(T_{\mathrm{hp}} = T_{\mathcal{F}})$ is a first-order high-pass filter with time constant $T_{\mathcal{F}}$. Thus, the filtered energy flow estimate is not equal to the true value $\hat{\dot{\vartheta}}_r \neq \dot{\vartheta}_r$. The influence of this filtering will be investigated in the next section.

In addition to the *flow imitation* follower from above, we presented an alternative follower in [40], which estimated the desired energy of the leader. Due to an increased number of tuning parameters and partial system knowledge requirements, we regard the goal estimation follower as the less elegant solution and focus on a thorough presentation and analysis of the flow imitation follower in this thesis.

6.5.3 Analysis of leader-follower structures

Here, we analyze stability, stationary transfer behavior and resultant follower energy share $\Gamma_{\mathcal{F}}$ for filtered energy flow estimates $\hat{\dot{\vartheta}}_r$ and estimation errors on the follower $B - \hat{B}_{\mathcal{F}} \neq 0$ and leader $B - \hat{B}_{\mathcal{L}} \neq 0$ side. Figure 6.7 shows a block diagram of the fundamental energy dynamics-based control structure for a leader and a follower controller. Detailed derivations of the transfer functions used in the following can be found in Appendix D.

The reference transfer function $\vartheta_r(s) = G^{\text{fi}}(s)\theta_E^{\text{d}}(s)$, which describes the closed-loop behavior resulting from the interconnection depicted in Fig. 6.7, results in

$$G^{\text{fi}} = \frac{\Gamma_{\mathcal{L}}^{\text{d}}\tau_{\mathcal{L}}\frac{B}{\hat{B}_{\mathcal{L}}}s + \Gamma_{\mathcal{L}}^{\text{d}}\tau_{\mathcal{L}}\frac{B}{\hat{B}_{\mathcal{L}}}\frac{1}{T_{\mathcal{F}}}}{s^2 + (\frac{1}{T_{\mathcal{F}}} - \Gamma_{\mathcal{F}}^{\text{d}}\frac{B}{\hat{B}_{\mathcal{F}}}\frac{1}{T_{\mathcal{F}}} + \Gamma_{\mathcal{L}}^{\text{d}}\tau_{\mathcal{L}}\frac{B}{\hat{B}_{\mathcal{L}}})s + \Gamma_{\mathcal{L}}^{\text{d}}\tau_{\mathcal{L}}\frac{B}{\hat{B}_{\mathcal{L}}}\frac{1}{T_{\mathcal{F}}}}. \tag{6.34}$$

Thus, $\vartheta_r(t \to \infty) = \theta_E^{\text{d}}$ and we have a stationary transfer behavior equal to one for a step of height θ_E^{d} in the reference variable $\theta_E^{\text{d}}(t) = \sigma(t)\theta_E^{\text{d}}$. This result holds irrespective of estimation errors $\hat{B}_{\mathcal{F}/\mathcal{L}} \neq B$.

Asymptotic stability of the closed-loop system is ensured for $(\frac{1}{T_{\mathcal{F}}} - \Gamma_{\mathcal{F}}^{\text{d}}\frac{B}{\hat{B}_{\mathcal{F}}}\frac{1}{T_{\mathcal{F}}} + \Gamma_{\mathcal{L}}^{\text{d}}\tau_{\mathcal{L}}\frac{B}{\hat{B}_{\mathcal{L}}}) > 0$. The stability constraint implies that $\hat{B}_{\mathcal{F}} > B$ is advantageous. This can be achieved by using a high initial value in the follower's $\hat{\omega}$-estimation (see (6.11)). Factors such as estimation errors, a high desired follower energy share $\Gamma_{\mathcal{F}}^{\text{d}}$ and a small time constant $T_{\mathcal{F}}$ can potentially destabilize the closed-loop system.

The follower transfer function $G_{\mathcal{F}}^{\text{fi}}$ from desired energy level θ_E^{d} to follower energy $\theta_{r\mathcal{F}}$ is

$$G_{\mathcal{L}}^{\text{fi}} = \frac{\Gamma_{\mathcal{L}}^{\text{d}}\tau_{\mathcal{L}}\frac{B}{\hat{B}_{\mathcal{L}}}\Gamma_{\mathcal{F}}^{\text{d}}\frac{B}{\hat{B}_{\mathcal{F}}}\frac{1}{T_{\mathcal{F}}}}{s^2 + (\frac{1}{T_{\mathcal{F}}} - \Gamma_{\mathcal{F}}^{\text{d}}\frac{B}{\hat{B}_{\mathcal{F}}}\frac{1}{T_{\mathcal{F}}} + \Gamma_{\mathcal{L}}^{\text{d}}\tau_{\mathcal{L}}\frac{B}{\hat{B}_{\mathcal{L}}})s + \Gamma_{\mathcal{L}}^{\text{d}}\tau_{\mathcal{L}}\frac{B}{\hat{B}_{\mathcal{L}}}\frac{1}{T_{\mathcal{F}}}}. \tag{6.35}$$

Application of the final value theorem to the follower transfer function (6.35) yields $\vartheta_{r,\mathcal{F}}(t \to \infty) = \Gamma_{\mathcal{F}}^{\text{d}}\frac{B}{\hat{B}_{\mathcal{F}}}\theta_E^{\text{d}}$. Consequently, $\Gamma_{\mathcal{F}} = \Gamma_{\mathcal{F}}^{\text{d}}\frac{B}{\hat{B}_{\mathcal{F}}}$ and the follower achieves its desired energy share for a correct estimate $\hat{B}_{\mathcal{F}} = B$.

6.6 Application to the t-pendulum

In this section, we extend the fundamental dynamics-based adaptive controllers presented in the previous section to control the t-pendulum. Figure 6.8 shows the block diagram of the controller implementation for the t-pendulum controlled by a follower agent.

The follower and the leader controllers are in principal the same as in Fig. 6.7, but extended by the ω-estimation. Also, we applied a second-order low-pass filter to the differentiation of ϑ_r instead of the first-order low-pass filter for the experiments in Section 6.8. The additional filtering damps out oscillations caused by modeling errors, as, e.g., the approximation $\vartheta_E \approx \vartheta_r$ and the assumption of a simple pendulum-like behavior of the t-pendulum. As a result of the additional filtering, the robot behaves calm also during periods of constant object energy $\theta_E \approx$ const. (see Section 6.4.2).

The *projection and energy-based controller* block in Fig. 6.8 implements the *projection onto the abstract cart-pendulum* and the *control law formulation* as introduced for the non-adaptive control approach in Chapter 5.5. Agent A1 $= \mathcal{F}$ obtains the projected deflection angle θ^* from the forces applied to the t-pendulum object. The observer with simple-pendulum dynamics in (5.11) and gain vector $\boldsymbol{l}$ takes θ^* as input and estimates the cartesian states of the abstract cart-pendulum $\boldsymbol{x}_{\text{c}}$. The cartesian states are then transformed into polar states $\boldsymbol{x}_{\text{p}}$ and are fed into the fundamental dynamics-based leader or follower controllers. The control law (6.9) is extended to filter out unwanted oscillations and to achieve non drift robot trajectories $r_{\mathcal{F}}$ as proposed by [188].

In Chapter 5, we proposed to saturate the amplitude factors $a_{\mathcal{L}}$ for the leader in (5.14) and $a_{\mathcal{F}}$ for the follower in (5.15) to limit the end effector motion to a confined workspace. This saturation introduces additional nonlinearities and is expendable for the fundamental dynamics-based controllers. For the leader a reasonable inverse time constant $\tau_{\mathcal{L}}$ restricts the amplitude of the robot motion $r_{\mathcal{L}}$. The follower motion $r_{\mathcal{F}}$ is dictated by the partner's behavior and will stay in viable bounds for a reasonable choice of desired energy share $\Gamma^{\mathrm{d}}_{\mathcal{F}}$.

6.7 Evaluation in simulation

The linear fundamental dynamics derived in Section 6.4 enabled the design of adaptive leader and follower controllers in Section 6.5. However, the fundamental dynamics approximates the behavior of the abstract cart-pendulum, which represents the desired dynamics of the t-pendulum. In this section, we analyze the fundamental dynamics-based controllers in interaction with the abstract cart-pendulum with respect to stability of the ω-estimation (Section 6.7.3), reference trajectory tracking (Section 6.7.4) and follower energy share (Section 6.7.5). For simplicity, we use the variables θ_E and θ^{d}_E also for the abstract cart-pendulum.

6.7.1 Simulation setup

The simulations were performed using *MATLAB/Simulink*. We modeled the cart-pendulum as a point mass $m_{\mathrm{o}} = 10\,\mathrm{kg}$ attached to a massless pole of length $l_{\mathrm{o}} = 0.6\,\mathrm{m}$. The following control gains stayed constant for all simulations: $\tau_{\mathcal{L}} = 0.4\,{}^{1}/_{\mathrm{s}}$, $T_{\mathcal{F}} = 1\,\mathrm{s}$. We started all abstract cart-pendulum simulations with a small angle $\vartheta(t = 0) = 2\,\mathrm{deg}$ and zero velocity $\dot{\vartheta}(t = 0) = 0\,{}^{\mathrm{rad}}/_{\mathrm{s}}$ in order to avoid initialization problems, e.g., of the phase angle φ.

6.7.2 Measures

Analysis of controller performance

We analyzed the controller performance based on settling time T_{s} and the steady state error e. The settling time T_{s} was computed as the time after which the energy θ_E stays within bounds $\pm\epsilon_\theta$ around the energetic steady state value $\bar{\theta}_E$. For the simulations we set the bounds to $\epsilon_\theta = 8\,\%$. We defined the steady state error as $e = \theta^{\mathrm{d}}_E - \bar{\theta}_E$.

Analysis of effort sharing

The energy flows to the abstract cart-pendulum were calculated based on velocities and applied force along the motion $\dot{E}_1 = \frac{1}{2}\dot{r}_1 f_x$, where $f_x = f_{1x} = f_{2x}$. The multiplication with $\frac{1}{2}$ reflects that the agents equally share the control over the abstract cart-pendulum in (6.3).

We based the analysis of the effort sharing between the agents on the energy share of the follower $\Gamma_{\mathcal{F}}$. The energy share definition in (6.2) is based on the time derivative of the oscillation amplitude $\dot{\theta}_{E,\mathcal{F}}$ and $\dot{\theta}_{E,\mathcal{L}}$, which requires use of the abstract cart-pendulum

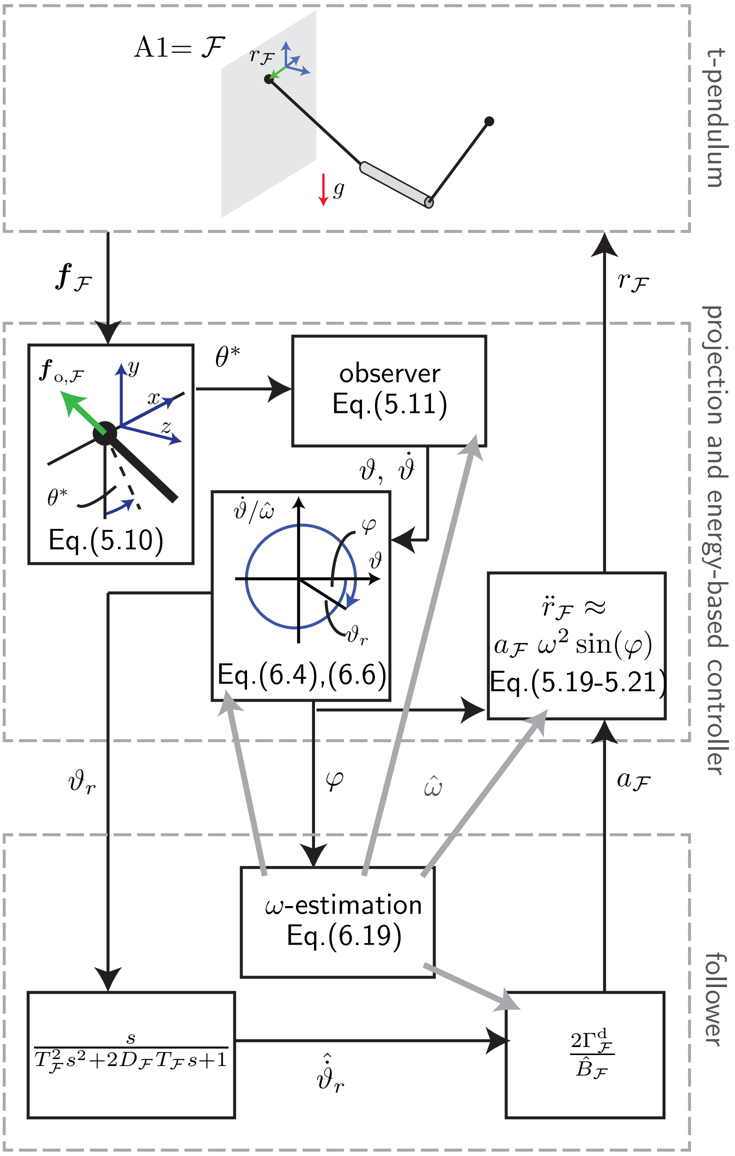

Fig. 6.8: Block diagram of the fundamental dynamics-based follower applied to the t-pendulum.

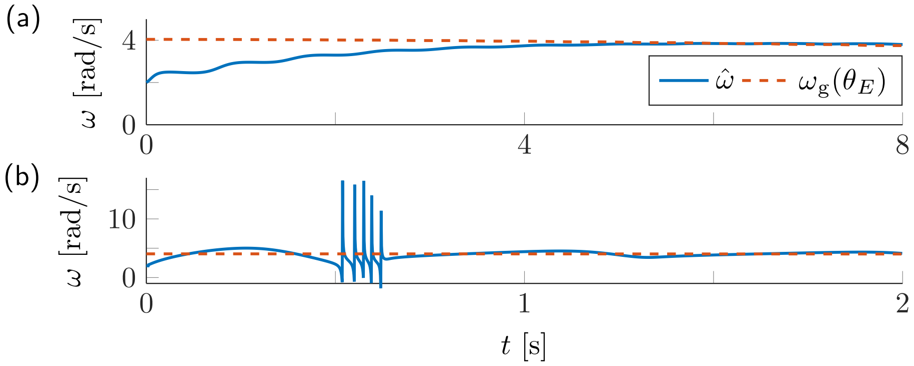

Fig. 6.9: Natural frequency estimation for the cart-pendulum: (a) The estimate $\hat{\omega}$ smoothly approaches the geometric mean approximation of the natural frequency $\omega_g(\theta_E)$ for a estimation time constant $T_\omega = 2\,\mathrm{s}$, (b) first signs of instability occur for $T_\omega = 0.17\,\mathrm{s}$. This result is in accordance with the theoretically found conservative stability bound $T_\omega > \frac{1}{2\hat{\omega}}$ which evaluates to $T_\omega > 0.25\,\mathrm{s}$ for $\hat{\omega} = 2\,{}^{\mathrm{rad}}\!/\mathrm{s}$.

approximation. In order not to rely on the simple pendulum approximation, we define the energy share of the follower $\Gamma_{\mathrm{in},\mathcal{F}}$ based on the integrals over energy flows to the system as in (5.31), but evaluated at the settling time T_s

$$\Gamma_{\mathrm{in},\mathcal{F}} = \frac{\int_0^{T_\mathrm{s}} \dot{E}_\mathcal{F} \mathrm{d}\tau}{\int_0^{T_\mathrm{s}} (\dot{E}_\mathcal{F} + \dot{E}_\mathcal{L}) \mathrm{d}\tau}. \tag{6.36}$$

The computation above has the drawback that for mechanisms with high damping, the estimated follower energy share will be smaller than the desired $\Gamma_{\mathrm{in},\mathcal{F}} < \Gamma^\mathrm{d}_\mathcal{F}$, because the follower reacts to changes in object energy and thus the leader accounts for damping compensation. Therefore, we define a second follower energy share based on the object energy E for comparison

$$\Gamma_{\mathrm{o},\mathcal{F}} = \frac{\int_0^{T_\mathrm{s}} \dot{E}_\mathcal{F} \mathrm{d}\tau}{E(T_\mathrm{s})}. \tag{6.37}$$

For the analysis of the abstract cart-pendulum we used the energy contained in the ϑ-oscillation as the object energy $E = E_\theta$. Note that $\Gamma_{\mathrm{o},\mathcal{F}} + \Gamma_{\mathrm{o},\mathcal{L}} \neq 1$ for a damped mechanism.

6.7.3 Stability limits of natural frequency estimation

The fundamental dynamics analysis in Section 6.5.1 revealed a theoretical stability bound of $T_\omega > \frac{1}{2\hat{\omega}}$. Here, we test its applicability to the cart-pendulum with energy dependent natural frequency ω. The lossless pendulum was controlled by one leader with constant amplitude factor $a_\mathcal{L} = 0.04\,\mathrm{m}$. The amplitude factor was chosen, such that approximately an energy level of $\theta_E \approx 60\,\mathrm{deg}$ is reached after 8 s. We initialized the natural frequency estimation with $\hat{\omega}(t=0) = 2\,{}^{\mathrm{rad}}\!/\mathrm{s}$. Figure 6.9 shows the geometric mean approximation of the natural frequency $\omega_g(\theta_E)$ and the estimate $\hat{\omega}$ for two different time constants T_ω. We use $\omega_g(\theta_E)$ as the ground truth against which we compare our estimate $\hat{\omega}$. A time constant $T_\omega = 2\,\mathrm{s}$ resulted in smooth ω-estimates which reach the actual natural frequency

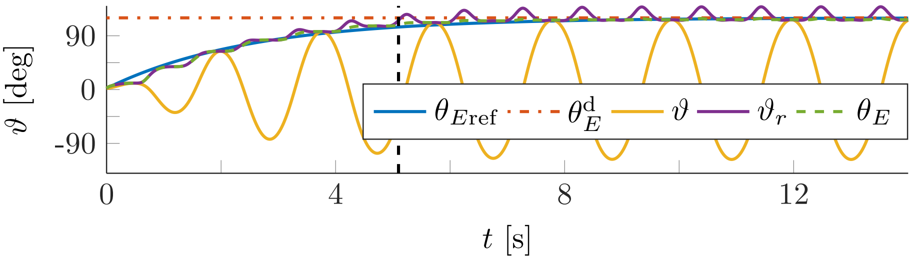

Fig. 6.10: Reference dynamics tracking for the cart-pendulum: Desired and resultant angles and energy equivalents. The vertical dashed line indicates settling time T_{s}. A single leader achieves close reference dynamics tracking with small steady state error.

at around $t = 5\,\mathrm{s}$. For smaller time constants, estimates $\hat{\omega}$ reached the natural frequency ω faster, but increasingly oscillated around ω. We observed first signs of unstable behavior for time constants $T_\omega = 0.17\,\mathrm{s}$. Note the different time and natural frequency scales. For further decreasing time constants, the ω-estimation is unable to recover after the severe transient effects. These results support the conservative constraint found from the Lyapunov stability analysis in Section 6.5.1.

6.7.4 Reference dynamics tracking

The leader controller is designed to track first-order reference dynamics. Here we evaluate how well reference dynamics tracking is achieved for a single leader interacting with the cart-pendulum, thus $\Gamma_{\mathcal{L}} = 1$. In order to focus on the reference dynamics tracking, we used the geometric mean $\omega_g(\theta_E)$ with exact ω_0 in (4.9) as an accurate natural frequency estimate for the leader controller. The leader's goal was to track first-order reference dynamics with inverse time constant $\tau_{\mathcal{L}} = 0.4\,{}^1\!/\mathrm{s}$ and desired energy level[1] $\theta_E^{\mathrm{d}} = 120\,\mathrm{deg}$. The results for the lossless pendulum are displayed in Fig. 6.10. The leader controller successfully tracked the reference dynamics with small steady state error of $e_{\bar{r}} = 2.7\,\mathrm{deg}$.

6.7.5 Energy share of the follower

For the follower energy share analysis, we ran simulations with a leader and a follower interacting with the abstract cart-pendulum for different desired follower energy shares $\Gamma_{\mathcal{F}}^{\mathrm{d}} = 0.3, 0.5, 0.7$. The pendulum was slightly damped with $t_{\mathrm{s},d\vartheta} = -d_{\mathrm{s}}\dot{\vartheta}$ and $\frac{d_{\mathrm{s}}}{j_\vartheta} = 0.01\,{}^1\!/\mathrm{s}$. The leader's desired energy level was $\theta_E^{\mathrm{d}} = 60\,\mathrm{deg}$. In accordance with the stability analysis in Section 6.5.3, we initialized the ω-estimation with $\hat{\omega}(t=0) = 6\,{}^{\mathrm{rad}}\!/\mathrm{s} > \omega$.

The first three lines of Table 6.1 list the results for $\Gamma_{\mathcal{F}}^{\mathrm{d}} + \Gamma_{\mathcal{L}}^{\mathrm{d}} = 1$, including the follower energy shares according to (6.36) and (6.37) and the overshoot $o = \max_t(\theta_E - \bar{\theta}_E)$ with respect to the energetic steady state $\bar{\theta}_E$. Figure 6.11 shows angles and energies over time for the most challenging case of $\Gamma_{\mathcal{F}}^{\mathrm{d}} = 0.7$. The damping resulted in increased steady state errors of $e_{\bar{r}} = 4.7\,\mathrm{deg}$. The ω-estimation and filtering for the energy flow estimate $\hat{\dot{\vartheta}}_r$ on

---

[1] In contrast to the t-pendulum, the simple pendulum approximation is modeled as rigid and can thus reach oscillation amplitudes beyond 90 deg. In order to challenge our approach, we command $\theta_E^{\mathrm{d}} > 90\,\mathrm{deg}$ here.

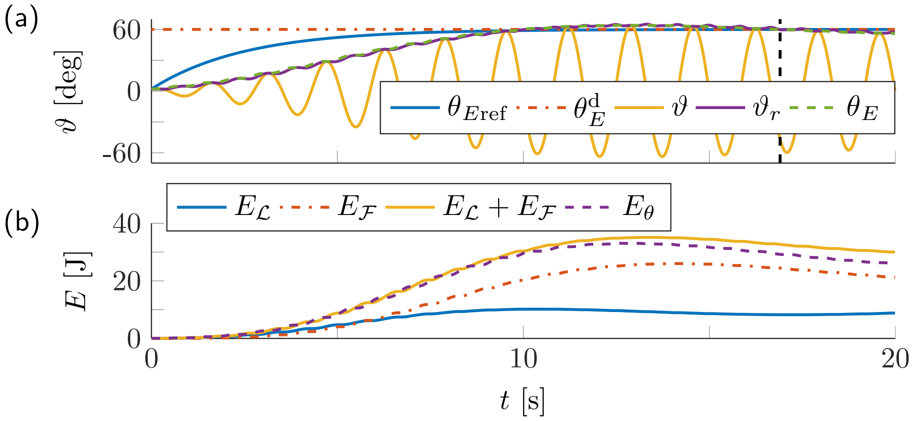

Fig. 6.11: Simulated follower and leader interacting with the abstract cart-pendulum for a desired follower energy share $\Gamma_\mathcal{F}^\text{d} = 0.7$: (a) Angles and energy equivalents and (b) energies. The vertical dashed line indicates the settling time T_s. The fundamental dynamics-based controllers allow for successful effort sharing.

the follower side caused a delay with respect to the reference dynamics θ_E^ref. With respect to effort sharing, higher desired follower energy shares resulted in increased overshoot o (see Table 6.1). Successful effort sharing was achieved, with energy shares close to the desired ones.

The last two lines of Table 6.1 list the results for $\Gamma_\mathcal{F}^\text{d} + \Gamma_\mathcal{L}^\text{d} \neq 1$. The resultant follower energy shares match the results of the fundamental dynamics analysis in Section 6.5.3: the follower energy share is close to its desired $\Gamma_{\text{in},\mathcal{F}} \approx \Gamma_\mathcal{F}^\text{d} \approx \Gamma_{\text{o},\mathcal{F}}$ with $\Gamma_{\text{in},\mathcal{L}} = 1 - \Gamma_{\text{in},\mathcal{F}}$. The desired leader energy share predominantly influences the transient behavior. Low values $\Gamma_\mathcal{F}^\text{d} + \Gamma_\mathcal{L}^\text{d} < 1$ yield slower convergence to the desired energy level with small overshoot o. High values $\Gamma_\mathcal{F}^\text{d} + \Gamma_\mathcal{L}^\text{d} > 1$ yield faster convergence to the desired energy level with increased overshoot o. The increased overshoot o comes along with increased transient behavior of the leader and follower energy shares that settles only after the settling T_s. As a consequence the energy shares $\Gamma_{\text{in},\mathcal{F}}$ and $\Gamma_{\text{o},\mathcal{F}}$, which are evaluated at T_s, exceed the desired $\Gamma_\mathcal{F}^\text{d}$.

Tab. 6.1: Effort sharing results for the abstract cart-pendulum

$\Gamma_\mathcal{F}^\text{d}/\Gamma_\mathcal{L}^\text{d}$	o[deg]	$\Gamma_{\text{in},\mathcal{F}}$	$\Gamma_{\text{o},\mathcal{F}}$
0.3/0.7	0.9	0.27	0.27
0.5/0.5	3.2	0.45	0.47
0.7/0.3	8.7	0.75	0.84
0.3/0.3	0.1	0.30	0.32
0.7/0.7	9.6	0.81	0.87

Fig. 6.12: Experimental setup for pendulum-like object swinging.

6.8 Real-world experiments

The simulations in Section 6.7 analyze the presented control approach for the abstract cart-pendulum. In this section, we report on the results of real world experiments with a t-pendulum to test the controllers in realistic conditions: noisy force measurements, non-ideal object and robot behavior and a human interaction partner.

6.8.1 Experimental setup

Hardware setup

Figure 6.12 shows the experimental setup with the same pendulum-like object. The experimental setup was essentially the same as in Chapter 5.7. The distance between the agents' interaction points was $C \approx 1.8\,\mathrm{m}$.

Software implementation

The same software implementation was used for the t-pendulum experiments in this chapter as in Chapter 5.7.

Controller parametrization

We used the following parameters for the experiments $\tau_{\mathcal{L}} = 0.4\,{}^{1}\!/\!{}_{\mathrm{s}}$, $T_{\mathcal{F}} = 1\,\mathrm{s}$, $D_{\mathcal{F}} = 1$ and $\boldsymbol{l} = [3.6\,{}^{1}\!/\!{}_{\mathrm{s}},\ 0]$. The ω-estimation used a time constant $T_{\omega} = 2\,\mathrm{s}$ and was initialized to $\hat{\omega}(t=0) = 6\,{}^{\mathrm{rad}}\!/\!{}_{\mathrm{s}}$.

6.8.2 Measures for analysis

The measures used to experimentally evaluate the fundamental dynamics-based controllers were based on the measures introduced in Chapter 5 and for the simulations in Section 6.7. In the following we highlight the differences.

Analysis of the projection onto the abstract cart-pendulum

The fundamental dynamics-based adaptive controllers operate on the reduced states of the abstract cart-pendulum. We extract the reduced states via a projection of the t-pendulum onto the abstract cart-pendulum. Ideally, during steady state the disturbance oscillations should be close to zero $\psi \approx 0$, the abstract pendulum angle should be close to the actual object deflection $\vartheta \approx \theta$ and the energies should match $\vartheta_r \approx \hat{\vartheta}_E \approx \theta_E$. For the analysis, we computed the object deflection θ and the undesired oscillation angle ψ from motion capture data. From θ, its numerical time derivative $\dot{\theta}$ and the small angle approximation of the natural frequency $\omega_0 = \sqrt{\frac{g}{l^*}}$, the energy equivalent θ_E was obtained based on (4.6).

Analysis of controller performance

As in Chapter 5.7 and for the simulations in Section 6.7, we analyzed the controller performance during the experiments based on settling time T_s and steady state error e.

Analysis of effort sharing

We used the relative follower contributions $\Gamma_{\mathrm{in},\mathcal{F}}$ and $\Gamma_{\mathrm{o},\mathcal{F}}$ defined in (6.36) and (6.37) to analyze effort sharing. Similarly to Chapter 5.7, we computed the energy flows of the agents $\dot{E}_i$ with $i = 1, 2$ to the t-pendulum and the energy of the t-pendulum E and the θ-oscillation E_θ. The energy contained in undesired system oscillations ψ can be approximated as $E_\psi \approx E - E_\theta$.

6.8.3 Experimental conditions and procedure

We performed experiments under multiple conditions: v- or t-pendulum, interaction with an active or passive human or with one side of the object being fixed to the environment and different leader/follower role assignments. The following t-pendulum experiments are presented in detail:

Maximum achievable energy (RL-HP)

The limitations of the controller with respect to the achievable energy levels were tested with a robot leader $\mathrm{A1} = \mathrm{R} = \mathcal{L}$. A human passively held the handle of agent $\mathrm{A2} = \mathrm{H} = \mathrm{P}$ in order to avoid extreme ψ-oscillation excitation at high energy levels due to a rigid fixed end. The t-pendulum started from rest ($\theta_E(t = 0) \approx \psi_E(t = 0) \approx 0$). The desired energy level θ_E^d was incrementally increased from 15 deg to 90 deg. The desired energy share of the robot was set to $\Gamma_\mathrm{R}^\mathrm{d} = 1$.

Robot follower and human leader (RF-HL)

A robot follower $\mathrm{A1} = \mathrm{R} = \mathcal{F}$ interacted with a human leader $\mathrm{A2} = \mathrm{H} = \mathcal{L}$. The t-pendulum started from rest ($\theta_E(t = 0) \approx \psi_E(t = 0) \approx 0$). The human leader was asked to first inject energy to reach $\theta_E^\mathrm{d} = 60$ deg, to hold the energy constant and finally to release the energy from the pendulum again. The desired energy level was displayed to the human via stripes of tape on the floor to which the cylindrical pendulum mass had to be aligned to at maximum deflection angles. The desired energy share of the robot was set to $\Gamma_{\mathrm{R}}^{\mathrm{d}} = 0.5$.

Excitation of the undesired oscillation (RL-0)

The pendulum mass was manually hold and released in a pose with high initial ψ-oscillation $\psi_E(t = 0) = 29\,\mathrm{deg}$ and zero desired oscillation $\theta_E(t = 0) \approx 0$. A goal energy of $\theta_E^{\mathrm{d}} = 40\,\mathrm{deg}$ was given to the robot leader $\mathrm{A1} = \mathrm{R} = \mathcal{L}$, while the handle of agent $\mathrm{A2} = 0$ was fixed at distance $C = 1.9\,\mathrm{m}$ from the robot end effector. The desired relative energy contribution of the robot was set to $\Gamma_{\mathrm{R}}^{\mathrm{d}} = 1$.

6.8.4 Results and Discussion

Maximum achievable energy (RL-HP)

The robot successfully controlled the t-pendulum energy to closely follow the desired reference dynamics (see Fig. 6.13). The steady state error increased with higher desired energy due to increased damping, e.g., $e = 0.4\,\mathrm{deg}$ at $\theta_E^{\mathrm{d}} = 15\,\mathrm{deg}$ and $e = 8.2\,\mathrm{deg}$ at $\theta_E^{\mathrm{d}} = 90\,\mathrm{deg}$. Note that the steady state error is computed based on the mean of the energy equivalent θ_E, which shows increased oscillations at high energies. The maximum deflection angle reached was $\theta = 82.3\,\mathrm{deg}$. The undesired ψ-oscillation was successfully kept in small ranges, but increased from $\psi_E = 1.4\,\mathrm{deg}$ at $\theta_E^{\mathrm{d}} = 15\,\mathrm{deg}$ to $\psi_E = 15.6\,\mathrm{deg}$ at $\theta_E^{\mathrm{d}} = 90\,\mathrm{deg}$. With increased ψ-oscillation, the t-pendulum behaves less simple pendulum-like, which also becomes apparent in an increased difference between ϑ_r and θ_E. Figure 6.13(c) shows the energy input of the robot and the human compared to the energy contained in the t-pendulum. The energy dissipated by the passive human had to be compensated for by the robot leader in addition to the natural damping of the t-pendulum. The ω-estimation was initialized to $\hat{\omega}(t = 0) = 6\,\mathrm{rad/s}$ and closely followed the actual natural frequency as can be seen by its small distance to the geometric mean approximation in Fig. 6.13(d).

The successful reference dynamics tracking and close estimate $\vartheta_r \approx \theta_E$ for smaller and intermediate energy levels as well as the close ω-estimation support the applicability of the fundamental dynamics-based leader controller. With a maximum energy at the turning points of $\theta_E = 82.3\,\mathrm{deg}$, the adaptive approach outperforms the approach based on parameter knowledge in Chapter 5, which only achieved $\theta_E = 70\,\mathrm{deg}$. An energy content of $\theta_E^{\mathrm{d}} = 82.3\,\mathrm{deg}$ for our pendulum of $l^* = 0.76\,\mathrm{m}$ would, e.g., allow the object to reach a height $y_{\mathrm{o},E} = 0.64\,\mathrm{m}$ at a distance $x = 0.81\,\mathrm{m}$ from the pivot point after being released at $\theta = 70\,\mathrm{deg}$. Robot manipulator motion for a controlled object placement at an elevated location as motivated in Fig. 6.1(b) could be realized, e.g., by similar methods as presented in [32].

Active follower contribution (RF-HL)

The results for a robot follower interacting with a human leader are displayed in Fig. 6.14. The human-robot team successfully injected energy until the desired energy level of $\theta_E^{\mathrm{d}} = 60\,\mathrm{deg}$ was reached with a settling time $T_s = 13.2\,\mathrm{s}$ and $e = 3\,\mathrm{deg}$. Similar to the

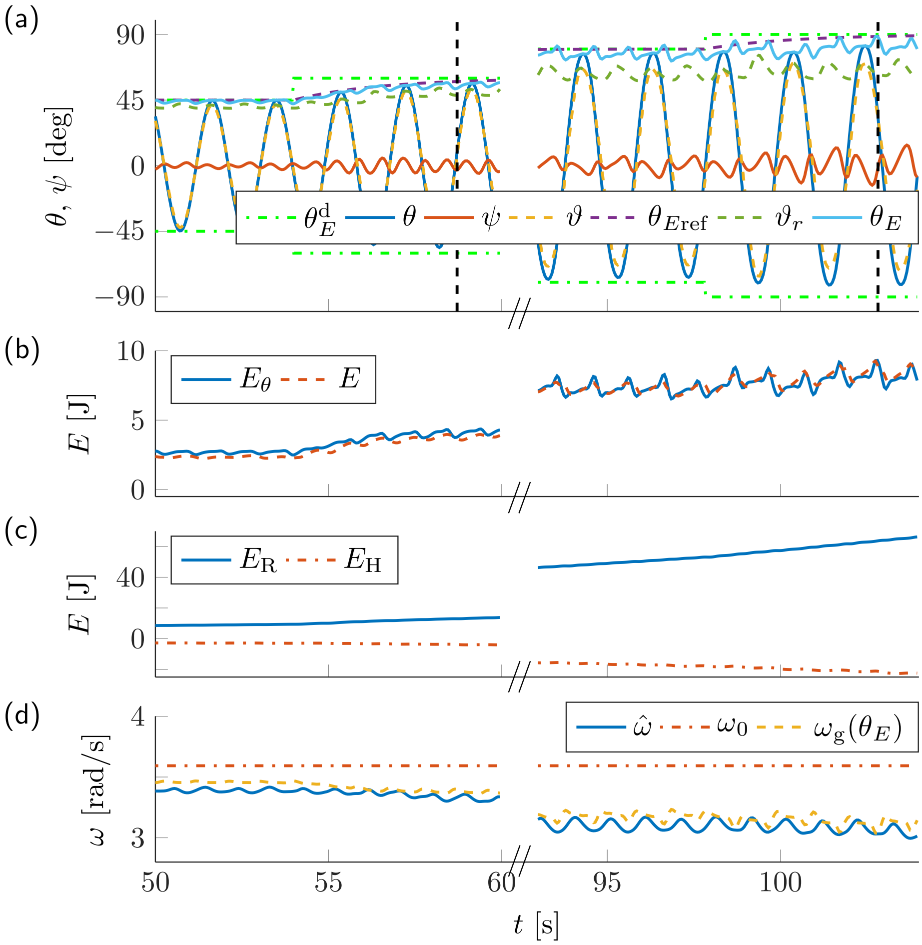

Fig. 6.13: Maximum achievable energies θ_E^{d} for the t-pendulum: (a) Deflection angles and energy equivalents, (b) energies contained in the t-pendulum and (c) contributed by the human and the robot (d) natural frequency estimates. Vertical dashed lines in (a) mark settling times T_{s}. A robot leader can reach deflection angles $\theta > 80\,\mathrm{deg}$ in interaction with a passive human.

simulations, the reference dynamics were tracked with a delay. The undesired oscillation increased, but did not exceed $\psi_E = 10.4\,\mathrm{deg}$.

Figure 6.14(b) and (c) visualize the effort sharing among the agents. The object energy flow $\dot{\theta}_E$ in Fig. 6.14(c) highly oscillated, which is in accordance with the results from human-human rigid object swinging in Chapter 4. Imitation of the filtered estimated system energy flow $\hat{\dot{\vartheta}}_r$, led to energy injection by the robot into the t-pendulum during swing-up. Once the desired energy level was reached and the object energy stayed constant, the robot stopped its energy injection. During the 20 s constant energy phase[2] the energy injected by the human steadily increases, because the human compensated for energy loss due to damping. The subsequent energy release initiated by the human was more difficult to detect by the robot due to damping. Still, the robot actively supported the human also during the energy release phase. The relative energy contributions $\Gamma_{\mathrm{in,R}} = 0.35$ and $\Gamma_{\mathrm{o,R}} = 0.57$ were close to the desired relative energy contribution $\Gamma_{\mathrm{R}}^{\mathrm{d}} = 0.5$.

The follower controller highly depends on the fundamental dynamics approximation. Thus, the successful energy sharing between a human leader and a robot follower further supports the efficacy of the fundamental dynamics-based controllers to human-robot dynamic object manipulation.

Excitation of undesired oscillation ψ (Robot leader and fixed end)

Figure 6.15 shows the experimental results for a significant initial undesired oscillation. The robot identified the natural frequency of the ψ-oscillation and tried to inject energy to reach the desired amplitude of $\theta_E^{\mathrm{d}} = 40\,\mathrm{deg}$. Thus, the robot failed to excite the desired θ-oscillation and keep unwanted oscillations in small bounds as defined in Section 6.3. However, considering the controller implementation given in Fig. 6.8, this experimental result supports the correct controller operation: the ω-estimation identified the frequency of the current oscillation, here the undesired ψ-oscillation. Based on the estimated frequency, the leader controller was able to inject energy into the ψ-oscillation; not enough to reach the desired amplitude of $\theta_E^{\mathrm{d}} = 40\,\mathrm{deg}$, but enough to sustain the oscillation. Note that the ψ-oscillation is highly damped, less simple pendulum-like and in general more difficult to excite than the θ-oscillation. Experiments with a controller that numerically differentiates the projected deflection angle θ^*, instead of using the observer, less accurately timed the energy injection. The result was a suppression of the ψ-oscillation through natural damping until the θ-oscillation dominated the estimated natural frequency and θ_E^{d} was reached.

On the one hand side, this experiment supports the control approach by showing that the controller is able to excite also less simple pendulum-like oscillations. On the other hand side, this experiment reveals the need for a higher level entity to detect failures as when the wrong oscillation is excited. Knowledge of the desired and undesired oscillation frequencies in Chapter 5 allowed to actively damp or at least to inhibit excitation of undesired oscillations. Aiming at an adaptive approach without prior parameter knowledge, the controllers in this chapter lacked such additional information. In the following chapter we will discuss how an embedding in an robotic architecture can circumvent such failures

---

[2] The constant energy phase is omitted for better visibility of the important swing-up and swing-down phases. See Online Resource 1 for the complete graphs.

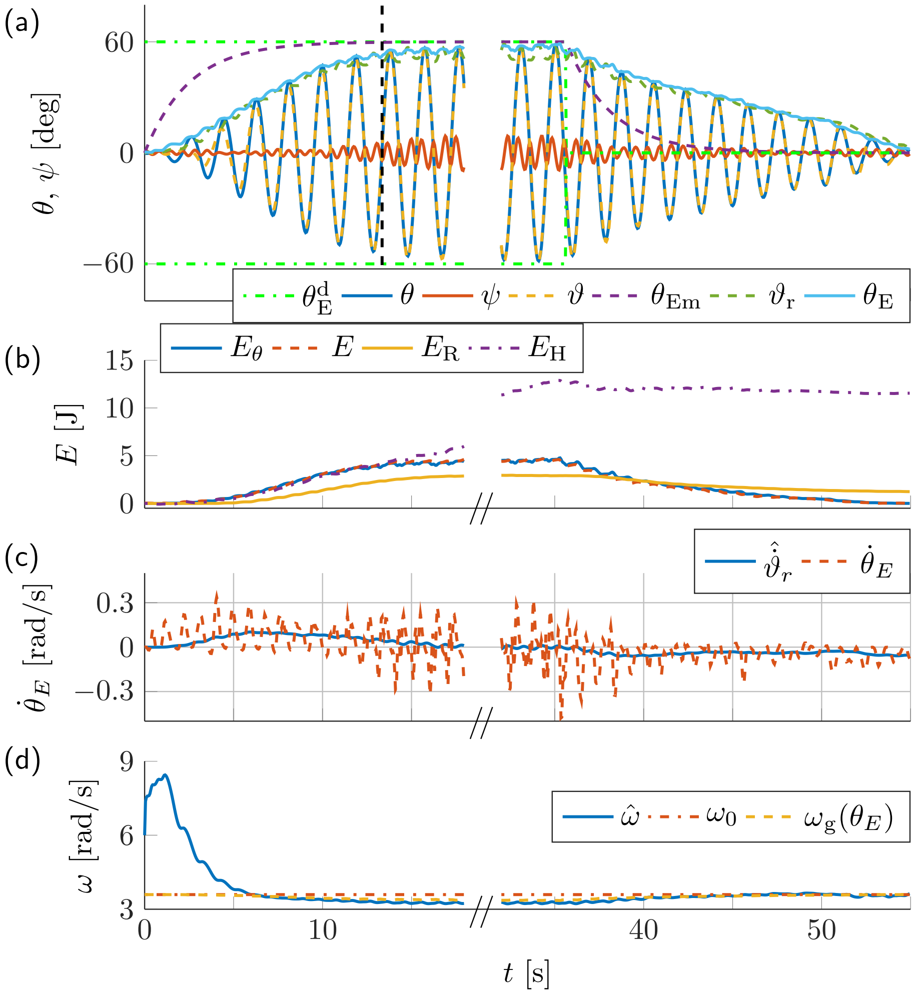

Fig. 6.14: Robot follower collaboratively injecting energy into the t-pendulum with a human leader: (a) Deflection angles and energy equivalents, (b) energies contained in the t-pendulum and contributed by the human and the robot, (c) actual and estimated energy flows, (d) natural frequency estimates. The vertical dashed line in (a) marks settling time T_s.

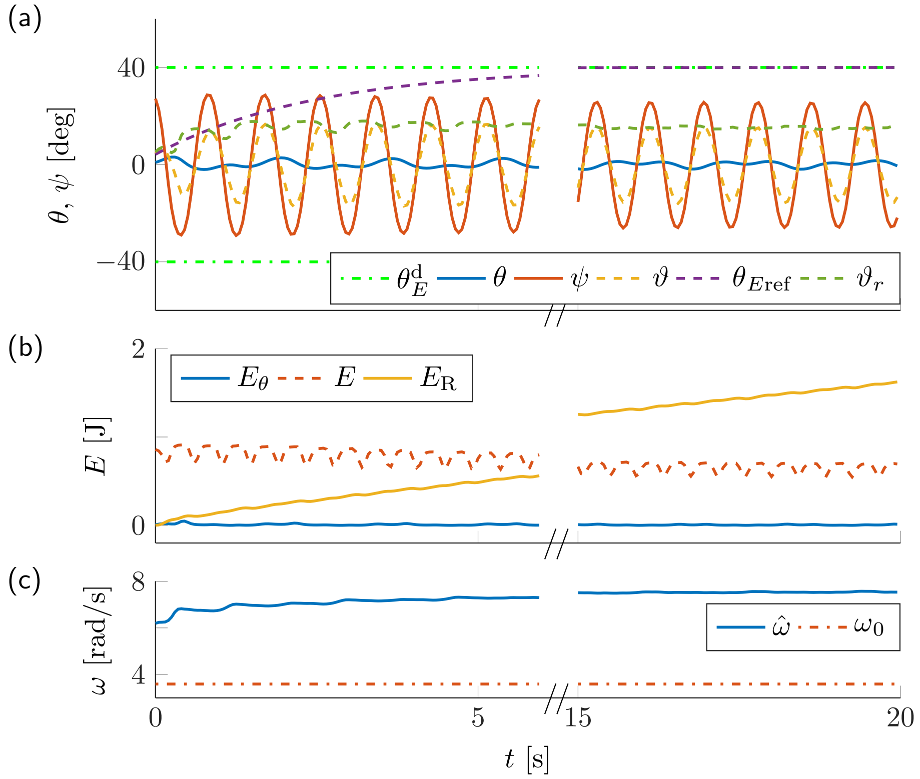

Fig. 6.15: Strong initial ψ_E for robot leader and fixed end: (a) Deflection angles and energy equivalents, (b) energies contained in the t-pendulum and contributed by the robot, (c) natural frequency estimates. The robot detects the natural frequency of the ψ-oscillation and sustains the less simple pendulum-like ψ-oscillation.

(see the discussion in Chapter 7.9.1).

6.9 Conclusions

In this chapter, we extended the control approach of Chapter 5 that required known object parameters to collaborative energy injection into pendulum-like objects of unknown dimensions. Identification of the underlying fundamental dynamics of the desired simple pendulum-like swinging motion allowed to design adaptive follower and leader controllers. The robot estimates the natural frequency of the system and controls the swing energy as a leader or follower from haptic information only. We extended the leader of Chapter 5 to track given reference dynamics during swing-up to a desired energy level and the follower to continuously imitate the system energy flow according to a desired energy share. Experimental results showed successful reference dynamics tracking of a robotic leader up to high energy levels of swinging amplitudes greater than 80 deg. Furthermore, a robot follower actively contributed to the swing-up effort in interaction with a human leader.

Open problems

The control approach presented in this chapter does not require any prior knowledge on system parameters and allows for immediate collaborative energy injection into unknown pendulum-like systems without a learning phase. The lack of additional information. however, prohibits a robotic partner to differentiate between desired and undesired oscillations and may under disadvantageous circumstances result in excitation of the wrong oscillation. We discuss the embedding in a robotic architecture with higher level controllers as a measure to detect and prevent such failures in the next chapter.

Chapters 4, 5 and the present chapter investigated the extremes of rigid object and pendulum-like object swinging. In the following chapter, we combine the insights and developed methods of this and the previous chapters towards achieving the goal of collaborative energy injection into unknown flexible objects.

7 Combining results from rigid and pendulum-like object manipulation for adaptive energy control of unknown flexible objects

Summary. *This chapter combines the control approaches for rigid objects of Chapter 4 and pendulum-like objects of Chapters 5 and 6 to control the swing energy contained in unknown flexible objects. The chapter demonstrates*

- *identification of the underlying fundamental dynamics of the desired simple pendulum-like oscillation*
- *passive simple pendulum-like robot arm behavior overlaid with active fundamental dynamics-based leader and follower behavior*
- *controller verification in simulation and real world experiments*

The results of this chapter were published in [44]. The student works [27, 118] contributed to this chapter.

7.1 Motivation

In the previous chapters, we approached collaborative energy injection into flexible objects as displayed in Fig. 7.1(b) by examining its extremes: rigid object swinging in Chapter 4 (Fig. 7.1(a)) and pendulum-like object swinging in Chapters 5 and 6 (Fig. 7.1(c)). Human-human experiments suggested that a human arm can be approximated as simple pendulums controlled via torque applied at a pivot point in front of the human's shoulder during collaborative swinging of heavy rigid objects (see Chapter 4). A system theoretic approach applied to the pendulum-like object swinging task showed that force signals are sufficient to to design actively contributing leader and follower controllers (see Chapters 5 and 6). By projecting the complex mechanism onto a simple pendulum with two-sided acceleration actuation, the desired oscillation can be extracted. Based on the underlying fundamental dynamics of the simple pendulum, adaptive controllers were designed that do not require parameter knowledge. In this chapter, we combine the results of the previous chapters to design leader and follower controllers for collaborative energy injection into unknown flexible objects.

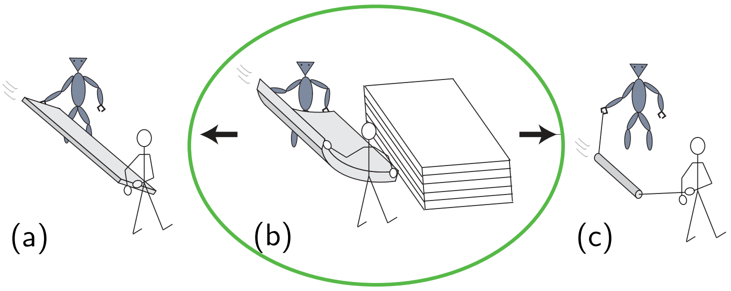

Fig. 7.1: Dynamic manipulation scenario: Collaborative energy injection into a sports mat to lift it onto a stack of mattresses (b). Interpretation of flexible object swinging (b) as a combination of rigid object swinging (a) and pendulum-like object swinging (c). This chapter combines findings from (a) and (c) to synthesize controllers for swinging of unknown flexible objects (b).

7.2 Related work

In the following, we brievly introduce related work in the context of flexible object modeling along with our approach. For related work in the areas of human motion modeling, suspended loads, role allocation, simple pendulum approximations and their control the reader is referred to Chapters 4-6.

Modeling of flexible objects

Manipulation of *flexible* and deformable objects is a challenging research topic also at slow velocities. For exact modeling, the finite element method is commonly used (e.g., in [116]). The pseudo-rigid object method approximates flexible links through rigid bodies, lumped masses and torsional springs. It offers an efficient tool to estimate deformation and natural frequency [192]. Within the robotics community, cloth manipulation from folding [128] to transport [3] has gained interest within the last years. The recent work on human-robot cloth transport [101] suggests to first compute a minimal internal cloth strain robot task pose through offline optimization. The robot base is then controlled online to maintain the desired pose with respect to a human leader. In [108], Langsfeld et al. tackle dual arm cleaning of flexible objects. They model the flexible object using the finite element method and update the object stiffness parameters based on observed deformation during cleaning.

In this thesis, we take a different approach. Our goal is to achieve stable oscillations with desired energy content of “arm – flexible object – arm” systems as shown in Fig. 7.2(a) with unknown parameters. We exploit the result that human arms behave as simple pendulums during rigid object swinging and approximate the human arms by simple pendulums actuated via torque at the shoulder joints (see Fig. 7.2(e)). We abbreviate the resultant “arm – flexible object – arm” system in Fig. 7.2(e) as *afa-system*. As in Chapters 4-6, we do not try to extract accurate dynamical models, but make use of the fact that the desired oscillation is *simple pendulum-like*. The desired oscillation of the pendulum-like object in Chapters 5 and 6 was approximated by a simple pendulum actuated by a cart (see, e.g., Fig. 6.2(e)). The afa-system can be approximated by a torque-actuated simple pendulum representing the two arms with a simple pendulum attached at the wrist, representing the flexible object. The simple pendulum variants above are commonly known as the cart-pendulum [29] and the pendubot [165].

Here, we further approximate the desired oscillation of the afa-system, as a torque-controlled simple pendulum, i.e. the pendubot approximately behaves as a single link (see Fig. 7.2(g)). The resultant abstract torque-pendulum is the same as used for energy injection into rigid objects in Chapter 4 (see Fig. 4.2(e)). The swing-up and stabilization of the simple pendulum variants in their unstable equilibrium point is commonly used as benchmark for linear and nonlinear control techniques [6, 58]. Instead of a full swing-up to the inverted pendulum configuration, our goal is to reach a periodic orbit of desired energy content. Based on virtual holonomic constraints, [160] and [63] achieve desired periodic motions of the cart-pendulum and the pendubot, respectively. The controllers above rely on thorough system knowledge, whereas our final goal is the manipulation of *unknown objects*.

Therefore, we extend the adaptive control approach derived for pendulum-like objects in Chapter 6 to swinging of unknown flexible objects. To this end, we extract the linear *fundamental dynamics* of the abstract torque-pendulum approximation (see Fig. 7.2(f)), which only differs in a constant system parameter to the fundamental dynamics of the abstract cart-pendulum derived in Chapter 6. We then apply the fundamental dynamics-based frequency estimation and leader and follower controllers derived in Chapter 6 (see Fig. 7.2(g) and (h)).

Chapter overview

Similar to Chapter 6, the remainder of this chapter is structured along Fig. 7.2 and Fig. 7.3. Note the similarity to Fig. 6.2 and Fig. 6.3. Further differences to Chapter 6 will be detailed in the Sections as indicated.

As in Chapters 5 and 6, the robot controllers are limited to haptic signals only to infer the state of the object and the partner's intention. In contrast to the pendulum-like objects considered in Chapters 5 and 6, flexible objects are of non negligible transverse rigidity. Therefore, measured applied torque $\boldsymbol{t}_1$ contains valuable information as well and is used as input to the *projection and energy-based controller* together with the measured applied force $\boldsymbol{f}_1$. Here, the robot arm is controlled to behave as a simple pendulum with the end effector position and orientation defined by the arm of deflection angle ρ

In Section 7.3 we give the problem formulation. This is followed by the fundamental dynamics derivations of the abstract torque-pendulum in Section 7.4 and the adaptive leader and follower controller design in Section 7.5. In Section 7.6, we apply the fundamental dynamics-based controllers to the control of the ara-system. We evaluate our controllers in simulation and experiments with a human interaction partner in Section 7.7 and Section 7.8, respectively. In Section 7.9, we discuss design choices, limitations and possible extensions of the presented control approach. Section 7.10 concludes the chapter and discusses open problems.

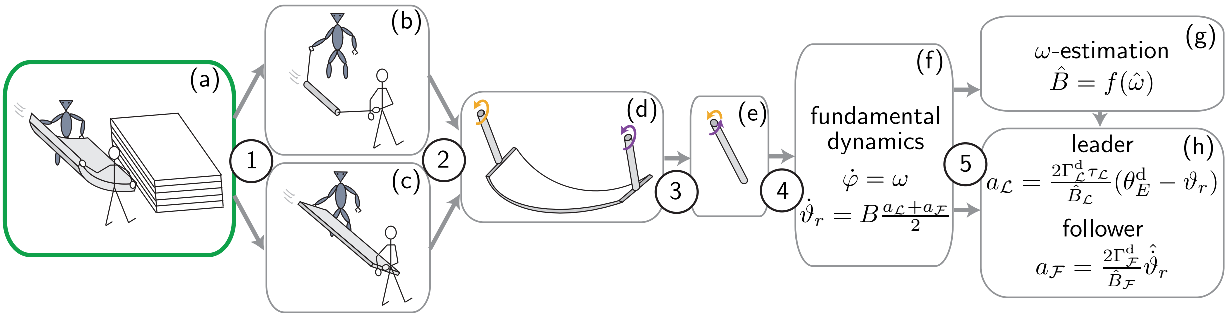

Fig. 7.2: Approach overview: (1) Interpretation of flexible object swinging as a combination of pendulum swinging and rigid object swinging. (2) Approximation of flexible object swinging by the afa-system with 1D torque inputs. (3) Projection of the afa-system onto the abstract torque-pendulum. (4) Extraction of the closed-loop fundamental dynamics. (5) Fundamental dynamics-based natural frequency estimation and leader and follower controller design

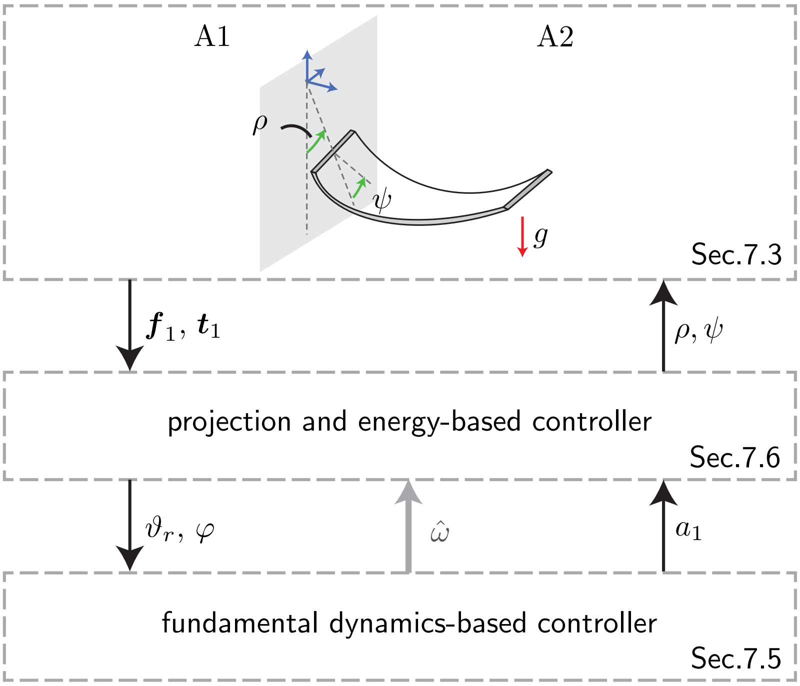

Fig. 7.3: Implementation overview block diagram.

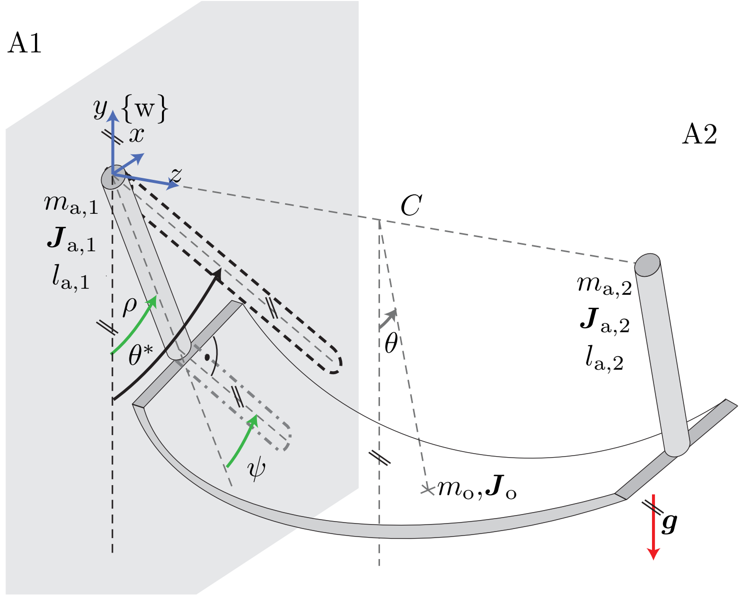

Fig. 7.4: The afa-system: Two cylindrical arms connected at their wrist joints through a flexible object of mass m_{o} and deformation dependent moment of inertia $\boldsymbol{J}_{\mathrm{o}}$ under the influence of gravity $\boldsymbol{g} = [0 \quad -g \quad 0]^\top$. The two cylindrical arms are of mass $m_{\mathrm{a},i}$, moment of inertia $\boldsymbol{J}_{\mathrm{a},i}$ and length $l_{\mathrm{a},i}$ with $i = 1, 2$ and have their pivot point at the origin of the world fixed coordinate system $\{\mathrm{w}\}$ and at $\boldsymbol{p} = [0,\ 0,\ C]^\top$ in $\{\mathrm{w}\}$, respectively. Pairs of parallel lines at the same angle indicate parallelity.

7.3 Problem formulation

In this section, we introduce the "arm – flexible object – arm" system, which we abbreviate as afa-system. Thereafter, we formally state our problem.

7.3.1 The afa-system

Figure 7.4 shows the afa-system. Based on the results of Chapter 4 that human arms during rigid object swinging can be approximated as simple pendulums, we model the agents' arms as cylinders actuated by shoulder torque around the z-axis $t_{s,1}$ and $t_{s,2}$. For simplicity, we limit the arm of agent A1 to rotations in the xy-plane. Note that we use the same approximations for the side of agent A2 for ease of illustration, although a human interaction partner can move freely. The angle between the y-axis and the arm of agent A1 is the oscillation DoF ρ. The angle ψ describes the wrist orientation with respect to the arm in the xy-plane (see right angle marking in Fig. 7.4). Thus, position and orientation of the interaction point of A1 are defined by the angles ρ and ψ. We regard excessive and unsynchronized ψ-oscillations as undesired. The wrist joint is subject to damping d_ψ and stiffness k_ψ. The desired oscillation DoF θ is defined as the angle between the y-axis and the line connecting the center between the two agents and the center of mass of the undeformed flexible object (indicated by a cross in Fig. 7.4). As our goal is an adaptive approach that can be applied to various different flexible objects, we refrain from defining more variables to more accurately describe the flexible object and the resultant afa-system state $\boldsymbol{x}_{\mathrm{afaS}}$. The input to the afa-system from the perspective of agent A1 is its shoulder torque $u_1 = t_{\mathrm{s},1}$. Agent A1 cannot directly control the torque input of agent A2, which is therefore classified as disturbance $z = t_{\mathrm{s},2}$. The only information agent A1 receives from the flexible object are the force and torque signals at its wrist: measurable output $\boldsymbol{y}_{\mathrm{m},1} = \left[\boldsymbol{f}_1^\top \; \boldsymbol{t}_1^\top\right]^\top$.

7.3.2 Problem statement

Similarly to Chapter 6, we formulate the desired periodic orbit of the afa-system in terms of the energy equivalents θ_E and ψ_E (see Definition 3)

$$\mathcal{O}(\boldsymbol{x}_{\mathrm{afaS}}) : \begin{cases} \theta_E = \theta_E^{\mathrm{d}}, \\ \psi_E = \psi_E^{\mathrm{d}} = 0. \end{cases} \tag{7.1}$$

The control goals for the leader and follower controllers in the following are identical to the ones in Chapter 6 (compare Problems 8 and 9).

Problem 10 (Leader $\mathcal{L}$)**.** *Find a control law $u_{\mathcal{L}}$ as a function of the measurable output and the desired object energies*

$$u_{\mathcal{L}} = t_{\mathrm{s},\mathcal{L}} = f(\boldsymbol{y}_{\mathrm{m}}, \theta_E^{\mathrm{d}}, \psi_E^{\mathrm{d}} = 0)$$

such that

$$\left|\theta_E^{\mathrm{ref}} - \theta_E\right| \leq \epsilon_\theta \textit{ with } \dot{\theta}_E^{\mathrm{ref}} = \tau_{\mathcal{L}}(\theta_E^{\mathrm{d}} - \theta_E^{\mathrm{ref}})$$

and

$$\left|\psi_E(t > T_{\mathrm{s}})\right| \leq \epsilon_\psi, \text{ for } 0 < T_{\mathrm{s}} < \infty.$$

Hence, the energy of the θ-oscillation should follow first-order reference dynamics θ_E^{ref} within bounds ϵ_θ. The reference dynamics is of inverse time constant $\tau_{\mathcal{L}}$ and converge to the desired energy θ_E^{d}. Furthermore, the energy contained in the ψ-oscillation should stay within $\pm\epsilon_\psi$ after the settling time T_{s}.

A *follower* A1 $= \mathcal{F}$ does not know the desired energy level θ_E^{d}, but should contribute with a desired energy share $\Gamma_{\mathcal{F}}^{\mathrm{d}} \in [0,\, 1)$ with follower energy share $\Gamma_{\mathcal{F}}$ defined in (6.2). The energy of the undesired oscillation ψ_E should be kept within $\pm\epsilon_\psi$.

Problem 11 (Follower $\mathcal{F}$)**.** *Find a control law $u_{\mathcal{F}}$ as a function of the measurable output and zero energy contained in the undesired oscillation*

$$u_{\mathcal{F}} = f(\boldsymbol{y}_{\mathrm{m},\mathcal{F}}, \psi_E^{\mathrm{d}} = 0)$$

such that

$$\left|\Gamma_{\mathcal{F}}^{\mathrm{d}} - \Gamma_{\mathcal{F}}\right| \leq \epsilon_{\mathcal{F}}$$

and

$$\left|\psi_E(t > T_{\mathrm{s}})\right| \leq \epsilon_\psi, \text{ for } 0 < T_{\mathrm{s}} < \infty.$$

7.4 Fundamental dynamics of the abstract torque-pendulum

In this section, we derive the fundamental dynamics of the abstract torque-pendulum in Fig. 7.1(e) introduced in (4.3) in Chapter 4.4.1, which only differs from the fundamental dynamics of the abstract cart-pendulum in Chapter 6 in the computation of one system parameter. In the following, we only highlight the differences. For details the reader is referred to Chapter 6.4.

7.4.1 Extraction of fundamental dynamics

Inspired by the control laws in Chapters 4-6, the agents actuate the abstract torque-pendulum via

$$t_{\mathrm{s},i} = -a_i \sin\varphi, \tag{7.2}$$

with amplitude factor a_i regulating the sign and amount of energy flow contributed by agent Ai and $\sin\varphi$ timing the energy flow.

Theorem 5. *The* fundamental dynamics *of the abstract torque-pendulum in* (4.3) *under application of the control law* (7.2) *can be written in terms of the polar states* $\boldsymbol{x}_{\mathrm{p}} = [\varphi,\ \vartheta_r]^\top$ *as*

$$\dot{\boldsymbol{x}}_{\mathrm{p}} = \begin{bmatrix}\dot\varphi\\ \dot\vartheta_r\end{bmatrix} = \begin{bmatrix}\omega\\ 0\end{bmatrix} + \begin{bmatrix}0\\ B\end{bmatrix}\frac{a_1+a_2}{2}, \tag{7.3}$$

with system parameter

$$B = \frac{1}{2\omega j_\vartheta} \tag{7.4}$$

when neglecting higher harmonics, applying 3rd order Taylor approximations and making use of the geometric mean approximation of the natural frequency ω_{g} *in* (4.9)*.*

Thus, the fundamental dynamics of the abstract cart- and torque-pendulums only differ in the system parameter B (compare to (6.10) and (6.11)). While $B = \frac{1}{2g}\omega^3$ of the abstract cart-pendulum only depends on the natural frequency ω, B of the abstract torque-pendulum also depends on the moment of inertia j_ϑ.

The proof is essentially the same as for Theorem 4. Thus, we refrain from repeating the complete proof and focus on the differences. The torque actuation leads to an actuation term

$$A = \frac{1}{j_\vartheta}\frac{t_{\mathrm{s},1}+t_{\mathrm{s},2}}{2} \tag{7.5}$$

in the phase φ and energy ϑ_r dynamics in (6.12) and (6.13), respectively. Insertion of the control law (7.2) into (6.12) and (6.13) yields the state space representation with inputs a_1 and a_2 of the form

$$\dot{\boldsymbol{x}}_{\mathrm{p}} = \boldsymbol{f}_{\mathrm{p}}(\boldsymbol{x}_{\mathrm{p}}) + {}^{a}\boldsymbol{g}_{\mathrm{p}}(\boldsymbol{x}_{\mathrm{p}})\frac{a_1+a_2}{2}. \tag{7.6}$$

Application of the following sequence of steps to (7.6) yields the fundamental dynamics

S4 Approximations through 3rd order Taylor polynomials,
e.g., $\sin(\vartheta_r \cos\varphi) \approx \vartheta_r \cos\varphi - \frac{\vartheta_r^3 \cos^3\varphi}{6}$

S5 Neglect of higher harmonics, e.g., $\cos^4\varphi = \frac{3}{8} + \frac{\cos 2\varphi}{2} + \frac{\cos 4\varphi}{8} \approx \frac{3}{8}$

While the abstract cart- and torque-pendulum dynamics are described by the same $\boldsymbol{f}_{\mathrm{p}}(\boldsymbol{x}_{\mathrm{p}})$, they differ in ${}^{a}\boldsymbol{g}_{\mathrm{p}}(\boldsymbol{x}_{\mathrm{p}})$. The approximation steps S4 and S5 yield ${}^{a}g_{\mathrm{p},1} \approx 0$, independent of the actuation terms A. Consequently, the phase dynamics of not only the abstract cart- but also of the abstract torque-pendulum result in $\dot{\varphi} \approx \omega$. The remaining term ${}^{a}g_{\mathrm{p},2}$ simplifies for the abstract torque-pendulum to

$$\begin{aligned} {}^{a}g_{\mathrm{p},2} &= \frac{1}{\omega I_\vartheta} \sin^2\varphi \\ &\overset{\mathrm{S5}}{\approx} \frac{1}{2\omega I_\vartheta} =: B. \end{aligned} \tag{7.7}$$

Thus, also the fundamental energy dynamics of the abstract torque-pendulum linearly depends on the amplitude factors $\dot{\vartheta}_r \approx B \frac{a_1 + a_2}{2}$.

7.5 Fundamental dynamics-based adaptive leader/follower structures

The fundamental dynamics equivalence for the abstract cart- and torque-pendulum allows direct application of the natural frequency estimation in (6.19) and leader (6.28) and follower (6.33) controllers derived in Chapter 6. The stability analysis of the natural frequency estimation and the leader/follower related analyses in Chapter 6.5 readily apply to the abstract torque-pendulum as well. The result that $\hat{B}_{\mathcal{F}} > B$ yields a higher stability margin with respect to (6.34) implies for the abstract torque-pendulum that the follower's $\hat{\omega}$-estimation should be initialized with a rather low value $\hat{\omega}(t = 0) < \omega$ (see (7.4)).

7.6 Application to the afa-system

In this section, we extend the fundamental dynamics-based adaptive controllers to control the afa-system. Figure 7.5 shows the block diagram of the controller implementation for the afa-pendulum controlled by a leader agent. Figure 6.8 depicts the block diagram for t-pendulum controlled by a follower agent. The *follower* and *leader* controllers are invariant with respect to the object types and can be simply exchanged. In Section 7.6.1, we discuss modifications of the fundamental dynamics-based controllers to cope with modeling errors. The *projection and energy-based controller* block differ between the t-pendulum and the afa-system and will be explained in detail for the afa-System in Section 7.6.2.

7.6.1 Fundamental dynamics-based controllers

The fundamental dynamics derivation is based on approximating the system energy ϑ_E by the phase space radius ϑ_r in Chapter 6.4.2. As already briefly discussed in Chapter 6.6, the state space radius ϑ_r represents the system energy ϑ_E less accurately at higher energy levels and increasingly oscillates for constant energy levels ϑ_E. As a consequence, unsettled follower behavior is expected even when the leading partner is trying to keep the system energy at a constant level. Furthermore, the discrepancy between ϑ_r and ϑ_E degrades the leader's reference dynamics tracking ability.

From the cartesian states ϑ and $\dot{\vartheta}$ we can estimate the system energy ϑ_E based on (4.6). To this end, we use the geometric mean relationship in (4.9) with current frequency estimate $\omega_g = \hat{\omega}$ and solve it for the unknown small angle approximation of the natural frequency

$$\hat{\omega}_0^2 = \hat{\omega}^2 \frac{1}{\cos\left(\frac{\hat{\vartheta}_E}{2}\right)}. \tag{7.8}$$

Insertion of (7.8) into (4.6) results in a quadratic equation which we solve for $\hat{\vartheta}_E$

$$\hat{\vartheta}_E = 2 \arccos\left(-\frac{\dot{\vartheta}^2}{8\hat{\omega}^2} + \frac{1}{4}\sqrt{\frac{\dot{\vartheta}^4}{4\hat{\omega}^4} + 8(\cos\vartheta + 1)}\right). \tag{7.9}$$

The estimate $\hat{\vartheta}_E$ can now be used instead of the state space radius ϑ_r within the leader and follower controllers.

Interestingly, the error caused by the state space radius approximation has a greater influence on the abstract torque-pendulum than on the abstract cart-pendulum. This is due to the fact that the error between ϑ_r and ϑ_E has its maximum for phase angles $\varphi = \pm\frac{\pi}{2}$ (see Fig. 4.4). The torque-based actuation in (7.2) contributes most energy when the multiplication of torque $t_{s,1}$ and rotational velocity $\dot{\vartheta}$ reaches a maximum. Both, $t_{s,1}$ and $\dot{\vartheta}$ reach their maxima for $\varphi = \pm\frac{\pi}{2}$. Thus, for the torque-based actuation, high energy injection and maximum error between ϑ_r and ϑ_E coincide. In contrast, the acceleration-based actuation in (6.9) contributes most energy when the multiplication of velocity $\dot{r}_1$ and applied force in x-direction reach a maximum, where $\dot{r}_1$ has its maximum at $\varphi = 0$ and $\varphi = \pi$. We will show the implications of the discussion above and the usage of the estimate $\hat{\vartheta}_E$ based on simulations of the abstract torque-pendulum in Section 7.7.

The main assumption of the presented control approach is that the desired oscillation is simple pendulum-like. Nevertheless, the realistic pendulum-like and flexible object do not exhibit perfect simple pendulum-like behavior. As we show with our experimental results in Section 7.8, such unmodeled dynamics have only little effect on the leader controller performance. In order to achieve calm follower behavior during constant energy phases, we use the same second-order low-pass filter along with the differentiation of ϑ_r for the experiments as for the t-pendulum instead of the first-order low-pass filter (compare Fig. 6.7 and 6.8). Besides the extension by the ω-estimation, the second-order filter for the follower is the only modification we apply to the fundamental dynamics-based controllers in Fig. 6.7 for the experiments. The use of the more accurate estimate $\hat{\vartheta}_E$ was not needed for the t-pendulum, due to the reasons above, and is not for the afa-system, as we are limited to relatively small energies, where $\vartheta_r \approx \vartheta_E$.

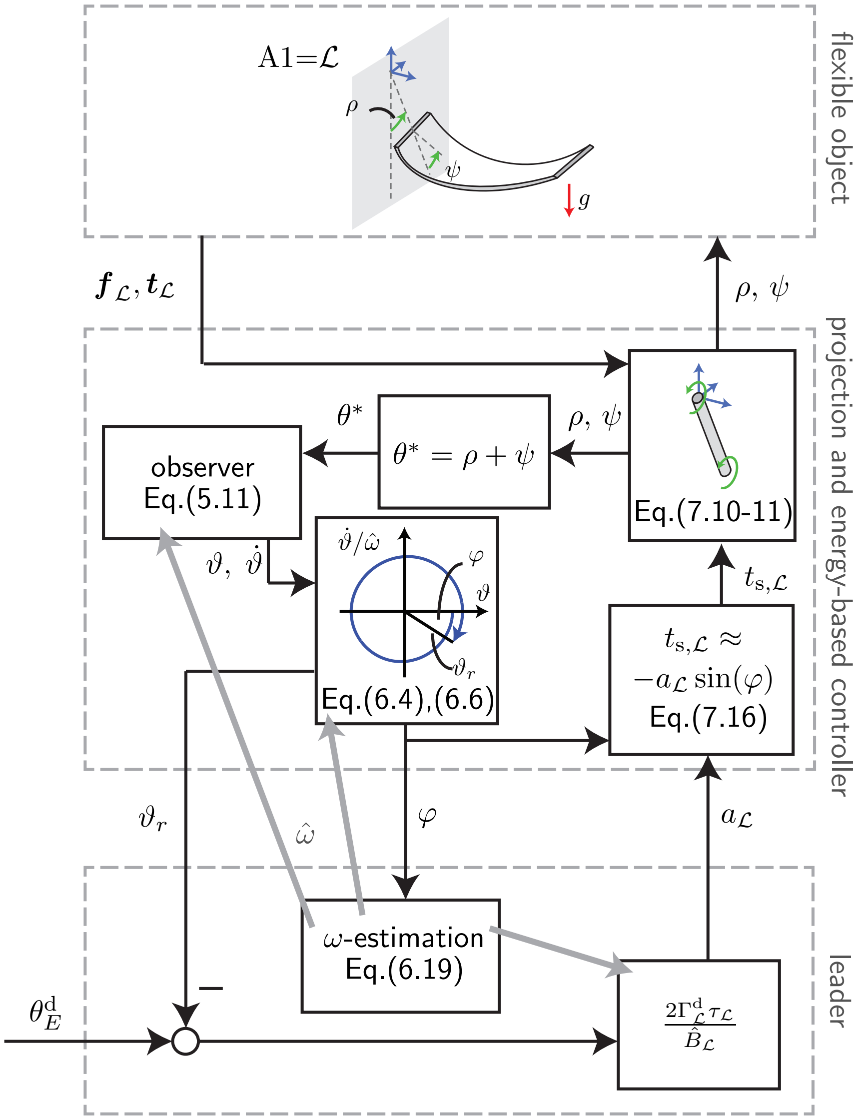

Fig. 7.5: Block diagram of the fundamental dynamics-based leader applied to the afa-system.

7.6.2 Projection and energy-based controller for the afa-system

Simple pendulum-like arm

Based on the results of Chapter 4, we model the robot end effector to behave as a cylindrical simple pendulum with human-like parameters of shoulder damping d_ρ, mass m_a, length l_a and density ϱ_a for the experiments with a robotic manipulator in Section 7.8. The robot arm dynamics is

$$j_\rho \ddot{\rho} = -d_\rho \dot{\rho} + t_g - t_{f1} + d_\psi \dot{\psi} + k_\psi \psi + t_{\mathrm{s},1} \tag{7.10}$$

where j_ρ is the arm moment of inertia with respect to the shoulder and t_g and t_{f1} are torques around the z-axis of coordinate system $\{\mathrm{w}\}$ caused by gravity and the applied interaction forces at the wrist $\boldsymbol{f}_1$, respectively. The wrist joint dynamics is

$$j_\psi(\ddot{\psi} + \ddot{\rho}) = -d_\psi \dot{\psi} - k_\psi \psi - t_{1z}, \tag{7.11}$$

with wrist moment of inertia j_ψ, damping d_ψ and stiffness k_ψ. The z-axis component t_{1z} of the applied torque $\boldsymbol{t}_1$ is measured at the interaction point with the flexible object.

Thus, the virtual arm/wrist system receives the measurable applied interaction force $\boldsymbol{f}_1$ and torque $\boldsymbol{t}_1$ and the control input shoulder torque $t_{\mathrm{s},1}$ and returns the resultant arm angle ρ and wrist orientation ψ, based on which position and orientation of the robot end effector are controlled (see Fig. 7.5).

Projection onto the abstract torque-pendulum

We base the projection of the afa-system onto the abstract torque-pendulum on a simple summation $\theta^* = \rho + \psi$ and the observer with simple pendulum dynamics in (5.11). The computation of the fundamental dynamics parameter B in (7.4) requires a moment of inertia estimate $\hat{j}_\vartheta$ in addition to the frequency estimate $\hat{\omega}$. For the experiments, we compute the moment of inertia estimate based on known parameters of the simple pendulum-like arm $j_{\vartheta\mathrm{a}} = j_\mathrm{a} + m_\mathrm{a}(\frac{l_\mathrm{a}}{2})^2$ and based on a point mass approximation of the flexible object $\hat{j}_{\vartheta\mathrm{o}} = \frac{m_\mathrm{o}}{2}(l_\mathrm{a} + \hat{l}_\mathrm{o}^*)^2$. The part of the object mass carried by the robot $\frac{m_\mathrm{o}}{2}$ is measured with the force sensor. We furthermore assume that an estimate of the projected object length $\hat{l}_\mathrm{o}^*$ is available. Alternatively, the object moment of inertia could be estimated from force measurements during manipulation (e.g., based on [7, 102]).

Complete control law for the afa-system

No additional filtering is applied for the computed shoulder torque. However, the wrist damping dissipates energy injected at the shoulder. The energy flow loss due to wrist damping is

$$\dot{E}_{d\psi} = -d_\psi \dot{\psi}^2. \tag{7.12}$$

The injected energy flow at the shoulder is approximated as

$$\dot{E}_{\mathrm{ts},d\psi} = t_{\mathrm{s},d\psi} \dot{\rho} \approx a_{d\psi} \vartheta_r \hat{\omega} \sin^2 \varphi \approx \frac{1}{2} a_{d\psi} \vartheta_r \hat{\omega} \tag{7.13}$$

where we inserted the modified control law (7.2)

$$t_{\mathrm{s},d\psi} = -a_{d\psi} \sin \varphi, \tag{7.14}$$

used $\dot{\rho} \overset{\dot{\rho}\approx\dot{\vartheta}}{=} -\vartheta_r \hat{\omega} \sin\varphi$ of (6.8) and approximated $\sin^2\varphi$ by its mean. Setting $\dot{E}_{d\psi} + \dot{E}_{\mathrm{ts},d\psi} \overset{!}{=} 0$ yields the amplitude factor $a_{d\psi}$ for wrist damping compensation

$$a_{d\psi} = \frac{2 d_\psi \dot{\psi}^2}{\vartheta_r \hat{\omega}}. \tag{7.15}$$

For the experiments, we add human-like shoulder damping d_ρ to the passive arm behavior. During active follower or leader control the shoulder damping is compensated for by applying an additional shoulder torque of $t_{\mathrm{s},d\rho} = d_\rho\, \dot{\rho}$. The complete control law consists of wrist and shoulder damping compensation and the commanded shoulder torque by the leader and follower controller with amplitude factor a_1 (see (7.2), (6.28), (6.33))

$$t_{\mathrm{s},1} = -a_1 \sin(\varphi) + t_{\mathrm{s},d\psi} + t_{\mathrm{s},d\rho}. \tag{7.16}$$

7.7 Evaluation in simulation

Similar as done for the cart-pendulum in Chapter 6.7, we analyze the fundamental dynamics-based controllers in interaction with the abstract torque-pendulum with respect to stability of the ω-estimation (Section 7.7.3), reference dynamics tracking (Section 7.7.4) and follower contribution (Section 7.7.5). For simplicity, we use the variables θ_E and θ_E^{d} also for the abstract cart- and torque-pendulum.

7.7.1 Simulation setup

The simulations were performed using *MATLAB/Simulink*. The torque-pendulum consisted of two rigidly attached cylinders with uniform mass distribution. The upper cylinder was of mass, density and length comparable to a human arm $m_{\mathrm{a}} = 3.35\,\mathrm{kg}$ [25], $\varrho_{\mathrm{a}} = 1100\,{}^{\mathrm{kg}}/_{\mathrm{m}^3}$ [34] and $l_{\mathrm{a}} = 0.56\,\mathrm{m}$ from Chapter 4. The lower cylinder was given the same radius, but mass $m_{\mathrm{o}} = 10\,\mathrm{kg}$ and length $l_{\mathrm{o}} = 0.4\,\mathrm{m}$.

We used the same control gains as for the abstract cart-pendulum for comparability: $\tau_{\mathcal{L}} = 0.4\,{}^{1}/_{\mathrm{s}}$, $T_{\mathcal{F}} = 1\,\mathrm{s}$. Also, we started all simulations with a small angle $\vartheta(t=0) = 2\,\mathrm{deg}$ and zero velocity $\dot{\vartheta}(t=0) = 0\,{}^{\mathrm{rad}}/_{\mathrm{s}}$ in order to avoid initialization problems, e.g., of the phase angle φ.

7.7.2 Measures

We used the same measures as for the abstract cart-pendulum simulations in Chapter 6.7.2, unless stated otherwise. For the effort sharing analysis, the energy flows to the abstract torque-pendulum were calculated based on angular velocity and applied torque $\dot{E}_1 = \frac{1}{2}\dot{\vartheta}\, t_{\mathrm{s},1}$, where $\vartheta = \vartheta_1 = \vartheta_2$. The multiplication with $\frac{1}{2}$ reflects that the agents equally share the control over the abstract torque pendulum in (4.3).

7.7.3 Stability limits of natural frequency estimation

The fundamental dynamics analysis in Chapter 6.5.1 revealed a theoretical stability bound of $T_\omega > \frac{1}{2\hat{\omega}}$. Here, we test its applicability to the torque-pendulum with energy dependent

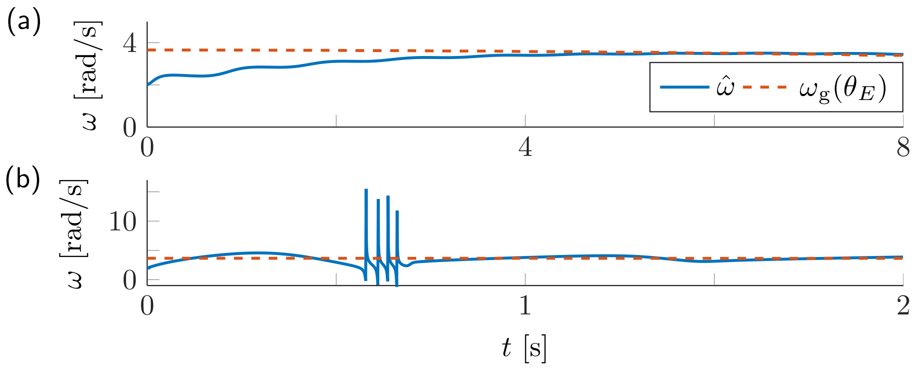

Fig. 7.6: Natural frequency estimation for the torque-pendulum: (a) The estimate $\hat{\omega}$ smoothly approaches the geometric mean approximation of the natural frequency $\omega_g(\theta_E)$ for a estimation time constant $T_\omega = 2\,\mathrm{s}$, (b) first signs of instability occur for $T_\omega = 0.19\,\mathrm{s}$. This result is in accordance with the theoretically found conservative stability bound $T_\omega > \frac{1}{2\hat{\omega}}$ which evaluates to $T_\omega > 0.25\,\mathrm{s}$ for $\hat{\omega} = 2\,\mathrm{rad/s}$.

natural frequency ω. Similar to the cart-pendulum, the lossless torque-pendulum was controlled by one leader with constant amplitude factor $a_\mathcal{L} = 5.5\,\mathrm{Nm}$, which was chosen such that an energy level of $\theta_E \approx 60\,\mathrm{deg}$ is reached after $8\,\mathrm{s}$. We initialized the natural frequency estimation with $\hat{\omega}(t = 0) = 2\,\mathrm{rad/s}$. Figure 7.6 shows the geometric mean approximation of the natural frequency $\omega_g(\theta_E)$ as ground truth and the estimate $\hat{\omega}$ for two different time constants T_ω. A time constant $T_\omega = 2\,\mathrm{s}$ resulted in smooth ω-estimates which reach the actual natural frequency at around $t = 5\,\mathrm{s}$. For smaller time constants, estimates $\hat{\omega}$ reached the natural frequency ω faster, but increasingly oscillated around ω. We observed first signs of unstable behavior for a time constant $T_\omega = 0.19\,\mathrm{s}$ for the torque-pendulum, which is comparable to $T_\omega = 0.17\,\mathrm{s}$ for the cart-pendulum in Chapter 6.5.1. For further decreasing time constants, the ω-estimation is unable to recover after the severe transient effects. These results support the conservative constraint found from the Lyapunov stability analysis in Section 6.5.1 also for the torque-pendulum.

7.7.4 Reference dynamics tracking

Here we evaluate how well reference dynamics tracking is achieved for a single leader interacting with the torque-pendulum, thus $\Gamma_\mathcal{L} = 1$. The conditions were the same as for the abstract cart-pendulum in Chapter 6.7.4.

The results for the lossless torque-pendulum are displayed in Fig. 7.7. The torque-pendulum simulation of Fig. 7.7(b) used the energy estimate $\hat{\vartheta}_E$ of (7.9) instead of the phase space radius ϑ_r in Fig. 7.7(a) for the amplitude factor computation in (6.28). The simulation results support the considerations made in Section 7.6.1. While the discrepancy between ϑ_r and the actual energy θ_E had only little effect on the reference dynamics tracking of the cart-pendulum (small $e_{\check{r}} = 2.7\,\mathrm{deg}$ in Fig. 6.10), the usage of ϑ_r yielded a comparatively high steady state error of $e_t = 8.3\,\mathrm{deg}$ for the torque-pendulum. The estimate $\hat{\vartheta}_E$ accurately recovered the true energy θ_E also at high energies. Usage of $\hat{\vartheta}_E$ instead of ϑ_r in the amplitude factor computation in (6.28) reduced the steady state error

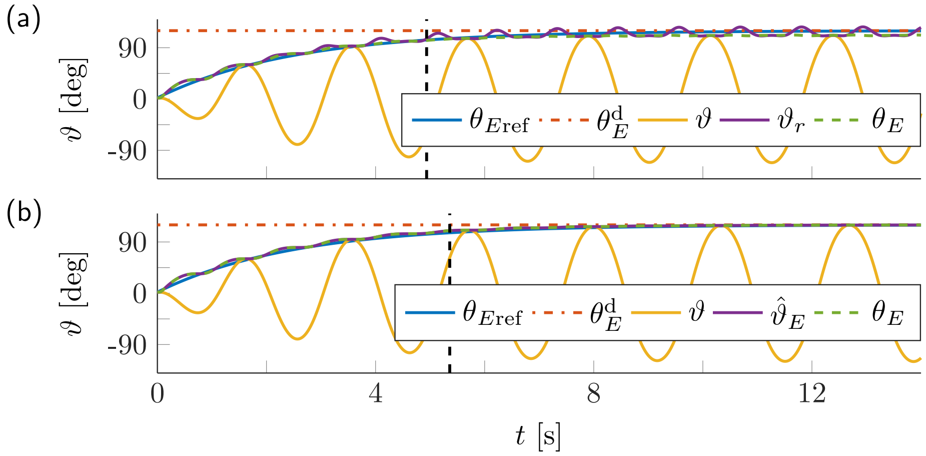

Fig. 7.7: Reference dynamics tracking for the torque-pendulum based on (a) energy equivalent phase space radius ϑ_r and (b) estimate $\hat{\vartheta}_E$: Desired and resultant angles and energy equivalents. Vertical dashed lines indicate settling times T_s. Usage of $\hat{\vartheta}_E$ instead of ϑ_r yields a smaller steady state error.

to $e_t = 0.5\,\mathrm{deg}$ for the torque-pendulum.

7.7.5 Follower contribution

For the follower contribution analysis, we ran simulations with a leader and a follower interacting with the abstract torque-pendulum under the same conditions as for the abstract cart-pendulum in Chapter 6.7.5. In accordance with the stability analysis in Chapter 6.5.3 and the considerations in Section 7.5, we initialized the ω-estimation with $\hat{\omega}(t=0) = 2\,{}^{\mathrm{rad}}/_{\mathrm{s}} < \omega$ for the abstract torque-pendulum. The follower and leader controller for the torque-pendulum made use of the approximation $\hat{\vartheta}_E$ in (7.9) instead of ϑ_r in (6.28) and (6.33).

The first three lines of Table 7.1 list the results for $\Gamma^\mathrm{d}_\mathcal{F} + \Gamma^\mathrm{d}_\mathcal{L} = 1$, including the relative follower contributions according to (6.36) and (6.37) and the overshoot $o = \max_t(\theta_E - \bar{\theta}_E)$ with respect to the energetic steady state $\bar{\theta}_E$. Figure 7.8 shows angles and energies over time for the most challenging case of $\Gamma^\mathrm{d}_\mathcal{F} = 0.7$. The last two lines of Table 7.1 list the results for $\Gamma^\mathrm{d}_\mathcal{F} + \Gamma^\mathrm{d}_\mathcal{L} \neq 1$. The results are in line with the results for the abstract cart-pendulum (compare Table 6.1 and Fig. 6.11).

7.8 Real-world experiments

The simulations in Section 7.7 analyze the presented control approach for the abstract torque-pendulum. In this section, we report on the results of real world experiments with a flexible object which test the controllers in realistic conditions: noisy force and torque measurements, non-ideal object and robot behavior and a human interaction partner.

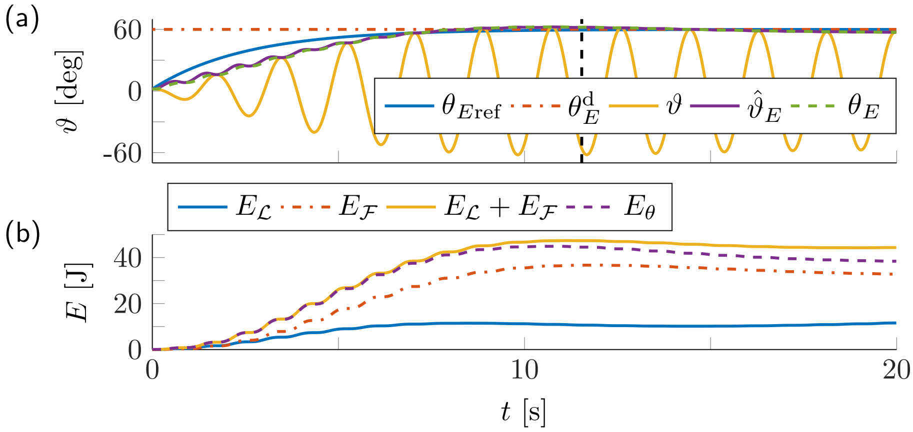

Fig. 7.8: Simulated follower and leader interacting with the abstract torque-pendulum for a desired relative follower contribution $\Gamma^{\mathrm{d}}_{\mathcal{F}} = 0.7$: (a) Angles and energy equivalents and (b) energies. The vertical dashed line indicates the settling time T_{s}. The fundamental dynamics-based controllers allow for successful effort sharing.

Tab. 7.1: Effort sharing results for the abstract torque-pendulum

$\Gamma^{\mathrm{d}}_{\mathcal{F}}/\Gamma^{\mathrm{d}}_{\mathcal{L}}$	o[deg]	$\Gamma_{\mathrm{in},\mathcal{F}}$	$\Gamma_{\mathrm{o},\mathcal{F}}$
0.3/0.7	0.1	0.33	0.33
0.5/0.5	1.1	0.52	0.54
0.7/0.3	4.9	0.78	0.82
0.3/0.3	0.1	0.31	0.33
0.7/0.7	6.5	0.86	0.90

7.8.1 Experimental setup

Hardware setup

Figure 7.9 shows the experimental setup with the flexible object. Except for the different object, we used the same hardware setup as for the experiments in Chapter 6.8. One side of the object was attached to the robot end effector. The other side was attached to a handle that was held by the human interaction partner.

Due to the small load capacity of the robotic manipulator, we used an object of relatively small mass $m_{\mathrm{o}} = 1.61\,\mathrm{kg}$. The flexible object was composed of an aluminum plate connected to two aluminum bars at a distance of $0.9\,\mathrm{m}$ through rubber bands. Such flexible object can be seen as an especially challenging object as it only loosely couples the agents and its high elasticity can cause unwanted oscillations. The distance between the agents' interaction points was $C \approx 1.5\,\mathrm{m}$.

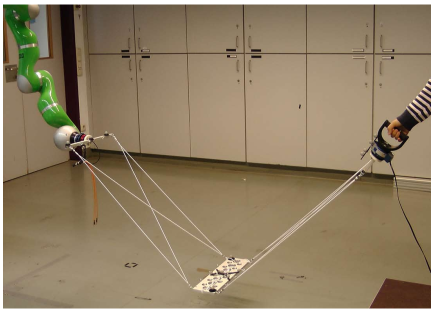

Fig. 7.9: Experimental setup for flexible object swinging: The robot behaved as a simple pendulum with human arm parameters.

Software implementation

The same software implementation was used as for the t-pendulum experiments in Chapters 5.7 and 6.8.

Controller parametrization

The following control parameters were the same as for the t-pendulum in Chapter 6.8: $\tau_{\mathcal{L}} = 0.4\,{}^{1}\!/\!{}_{\mathrm{s}}$, $T_{\mathcal{F}} = 1\,\mathrm{s}$, $D_{\mathcal{F}} = 1$, $\boldsymbol{l} = [3.6\,{}^{1}\!/\!{}_{\mathrm{s}},\ 0]$. We controlled the robot to behave as a simple pendulum (see Section 7.6.2) with human arm parameters given in Section 7.7.1. The wrist parameters were $j_\psi = 0.01\,\mathrm{kg\,m^2}$, $d_\psi = 4\,{}^{\mathrm{Nm\,s}}\!/\!{}_{\mathrm{rad}}$, $k_\psi = 3\,{}^{\mathrm{Nm}}\!/\!{}_{\mathrm{rad}}$. The projected object length estimate needed for the approximation of the abstract torque-pendulum moment of inertia $\hat{j}_\vartheta$ was set to $\hat{l}_{\mathrm{o}}^{*} = 0.64\,\mathrm{m}$. The ω-estimation used a time constant $T_\omega = 4\,\mathrm{s}$ and was initialized to $\hat{\omega}(t=0) = 2\,{}^{\mathrm{rad}}\!/\!{}_{\mathrm{s}}$.

7.8.2 Measures for analysis

We used the same measures as for the analysis of the t-pendulum experiments in Chapter 6.8. From θ, its numerical time derivative $\dot{\theta}$ and the small angle approximation of the natural frequency $\omega_0 = \frac{m_\vartheta c_\vartheta g}{j_\vartheta}$ approximated from actual system dimensions, the energy equivalent θ_E was obtained based on (4.6). For the controller performance analysis, the bounds for the settling time definition were set to $\epsilon_\theta = 8\,\%$.

For the flexible object, energy can also be injected through applied torque $\boldsymbol{t}_i$. Thus, the agents' energy flows to the flexible object result in $\dot{E}_{\mathrm{o},i} = \boldsymbol{f}_i^\top \dot{\boldsymbol{r}}_i + \boldsymbol{t}_i^\top \boldsymbol{\Omega}_i$, with rotational interaction point velocity $\boldsymbol{\Omega}_i$. Note that $\dot{E}_{\mathrm{o},i}$ only captures the energy flow to the flexible object contributed by agent Ai. As the complete energy flow contributed by the human to the afa-system (including energy flow injected into the arms) is unknown, we report on the energies related to the flexible object. Consequently, energy shares computed according to (6.36) and (6.37) based on $\dot{E}_{\mathrm{o},i}$ do only consider the energy contributions to the flexible object.

For the computation of the object energy E_{o}, we neglected energy contained in the rubber bands and the aluminum bars attached to the force/torque sensors and computed the energy contained in the aluminum plate of mass $m_{\mathrm{pl}} = 1.15\,\mathrm{kg}$ and dimensions length

$l_{\mathrm{pl}} = 0.115\,\mathrm{m}$, height $h_{\mathrm{pl}} = 0.012\,\mathrm{m}$ and width $w_{\mathrm{pl}} = 0.4\,\mathrm{m}$ under the simplifying assumption of uniform mass distribution.

7.8.3 Experimental conditions and procedure

Joint velocity limitations of the KUKA LWR restricted us to energies $\theta_E^{\mathrm{d}} \leq 30\,\mathrm{deg}$ for the afa-system experiments. We performed experiments under multiple conditions: different flexible objects, interaction with an active or passive human and different leader/follower role assignments. The following afa-system experiments are presented in detail:

Maximum achievable energy (RL-HP)

A human passively held the handle of agent A2 = H = P and interacted with a robot leader A1 = R = $\mathcal{L}$. The afa-system started from rest ($\theta_E(t=0) \approx \psi_E(t=0) \approx 0$). The desired energy level θ_E^{d} was incrementally increased from 10 deg to 30 deg. The desired relative energy contribution of the robot was set to $\Gamma_{\mathrm{R}}^{\mathrm{d}} = 1$.

Active follower contribution (RF-HL)

A robot follower A1 = R = $\mathcal{F}$ interacted with a human leader A2 = H = $\mathcal{L}$. The afa-system started from rest ($\theta_E(t=0) \approx \psi_E(t=0) \approx 0$). The human leader was asked to first inject energy to reach $\theta_E^{\mathrm{d}} = 25\,\mathrm{deg}$, to hold the energy constant and finally to release the energy from the object again. The desired energy limit was displayed to the human via stripes of tape on the floor to which the flexible object had to be aligned to at maximum deflection angles. Due to the limited maximum achievable system energy, we chose a higher and thus more challenging desired relative energy contribution of the robot follower of $\Gamma_{\mathrm{R}}^{\mathrm{d}} = 0.65$.

7.8.4 Results and Discussion

Maximum achievable energy (RL-HP)

Figure 7.10 shows the experimental results for a robot leader interacting with a passive human. The robot leader closely followed desired reference dynamics when swinging up the afa-system from rest to $\theta_E^{\mathrm{d}} = 10\,\mathrm{deg}$ with settling time $T_{\mathrm{s}} = 5.3\,\mathrm{s}$ and small steady state error $e = -0.9\,\mathrm{deg}$. As for the t-pendulum in Chapter 6.8.4, the steady state error increased with increasing system energy. The last step from $\theta_E^{\mathrm{d}} = 25\,\mathrm{deg}$ to $\theta_E^{\mathrm{d}} = 30\,\mathrm{deg}$ was reached with a small settling time $T_{\mathrm{s}} = 1.9\,\mathrm{s}$ and small steady state error $e = -0.6\,\mathrm{deg}$. Undesired oscillations ψ at the wrist stayed below $\psi_E < 4.3\,\mathrm{deg}$. The projection of the flexible object onto the abstract torque-pendulum was performed based on the sum $\theta^* = \psi + \rho$ and the simple pendulum observer. From Fig. 7.4 it seems like the sum $\psi + \rho$ overestimates the deflection angle at the shoulder. However, the known wrist angle ψ only reflects the orientation of the flexible object at the robot interaction point. The flexibility of the object caused greater deflection angles θ. Consequently, the abstract torque-pendulum energy equivalent ϑ_r closely followed the energy equivalent θ_E at small energies, but underestimated θ for increased energies. Nevertheless, the results are promising as they show

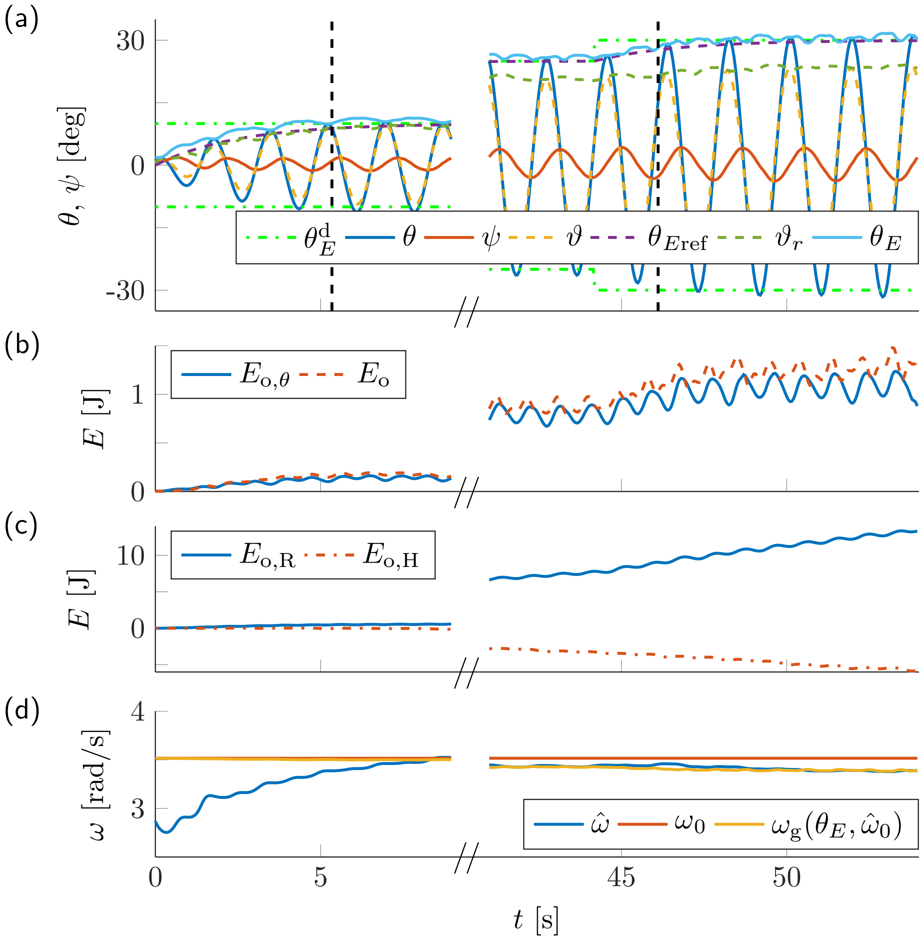

Fig. 7.10: Maximum achievable energies are limited by joint velocity limits for the afa-system to $\theta_E = 30\,\mathrm{deg}$: (a) Deflection angles and energy equivalents, (b) energies contained in the flexible object and (c) contributed by the human and the robot, (d) natural frequency estimates

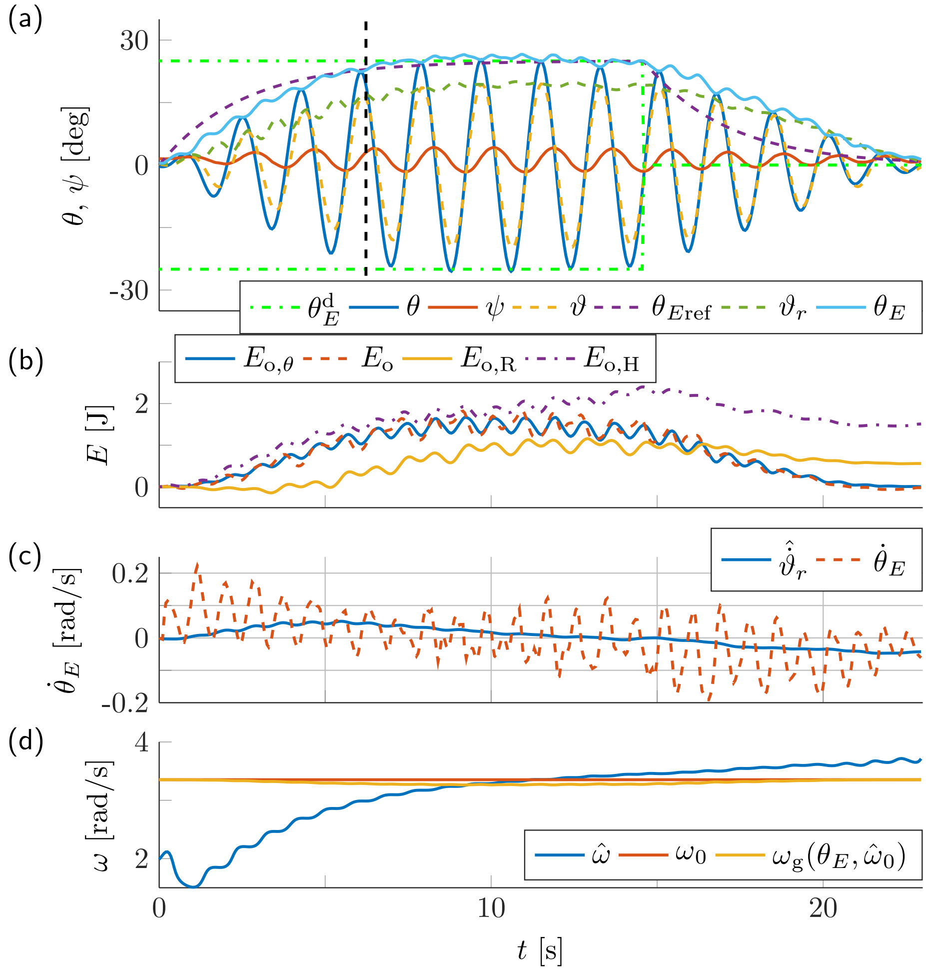

Fig. 7.11: Robot follower collaboratively injecting energy into the flexible object with a human leader: (a) Deflection angles and energy equivalents, (b) energies contained in the flexible object and contributed by the human and the robot, (c) actual and estimated energy flows, (d) natural frequency estimates. The energy contributions of the robot and the human show similar characteristics

that a controlled swing-up was achieved based on the virtual energy ϑ_r of the abstract torque-pendulum.

Active follower contribution (RF-HL)

The results of a human leader and a robot follower are displayed in Fig 7.11. The desired energy level of $\theta_E^{\mathrm{d}} = 25\,\mathrm{deg}$ was reached with a settling time $T_{\mathrm{s}} = 6.5\,\mathrm{s}$ and a steady state error $e = -0.9\,\mathrm{deg}$. Fig. 7.11(c) shows that that the robot correctly identified the swing-up and the swing-down initiated by the human partner. The human first injected energy into the passive robot arm which is equivalent to the robot initially withdrawing some energy from the object, before the robot can detect the object energy increase. Therefore and due to the filtering for the estimate $\hat{\dot{\vartheta}}_r$, the relative energy contributions of the follower yield only $\Gamma_{\mathrm{in,R}} = 0.22$ and $\Gamma_{\mathrm{o,R}} = 0.34$, when evaluated at the settling time T_{s}. However, the relative follower contribution increased and reached, e.g., $\Gamma_{\mathrm{in,R}} = 0.35$ and $\Gamma_{\mathrm{o,R}} = 0.62$ at $t = 11\,\mathrm{s}$. Thus, the follower successfully contributed to swing-up effort. Note that the flexible object exhibited higher natural damping than the t-pendulum (e.g., compare Fig. 7.11(b) and Fig. 6.14(b)), which caused the increased difference between $\Gamma_{\mathrm{in,R}}$ and $\Gamma_{\mathrm{o,R}}$.

Interestingly, the energy contribution of the human and the robot were of similar shape, both for a robot follower and a robot leader. Thus, the simple pendulum-like behavior of the robot end effector allows to replicate human whole-arm swinging characteristics.

7.9 Discussion of the fundamental dynamics-based approach

In the following, we discuss the fundamental dynamics-based controller synthesis approach followed in this and the previous chapter with respect to robotic architectures, generalizability, dependence on the human partner's behavior and alternative control concepts.

7.9.1 Embedding of proposed controllers in a robotic architecture

One of the major goals of robotics research is to design robots that are able to manipulate unknown objects in a goal-directed manner without prior model knowledge or tuning. Robot architectures are employed to manage such complex robot functionality [161]. These architectures are often organized in three layers: the lowest layer realizes behaviors which are coordinated by an intermediate executive layer based on a plan provided by the highest layer. In this work, our focus is on the lowest layer: the behavior of collaborative energy injection into swinging motion, which is challenging in itself due to the underactuation caused by the multitude of DoFs of the pendulum-like and flexible objects. On the behavioral layer, we use high-frequency force and torque measurements to achieve continuous energy injection and robustness with respect to disturbances. The controllers presented implement the distinct roles of a leader and a follower. As known from human studies, humans tend to specialize, but do not rigidly stick to one role but continuously blend between leader and follower behaviors [152]. Role mixing or blending would be triggered by the executive layer. The executive layer would operate at a lower frequency and would have access to additional sensors as, e.g., a camera that allows to monitor task execution. Based on the additional sensor measurements, exceptions could be handled (e.g., when a wrong oscillation degree of freedom is excited as in Chapter 6.8.4), the required swinging amplitude θ_E^{d} could be set and behavior switching could be triggered (e.g., from the object swing-up behavior to an object placement behavior).

Furthermore, additional object specific parameters could be estimated on the executive layer, as, e.g., damping or the elastic deformation of the object. The fundamental dynamics approach does not model damping, and consequently $\Gamma_{\mathrm{o,R}} \approx \Gamma_{\mathrm{R}}^{\mathrm{d}}$ indicates that the controller exhibits the desired behavior. However, that also means that $\Gamma_{\mathrm{in,R}} < \Gamma_{\mathrm{R}}^{\mathrm{d}}$, as the leader compensates for damping. As all realistic objects exhibit non negligible damping, an increased robot contribution during swing-up can be achieved by increasing $\Gamma_{\mathrm{R}}^{\mathrm{d}}$. The desired relative energy contribution $\Gamma_{\mathrm{R}}^{\mathrm{d}}$ could thus serve as a single parameter that could, for instance, be adjusted online by the executive layer to achieve a desired robot contribution to the swing-up. Alternatively to an executive layer, a human partner could adjust a parameter as $\Gamma_{\mathrm{R}}^{\mathrm{d}}$ online to achieve desired robot follower behavior and could also assure excitation of the desired oscillation.

7.9.2 Dependence of robot follower performance on the human interaction partner

Performance measures as settling time T_{s} and steady state error e strongly depend on the behavior of the human partner. The robot follower is responsible for the resultant effort sharing. Ideally, the robot follower contributes with the desired fraction to the current change in object energy at all times $\dot{\vartheta}_{r,\mathcal{F}} = \Gamma_{\mathcal{F}}^{\mathrm{d}}\dot{\vartheta}_r$. Necessary filtering and the approximations made by the fundamental dynamics do result in a delayed follower response and deviation from the desired relative energy contribution. However, for the follower, we do not make any assumptions on the way how humans inject energy into the system, e.g., we do not assume that human leaders follow the desired reference dynamics that we defined for robot leaders. This is in contrast to the controllers presented in Chapter 5, where additional thresholds could be tuned with respect to human swing-up behavior and the follower required model knowledge to compute the energy contained in the oscillation. For demonstration purposes, we aimed for a smooth energy injection of the human leader for the experiments presented in the previous section. Energy was not injected smoothly to match modeled behavior, but only to enable the use of measures as the relative energy contribution at the settling time for effort sharing analysis.

7.9.3 Alternatives to energy-based swing-up controllers

Energy-based controllers as [188] are known to be less efficient than, e.g., model predictive control (MPC) based controllers [122]. MPC can improve performance with respect to energy and time needed to reach a desired energy content. However, in this work, we do not aim for an especially efficient robot controller, but for collaborative energy injection into unknown objects. Use of MPC requires a model, including accurate mass and moment of inertia properties. Use of the energy-based controller of [188] allows to derive the fundamental dynamics as an approximate model. The fundamental dynamics reduces the unknowns to the natural frequency ω and moment of inertia estimate j_{ϑ} for the afa-system, which can be estimated online. Design of a follower controller is only possible, because the fundamental dynamics allows for a comparison of expectation to observation. How to formulate the expectation for an MPC-based approach is unclear and would certainly be more involved. The great advantage of the fundamental dynamics-based approach lies in its simplicity.

7.9.4 Alternative parameter estimation approaches

In this work, the goal of a leader controller is to track desired reference dynamics. Such behavior could also be achieved by employing model reference adaptive control (MRAC) [5] or by employing filters to compare applied amplitude factors a to the achieved energy increase to estimate the unknown fundamental dynamics parameter B. The disadvantage of MRAC and other approaches is that they need to observe the system energy ϑ_r online to estimate the system constant B. Having another agent interacting with the system as well, does not only challenge the stability properties of MRAC, but also makes it impossible to design a follower agent that requires a parameter estimate of B to be able to differentiate between its own and external influence on the system energy.

The fundamental dynamics approximates the system parameter B by its mean, while the true value oscillates. The mean parameter B depends on the natural frequency ω, which can be approximated by observing the phase angle φ. Because the fundamental dynamics states system energy ϑ_r and phase angle φ are approximately decoupled, reference dynamics tracking and energy flow imitation can be achieved for unknown objects.

The natural frequency ω could alternatively be estimated by observing the time required by a full swing. Decrease of the observation period yields the continuous simple low-pass filter used in this article. Alternatively, the desired circularity of the phase space could be used to employ methods such as gradient descent [138] or Newton Raphson to estimate the natural frequency. We chose the presented approach for its continuity and simplicity, as well as its stability properties with respect to the fundamental dynamics assumption.

7.9.5 Stability of human-robot object manipulation

We proved global stability of the presented control approach for the linear fundamental dynamics. Stability investigations of the human-robot flexible object manipulation face several challenges. Firstly, dynamic models of the complex t-pendulum and afa-system would be required. Furthermore, the human interaction partner acts as a non-autonomous and non-reproducible system that is difficult to model and whose stability cannot be analyzed based on common methods [17]. In [80], Hogan presents results that indicate that the human arm exhibits the impedance of a passive object; however, this result cannot be directly applied to show stabilization of limit cycles, as the simple pendulum oscillation in this work, for a passivity-based stability analysis [95]. A stability analysis of the simpler, but nonlinear abstract simple pendulums requires a reformulation of the system dynamics in terms of the errors $\Delta\hat{\omega} = \omega - \hat{\omega}$ and $\Delta\vartheta_E = \vartheta_E^{\mathrm{d}} - \vartheta_E$. The lack of analytic solutions for $\omega(\vartheta_E)$ [24] and $\vartheta(\vartheta_E, \varphi)$ (see Section 6.4.2) impede the derivation of the error dynamics above.

As our final goal is collaborative dynamic human-robot interaction, we refrained from further stability investigations and focused on simulation- and experiment-based analyses. The simulations and human-robot experiments suggest that the domain of attraction of the presented fundamental dynamics-based controllers is sufficiently large to allow for collaborative energy injection into nonlinear high energy regimes.

7.10 Conclusions

This chapter combined the insights gained from studying rigid object swinging in Chapter 4 and swinging of pendulum-like objects in Chapters 5 and 6. Based on the results of Chapter 4, we controlled the robot arm to behave as a passive simple pendulum of human-like arm parameters. The simple pendulum-like nature of the desired swinging motion showed to be have similar underlying fundamental dynamics as for the pendulum-like objects in Chapter 6. As a consequence, the fundamental dynamics-based adaptive leader and follower controllers derived in Chapter 6 could be used. Follower and leader controllers shape the shoulder torque of the simple pendulum-like robot arm to control the oscillating entity composed of the agents' arms and a flexible object to a desired periodic orbit. Experimental results showed that a robotic leader can track desired reference dynamics during swing-up to a desired energy level. Furthermore, a robot follower actively contributed to the swing-up effort in interaction with a human leader according to a desired energy share. Although joint velocity limits of the robotic manipulator restricted swinging amplitudes to 30 deg for the "arm – flexible object – arm" system, the experimental results support the efficacy of our approach to human-robot collaborative swinging of unknown flexible objects.

Open problems

Having tackled collaborative energy injection, a second step towards human-robot collaborative dynamic object manipulation can be taken by investigating controlled object placement as the phase following the joint energy injection. Another interesting future work is the application of the presented technique of approximating the desired behavior by its fundamental dynamics to different manipulation tasks.

8 Conclusions and future directions

This thesis addressed collaborative human-robot object manipulation along two distinct scenarios: collaborative object transport as an example for kinematic manipulation and collaborative energy injection into flexible objects as an example for dynamic manipulation. The focus was on exploiting the physical coupling through the jointly manipulated object: robot agents were limited to information on the own effector configuration and wrench measured at the own end effector. In the following, we summarize our contributions and present our main conclusions along the design methodology followed throughout this thesis (see Fig. 8.1 and 8.2): combining insights gained from studying physical human-human collaboration (pHHC) with system theoretic approaches to synthesize controllers for physical human robot collaboration (pHRC). The thesis concludes with an outlook on topics of interest for future research.

Kinematic manipulation

Tight grasps of rigid objects allow inference of the object state through kinematic considerations based on knowledge of the own end effector configuration. Beyond the possibility of object state estimation, the physical coupling through the object establishes a haptic communication channel, i.e. the agents can convey intent as desired movement direction and speed via applied force and torque. Interpretation of the measured interaction forces and torques requires appropriate measures, which we derived in Chapter 2. In Chapter 3, we conducted a human-human study to understand the role of haptic communication during collaborative object transport. Thus, with respect to kinematic manipulation we mainly addressed the building blocks *analysis of pHHC* and *measures* of our design methodology as depicted in Fig. 8.1.

During multi-effector object manipulation not all applied forces and torques (i.e. wrench) lead to motion, but partly compensate each other. Chapter 2 proposed a wrench decomposition that allows for the first time to separate applied wrench into compensation and manipulation wrench for general rigid objects manipulated by multiple effectors, while ensuring physically consistent results. We formulated the wrench decomposition problem as a convex optimization with physical consistency constraints on the actually applied wrench. For the task of two agent object transport, we presented a real-time capable analytical solution that requires approximation only for special cases. Based on the wrench decomposition, measures to quantify disagreement, load and energy share as of interest in evaluating physical human-human and human-robot interaction were derived.

Chapter 3 presented a human-human study aimed at analyzing intention communication strategies and coordination patterns during collaborative object transport. The wrench-based measures derived in Chapter 2 allowed to analyze the importance of haptic communication and dominance related coordination patterns. The study confirmed our expectation that humans make use of a combination of haptic communication and

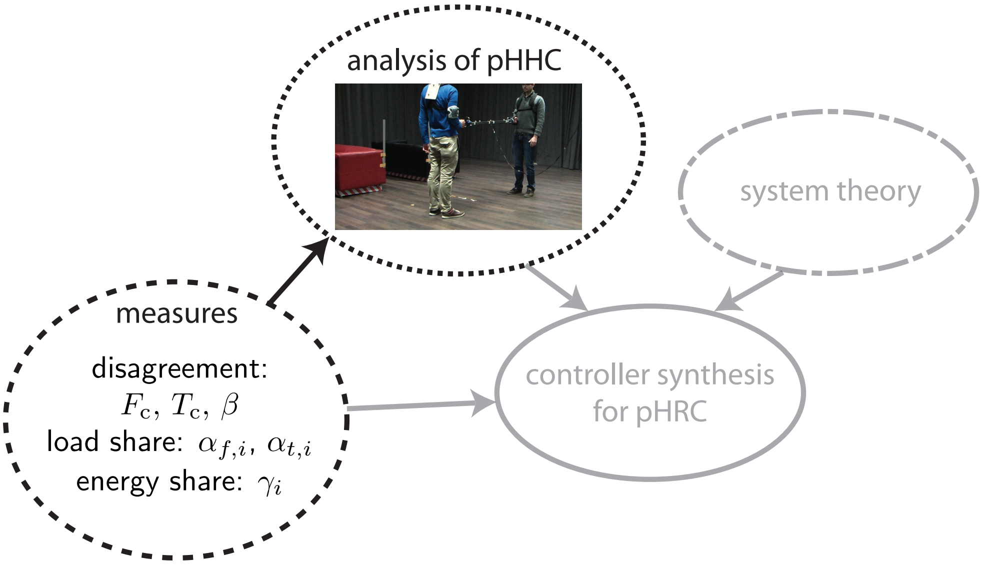

Fig. 8.1: Design methodology followed for controller synthesis for human-robot collaborative kinematic object manipulation: A pHHC study revealed intention communication strategies and coordination patterns apparent during human-human collaborative object transport. Physically consistent wrench decomposition and derived measures allow to quantify disagreement, load and energy share for analysis, comparison and evaluation of pHHC and pHRC.

legible motion depending on task setup and role assignments in order to convey intent during collaborative object transport: when intention clarification was needed, the participants altered the object motion and applied wrench to convey their intent. Compensation wrench analysis showed that the participants slightly pushed against each other also after a decision had been made, supporting the hypothesis that humans aim for non zero compensation force, e.g., in order to "feel each other". Increasing compensation wrench with increasing uncertainty suggests the establishment of a haptic communication channel. Dominance analysis based on the measures load and energy share revealed different coordination patterns during collaborative object transport, reflecting task knowledge and task setup.

The proposed wrench decomposition is the first to yield physically consistent results for general manipulation tasks without assumptions. Only effector interaction point locations with respect to the CoM of the object and the applied wrenches have to be known. Application of the derived wrench-based measures to the human-human study exemplified their extensive applicability as a powerful tool for pHHC analysis. The proposed measures can now be readily applied to pHRI tasks, e.g., to compare different wrench synthesis methods. While the focus of this thesis was on human-robot collaborative object manipulation, the derived measures can be applied to any physical interaction task that allows to measure applied wrench: e.g., to investigate human multi-digit grasping or to evaluate controllers for multi-robot object manipulation. The simulated assistance scenario of a human being supported by a robotic walker illustrates the straight forward applicability of the proposed approach to physical human-robot interaction scenarios beyond collaborative object

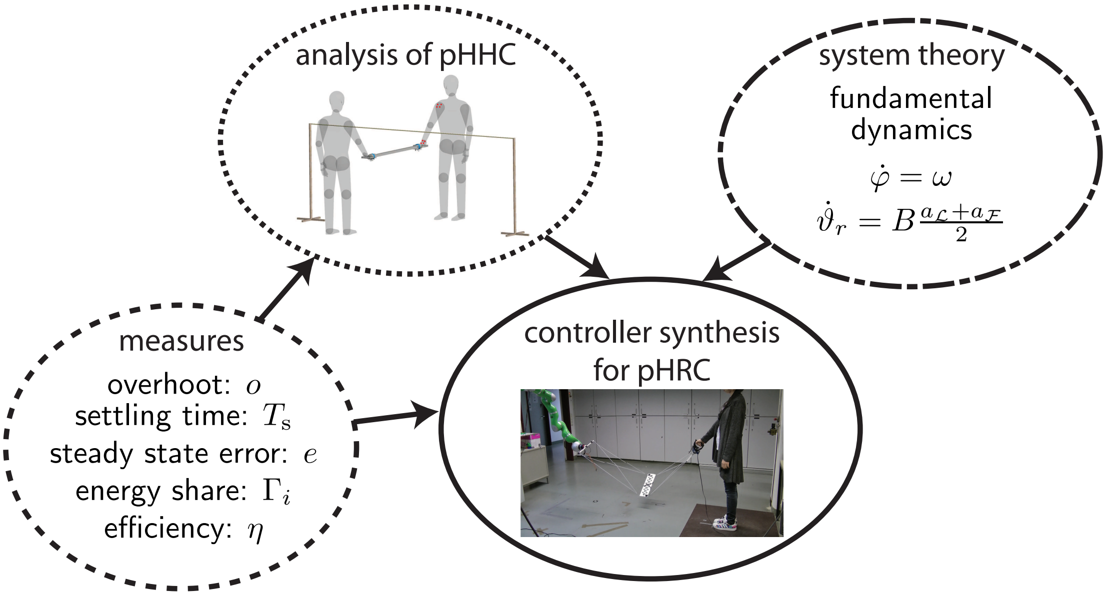

Fig. 8.2: Design methodology followed for controller synthesis for human-robot collaborative dynamic object manipulation: Combining insights from human-human rigid object swinging with simple pendulum fundamental dynamics to synthesize adaptive leader and follower controllers for human-robot collaborative energy injection into unknown flexible objects. Measures as integrated energy share, efficiency and steady state error are used to continuously analyze, compare and evaluate pHHC and pHRC.

manipulation.

An important finding of this thesis is that there is no unique wrench decomposition solution. The proposed scalarized multi-objective optimization depends on the choice of weighting and selection parameters. Thus, it is possible to find physically consistent decompositions, but the multitude of solutions makes us conclude that the one and only correct wrench decomposition solution does not exist.

Dynamic manipulation

This thesis took a first step into the largely unexplored field of collaborative dynamic object manipulation by studying collaborative energy injection into flexible objects. In contrast to kinematic manipulation, dynamic manipulation requires to take the object dynamics into account, i.e. the object state cannot be inferred from the effector configuration based on kinematic relationships.

We approached the complex task of flexible object swinging by splitting it up into its extremes with respect to the strength of the physical coupling: swinging of rigid objects and swinging of pendulum-like objects. While the strong coupling through a rigid object makes human-likeness of the robot trajectory a necessity for comfortable pHRC, and thus pushed our focus to pHHC studies in Chapter 4, the rather weak coupling through pendulum-like objects allowed us to take a more system theoretic approach in Chapters 5 and 6 (see Fig. 8.2). Chapter 7 combined the human insights gained with system theoretic developments for human-robot collaborative flexible object swinging.

For dynamic manipulation tasks, a direct mapping from applied wrench to intended trajectory is not applicable. Instead, the intention for the swing-up task was captured in a desired periodic orbit described by a constant level of swing energy to be reached. We introduced energy flow observation and imitation based on measured wrench as a novel follower approach for active contribution to the swing-up effort. For the analysis of pHHC and evaluation of the proposed controllers in pHRC we adapted existing measures as steady state error, overshoot and settling time, introduced an efficiency measure and extended the energy share measure derived in Chapter 2.

Chapter 4 addressed rigid object swinging by investigating pHHC. Movement path and frequency characteristics indicated that human arms behave simple pendulum-like during collaborative swinging of heavy objects. Based on the experimental results, we modeled human-human rigid object swinging as the ara-system: shoulder torque actuated cylindrical arms connected through the rigid object. Synchronized swinging of the ara-system was further approximated as an abstract torque-pendulum: a simple pendulum with additive shoulder torque inputs of the two agents. We synthesized a leader controller projecting the ara-oscillation onto the abstract torque-pendulum and applying unidirectional pulsed forcing as observed during the human-human experiments. In interaction with a simple disturbance damping follower controller, the simulated ara-system achieved a synchronized swing-up while replicating observed characteristics of human-human rigid object swinging.

Chapter 5 took a system theoretic approach to swinging of known complex pendulum-like objects. The weak coupling through the pendulum-like object inspired approximation of the agents' influence as one-dimensional acceleration inputs. Synchronized swing-up was then modeled through an abstract cart-pendulum with additive acceleration inputs. Projection of the complex pendulum-like objects onto the abstract cart-pendulum allowed to differentiate between and to individually control desired and disturbance oscillations. Actively contributing follower behavior was achieved through energy flow monitoring based on measured applied force. A virtual reality study of mixed human and robot teams swinging up a v-shaped pendulum revealed similar performance of human and robot leaders and followers. A full scale human-robot experiment showed that active damping of the disturbance oscillation was not necessary and even irritated a human partner.

Chapter 6 alleviated the restrictions of known object properties and advanced the leader and follower controllers proposed in Chapter 5. We derived the fundamental dynamics of the desired abstract cart-pendulum swing-up behavior. The fundamental dynamics enabled estimation of the natural frequency of the desired oscillation and the synthesis of adaptive leader and follower controllers: a leader tracking desired energy dynamics and a follower controller imitating the leader's energy flow according to a desired energy share. The control approach was successfully validated in human-robot interaction: a robot leader achieved swinging amplitudes of more than 80 deg and a robot follower actively contributed to the swing-up effort when interacting with a human leader.

Chapter 7 combined the fundamental dynamics-based control approach derived in Chapter 6 with the human insights gained from rigid object swinging in Chapter 4 for collaborative swinging of unknown flexible objects. We modeled the flexible object together with the agents' arms as the afa-system: shoulder torque actuated cylinders of human-like arm parameters connected to the flexible object via passive wrist joints. As in Chapter 4, an abstract torque-pendulum approximated the desired synchronized oscillation. The fundamental dynamics of the abstract torque-pendulum turned out to be similar to the one of the abstract cart-pendulum in Chapter 6 allowing for an application of the same leader and follower controllers. We successfully validated the proposed controller in human-robot experiments. To this end, the robotic manipulator was controlled to behave as a shoulder torque actuated simple pendulum of human-like arm parameters. The maximum reachable swinging amplitude was limited to 30 deg due to joint velocity limits.

The main assumption made in this thesis with respect to collaborative energy injection is that the desired oscillation is simple pendulum-like. Based on this assumption, the proposed approach is generalizable in the sense that it can be directly applied to the joint swing-up of unknown objects without parameter tuning. We regard the case of a robotic follower interacting with a human leader as an interesting and challenging scenario and therefore presented our method from the human-robot collaboration perspective. Nevertheless, the proposed method can also directly be employed for robot-robot teams or single robot systems as, e.g., quadrotors and can also be used to damp oscillations instead of exciting them. The task of joint energy injection into a flexible bulky object might appear to be a rare special case. However, it is a basic dynamic manipulation skill that humans possess and should be investigated in order to equip robots with universal manipulation skills. We see the main take away message for future research from this work in the advantage of an understanding of the underlying fundamental dynamics. Based on the fundamental dynamics that encodes desired behavior, simple adaptive controllers can be designed and readily applied to complex tasks and even when task parameters change drastically, as, e.g., when objects of different dimensions have to be manipulated.

8.1 Outlook

From wrench analysis to wrench synthesis

The physically consistent wrench decomposition derived in Chapter 2 can be readily applied to the analysis of pHHI and pHRI tasks, e.g., to study human-human interaction as done in Chapter 3 or to evaluate and compare robot controllers in human-robot interaction. For wrench synthesis, common pseudoinverse approaches can be straightforwardly used, if equal load share and a fixed force induced torque to applied torque relation are acceptable. The parametrized pseudoinverse proposed in [55] only partly alleviates the restrictions above; i.e. for the beam transport task only the induced torque to applied torque relation is adjustable, while the load share between the agents remains fixed. The null space approach of [131] allows to choose a desired load share along a redundant direction. Nonetheless, their approach is currently limited to 1D, ignoring rotation, with the result of not directly relating to our proposed general load share measures. The derivation of a general wrench synthesis method that achieves a desired load share or controls compensation wrench for haptic communication is an interesting and challenging topic for future research. A generally applicable wrench synthesis method would add a valuable system theoretic tool (Fig. 8.1) allowing to further exploit the null-space available during object manipulation along a desired trajectory. Robot control can then be tuned more accurately to user behavior and intention in pHRC.

Transfer of pHHC intention communication strategies to pHRC

The pHHC study presented in Chapter 3 revealed legible motion and wrench as intention communication strategies during collaborative object transport. In a next step, the identified intention communication strategies can be transferred to a high-level robot controller, that on the one hand side observes measured wrench and object motion to infer the partner's movement intention and on the other hand modifies its applied wrench and motion to convey its own intent. Our focus on object information only, i.e. the participants' wrench applied to the object and the object motion, simplifies transfer to robot controllers as no additional sensors to, e.g., interpret the partner's gaze are needed. Nevertheless, humans likely retrieve further valuable information through observation of the partner's body and head orientation, and through gestures, mimicry and speech. Whether object information, preferably pose and wrench measurements at the own effector, are sufficient for intention communication during collaborative object transport needs to be evaluated in pHRC experiments.

Online estimation of wrench measures

In order to transfer pHHC wrench-based intention communication strategies to pHRC, robot controllers need to be able to mimic observed wrench measures. The measures proposed in Chapter 2 take as input the applied wrench of all agents to compute disagreement, load and energy share measures. Feedforward control is often based on, e.g., a desired energy or load share and thus the assumption that the other agents comply with it (see, e.g., [131] or the follower controllers in Chapter 6 and 7). Thus, a feedback controller would be desirable that drives the difference between desired and current wrench measures to zero. Online monitoring of wrench measures as proposed in Chapter 2 does, however, require access to the applied wrench of all agents. As stated above, a robotic agent preferably only needs to have access to pose and wrench measurements at the own effector. Hence, research towards online estimation of the other agents' applied wrench given restricted a priori knowledge of object parameters is of interest.

Legible trajectory planning

The transfer of the observed pHHC motion-based intention communication strategies to pHRC requires legible trajectory generation. Dragan and Srinivasa proposed to generate legible reaching trajectories by iteratively altering a predictable trajectory towards a legible trajectory [48]. Predictable trajectories for reaching tasks were shown to minimize a simple cost function: the sum of squared velocities. As a result, also modification of predictable trajectories towards legible trajectories can be performed efficiently through repeated optimizations. The cost function describing predictable collaborative object transport is, however, unknown and expected to be highly complex. Lawitzky et al. found that even for a simple point mass, online trajectory generation based on squared velocity and squared applied force minimization is computationally not tractable [110]. As the observed behavior in Chapter 3 indicates that additionally a collaborative aspect should be incorporated into the cost function, we conclude that repeated optimization for online legible motion generation during physical interaction is not feasible. Approaches to be investigated in future work could range online modification of offline computed trajectories based on simple rules deduced from pHHC experiments to learning from interaction-based approaches, as, e.g., [167].

Analysis of different object manipulation setups

The study in Chapter 3 analyzed one specific setup with a tendency to favor motion-based over wrench-based intention communication. With the partners starting at equal distance from the final platform, applied wrench along the beam at the initial configuration did not represent an unambiguous haptic signal. The one-handed interaction with the beam further impeded the application of torque, which would have represented an unambiguous haptic signal. Thus, the investigation of object manipulation scenarios that differ with respect to the manipulated object, interaction points, start and goal configuration, task type and difficulty and number of interacting agents are of interest to further investigate the importance of haptic communication. The objects to be manipulated could be non-symmetric and could vary from small and heavy to light but bulky. Besides object transport through scenes of different complexity, e.g., static and dynamic obstacles, collaborative mounting and tasks leaving purely kinematic manipulation towards dynamic manipulation can reveal interesting insights to pHHC.

Controlled object placement

In this thesis, we took a first step towards collaborative dynamic object manipulation by investigating the task of joint energy injection into flexible objects. A second step towards human-robot collaborative dynamic object manipulation can now be taken by investigating controlled object placement at elevated locations as the phase following the joint energy injection. Along our pHRC design methodology, we propose to initially investigate human motion during dynamic object placement. From a system theoretic point of view, the approaches presented in [32] and investigation of the fundamental dynamics describing desired object placement are of interest. The gained human and system theoretic insights can then be combined for robot controller synthesis.

Extended user studies of dynamic pHHC and pHRC

Along our design methodology in Fig. 8.2, we investigated pHHC, derived and applied system theoretic approaches and combined our results to synthesize robot controllers for pHRC. Nevertheless, the studies presented were limited in the number of participants and the participants had prior experience with robots. An extended user study comparing human-human object swinging to human-robot object swinging to further evaluate the proposed fundamental dynamics-based controller would be of interest.

Integration of the collaborative energy injection behavior into a robotic architecture

Design of robotic agents capable of robustly manipulating unknown objects in a goal-directed manner without prior model knowledge or tuning requires perception, reasoning, planning and control at different levels. Hierarchical robot architectures aim at achieving complex robot functionality by breaking it up into different layers [161]: e.g., the top layer generates a plan based on which an intermediate executive layer coordinates a behavior realized at the lowest layer. Chapters 4- 7 designed low-level behavior of collaborative energy injection into swinging motion implemented in a high frequency control loop. An executive layer would monitor the low-level task execution at a lower frequency based on additional sensors as, e.g., cameras, handle exceptions and trigger switching between behaviors. An example for exception handling would be oscillation damping in case the wrong oscillation has been excited (see Chapter 6.8.4). Behavior switching could, e.g., be performed from object swing-up behavior to an object placement behavior once a required swinging amplitude is reached. Also role blending could be initiated between leader and follower low-level behavior as observed for humans [152]. Additionally, the executive layer can coordinate parameter identification behaviors, e.g., of object parameters as damping or elastic deformation.

A Work vs. force constraints

Schmidts et al. derive the force constraint (2.9) based on the requirement that a manipulation force $f_{\mathrm{m},i}$ cannot do more mechanical work than the projection of the corresponding applied force f_i onto the manipulation force (see Lemma 1 in [158]). In the following, we show that for work computations, the applied force f_i instead of its projection onto $f_{\mathrm{m},i}$ needs to be considered. Work constraints that ensure that a manipulation force cannot do more work than its corresponding applied force can be formulated as

$$0 \overset{(>)}{\leq} f_{\mathrm{m},i}^{\top} n \mathrm{d}s \overset{(>)}{\leq} f_i^{\top} n \mathrm{d}s, \tag{A.1}$$

$$0 \overset{(>)}{\leq} t_{f\mathrm{m},i}^{\top} q \mathrm{d}\phi \overset{(>)}{\leq} t_{f,i}^{\top} q \mathrm{d}\phi, \tag{A.2}$$

for an infinitesimal translational displacement $\mathrm{d}n = n\mathrm{d}s \in \mathbb{R}^3$ with $\left\|n\right\| = 1$ and an infinitesimal rotational displacement $\mathrm{d}q = q\mathrm{d}\phi \in SE(3)$ with $\left\|q\right\| = 1$.

However, above work constraints are not equivalent to the circular force constraint (2.9), as illustrated for an example decomposition in Fig. A.1. In order to ensure the work of $f_{\mathrm{m},i}$ is bounded by the work of f_i, the current direction of translational velocity $n = \dot{p}_{\mathrm{o}} / \left\|\dot{p}_{\mathrm{o}}\right\|$ and rotational velocity $q = \omega_{\mathrm{o}} / \left\|\omega_{\mathrm{o}}\right\|$ of $\{\mathrm{o}\}$ have to be taken into account. In this work, we refrain from requiring a manipulation wrench to obey work constraints (A.1) and (A.2). The resultant object wrench h_{o} could also be needed to withstand an external force such as gravity, which might come along with zero velocity. Our aim is to use wrench decomposition to analyze the extent to which the wrench applied at the individual effectors h_i effects the resultant object wrench h_{o}, and how much of it is compensated, independent of the current object velocity. Such analyses could reflect control delegation or coordination efficiency of multi-fingered grasping as well as among physically interacting agents. An important result of above considerations is that h, and not h_{m}, needs to be used to compute energy measures as illustrated in the case of energy share in Sec. 2.5.

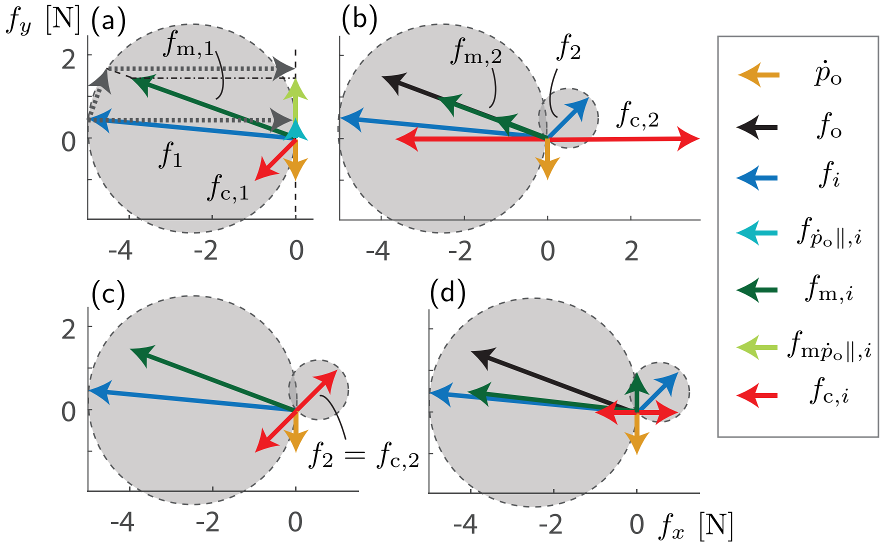

Fig. A.1: Effect of work and force constraints: (a) the decomposition of f_1 into $f_{\mathrm{m},1}$ and $f_{\mathrm{c},1}$ adheres to the circular force constraint (2.9), but not to the work constraint $(\mathrm{A}.1)$ as the projections onto velocity $\dot{p}_\mathrm{o}$, $f_{\dot{p}_\mathrm{o}\|,1}$ and $f_{\mathrm{m}\dot{p}_\mathrm{o}\|,1}$, show that $0 > f_1^\top n ds > f_{\mathrm{m},1}^\top n ds$ for $n = \dot{p}_\mathrm{o}/\left\|\dot{p}_\mathrm{o}\right\|$. The gray dotted arrows illustrate that the applied force f_1 and not its projection onto the manipulation force $f_{\mathrm{m},1}$ is relevant for work computations. Optimization results for cost (2.18) and a point mass $n = 2$ with (b) only work constraint $(\mathrm{A}.1)$, (c) only force constraint (2.9), (d) work and force constraints $(\mathrm{A}.1)$ and (2.9).

B The 2D beam solution

For the 2D beam, analytic solutions for the wrench decomposition according to (2.18)-(2.22) exist for almost all cases, which are the same for all selection variables $s \in \{0, 1\}$ and weightings $w \in \,]0,\ 1[$. Only for special cases (cases 2d and 4d in the following), optimization is needed or the solution can be approximated through what we refer to as the "prioritized torque through torque compensation" (pTtTC). In the following, we seperate the wrench decomposition problem into different cases based on the signs of the applied forces (cases 1-4) and the signs and magnitudes of the applied torques (sub cases a-e)

- **Case 1:** $\mathrm{sgn}(f_{1x}) = \mathrm{sgn}(f_{2x}) \wedge \mathrm{sgn}(f_{1y}) = \mathrm{sgn}(f_{2y})$
- **Case 2:** $\mathrm{sgn}(f_{1x}) = \mathrm{sgn}(f_{2x}) \wedge \mathrm{sgn}(f_{1y}) \neq \mathrm{sgn}(f_{2y})$
  - **a:** $|t_{\mathrm{c},iz}| = 0$
  - **b:** $\mathrm{sgn}(t_{1z}) = \mathrm{sgn}(t_{2z}) \neq \mathrm{sgn}(t_{f,1z}) \wedge |t_{1z} + t_{2z}| > |2t_{f\mathrm{c,max}z}|$
  - **c:** $\mathrm{sgn}(t_{1z}) = \mathrm{sgn}(t_{2z}) \neq \mathrm{sgn}(t_{f,1z}) \wedge |t_{1z} + t_{2z}| < |2t_{f\mathrm{c,max}z}|$
  - **d:** $(\mathrm{sgn}(t_{f,1z}) = \mathrm{sgn}(t_{kz}) \neq \mathrm{sgn}(t_{jz}))$
    $\wedge\, (|2t_{f\mathrm{c,max}z} + t_{kz}| > |t_{jz}|)\ \forall k, j \in \{1,\ 2\}, k \neq j$
  - **e:** $(\mathrm{sgn}(t_{f,1z}) = \mathrm{sgn}(t_{kz}) \neq \mathrm{sgn}(t_{jz}))$
    $\wedge\, (|2t_{f\mathrm{c,max}z} + t_{kz}| < |t_{jz}|)\ \forall k, j \in \{1,\ 2\}, k \neq j$
- **Case 3:** $\mathrm{sgn}(f_{1x}) \neq \mathrm{sgn}(f_{2x}) \wedge \mathrm{sgn}(f_{1y}) = \mathrm{sgn}(f_{2y})$
- **Case 4:** $\mathrm{sgn}(f_{1x}) \neq \mathrm{sgn}(f_{2x}) \wedge \mathrm{sgn}(f_{1y}) \neq \mathrm{sgn}(f_{2y})$
  - **a:** $|t_{\mathrm{c},iz}| = 0$
  - **b:** $\mathrm{sgn}(t_{1z}) = \mathrm{sgn}(t_{2z}) \neq \mathrm{sgn}(t_{f,1z}) \wedge |t_{1z} + t_{2z}| > |2t_{f\mathrm{c,max}z}|$
  - **c:** $\mathrm{sgn}(t_{1z}) = \mathrm{sgn}(t_{2z}) \neq \mathrm{sgn}(t_{f,1z}) \wedge |t_{1z} + t_{2z}| < |2t_{f\mathrm{c,max}z}|$
  - **d:** $(\mathrm{sgn}(t_{f,1z}) = \mathrm{sgn}(t_{kz}) \neq \mathrm{sgn}(t_{jz}))$
    $\wedge\, (|2t_{f\mathrm{c,max}z} + t_{kz}| > |t_{jz}|)\ \forall k, j \in \{1,\ 2\}, k \neq j$
  - **e:** $(\mathrm{sgn}(t_{f,1z}) = \mathrm{sgn}(t_{kz}) \neq \mathrm{sgn}(t_{jz}))$
    $\wedge\, (|2t_{f\mathrm{c,max}z} + t_{kz}| < |t_{jz}|)\ \forall k, j \in \{1,\ 2\}, k \neq j$

B.1 Case 1

$$\mathrm{sgn}(f_{1x}) = \mathrm{sgn}(f_{2x}) \wedge \mathrm{sgn}(f_{1y}) = \mathrm{sgn}(f_{2y})$$

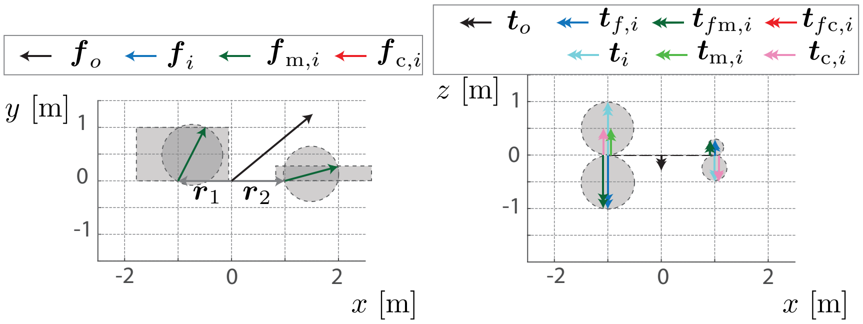

Fig. B.1: Case 1 example.

No compensation force on force level or torque level is possible: $\boldsymbol{f}_{\mathrm{c},1} = \boldsymbol{f}_{\mathrm{c},2} = 0$ (see example in Fig. B.1). Compensation on torque level possible only through applied torques according to the 1D solution

$$t_{\mathrm{c},iz} = \operatorname{sgn}(t_{iz})\frac{1}{2}(|t_{1z}| + |t_{2z}| - |t_{1z} + t_{2z}|) \tag{B.1}$$

with $i = 1, 2$.

B.2 Case 2

$$\operatorname{sgn}(f_{1x}) = \operatorname{sgn}(f_{2x}) \wedge \operatorname{sgn}(f_{1y}) \neq \operatorname{sgn}(f_{2y})$$

Case 2 can be subdivided into 2a-e dependent on the applied torques. Compensation force can occur on torque level. As the forces $f_{\mathrm{c},1y}$ and $f_{\mathrm{c},2y}$ producing torque that compensates on torque level need to compensate each other on force level $f_{\mathrm{c},1y} + f_{\mathrm{c},2y} = 0$, the torques produced by those forces need to be equal $t_{f\mathrm{c},1z} = t_{f\mathrm{c},2z}$ for our setup of $r_{1x} = -r_{2x}$. Consequently, the maximum torque compensation through each applied force is

$$t_{f\mathrm{c,max}z} = \operatorname{sgn}(t_{f,1z}) \min(t_{f,1z}, t_{f,2z}). \tag{B.2}$$

The absolute value of compensation torque is

$$|t_{\mathrm{c},iz}| = \frac{1}{2}(|t_{1z}| + |t_{2z}| + 2|t_{f\mathrm{c,max}z}| - |t_{1z} + t_{2z} + 2t_{f\mathrm{c,max}z}|) \tag{B.3}$$

Case 2a

$$|t_{\mathrm{c},iz}| = 0$$

No compensation on torque level occurs if $|t_{\mathrm{c},iz}| = 0$ in (B.3) (see example in Fig. B.2). As further $\operatorname{sgn}(f_{1x}) = \operatorname{sgn}(f_{2x})$, no compensation on force level. Thus, $\boldsymbol{h}_{\mathrm{c},1} = \boldsymbol{h}_{\mathrm{c},2} = 0$.

Case 2b

$$\operatorname{sgn}(t_{1z}) = \operatorname{sgn}(t_{2z}) \neq \operatorname{sgn}(t_{f,1z}) \wedge |t_{1z} + t_{2z}| > |2t_{f\mathrm{c,max}z}|$$

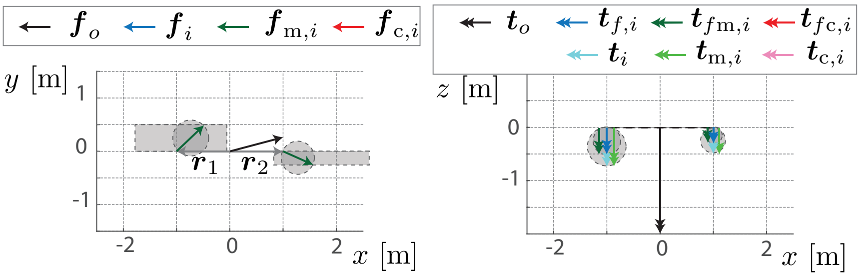

Fig. B.2: Case 2a example.

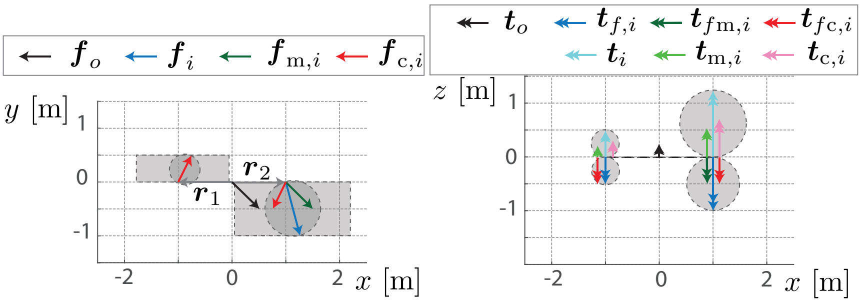

Fig. B.3: Case 2b example.

For case 2b, the applied torques act into the opposite direction and are of greater Euclidean norm than the maximum compensation torque produced by forces $t_{f\mathrm{c},\mathrm{max}z}$ in (B.2) (see example in Fig. B.3). Consequently, we have the case of maximum possible compensation torque produced by forces $t_{f\mathrm{c},\mathrm{max}z}$. Infinite solutions with same cost J exist for different combinations of $t_{\mathrm{c},1z}$ and $t_{\mathrm{c},2z}$, such that $t_{\mathrm{c},1z} + t_{\mathrm{c},2z} + 2t_{f\mathrm{c},\mathrm{max}z} = 0$. We choose $t_{\mathrm{c},iz}$ to be proportional to t_{iz}, similar to $\theta(x)$ in (2.27)

$$t_{\mathrm{c},iz} = \theta_t \, t_{iz}, \tag{B.4}$$

with $i = 1, 2$ and $\theta_t = 1 - \frac{A_x - B_x}{A_x + B_x}$ where $A_x = |t_{1z}| + |t_{2z}| + |2t_{f\mathrm{c},\mathrm{max}z}|$ and $B_x = |t_{1z} + t_{2z} + 2t_{f\mathrm{c},\mathrm{max}z}|$, which for this case simplifies to $\theta_t = -\frac{2t_{f\mathrm{c},\mathrm{max}z}}{t_{1z}+t_{2z}}$.

From $t_{f\mathrm{c},\mathrm{max}z}$ we know the compensation force in y-direction $f_{\mathrm{c},iy} = \frac{1}{r_{ix}} t_{f\mathrm{c},\mathrm{max}z}$ with $i = 1, 2$. Thus, the rotational constraint of the smaller force in y-direction will be active (see (B.2)). We refer to the effector with the bigger (smaller) force in y-direction as $k(j)$: $f_{\mathrm{c},ky} > f_{\mathrm{c},jy}$ with $j, k \in \{1, 2\}, j \neq k$. The cost J has a minimum on the intersection of the translational force constraint of effector k with the active rotational force constraint projected along the x-axis. The circular constraint in (2.9) can be equivalently written in terms of the compensation force for a specific effector k: $f_{\mathrm{c},k}^\top f_{\mathrm{c},k} - f_k^\top f_{\mathrm{c},k} = f_{\mathrm{c},kx}^2 + f_{\mathrm{c},ky}^2 - f_{kx} f_{\mathrm{c},kx} - f_{ky} f_{\mathrm{c},ky} = 0$. The intersection of above circle with the projection of the active rotational force constraint can be obtained by inserting the known $f_{\mathrm{c},ky}$ into above equation and solving for the unknown $f_{\mathrm{c},kx}$

$$f_{\mathrm{c},kx} = 0.5 \left(f_{kx} - c\sqrt{f_{kx}^2 - 4(f_{\mathrm{c},ky}^2 - f_{ky} f_{\mathrm{c},ky})} \right), \tag{B.5}$$

where $c = \mathrm{sgn}(f_{kx})$ selects the appropriate intersection point. As the compensation forces need to cancel each other $f_{\mathrm{c},kx} + f_{\mathrm{c},jx} = 0$, we deduce that $f_{\mathrm{c},jx} = -f_{\mathrm{c},kx}$.

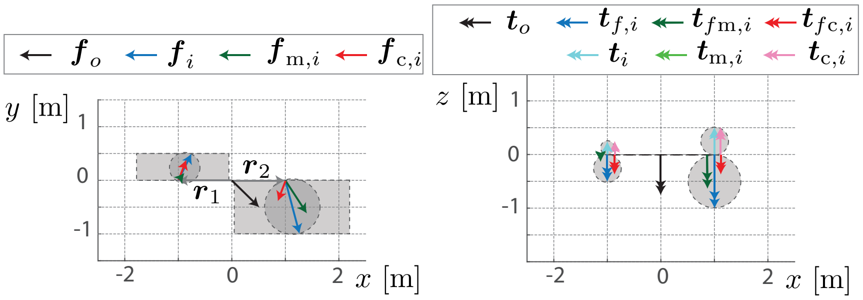

Fig. B.4: Case 2c example.

For certain cases, the resulting compensation force $f_{\mathrm{c},j} = (f_{\mathrm{c},jx} \quad f_{\mathrm{c},jy} \quad 0)^\top$ lies outside the circular translational constraint of f_j. This is also the case for the displayed example, where $j = 1$ and $k = 2$. For this case $f_{\mathrm{c},jx} > f_{jx}$ and the solution is $f_{\mathrm{c},jx} = f_{jx}$ and $f_{\mathrm{c},kx} = -f_{jx}$.

Case 2c

$$\operatorname{sgn}(t_{1z}) = \operatorname{sgn}(t_{2z}) \neq \operatorname{sgn}(t_{f,1z}) \wedge |t_{1z} + t_{2z}| < |2t_{f\mathrm{c,max}z}|$$

As for 2b, the applied torques act into the opposite direction than the torques produced by forces. However, in case 2c the sum of applied torques is of smaller Euclidean norm than the sum of maximum compensation torques produced by forces $t_{f\mathrm{c,max}z}$ in (B.2) (see example in Fig. B.4). Consequently, the applied torque is completely compensated $t_{\mathrm{c},iz} = t_{iz}$ for $i = 1, 2$. The force produced compensation torque is $t_{f\mathrm{c},iz} = 0.5(t_{\mathrm{c},1z} + t_{\mathrm{c},2z})$ and consequently $f_{\mathrm{c},iy} = \frac{1}{r_{ix}} t_{f\mathrm{c},iz}$ for $i = 1, 2$. Similar to case 2b, we now need to compute the compensation force in x-direction. In contrast to case 2b, the cost J can also have a real minimum inside the circular constraint. The optimization problem for given $t_{\mathrm{m},iz} = t_{iz} - t_{\mathrm{c},iz}$ and $f_{\mathrm{m},iy} = f_{iy} - f_{\mathrm{c},iy}$ for the 2D case simplifies to

$$\text{minimize} \qquad J = \sqrt{f_{\mathrm{m},1x}^2 + f_{\mathrm{m},1y}^2} + \sqrt{f_{\mathrm{m},2x}^2 + f_{\mathrm{m},2y}^2} \tag{B.6}$$

$$\text{subject to} \qquad f_{\mathrm{m},1x} + f_{\mathrm{m},2x} = f_{\mathrm{o},x} \tag{B.7}$$

$$f_{\mathrm{m},ix}^2 + f_{\mathrm{m},iy}^2 - f_{ix} f_{\mathrm{m},ix} - f_{iy} f_{\mathrm{m},iy} \leq 0 \quad \text{with} \quad i = 1, 2. \tag{B.8}$$

For inactive inequality constraints above optimization has extrema at

$$f_{\mathrm{m},1x} = \frac{-f_{\mathrm{o},x} f_{\mathrm{m},1y} \pm \sqrt{f_{\mathrm{o},x}^2 f_{\mathrm{m},1y}^4 + (f_{\mathrm{m},2y}^2 - f_{\mathrm{m},1y}^2) f_{\mathrm{o},x}^2 f_{\mathrm{m},1y}^2}}{f_{\mathrm{m},2y}^2 - f_{\mathrm{m},1y}^2}. \tag{B.9}$$

In case above extrema violate the translational constraints, the minimum of J lies on the translational constraints. The given y-values result in 4 possible intersections with the translational constraints for effectors 1 and 2, which are computed according to (B.5), but here for $k = 1, 2$. Examination of the constraints and evaluation of the cost function J at the 6 possible compensation force pairs $f_{\mathrm{c},i} = ((f_{ix} - f_{\mathrm{m},ix}) \quad f_{\mathrm{c},iy} \quad 0)^\top$ with $i = 1, 2$ yields the optimal solution.

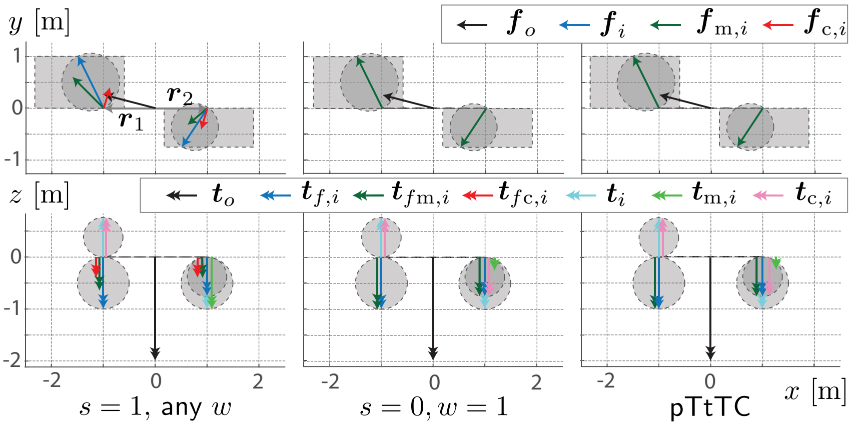

Fig. B.5: Case 2d examples.

Case 2d

$$(\mathrm{sgn}(t_{f,1z}) = \mathrm{sgn}(t_{kz}) \neq \mathrm{sgn}(t_{jz})) \wedge (|2t_{fc,\mathrm{max}z} + t_{kz}| > |t_{jz}|)\ \forall k, j \in \{1,\ 2\}, k \neq j$$

The case 2d and the case 4d represent the special cases for which the compensation wrench depends on weighting w and selection variable s (see examples for case 2d in Fig. B.5). Consequently, solving of the optimization gets complicated and we make use of numerical optimization tools (e.g. *fmincon* of the *Optimization Toolbox* by *MathWorks*). The example shows on the left the optimization result for $s = 1$ which is weighting independent and equal to solutions for $s = 0$ and small weighting, e.g. $w = 0.001$. The middle displays the solution for $s = 0$ and $w = 1$ and the right the solution for $s = 0$ and high weighting, e.g. $w = 0.999$, which are visually not differentiable for the displayed example. High weighting results in the same solution as what we refer to as the “prioritized torque through torque compensation“ (pTtTC). The pTtTC solution can be obtained analytically and is explained in the following.

Case 2d and 4d require optimization, because applied torque at effector j can be compensated by torque produced through applied forces or by torque applied at effector k. For the displayed example $j = 1$ and $k = 2$. We know that $t_{\mathrm{c},jz} = t_{jz}$. “Prioritized torque through torque compensation“ signifies that we use the torque t_{kz} to compensate for t_{jz} as much as possible. Thus, $t_{\mathrm{c},kz} = -t_{jz}$ if $|t_{jz}| \leq |t_{\mathrm{c},kz}|$ and $\boldsymbol{f}_{\mathrm{c},1} = \boldsymbol{f}_{\mathrm{c},2} = \boldsymbol{0}_{3\times1}$. In case that $|t_{jz}| > |t_{\mathrm{c},kz}|$, $t_{\mathrm{c},kz} = t_{kz}$ and the remaining part of $t_{\mathrm{c},jz}$ is split among the torques produced by forces $t_{f\mathrm{c},1z} = t_{f\mathrm{c},2z} = 0.5(-t_{\mathrm{c},jz} - t_{\mathrm{c},kz})$. The optimal compensation forces are obtained based on the procedure detailed for case 2c.

Case 2e

$$(\mathrm{sgn}(t_{f,1z}) = \mathrm{sgn}(t_{kz}) \neq \mathrm{sgn}(t_{jz})) \wedge (|2t_{fc,\mathrm{max}z} + t_{kz}| < |t_{jz}|)\ \forall k, j \in \{1,\ 2\}, k \neq j$$

In contrast to case 2d, for case 2e, the applied torque t_{jz} is big enough to cancel applied torque t_{kz} and the maximum possible compensation torques produced by forces $2t_{f\mathrm{c},\mathrm{max}z}$ (see example in Fig. B.6). Thus, $t_{\mathrm{c},kz} = t_{kz}$, $t_{\mathrm{c},jz} = -t_{kz} - 2t_{f\mathrm{c},\mathrm{max}z}$ and $t_{f\mathrm{c},1z} = t_{f\mathrm{c},2z} = t_{f\mathrm{c},\mathrm{max}z}$. The optimal compensation forces are obtained based on the procedure detailed for case 2b.

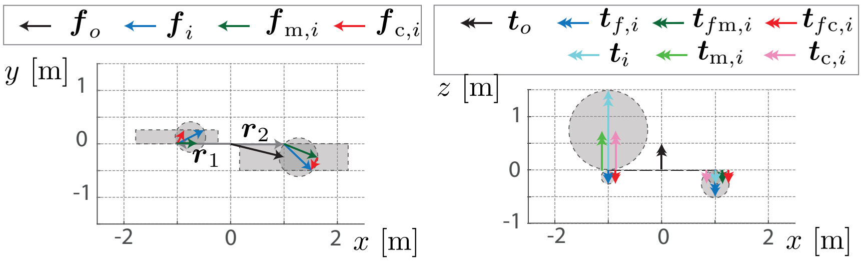

Fig. B.6: Case 2e example.

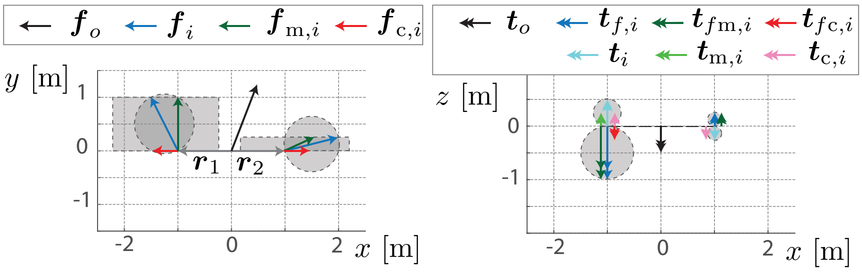

Fig. B.7: Case 3 example.

B.3 Case 3

$$\operatorname{sgn}(f_{1x}) \neq \operatorname{sgn}(f_{2x}) \wedge \operatorname{sgn}(f_{1y}) = \operatorname{sgn}(f_{2y})$$

No torques can be compensated via forces, as this requires $\operatorname{sgn}(f_{\mathrm{c},1y}) = -\operatorname{sgn}(f_{\mathrm{c},2y})$, which is impossible for $\operatorname{sgn}(f_{1y}) = \operatorname{sgn}(f_{2y})$ (see example in Fig. B.7). Consequently, $f_{\mathrm{c},1y} = f_{\mathrm{c},2y} = 0$ and determination of compensation forces and torques simplifies to 1D problems, with $t_{\mathrm{c},iz}$ according to (B.1) and similarly compensation forces along the x-direction

$$f_{\mathrm{c},ix} = \operatorname{sgn}(f_{ix})\frac{1}{2}(|f_{1x}| + |f_{2x}| - |f_{1x} + f_{2x}|) \tag{B.10}$$

with $i = 1, 2$.

B.4 Case 4

$$\operatorname{sgn}(f_{1x}) \neq \operatorname{sgn}(f_{2x}) \wedge \operatorname{sgn}(f_{1y}) \neq \operatorname{sgn}(f_{2y})$$

Case 4a

$$|t_{\mathrm{c},iz}| = 0$$

No compensation on torque level, because all torques are of same sign (see example in Fig. B.8). Compensation on force level along the x-direction according to the 1D solution in (B.10).

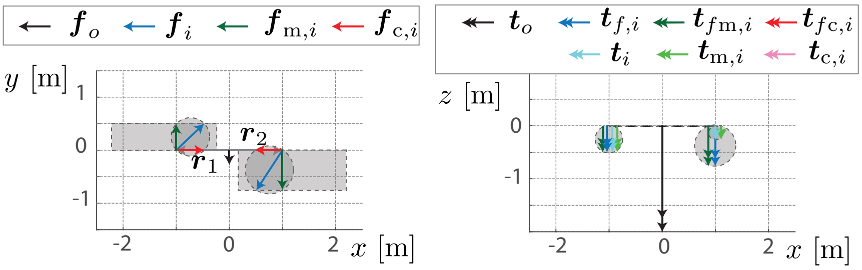

Fig. B.8: Case 4a example.

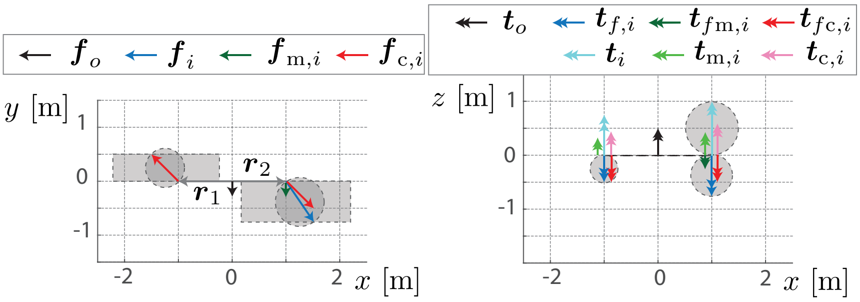

Fig. B.9: Case 4b example.

Case 4b

$$\operatorname{sgn}(t_{1z}) = \operatorname{sgn}(t_{2z}) \neq \operatorname{sgn}(t_{f,1z}) \wedge |t_{1z} + t_{2z}| > |2t_{fc,\max z}|$$

As for case 2b, the applied torques act into the opposite direction and are of greater Euclidean norm than the maximum compensation torque produced by forces $t_{fc,\max z}$ in (B.2) (see example in Fig. B.9). Consequently, we have the case of maximum possible compensation torque produced by forces $t_{fc,\max z}$. As for case 2b, we choose $t_{c,1z}$ and $t_{c,2z}$ such that they are proportional to t_{1z} and t_{2z} according to (B.4) with $\theta_t = -\frac{2t_{fc,\max z}}{t_{1z}+t_{2z}}$.

The compensation force in y-direction follows from the geometry and the known torque compensation $f_{c,iy} = \frac{1}{r_{ix}} t_{fc,\max z}$ with $i = 1, 2$. The compensation force in x-direction is computed based on the intersections of the circular constraint belonging to the greater applied torque through force $t_{f,k} > t_{f,j}$ with the known $f_{c,ky}$ value according to (B.5) with $c = \operatorname{sgn}(-f_{kx})$. For certain cases, the resulting compensation force $f_{c,j} = (f_{c,jx} \quad f_{c,jy} \quad 0)^\top$ lies outside the circular translational constraint of f_j. As for case 2b, this is also the case for the displayed example, where $j = 1$ and $k = 2$. Here, $f_{c,jx} > f_{jx}$ and the solution is $f_{c,jx} = f_{jx}$ and $f_{c,kx} = -f_{jx}$.

Case 4c

$$\operatorname{sgn}(t_{1z}) = \operatorname{sgn}(t_{2z}) \neq \operatorname{sgn}(t_{f,1z}) \wedge |t_{1z} + t_{2z}| < |2t_{fc,\max z}|$$

The 4c case can be similarly solved as the 2c case. The applied torque is completely compensated $t_{c,iz} = t_{iz}$ for $i = 1, 2$ (see example in Fig. B.10). The compensation force in y-direction is $f_{c,iy} = \frac{1}{r_{ix}} t_{fc,iz}$ with $t_{fc,iz} = 0.5(t_{c,1z} + t_{c,2z})$ for $i = 1, 2$. The compensation force in x-direction is computed by comparing the optimal solution of the reduced problem (B.6)

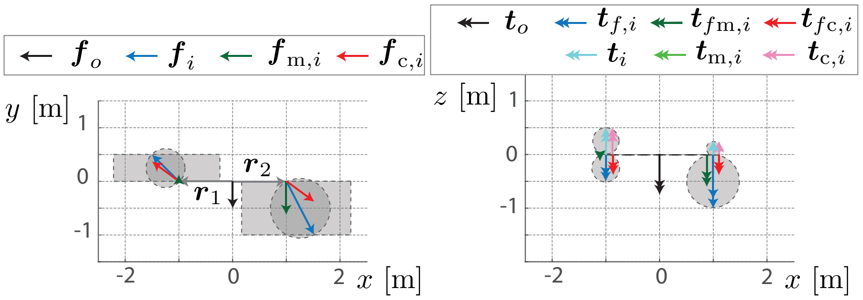

Fig. B.10: Case 4c example.

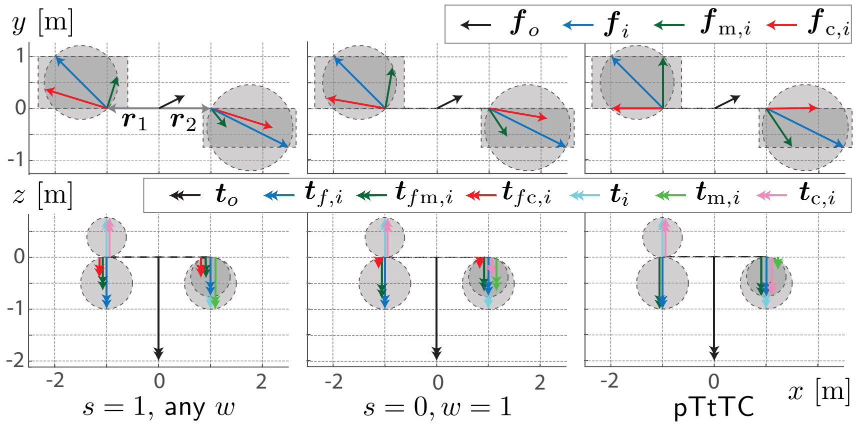

$s = 1$, any w $s = 0, w = 1$ pTtTC

Fig. B.11: Case 4d examples.

without constraints to the solutions on the constraints (B.9), based on cost J and fulfillment of constraints.

Case 4d

$$(\mathrm{sgn}(t_{f,1z}) = \mathrm{sgn}(t_{kz}) \neq \mathrm{sgn}(t_{jz})) \wedge (|2t_{f\mathrm{c,max}z} + t_{kz}| > |t_{jz}|)\ \forall k, j \in \{1,\ 2\}, k \neq j$$

As for case 2d, the optimal solution for case 4d is s and w dependent. The displayed example is the same as the one discussed in Fig 2.9. Similar to case 2d, the pTtTC solution can be obtained analytically. As the displayed example shows, torque at effector $j = 1$ can be compensated by torque produced through applied forces or by torque applied at effector $k = 2$. We know that $t_{\mathrm{c},jz} = t_{jz}$. "Prioritized torque through torque compensation" signifies that we use the torque t_{kz} to compensate for t_{jz} as much as possible. Thus, $t_{\mathrm{c},kz} = -t_{jz}$ if $|t_{jz}| \leq |t_{\mathrm{c},kz}|$. In contrast to case 2d, non zero compensation forces along the x-direction can be present, which are computed according to the 1D solution in (B.10). In case that $|t_{jz}| > |t_{\mathrm{c},kz}|$, $t_{\mathrm{c},kz} = t_{kz}$ and the remaining part of $t_{\mathrm{c},jz}$ is split among the torques produced by forces $t_{f\mathrm{c},1z} = t_{f\mathrm{c},2z} = 0.5(-t_{\mathrm{c},jz} - t_{\mathrm{c},kz})$. The optimal compensation forces are obtained based on the procedure detailed for case 2c (4c).

Case 4e

$$(\mathrm{sgn}(t_{f,1z}) = \mathrm{sgn}(t_{kz}) \neq \mathrm{sgn}(t_{jz})) \wedge (|2t_{f\mathrm{c,max}z} + t_{kz}| < |t_{jz}|)\ \forall k, j \in \{1,\ 2\}, k \neq j$$

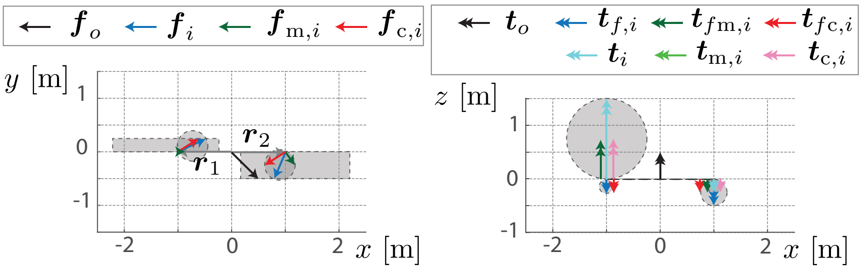

Fig. B.12: Case 4e example.

As for case 2e, the applied torque t_{jz} is big enough to cancel applied torque t_{kz} and the maximum possible compensation torques produced by forces $2t_{fc,\max z}$. Thus, $t_{c,kz} = t_{kz}$, $t_{c,jz} = -t_{kz} - 2t_{fc,\max z}$ and $t_{fc,1z} = t_{fc,2z} = t_{fc,\max z}$. The optimal compensation forces are obtained based on the procedure detailed for case 2b (4b).

C Comparison of SoA wrench decomposition methods based on pHHI data

Here, we contrast the internal wrench estimated by different decomposition methods during a real pHHI task in order to illustrate how key behavioral measures for pHHI and pHRI are sensitive to a decomposition method. The results confirm the results found in simulation in Chapter 2: our proposed wrench decomposition method is more resilient to the inflation of the disagreement measure than the other SoA methods.

Fig. C.1 shows the disagreement measures F_c and T_c of an example trial and Table C.1 lists their mean values $\bar{F}_\mathrm{c}$ and $\bar{T}_\mathrm{c}$ across all trials and participants starting from far Distance for the proposed decomposition and other SoA approaches. The simplifying assumptions of other SoA approaches lead to an overestimation of disagreement/compensation, which is in line with our simulation results in Chapter 2 and the observations for multi-digit grasping in [158]. The experimental setup caused an especially high inflation on internal torque, for which we present a comparison via a repeated-measures ANOVA in the following. The first factor was the Method of decomposition and the second factor was the Guiding instruction. The analysis showing the main effect of Method, $F(4, 44) = 128.39,\ p < .005$, confirming our method to be the most resilient to inflation of disagreement/compensation (Fig. C.2). While there was a small effect of Guide ($p = .02$), a clear interaction effect of Method and Guide was found, $F(8, 88) = 3.1,\ p < .005$. Further analysis indicated our disagreement measure is consistent with the amount of guidance information given to the participants such that the largest disagreement was observed in One-Guide ($0.1548\mathrm{Nm} \pm 0.0693$) cases and the smallest in Two-Guide cases ($0.1486\mathrm{Nm} \pm 0.0623$).

Tab. C.1: Mean internal wrench compared to SoA decompositions

	B (pTtTC)	PM	$G^\dagger$	G^+_Δ	VL
$\bar{F}_\mathrm{c}$ [N]	4.7125	5.2310	6.5021	6.5391	6.3862
$\bar{T}_\mathrm{c}$ [Nm]	0.2364	0.8678	0.3443	1.1585	0.3811

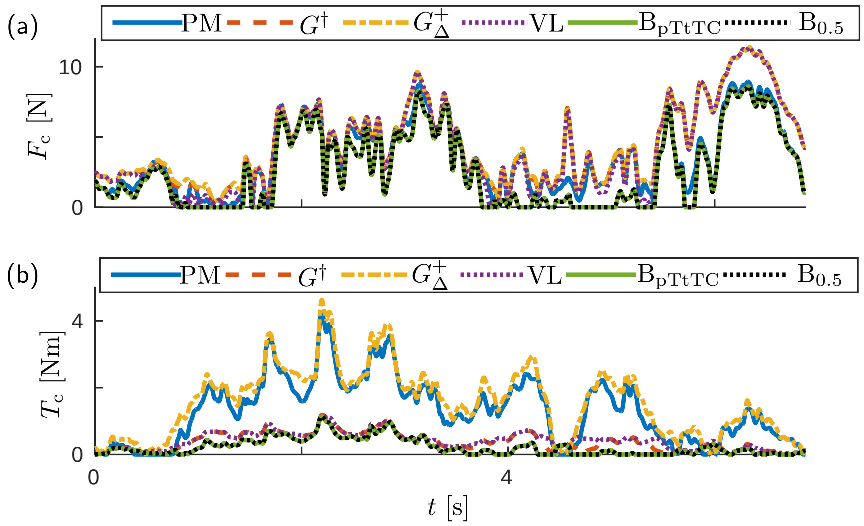

Fig. C.1: Disagreement on force and torque level for an example trial: SoA wrench decomposition approaches PM, $G^\dagger$, G_Δ^+ and VL overestimate disagreement as predicted by our simulations.

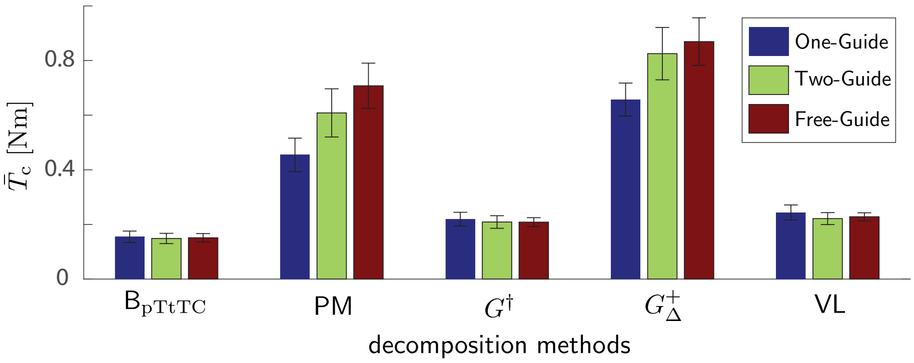

Fig. C.2: Average internal torque $\bar{T}_\mathrm{c}$ during the first 600 ms of each trial and agent 1 (leading partner during One-Guide) entering the final platform first: SoA wrench decomposition approaches PM, $G^\dagger$, G_Δ^+ and VL inflate the disagreement measure. Differing guide to disagreement relations ($\bar{T}_\mathrm{c}$(Free-Guide) $>$ $\bar{T}_\mathrm{c}$(Two-Guide) $>$ $\bar{T}_\mathrm{c}$(One-Guide) for PM and G_Δ^+, $\bar{T}_\mathrm{c}$(One-Guide) $>$ $\bar{T}_\mathrm{c}$(Two-Guide) $>$ $\bar{T}_\mathrm{c}$(Free-Guide) for $G^\dagger$ and $\bar{T}_\mathrm{c}$(One-Guide) $>$ $\bar{T}_\mathrm{c}$(Free-Guide) $>$ $\bar{T}_\mathrm{c}$(Two-Guide) for VL and the proposed decomposition) confirm the need for a physically consistent wrench decomposition for interpretable results. The error bar indicates one standard error.

D Detailed derivations for the analysis of the fundamental dynamics based leader-follower structure

Reference input transfer function

Rearrangement of the block diagram in Fig. 6.7 leads to the block diagram displayed in Fig. D.1. The highlighted intermediate transfer function G_1^{fi} is

$$G_1^{\mathrm{fi}} = \frac{\frac{1}{s}}{1 - \frac{1}{s}\Gamma_{\mathcal{F}}\frac{B}{\hat{B}_{\mathcal{F}}}\frac{s}{T_f s+1}}. \tag{D.1}$$

Based on (D.1) the reference input transfer function $\vartheta_r(s) = G^{\mathrm{fi}}(s)\theta_E^{\mathrm{d}}(s)$ of a leader interacting with a flow imitation follower is computed to

$$G^{\mathrm{fi}} = \frac{\Gamma_{\mathcal{L}}^{\mathrm{d}}\tau_{\mathcal{L}}\frac{B}{\hat{B}_{\mathcal{L}}}s + \Gamma_{\mathcal{L}}^{\mathrm{d}}\tau_{\mathcal{L}}\frac{B}{\hat{B}_{\mathcal{L}}}\frac{1}{T_f}}{s^2 + \left(\frac{1}{T_f} - \Gamma_{\mathcal{F}}^{\mathrm{d}}\frac{B}{\hat{B}_{\mathcal{F}}}\frac{1}{T_f} + \Gamma_{\mathcal{L}}^{\mathrm{d}}\tau_{\mathcal{L}}\frac{B}{\hat{B}_{\mathcal{L}}}\right)s + \Gamma_{\mathcal{L}}^{\mathrm{d}}\tau_{\mathcal{L}}\frac{B}{\hat{B}_{\mathcal{L}}}\frac{1}{T_f}}. \tag{D.2}$$

Stationary transfer behavior

According to the final value theorem, the system energy ϑ_r approaches

$$\vartheta_r(t \to \infty) = \lim_{s\to 0} sG^{\mathrm{fi}}(s)\frac{1}{s}\theta_E^{\mathrm{d}} \overset{\text{(D.2)}}{=} \theta_E^{\mathrm{d}}, \tag{D.3}$$

as $t \to \infty$ for a step of height θ_E^{d} in the reference variable $\theta_E^{\mathrm{d}}(t) = \sigma(t)\theta_E^{\mathrm{d}}$.

Energy share

For the computation of the energy share $\Gamma_{\mathcal{F}}$, consider the block diagram rearrangement in Fig. D.2. From Fig. D.2 with

$$G_2^{\mathrm{fi}} = \frac{1}{1 - \Gamma_{\mathcal{F}}^{\mathrm{d}}\frac{B}{\hat{B}_{\mathcal{F}}}\frac{1}{T_f s+1}}. \tag{D.4}$$

we can compute the transfer function which yields the amount of energy the leader contributed $\vartheta_{r,\mathcal{L}}(s)$ based on the reference input $\theta_E^{\mathrm{d}}(s)$

$$G_{\mathcal{L}}^{\mathrm{fi}} = \frac{\Gamma_{\mathcal{L}}^{\mathrm{d}}\tau_{\mathcal{L}}\frac{B}{\hat{B}_{\mathcal{L}}}\left(s + \frac{1}{T_f} - \Gamma_{\mathcal{F}}^{\mathrm{d}}\frac{B}{\hat{B}_{\mathcal{F}}}\frac{1}{T_f}\right)}{s^2 + \left(\frac{1}{T_f} - \Gamma_{\mathcal{F}}^{\mathrm{d}}\frac{B}{\hat{B}_{\mathcal{F}}}\frac{1}{T_f} + \Gamma_{\mathcal{L}}^{\mathrm{d}}\tau_{\mathcal{L}}\frac{B}{\hat{B}_{\mathcal{L}}}\right)s + \Gamma_{\mathcal{L}}^{\mathrm{d}}\tau_{\mathcal{L}}\frac{B}{\hat{B}_{\mathcal{L}}}\frac{1}{T_f}}. \tag{D.5}$$

Based on the final value theorem the energy share of the leader $\Gamma_{\mathcal{L}}$ can be defined

$$\vartheta_{r,\mathcal{L}}(t \to \infty) = \lim_{s\to 0} sG_{\mathcal{L}}^{\mathrm{fi}}(s)\frac{1}{s}\theta_E^{\mathrm{d}} \overset{!}{=} \Gamma_{\mathcal{L}}\theta_E^{\mathrm{d}}, \tag{D.6}$$

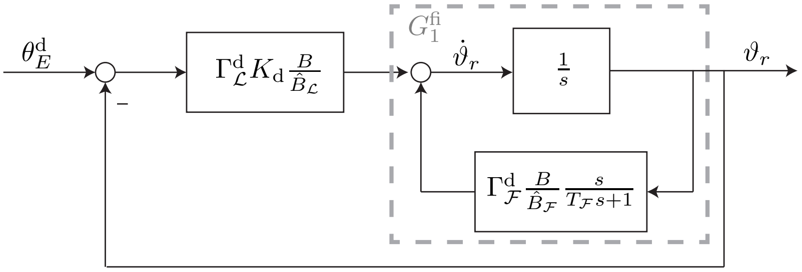

Fig. D.1: Rearranged block diagram of the flow imitation control structure for the computation of the transfer function $G(s)$: $\vartheta_r(s) = G^{\mathrm{fi}}(s)\theta_E^{\mathrm{d}}(s)$.

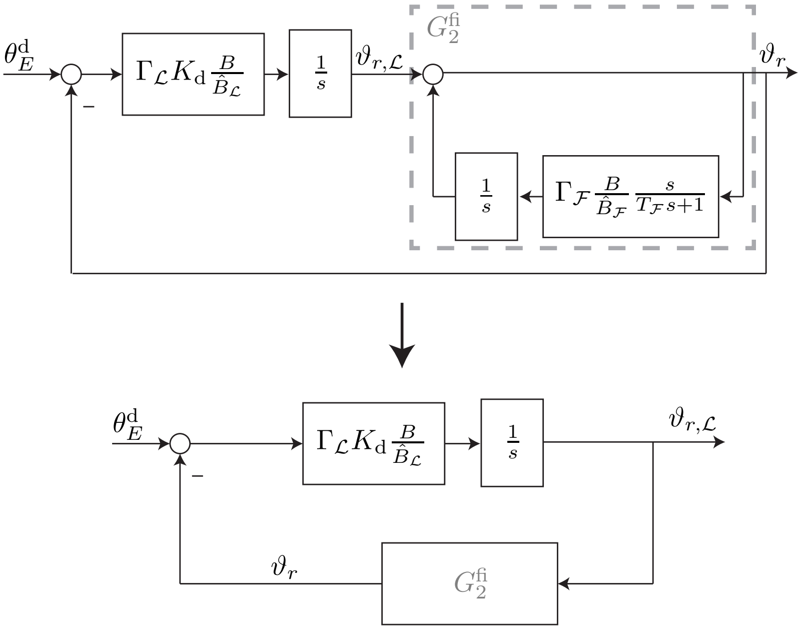

Fig. D.2: Rearranged block diagram of the flow imitation control structure for the computation of the energy contributed by the leader $\vartheta_{r,\mathcal{L}} = G_{\mathcal{L}}^{\mathrm{fi}}(s)\theta_E^{\mathrm{d}}(s)$.

which yields for the flow imitation approach

$$\Gamma_{\mathcal{L}} = \lim_{s\to 0} G_{\mathcal{L}}^{\mathrm{fi}}(s) = 1 - \Gamma_{\mathcal{F}}^{\mathrm{d}} \frac{B}{\hat{B}_{\mathcal{F}}}, \tag{D.7}$$

and consequently an energy share of the follower

$$\Gamma_{\mathcal{F}} = 1 - \Gamma_{\mathcal{L}} = \Gamma_{\mathcal{F}}^{\mathrm{d}} \frac{B}{\hat{B}_{\mathcal{F}}}. \tag{D.8}$$

Stability

From the system denominator we know that according to the Routh-Hurwitz criterion, the linear system is asymptotically stable if $(\frac{1}{T_f} - \Gamma_{\mathcal{F}}^{\mathrm{d}} \frac{B}{\hat{B}_{\mathcal{F}}} \frac{1}{T_f} + \Gamma_{\mathcal{L}}^{\mathrm{d}} \frac{B}{\hat{B}_{\mathcal{L}}} \tau_{\mathcal{L}}) > 0$ and $\Gamma_{\mathcal{L}}^{\mathrm{d}} \tau_{\mathcal{L}} \frac{B}{\hat{B}_{\mathcal{L}}} \frac{1}{T_f} > 0$. The latter is always fulfilled, as $\Gamma_{\mathcal{L}}^{\mathrm{d}}, \tau_{\mathcal{L}}, B, \hat{B}_{\mathcal{L}}, T_f > 0$.

Bibliography

[1] E. M. Abdel-Rahman, A. H. Nayfeh, and Z. N. Masoud. “Dynamics and Control of Cranes: A Review.” In: *Journal of Vibration and Control* 9.7 (2003), pp. 863–908.

[2] D. J. Agravante, A. Cherubini, A. Bussy, P. Gergondet, and A. Kheddar. “Collaborative human-humanoid carrying using vision and haptic sensing.” In: *Proc. IEEE International Conference on Robotics and Automation*. May 2014, pp. 607–612.

[3] J. Alonso-Mora, R. Knepper, R. Siegwart, and D. Rus. “Local motion planning for collaborative multi-robot manipulation of deformable objects.” In: *Proc. IEEE International Conference on Robotics and Automation*. May 2015, pp. 5495–5502.

[4] E. D. Andersen and K. D. Andersen. “The Mosek Interior Point Optimizer for Linear Programming: An Implementation of the Homogeneous Algorithm.” In: *High Performance Optimization*. Ed. by H. Frenk, K. Roos, T. Terlaky, and S. Zhang. Boston, MA: Springer US, 2000, pp. 197–232.

[5] K. J. Åström and B. Wittenmark. *Adaptive control*. Courier Corporation, 2013.

[6] K. Åström and K. Furuta. “Swinging up a pendulum by energy control.” In: *Automatica* 36.2 (2000), pp. 287–295.

[7] C. G. Atkeson, C. H. An, and J. M. Hollerbach. “Estimation of Inertial Parameters of Manipulator Loads and Links.” In: *International Journal of Robotics Research* 5.3 (1986), pp. 101–119.

[8] C. G. Atkeson and S. Schaal. “Robot learning from demonstration.” In: *Proc. International Conference on Machine Learning*. Vol. 97. 1997, pp. 12–20.

[9] G. L. Baker and J. A. Blackburn. *The pendulum: a case study in physics*. Vol. 8. Oxford University Press Oxford, 2005.

[10] P. Basili, M. Huber, O. Kourakos, T. Lorenz, T. Brandt, S. Hirche, and S. Glasauer. “Inferring the goal of an approaching agent: A human-robot study.” In: *Proc. IEEE International Symposium on Robot and Human Interactive Communication*. Sept. 2012, pp. 527–532.

[11] M. Beetz, F. Stulp, P. Esden-Tempski, A. Fedrizzi, U. Klank, I. Kresse, A. Maldonado, and F. Ruiz. “Generality and legibility in mobile manipulation.” In: *Autonomous Robots* 28.1 (Sept. 2009), p. 21.

[12] M. Bernard and K. Kondak. “Generic slung load transportation system using small size helicopters.” In: *Proc. IEEE International Conference on Robotics and Automation*. 2009, pp. 3258–3264.

[13] R. Bonitz and T. Hsia. “Force decomposition in cooperating manipulators using the theory of metric spaces and generalized inverses.” In: *Proc. IEEE International Conference on Robotics and Automation*. Vol. 2. May 1994, pp. 1521–1527.

[14] S. Boyd and L. Vandenberghe. *Convex optimization*. Cambridge university press, 2004.

[15] D. Braun, M. Howard, and S. Vijayakumar. “Exploiting Variable Stiffness in Explosive Movement Tasks.” In: *Proc. Robotics: Science and Systems*. Los Angeles, CA, USA, June 2011.

[16] L. Bucciarelli. *Engineering Mechanics for Structures*. Dover, 2009.

[17] E. Burdet, K. P. Tee, I Mareels, T. E. Milner, C.-M. Chew, D. W. Franklin, R. Osu, and M. Kawato. “Stability and motor adaptation in human arm movements.” In: *Biological cybernetics* 94.1 (2006), pp. 20–32.

[18] L. Busoniu, R. Babuska, B. De Schutter, and D. Ernst. *Reinforcement learning and dynamic programming using function approximators.* Vol. 39. CRC press, 2010.

[19] M. Buss, H. Hashimoto, and J. Moore. “Dextrous hand grasping force optimization.” In: *IEEE Transactions on Robotics and Automation* 12.3 (June 1996), pp. 406–418.

[20] A. Bussy, A. Kheddar, A. Crosnier, and F. Keith. “Human-humanoid haptic joint object transportation case study.” In: *Proc. IEEE/RSJ International Conference on Intelligent Robots and Systems.* Oct. 2012, pp. 3633–3638.

[21] A. Bussy, P. Gergondet, A. Kheddar, F. Keith, and A. Crosnier. “Proactive behavior of a humanoid robot in a haptic transportation task with a human partner.” In: *Proc. IEEE International Symposium on Robot and Human Interactive Communication.* Sept. 2012, pp. 962–967.

[22] D. D. Carli, E. Hohert, C. A. C. Parker, S. Zoghbi, S. Leonard, E. Croft, and A. Bicchi. “Measuring intent in human-robot cooperative manipulation.” In: *Proc. IEEE International Workshop on Haptic Audio Visual Environments and Games.* Nov. 2009, pp. 159–163.

[23] D. Carton, W. Olszowy, D. Wollherr, and M. Buss. “Socio-Contextual Constraints for Human Approach with a Mobile Robot.” In: *International Journal of Social Robotics* 9.2 (Apr. 2017), pp. 309–327.

[24] C. G. Carvalhaes and P. Suppes. “Approximations for the period of the simple pendulum based on the arithmetic-geometric mean.” In: *American Journal of Physics* 76.12 (2008), pp. 1150–1154.

[25] R. Chandler, C. E. Clauser, J. T. McConville, H. Reynolds, and J. W. Young. *Investigation of inertial properties of the human body.* Tech. rep. DTIC Document, 1975.

[26] F. Christange. “Haptic Control of Energy and Energy Flow in Complex Pendulums.” Research Internship. Technische Universität München, 2012.

[27] F. Christange. “Adaptive Controllers for Cooperative Swinging of Flexible Objects.” Master Thesis. Technische Universität München, 2014.

[29] C. C. Chung and J. Hauser. “Nonlinear control of a swinging pendulum.” In: *Automatica* 31.6 (1995), pp. 851–862.

[30] L. S. Cicolani and G. Kanning. *Equations of motion of slung-load systems, including multilift systems.* Vol. 3280. National Aeronautics, Space Administration, Office of Management, Scientific, and Technical Information Program, 1992.

[31] C. de Crousaz, F. Farshidian, and J. Buchli. “Aggressive Optimal Control for Agile Flight with a Slung Load.” In: *Proc. IEEE/RSJ IROS Workshop on Machine Learning in Planning and Control of Robot Motion.* 2014.

[32] D. Cunningham and H. Asada. “The Winch-Bot: A cable-suspended, underactuated robot utilizing parametric self-excitation.” In: *Proc. IEEE International Conference on Robotics and Automation.* May 2009, pp. 1844–1850.

[33] M. Deisenroth, D. Fox, and C. Rasmussen. “Gaussian Processes for Data-Efficient Learning in Robotics and Control.” In: *IEEE Transactions on Pattern Analysis and Machine Intelligence* 37.2 (Feb. 2015), pp. 408–423.

[34] W. T. Dempster. *Space requirements for the seated operator.* Tech. rep. Wright-Patterson Air Force Base, Ohio (AD 85 892): Wright Air Development Center TH-55-159, 1955.

[35] P. Dillenbourg, M. J. Baker, A. Blaye, and C. O'Malley. "The evolution of research on collaborative learning." In: *Learning in Humans and Machine: Towards an interdisciplinary learning science.* Ed. by E. Spada and P. Reiman. Elsevier, Oxford, 1995, pp. 189–211.

[36] A. Domahidi, E. Chu, and S. Boyd. "ECOS: An SOCP solver for embedded systems." In: *Proc. IEEE European Control Conference.* July 2013, pp. 3071–3076.

[45] K. Doya. "Reinforcement learning in continuous time and space." In: *Neural computation* 12.1 (2000), pp. 219–245.

[46] A. D. Dragan, K. C. T. Lee, and S. S. Srinivasa. "Legibility and predictability of robot motion." In: *Proc. ACM/IEEE International Conference on Human-Robot Interaction.* Mar. 2013, pp. 301–308.

[47] A. Dragan and S. Srinivasa. "Formalizing Assistive Teleoperation." In: *Proc. Robotics: Science and Systems.* July 2012.

[48] A. Dragan and S. Srinivasa. "Generating Legible Motion." In: *Proc. Robotics: Science and Systems.* June 2013.

[49] A. Dragan and S. Srinivasa. "Integrating human observer inferences into robot motion planning." In: *Autonomous Robots* 37.4 (2014), pp. 351–368.

[50] A. D. Dragan, S. Bauman, J. Forlizzi, and S. S. Srinivasa. "Effects of Robot Motion on Human-Robot Collaboration." In: *Proc. ACM/IEEE International Conference on Human-Robot Interaction.* Portland, Oregon, USA: ACM, 2015, pp. 51–58.

[51] V. Duchaine and C. M. Gosselin. "General Model of Human-Robot Cooperation Using a Novel Velocity Based Variable Impedance Control." In: *Proc. Joint World-Haptics, EuroHaptics Conference and Symposium on Haptic Interfaces for Virtual Environment and Teleoperator Systems.* Mar. 2007, pp. 446–451.

[52] J. Dumora, F. Geffard, C. Bidard, T. Brouillet, and P. Fraisse. "Experimental study on haptic communication of a human in a shared human-robot collaborative task." In: *Proc. IEEE/RSJ International Conference on Intelligent Robots and Systems.* Oct. 2012, pp. 5137–5144.

[53] J. Dumora, F. Geffard, C. Bidard, N. Aspragathos, and P. Fraisse. "Robot Assistance Selection for Large Object Manipulation with a Human." In: *Proc. IEEE International Conference on Systems, Man, and Cybernetics.* Oct. 2013, pp. 1828–1833.

[54] A. Engin. "On the damping properties of the shoulder complex." In: *Journal of Biomechanical Engineering* 106.4 (1984), pp. 360–363.

[55] S. Erhart and S. Hirche. "Internal force analysis and load distribution for cooperative multi-robot manipulation." In: *IEEE Transactions on Robotics* 31.5 (Aug. 2015), pp. 1238–1243.

[56] S. Erhart and S. Hirche. "Model and analysis of the interaction dynamics in cooperative manipulation tasks." In: *IEEE Transactions on Robotics* 32.3 (May 2016), pp. 672–683.

[57] P. Evrard and A Kheddar. "Homotopy switching model for dyad haptic interaction in physical collaborative tasks." In: *Proc. Joint WorldHaptics, EuroHaptics Conference and Symposium on Haptic Interfaces for Virtual Environment and Teleoperator Systems.* Mar. 2009, pp. 45–50.

[58] I. Fantoni, R. Lozano, M. W. Spong, et al. "Energy based control of the pendubot." In: *IEEE Transactions on Automatic Control* 45.4 (2000), pp. 725–729.

[59] A. Faust, I. Palunko, P. Cruz, R. Fierro, and L. Tapia. "Learning swing-free trajectories for UAVs with a suspended load." In: *Proc. IEEE International Conference on Robotics and Automation.* May 2013, pp. 4902–4909.

[60] V. Fernandez, C. Balaguer, D. Blanco, and M. Salichs. “Active human-mobile manipulator cooperation through intention recognition.” In: *Proc. IEEE International Conference on Robotics and Automation.* Vol. 3. 2001, pp. 2668–2673.

[61] D. Feth, R. Groten, A. Peer, S. Hirche, and M. Buss. “Performance related energy exchange in haptic human-human interaction in a shared virtual object manipulation task.” In: *Proc. Joint WorldHaptics, EuroHaptics Conference and Symposium on Haptic Interfaces for Virtual Environment and Teleoperator Systems.* Mar. 2009, pp. 338–343.

[62] T. Fong, I. Nourbakhsh, and K. Dautenhahn. “A survey of socially interactive robots.” In: *Robotics and Autonomous Systems* 42.3 (2003). Socially Interactive Robots, pp. 143 –166.

[63] L. Freidovich, A. Robertsson, A. Shiriaev, and R. Johansson. “Periodic motions of the Pendubot via virtual holonomic constraints: Theory and experiments.” In: *Automatica* 44.3 (2008), pp. 785 –791.

[64] R. Full and D. Koditschek. “Templates and anchors: neuromechanical hypotheses of legged locomotion on land.” In: *Journal of Experimental Biology* 202.23 (1999), pp. 3325–3332.

[65] G Ganesh, A Takagi, R Osu, T Yoshioka, M Kawato, and E Burdet. “Two is better than one: Physical interactions improve motor performance in humans.” In: *Scientific Reports* 4 (2014).

[66] F. Gao, M. L. Latash, and V. M. Zatsiorsky. “Internal forces during object manipulation.” English. In: *Experimental Brain Research* 165.1 (2005), pp. 69–83.

[67] M. Geravand, C. Werner, K. Hauer, and A. Peer. “An Integrated Decision Making Approach for Adaptive Shared Control of Mobility Assistance Robots.” In: *International Journal of Social Robotics* 8.5 (2016), pp. 631–648.

[68] G. Goller and J. Bernhard. “1D 2D Experimental Setup for Analysis of Cooperative Swinging.” Practical Course. Technische Universität München, 2014.

[69] C. Gosselin and S. Foucault. “Dynamic Point-to-Point Trajectory Planning of a Two-DOF Cable-Suspended Parallel Robot.” In: *IEEE Transactions on Robotics* 30.3 (June 2014), pp. 728–736.

[70] M. Grant and S. Boyd. “Graph implementations for nonsmooth convex programs.” In: *Recent Advances in Learning and Control.* Lecture Notes in Control and Information Sciences. Springer-Verlag Limited, 2008, pp. 95–110.

[71] M. Grant and S. Boyd. *CVX: Matlab Software for Disciplined Convex Programming, version 2.1.* `http://cvxr.com/cvx`. Mar. 2014.

[72] R. Groten, D. Feth, H. Goshy, A. Peer, D. Kenny, and M. Buss. “Experimental analysis of dominance in haptic collaboration.” In: *Proc. IEEE International Symposium on Robot and Human Interactive Communication.* Sept. 2009, pp. 723–729.

[73] R. Groten, D. Feth, A. Peer, and M. Buss. “Shared decision making in a collaborative task with reciprocal haptic feedback - an efficiency-analysis.” In: *Proc. IEEE International Conference on Robotics and Automation.* May 2010, pp. 1834–1839.

[74] R. Groten, D. Feth, R. Klatzky, and A. Peer. “The Role of Haptic Feedback for the Integration of Intentions in Shared Task Execution.” In: *IEEE Transactions on Haptics* 6.1 (2013), pp. 94–105.

[75] R. K. Groten. “Haptic human-robot collaboration: How to learn from human dyads.” Dissertation. Technical University of Munich, 2011.

[76] Y. Guiard. “Asymmetric Division of Labor in Human Skilled Bimanual Action.” In: *Journal of Motor Behavior* 19.4 (1987). PMID: 15136274, pp. 486–517.

[77] *Gurobi Optimizer Reference Manual.* 2016.

[78] N. G. Hatsopoulos and W. H. Warren. "Resonance Tuning in Rhythmic Arm Movements." In: *Journal of Motor Behavior* 28.1 (1996), pp. 3–14.

[79] J. M. Hernández, M. Lawitzky, A. Mörtl, D. Lee, and S. Hirche. "An Experience-Driven Robotic Assistant Acquiring Human Knowledge to Improve Haptic Cooperation." de. In: *Proc. IEEE/RSJ International Conference on Intelligent Robots and Systems.* 2011.

[80] N. Hogan. "Controlling impedance at the man/machine interface." In: *Proc. IEEE International Conference on Robotics and Automation.* Vol. 3. May 1989, pp. 1626–1631.

[81] R. M. Holladay, A. D. Dragan, and S. S. Srinivasa. "Legible robot pointing." In: *Proc. IEEE International Symposium on Robot and Human Interactive Communication.* Aug. 2014, pp. 217–223.

[82] R. D. Howe and Y. Matsuoka. "Robotics for surgery." In: *Annual Review of Biomedical Engineering* 1.1 (1999), pp. 211–240.

[83] R. Ikeura and H. Inooka. "Variable impedance control of a robot for cooperation with a human." In: *Proc. IEEE International Conference on Robotics and Automation.* Vol. 3. May 1995, 3097–3102 vol.3.

[84] R. Ikeura, T. Moriguchi, and K. Mizutani. "Optimal variable impedance control for a robot and its application to lifting an object with a human." In: *Proc. IEEE International Workshop on Robot and Human Interactive Communication.* 2002, pp. 500–505.

[85] N. Jarrassé, J. Paik, V. Pasqui, and G. Morel. "How can human motion prediction increase transparency?" In: *Proc. IEEE International Conference on Robotics and Automation.* May 2008, pp. 2134–2139.

[86] N. Jarrassé, T. Charalambous, and E. Burdet. "A Framework to Describe, Analyze and Generate Interactive Motor Behaviors." In: *PLoS ONE* 7.11 (Nov. 2012), e49945.

[87] N. Jarrassé, V. Sanguineti, and E. Burdet. "Slaves no longer: review on role assignment for human-robot joint motor action." In: *Adaptive Behavior* 22.1 (2014), pp. 70–82.

[88] A. Joshi, S. Ghosh, M. Betke, S. Sclaroff, and H. Pfister. "Personalizing Gesture Recognition Using Hierarchical Bayesian Neural Networks." In: *Proc. IEEE Conference on Computer Vision and Pattern Recognition.* July 2017, pp. 455–464.

[89] S. Kajita, F. Kanehiro, K. Kaneko, K. Yokoi, and H. Hirukawa. "The 3D linear inverted pendulum mode: a simple modeling for a biped walking pattern generation." In: *Proc. IEEE/RSJ International Conference on Intelligent Robots and Systems.* Vol. 1. 2001, pp. 239–246.

[90] M. Karmann. "Physical Human-Robot Interaction: Collaborative Goal-directed Swinging of Bulky Objects." Bachelor Thesis. Technische Universität München, 2012.

[91] M. Karmann and M. Wiedemann. "Experimental Validation of Controllers for Human-Robot Cooperative Object Swinging." Practical Course. Technische Universität München, 2014.

[92] S. Katsura and K. Ohnishi. "Human cooperative wheelchair for haptic interaction based on dual compliance control." In: *IEEE Transactions on Industrial Electronics* 51.1 (Feb. 2004), pp. 221–228.

[93] M. Keller. "Towards Inverse Optimal Control for Human-Human Cooperative Object Transport." Bachelor Thesis. Technische Universität München, 2014.

[94] J. Kerr and B. Roth. “Analysis of Multifingered Hands.” In: *International Journal of Robotics Research* 4.4 (1986), pp. 3–17.

[95] H. K. Khalil and J. Grizzle. *Nonlinear systems*. Vol. 3. Prentice hall Upper Saddle River, 2002.

[96] A. Kheddar. “Human-robot haptic joint actions is an equal control-sharing approach possible?” In: *Proc. International Conference on Human System Interactions*. May 2011, pp. 268–273.

[97] C. H. Kim, K. Yonekura, H. Tsujino, and S. Sugano. “Physical control of the rotation center of an unsupported object rope turning by a humanoid robot.” In: *Proc. IEEE-RAS International Conference on Humanoid Robots*. Dec. 2009, pp. 148–153.

[98] K. Kosuge, H. Yoshida, and T. Fukuda. “Dynamic control for robot-human collaboration.” In: *Proc. IEEE International Workshop on Robot and Human Interactive Communication*. Nov. 1993, pp. 398–401.

[99] K. Kosuge, T. Hayashi, Y. Hirata, and R. Tobiyama. “Dance partner robot - Ms DanceR.” In: *Proc. IEEE/RSJ International Conference on Intelligent Robots and Systems*. Vol. 4. Oct. 2003, 3459–3464 vol.3.

[100] H. Krebs, J. Palazzolo, L. Dipietro, M. Ferraro, J. Krol, K. Rannekleiv, B. Volpe, and N. Hogan. “Rehabilitation Robotics: Performance-Based Progressive Robot-Assisted Therapy.” In: *Autonomous Robots* 15.1 (2003), pp. 7–20.

[101] D. Kruse, R. J. Radke, and J. T. Wen. “Human-robot collaborative handling of highly deformable materials.” In: *Proc. American Control Conference*. May 2017, pp. 1511–1516.

[102] D. Kubus, T. Kroger, and F. M. Wahl. “On-line estimation of inertial parameters using a recursive total least-squares approach.” In: *Proc. IEEE/RSJ International Conference on Intelligent Robots and Systems*. Sept. 2008, pp. 3845–3852.

[103] P. Kugler and M. Turvey. *Information, natural law, and the self-assembly of rhythmic movement.* Lawrence Erlbaum Associates, Inc, 1987.

[104] B. Kuipers and S. Ramamoorthy. “Qualitative modeling and heterogeneous control of global system behavior.” In: *Hybrid Systems: Computation and Control*. Springer, 2002, pp. 294–307.

[105] V. Kumar and K. Waldron. “Force distribution in closed kinematic chains.” In: *IEEE Journal on Robotics and Automation* 4.6 (Dec. 1988), pp. 657–664.

[106] M. G. Lagoudakis and R. Parr. “Least-squares policy iteration.” In: *Journal of Machine Learning Research* 4.Dec (2003), pp. 1107–1149.

[107] D. Lakatos, F. Petit, and A. Albu-Schaffer. “Nonlinear Oscillations for Cyclic Movements in Human and Robotic Arms.” In: *IEEE Transactions on Robotics* 30.4 (Aug. 2014), pp. 865–879.

[108] J. D. Langsfeld, A. M. Kabir, K. N. Kaipa, and S. K. Gupta. “Integration of Planning and Deformation Model Estimation for Robotic Cleaning of Elastically Deformable Objects.” In: *IEEE Robotics and Automation Letters* 3.1 (Jan. 2018), pp. 352–359.

[109] M. Lawitzky, J. R. Medina, D. Lee, and S. Hirche. “Feedback motion planning and learning from demonstration in physical robotic assistance: differences and synergies.” In: $IEEE_IROS$. Oct. 2012, pp. 3646–3652.

[110] M. Lawitzky, M. Kimmel, P. Ritzer, and S. Hirche. “Trajectory Generation under the Least Action Principle for Physical Human-Robot Cooperation.” en. In: *Proc. IEEE International Conference on Robotics and Automation*. Karlsruhe, Germany, May 2013, pp. 4285–4290.

[111] S. Lefrancois and C. Gosselin. “Point-to-point motion control of a pendulum-like 3-dof underactuated cable-driven robot.” In: *Proc. IEEE International Conference on Robotics and Automation.* May 2010, pp. 5187–5193.

[112] S. P. Levine, D. A. Bell, L. A. Jaros, R. C. Simpson, Y. Koren, and J. Borenstein. “The NavChair Assistive Wheelchair Navigation System.” In: *IEEE Transactions on Rehabilitation Engineering* 7.4 (Dec. 1999), pp. 443–451.

[113] H. Li, K. Furuta, and F. Chernousko. “A pendulum-driven cart via internal force and static friction.” In: *Proc. International Conference on Physics and Control.* Aug. 2005, pp. 15–17.

[114] H. Li, K. Furuta, and F. Chernousko. “Motion Generation of the Capsubot Using Internal Force and Static Friction.” In: *Proc. IEEE Conference in Decision and Control.* Dec. 2006, pp. 6575–6580.

[115] C. Lichtenthäler and A. Kirsch. “Towards legible robot navigation-how to increase the intend expressiveness of robot navigation behavior.” In: *Proc. International Conference on Social Robotics - Workshop Embodied Communication of Goals and Intentions.* 2013.

[116] H. Lin, F. Guo, F. Wang, and Y.-B. Jia. “Picking up a soft 3D object by feeling the grip.” In: *International Journal of Robotics Research* 34.11 (2015), pp. 1361–1384.

[117] R. Lozano, I. Fantoni, and D. Block. “Stabilization of the inverted pendulum around its homoclinic orbit.” In: *Systems and Control Letters* 40.3 (2000), pp. 197–204.

[118] J. Lu. “Experimental Validation of Adaptive Controllers for Human-Robot Cooperative Swinging of Complex Pendulum-like and Flexible Objects.” Research Internship. Technische Universität München, 2015.

[119] K. M. Lynch and M. T. Mason. “Dynamic Nonprehensile Manipulation: Controllability, Planning, and Experiments.” In: *International Journal of Robotics Research* 18.1 (1999), pp. 64–92.

[120] C. Madan, A. Kucukyilmaz, T. Sezgin, and C. Basdogan. “Recognition of Haptic Interaction Patterns in Dyadic Joint Object Manipulation.” In: *IEEE Transactions on Haptics* 8.1 (Jan. 2015), pp. 54–66.

[121] Y. Maeda, A Takahashi, T. Hara, and T. Arai. “Human-robot cooperation with mechanical interaction based on rhythm entrainment-realization of cooperative rope turning.” In: *Proc. IEEE International Conference on Robotics and Automation.* Vol. 4. 2001, pp. 3477–3482.

[122] L. Magni, R. Scattolini, and K. Åström. “Global stabilization of the inverted pendulum using model predictive control.” In: *Proc. IFAC World Congress.* Vol. 35. 1. 2002, pp. 141–146.

[123] M. T. Mason and K. Lynch. “Dynamic manipulation.” In: *Proc. IEEE/RSJ International Conference on Intelligent Robots and Systems.* Vol. 1. July 1993, pp. 152–159.

[124] J. R. Medina, T. Lorenz, D. Lee, and S. Hirche. “Disagreement-aware physical assistance through risk-sensitive optimal feedback control.” In: *Proc. IEEE/RSJ International Conference on Intelligent Robots and Systems.* Oct. 2012, pp. 3639–3645.

[125] J. Medina, T. Lorenz, and S. Hirche. “Synthesizing Anticipatory Robotic Haptic Assistance Considering Human Behavior Uncertainty.” In: *IEEE Transactions on Robotics* 31.1 (Feb. 2015), pp. 180–190.

[126] J. Medina, M. Lawitzky, A. Mörtl, D. Lee, and S. Hirche. “An experience-driven robotic assistant acquiring human knowledge to improve haptic cooperation.” In: *Proc. IEEE/RSJ International Conference on Intelligent Robots and Systems.* Sept. 2011, pp. 2416–2422.

[127] J. R. Medina Hernandez. “Model-based Control and Learning in Physical Human-Robot Interaction.” Dissertation. München: Technische Universität München, 2015.

[128] S. Miller, J. van den Berg, M. Fritz, T. Darrell, K. Goldberg, and P. Abbeel. “A geometric approach to robotic laundry folding.” In: *International Journal of Robotics Research* 31.2 (2012), pp. 249–267.

[129] N. Miyake. “Constructive Interaction and the Iterative Process of Understanding.” In: *Cognitive Science* 10.2 (1986), pp. 151–177.

[130] K. Mojtahedi, B. Whitsell, P. Artemiadis, and M. Santello. “Communication and Inference of Intended Movement Direction during Human-Human Physical Interaction.” In: *Frontiers in Neurorobotics* 11 (2017), p. 21.

[131] A. Mörtl, M. Lawitzky, A. Kucukyilmaz, M. Sezgin, C. Basdogan, and S. Hirche. “The role of roles: Physical cooperation between humans and robots.” In: *International Journal of Robotics Research* 31.13 (2012), pp. 1656–1674.

[132] A. Mörtl. “Design of Interactive Motor Behaviors for Close Joint Action of Humans and Robots.” Dissertation. München: Technical University of Munich, 2014.

[133] E. Najafi, G. Lopes, and R. Babuska. “Reinforcement learning for sequential composition control.” In: *Proc. IEEE Conference in Decision and Control*. Dec. 2013, pp. 7265–7270.

[134] Y. Nakamura, K. Nagai, and T. Yoshikawa. “Dynamics and Stability in Coordination of Multiple Robotic Mechanisms.” In: *International Journal of Robotics Research* 8.2 (1989), pp. 44–61.

[135] J. Nakanishi, T. Fukuda, and D. Koditschek. “A brachiating robot controller.” In: *IEEE Transactions on Robotics and Automation* 16.2 (Apr. 2000), pp. 109–123.

[136] E. Noohi, M. Zefran, and J. L. Patton. “A Model for Human-Human Collaborative Object Manipulation and Its Application to Human-Robot Interaction.” In: *IEEE Transactions on Robotics* 32.4 (Aug. 2016), pp. 880–896.

[137] I. Palunko, A. Faust, P. Cruz, L. Tapia, and R. Fierro. “A reinforcement learning approach towards autonomous suspended load manipulation using aerial robots.” In: *Proc. IEEE International Conference on Robotics and Automation*. May 2013, pp. 4896–4901.

[139] S. P. Parikh, J. M. Esposito, and J. Searock. “The Role of Verbal and Nonverbal Communication in a Two-person, Cooperative Manipulation Task.” In: *Advances in Human-Computer Interaction* 2014 (Jan. 2014), 9:9–9:9.

[140] C. Passenberg, A. Glaser, and A. Peer. “Exploring the Design Space of Haptic Assistants: The Assistance Policy Module.” In: *IEEE Transactions on Haptics* 6.4 (Oct. 2013), pp. 440–452.

[141] C. Passenberg, N. Stefanov, A. Peer, and M. Buss. “Enhancing task classification in human-machine collaborative teleoperation systems by real-time evaluation of an agreement criterion.” In: *Proc. IEEE World Haptics Conference*. June 2011, pp. 493–498.

[142] A. Pekarovskiy, T. Nierhoff, J. Schenek, Y. Nakamura, S. Hirche, and M. Buss. “Online deformation of optimal trajectories for constrained nonprehensile manipulation.” In: *Proc. IEEE International Conference on Robotics and Automation*. May 2015, pp. 2481–2487.

[143] L. Peternel, T. Petrič, E. Oztop, and J. Babič. “Teaching robots to cooperate with humans in dynamic manipulation tasks based on multi-modal human-in-the-loop approach.” English. In: *Autonomous Robots* 36.1-2 (2014), pp. 123–136.

[144] L. Peternel, N. Tsagarakis, D. Caldwell, and A. Ajoudani. “Robot adaptation to human physical fatigue in human–robot co-manipulation.” In: *Autonomous Robots* (2017), pp. 1–11.

[145] T. Petrič, A. Gams, A. J. Ijspeert, and L. Žlajpah. “On-line frequency adaptation and movement imitation for rhythmic robotic tasks.” In: *International Journal of Robotics Research* 30.14 (2011), pp. 1775–1788.

[146] B. Piccoli and J. Kulkarni. “Pumping a swing by standing and squatting: do children pump time optimally?” In: *IEEE Control Systems* 25.4 (Aug. 2005), pp. 48–56.

[147] X. Provot. “Deformation constraints in a mass-spring model to describe rigid cloth behaviour.” In: *Graphics Interface.* Canadian Information Processing Society. 1995, pp. 147–155.

[148] M Rahman, R Ikeura, and K. Mizutani. “Investigation of the Impedance Characteristic of Human Arm for Development of Robots to Cooperate with Humans.” In: *JSME International Journal Series C Mechanical Systems, Machine Elements and Manufacturing* 45.2 (2002), pp. 510–518.

[149] N. Ratliff, M. Zucker, J. A. Bagnell, and S. Srinivasa. “CHOMP: Gradient optimization techniques for efficient motion planning.” In: *Proc. IEEE International Conference on Robotics and Automation.* May 2009, pp. 489–494.

[150] K. B. Reed and M. A. Peshkin. “Physical Collaboration of Human-Human and Human-Robot Teams.” In: *IEEE Transactions on Haptics* 1.2 (July 2008), pp. 108–120.

[151] K. Reed, J. Patton, and M. Peshkin. “Replicating Human-Human Physical Interaction.” In: *Proc. IEEE International Conference on Robotics and Automation.* Apr. 2007, pp. 3615–3620.

[152] K. Reed, M. Peshkin, M. Hartmann, J. Patton, P. Vishton, and M. Grabowecky. “Haptic cooperation between people, and between people and machines.” In: *Proc. IEEE/RSJ International Conference on Intelligent Robots and Systems.* Oct. 2006, pp. 2109–2114.

[153] J. Roschelle and S. D. Teasley. “Computer Supported Collaborative Learning.” In: ed. by C. O’Malley. Berlin, Heidelberg: Springer Berlin Heidelberg, 1995. Chap. The Construction of Shared Knowledge in Collaborative Problem Solving, pp. 69–97.

[154] L. Rozo, S. Calinon, D. G. Caldwell, P. Jiménez, and C. Torras. “Learning Physical Collaborative Robot Behaviors From Human Demonstrations.” In: *IEEE Transactions on Robotics* 32.3 (June 2016), pp. 513–527.

[155] K. Sakita, K. Ogawara, S. Murakami, K. Kawamura, and K. Ikeuchi. “Flexible cooperation between human and robot by interpreting human intention from gaze information.” In: *Proc. IEEE/RSJ International Conference on Intelligent Robots and Systems.* Vol. 1. Sept. 2004, 846–851 vol.1.

[156] J. K. Salisbury and J. J. Craig. “Articulated Hands: Force Control and Kinematic Issues.” In: *International Journal of Robotics Research* 1.1 (1982), pp. 4–17.

[157] M. M. Schill, F. Gruber, and M. Buss. “Quasi-direct nonprehensile catching with uncertain object states.” In: *Proc. IEEE International Conference on Robotics and Automation.* May 2015, pp. 2468–2474.

[158] A. M. Schmidts, M. Schneider, M. Kühne, and A. Peer. “A new interaction force decomposition maximizing compensating forces under physical work constraints.” In: *Proc. IEEE International Conference on Robotics and Automation.* May 2016, pp. 4922–4929.

[159] L. Sentis, J. Park, and O. Khatib. “Compliant Control of Multicontact and Center-of-Mass Behaviors in Humanoid Robots.” In: *IEEE Transactions on Robotics* 26.3 (June 2010), pp. 483–501.

[160] A. Shiriaev, J. Perram, and C. Canudas-de Wit. “Constructive Tool for Orbital Stabilization of Underactuated Nonlinear Systems: Virtual Constraints Approach.” In: *IEEE Transactions on Automatic Control* 50.8 (Aug. 2005), pp. 1164–1176.

[161] B. Siciliano and O. Khatib. *Springer handbook of robotics.* Springer Science & Business Media, 2016, pp. 187 –206.

[162] G. Slota, M. Latash, and V. Zatsiorsky. “Grip forces during object manipulation: experiment, mathematical model, and validation.” English. In: *Experimental Brain Research* 213.1 (2011), pp. 125–139.

[163] J.-J. E. Slotine, W. Li, et al. *Applied nonlinear control.* Vol. 199. 1. Prentice hall New Jersey, 1991.

[164] M. Spong. “The swing up control problem for the Acrobot.” In: *IEEE Control Systems* 15.1 (Feb. 1995), pp. 49–55.

[165] M. Spong and D. Block. “The Pendubot: a mechatronic system for control research and education.” In: *Proc. IEEE Conference in Decision and Control.* Vol. 1. Dec. 1995, pp. 555–556.

[166] N. Stefanov, A. Peer, and M. Buss. “Role determination in human-human interaction.” In: *Proc. Joint WorldHaptics, EuroHaptics Conference and Symposium on Haptic Interfaces for Virtual Environment and Teleoperator Systems.* Mar. 2009, pp. 51–56.

[167] F. Stulp, J. Grizou, B. Busch, and M. Lopes. “Facilitating intention prediction for humans by optimizing robot motions.” In: *Proc. IEEE/RSJ International Conference on Intelligent Robots and Systems.* Sept. 2015, pp. 1249–1255.

[168] J. F. Sturm. “Using SeDuMi 1.02, A Matlab toolbox for optimization over symmetric cones.” In: *Optimization Methods and Software* 11.1-4 (1999), pp. 625–653.

[169] R. S. Sutton. “Learning to predict by the methods of temporal differences.” In: *Machine Learning* 3.1 (Aug. 1988), pp. 9–44.

[170] A. Thobbi, Y. Gu, and W. Sheng. “Using human motion estimation for human-robot cooperative manipulation.” In: *Proc. IEEE/RSJ International Conference on Intelligent Robots and Systems.* Sept. 2011, pp. 2873–2878.

[171] A. Turnwald, D. Althoff, D. Wollherr, and M. Buss. “Understanding Human Avoidance Behavior: Interaction-Aware Decision Making Based on Game Theory.” In: *International Journal of Social Robotics* 8.2 (2016), pp. 331–351.

[172] F. E. Udwadia and R. E. Kalaba. “A new perspective on constrained motion.” In: *Proceedings: Mathematical and Physical Sciences* (1992), pp. 407–410.

[173] C. Vesper, R. van der Wel, G. Knoblich, and N. Sebanz. “Making oneself predictable: reduced temporal variability facilitates joint action coordination.” English. In: *Experimental Brain Research* 211.3-4 (2011), pp. 517–530.

[174] B. L. Walcott, M. J. Corless, and S. H. Żak. “Comparative study of non-linear state-observation techniques.” In: *International Journal of Control* 45.6 (1987), pp. 2109–2132.

[175] I. D. Walker, R. A. Freeman, and S. I. Marcus. “Analysis of Motion and Internal Loading of Objects Grasped by Multiple Cooperating Manipulators.” In: *International Journal of Robotics Research* 10.4 (1991), pp. 396–409.

[176] H. Wang and K. Kosuge. “Control of a Robot Dancer for Enhancing Haptic Human-Robot Interaction in Waltz.” In: *IEEE Transactions on Haptics* 5.3 (Mar. 2012), pp. 264–273.

[177] H. Wang and K. Kosuge. "Understanding and reproducing waltz dancers' body dynamics in physical human-robot interaction." In: *Proc. IEEE International Conference on Robotics and Automation.* May 2012, pp. 3134–3140.

[178] Z. Wang, A. Peer, and M. Buss. "An HMM approach to realistic haptic human-robot interaction." In: *Proc. Joint WorldHaptics, EuroHaptics Conference and Symposium on Haptic Interfaces for Virtual Environment and Teleoperator Systems.* Mar. 2009, pp. 374–379.

[179] P. Weiß. "Conduction and Analysis of Human-Human Cooperative Object Transport Experiments." Internship. Technische Universität München, 2014.

[180] R. P. van der Wel, G. Knoblich, and N. Sebanz. "Let the force be with us: dyads exploit haptic coupling for coordination." In: *Journal of Experimental Psychology: Human Perception and Performance* 37.5 (2011), p. 1420.

[181] D. Williams and O. Khatib. "The virtual linkage: a model for internal forces in multi-grasp manipulation." In: *Proc. IEEE International Conference on Robotics and Automation.* Vol. 1. May 1993, pp. 1025–1030.

[182] F. Wirnshofer. "Cooperative Object Swinging: Analysis and Modeling of Human Dyads." Bachelor Thesis. Technische Universität München, 2013.

[183] F. Wirnshofer. "Experimental Validation of Controllers for Human-Robot Cooperative Swinging of Complex Pendulum-like Objects." Research Internship. Technische Universität München, 2014.

[184] T. Wojtara, M. Uchihara, H. Murayama, S. Shimoda, S. Sakai, H. Fujimoto, and H. Kimura. "Human-robot collaboration in precise positioning of a three-dimensional object." In: *Automatica* 45.2 (2009), pp. 333 –342.

[185] C. Yang, G. Ganesh, S. Haddadin, S. Parusel, A. Albu-Schaeffer, and E. Burdet. "Human-Like Adaptation of Force and Impedance in Stable and Unstable Interactions." In: *IEEE Transactions on Robotics* 27.5 (Oct. 2011), pp. 918–930.

[186] K. Yano and K. Terashima. "Robust liquid container transfer control for complete sloshing suppression." In: *IEEE Transactions on Control Systems Technology* 9.3 (May 2001), pp. 483–493.

[187] K. Yokoyama, H. Handa, T. Isozumi, Y. Fukase, K. Kaneko, F. Kanehiro, Y. Kawai, F. Tomita, and H. Hirukawa. "Cooperative works by a human and a humanoid robot." In: *Proc. IEEE International Conference on Robotics and Automation.* Vol. 3. Sept. 2003, 2985–2991 vol.3.

[188] K. Yoshida. "Swing-up control of an inverted pendulum by energy-based methods." In: *Proc. American Control Conference.* Vol. 6. 1999, pp. 4045–4047.

[189] T. Yoshikawa. "Virtual truss model for characterization of internal forces for multiple finger grasps." In: *IEEE Transactions on Robotics and Automation* 15.5 (Oct. 1999), pp. 941–947.

[190] T. Yoshikawa and K. Nagai. "Manipulating and grasping forces in manipulation by multifingered robot hands." In: *IEEE Transactions on Robotics and Automation* 7.1 (Feb. 1991), pp. 67–77.

[191] T. Yoshikawa and X.-Z. Zheng. "Coordinated Dynamic Hybrid Position/Force Control for Multiple Robot Manipulators Handling One Constrained Object." In: *International Journal of Robotics Research* 12.3 (1993), pp. 219–230.

[192] Y.-Q. Yu, L. L. Howell, C. Lusk, Y. Yue, and M.-G. He. "Dynamic modeling of compliant mechanisms based on the pseudo-rigid-body model." In: *Journal of Mechanical Design* 127.4 (2005), pp. 760–765.

[193] D. Zameroski, G. Starr, J. Wood, and R. Lumia. “Rapid swing-free transport of nonlinear payloads using dynamic programming.” In: *ASME Journal of Dynamic Systems, Measurement, and Control* 130.4 (2008), 041001–041001–11.

[194] D. Zanotto, G. Rosati, and S. Agrawal. “Modeling and Control of a 3-DOF pendulum-like manipulator.” In: *Proc. IEEE International Conference on Robotics and Automation*. May 2011, pp. 3964–3969.

[195] M. Zhao, R. Shome, I. Yochelson, K. Bekris, and E. Kowler. “An Experimental Study for Identifying Features of Legible Manipulator Paths.” In: *Proc. International Symposium on Experimental Robotics*. Ed. by M. A. Hsieh, O. Khatib, and V. Kumar. Cham: Springer International Publishing, 2016, pp. 639–653.

[196] N. Zoso and C. Gosselin. “Point-to-point motion planning of a parallel 3-dof underactuated cable-suspended robot.” In: *Proc. IEEE International Conference on Robotics and Automation*. May 2012, pp. 2325–2330.

[197] B.-R. Zuo and W.-H. Qian. “A general dynamic force distribution algorithm for multifingered grasping.” In: *IEEE Transactions on Systems, Man, and Cybernetics, Part B: Cybernetics* 30.1 (Feb. 2000), pp. 185–192.

Own Publications

[28] F. Christange, P. Donner, and M. Buss. “Energy control for complex pendulums based on tracking of online computed force trajectories.” In: *Proc. IEEE International Conference on Robotics and Automation*. May 2015, pp. 6044–6051.

[37] P. Donner and M. Buss. “Cooperative Swinging of Complex Pendulum-Like Objects: Experimental Evaluation.” In: *IEEE Transactions on Robotics* 32.3 (June 2016), pp. 744–753.

[38] P. Donner, F. Christange, and M. Buss. “Human-robot cooperative swinging of complex pendulum-like objects.” In: *Proc. IEEE/RSJ International Conference on Intelligent Robots and Systems*. Nov. 2013, pp. 4602–4608.

[39] P. Donner, F. Christange, and M. Buss. “Adaptive simple pendulum swing-up controller based on the closed-loop fundamental dynamics.” In: *Proc. IEEE European Control Conference*. July 2015, pp. 2798–2805.

[40] P. Donner, F. Christange, and M. Buss. “Fundamental Dynamics based Adaptive Energy Control for Cooperative Swinging of Complex Pendulum-like Objects.” In: *Proc. IEEE Conference in Decision and Control*. Dec. 2015, pp. 392–399.

[41] P. Donner, S. Endo, and M. Buss. “Physically Plausible Wrench Decomposition for Multi-effector Object Manipulation.” In: *IEEE Transactions on Robotics* (2018 (accepted)).

[42] P. Donner, F. Wirnshofer, and M. Buss. “Controller synthesis for human-robot cooperative swinging of rigid objects based on human-human experiments.” In: *Proc. IEEE International Symposium on Robot and Human Interactive Communication*. Aug. 2014, pp. 586–592.

[43] P. Donner, A. Mörtl, S. Hirche, and M. Buss. “Human-robot cooperative object swinging.” In: *Proc. IEEE International Conference on Robotics and Automation*. May 2013, pp. 4343–4349.

[44] P. Donner, F. Christange, J. Lu, and M. Buss. “Cooperative Dynamic Manipulation of Unknown Flexible Objects: Joint Energy Injection Based on Simple Pendulum Fundamental Dynamics.” In: *International Journal of Social Robotics* 9.4 (Sept. 2017), pp. 575–599.

[138] I. Palunko, P. Donner, M. Buss, and S. Hirche. “Cooperative suspended object manipulation using reinforcement learning and energy-based control.” In: *Proc. IEEE/RSJ International Conference on Intelligent Robots and Systems*. Sept. 2014, pp. 885–891.